X-ray Probing of the Matter Surrounding Accretion-Powered X-ray Pulsars

Yuki Yoshida

Department of Physics, College of Science, Rikkyo University, 3-34-1 Nishi-Ikebukuro, Toshima, Tokyo 171-8501, Japan

A thesis submitted to the Department of Physics, College of Science, Rikkyo University on May 14, 2018
in partial fulfillment of the requirements of the degree of Doctor of Philosophy in Physics

ABSTRACT

Accretion-powered X-ray pulsar consists of a magnetized neutron star and a normal stellar companion. The magnetized neutron stars are astrophysical laboratories for testing theories of dense matter physics and propagation of radiation in strong magnetic fields. They are also good laboratories for study of an accretion flow onto a compact star, and for investigation of interactions between matters and X-rays. The X-ray emission lines, observed in their energy spectrum, provide information on the accretion flow and the interaction between intense X-rays and the accreting matter onto the neutron star in their strong magnetic field. The photoelectric absorption by the matter along the line of sight is also helpful to investigate the matter around the accretion-powered X-ray pulsars. We diagnostic the physical characteristic, such as the size, geometry, density and ionization state of the matter surrounding the accretion-powered X-ray pulsar through the X-ray spectroscopy, focusing on emission line as well as the photoelectric absorption edge.

In this thesis, we present the results of the *Suzaku* observation of 23 accretion-powered X-ray pulsars. From phase-averaged spectroscopies, iron K_α emission lines were detected at almost 6.40 keV from the all the sources in our samples. Their emission mechanism is considered to be the fluorescent reprocessing of the X-rays from the X-ray pulsar by cold matter surrounding the X-ray sources. Detailed phase-resolved spectral analyses reveal clear flux modulations of the iron K_α line with their rotation period of the neutron star, in the four sources; 4U 1907+097, 4U 1538-522, GX 301-2, and GX 1+4. We point out an apparent flux modulation of emission line with rotation period of neutron star due to the finite speed of light (we call this effect the "finite light speed effect"), if the mechanism of the line emission is a kind of reprocessing, such as the fluorescence by X-ray irradiation from X-ray pulsars. This effect is applied to the observed pulse phase modulation of the iron line flux of GX 1+4.

We first discovered the significant modulation of the iron absorption K-edge depth with pulse period from four pulsars; GX 301-2, Vela X-1, GX 1+4, and OAO 1657-415. The modulation of the iron K-edge depth can be reasonably explained by the following scenario. The accreting matter along the magnetic filed line, which is constrained into a part of the Alfvén shell, is responsible for the absorption edge. The constrained accreting matter co-rotates with the neutron star spin because they are confined by the strong magnetic field of the pulsar. We further discuss the matter surrounding the accretion-powered X-ray pulsar based on the knowledge provided by our analyses of the emission lines and absorption edge of iron.

Contents

List of Figures

List of Tables

Chapter 1

Introduction

Soon after the first X-ray observation with the satellite, rapid and sometimes periodic variations in the X-ray intensity of many point-like X-ray sources were discovered. With combination of observational results with optical and X-ray telescopes, it have been demonstrated that these X-ray sources are members of binary systems, namely X-ray binaries, which consist of a normal star and a collapsed star. In the system, matter streams from the normal star onto the nearby collapsed star with an intense gravitational field. Most of point X-ray sources discovered in our Galaxy belong to this class. The first discovered extra-solar X-ray source, Scorpius X-1 (Giacconi et al. 1962), was also identified as the X-ray binary system. Further studies suggested that the X-ray luminosity of Scorpius X-1 was about ten thousand times the total luminosity of the Sun, integrated over the all wavelength. In later the optical counterpart of Scorpius X-1 was identified to a faint 13th magnitude star, which puzzled astronomers to understand the cause of X-ray emission from the source. On the basis of these sparkling results, the concept of mass accretion on to a compact object was considered to explain the presence of strong X-ray emission from extra-solar sources, where gravitational potential energy of accreted matter is converted into kinetic energy, which are released in a form of X-rays when the matter decelerates through a radiative shock and settles onto the stellar surface.

An "accretion-powered X-ray pulsar (APXP)" is a subclass of the X-ray binaries, which consists of a rotating neutron star (NS) involving strong magnetic field, orbiting a normal star. The NS has its typically radius of 10 km and mass of $1.4 M_{\odot}$ ($M_{\odot}$ is the solar mass; 1.99×10^{33} g) and then its core has higher density than nuclear matter (2.3×10^{14} g cm^{-3}). In the APXP, mass transfer from the companion star to the NS occurs and the matter from the stellar companion falls toward the NS, as forming a so-called accretion disk around the NS. Eventually the accretion matter is channeled by the strong magnetic field of the NS, and forms a columnar geometry. Although this general picture is widely accepted, how gas flows from the circumstellar accretion disk into the magnetosphere of the rapidly rotating NS and eventually to the NS surface is a complex and as yet unsolved problem.

Past observations have revealed that most of the APXPs exhibit prominent emission lines from neutral iron atoms at 6.4 keV as well as their absorption K-edge at 7.1 keV (e.g., White et al. 1983; Nagase 1989). These iron lines from the APXPs are considered to be

produced through fluorescence of nearby cold matters illuminated by X-rays with energies above the ionization energy from compact stars (Koyama 1985; Inoue 1985; Makino et al. 1985; Makishima 1986; Nagase 1989). Since the emission line and absorption K-edge of iron can be hence associated with each other, a detailed investigation of them is necessary for diagnostics of their mechanism and origin. Identification of emission lines (ionization state of elements) and observed changes in line parameters with time and source luminosity provide important information on the line emitting regions such as relatively thick inhomogeneous and clumpy stellar wind from the companion star (Sako et al. 2002; Watanabe et al. 2006), surface or photosphere of the companions star, and probably the accreting matter around the Alfvén shell (Pravdo et al. 1977; Basko 1980). The observed absorption edge parameter provides us with the information of the matter placed between the X-ray source and an observer. This information is an independent one from those obtained by the emission line. Therefore, a thorough investigation of not only the emission lines but also the absorption edge in the spectrum of APXPs will provide new information on the matter surrounding the NS, e.g., the accreting matter onto the NS interacted with its strong magnetic field.

In this thesis, we analyzed the data of the *Suzaku* observation of the several APXPs. The main aim of this thesis is to reveal the distribution of the matter in APXP systems through the understanding of the physical mechanisms relevant to the production of emission lines, especially the 6.4 keV iron K_α line emissions, as well as absorption K-edge of iron at 7.1 keV. This thesis is organized as below. Chapter 2 gives an introduction to the close X-ray binary systems and the APXPs. In chapter 3 we show instrumentation of *Suzaku*. Chapter 4 shows the *Suzaku* observations of APXPs. In chapter 5 the *Suzaku* data of APXPs were analyzed. In chapter 6, we make discussion with the results of our analysis and provide interpretations of them. Chapter 7 is the conclusion of this thesis.

Chapter 2

Review

Contents

2.1 X-ray Binary Source and Accretion

2.1.1 X-ray Binaries

A binary system consists of two stars, which orbit around a common center of mass, that is they are gravitationally bound to each other. In very general terms, one can simply define X-ray binaries as systems that contain a compact object orbiting an optical companion, which is a sub-class of binary systems. They are close binary systems and there exists a mass-transfer from the companion star to the compact object. The falling or accreting matter toward the compact object often forms a so-called accretion disk around the compact object. Gravitational energy of the accreted matter heats the gas around the compact object to very high temperatures (10^6 to 10^8 K), and the gas brightly shines in X-ray regime ($L_{\rm X} = 10^{33}$–10^{38} ergs s^{-1}). Figure 2.1 shows a sketch of an X-ray binary system as it would be seen by a nearby observer (Klochkov 2007). There are several classification schemes depending on whether the emphasis is put on the type of the compact star or the physical properties of the optical star. Indicating by a tree-diagram depicting all the different subsystems in Figure 2.2, X-ray binaries divide up into black hole systems, NS binaries or cataclysmic variables (if the compact object is a white dwarf). The X-ray binaries are also conventionally classified as low mass X-ray binaries (LMXBs) and high mass X-ray binaries (HMXBs) according to the mass of the companion star. HMXBs contain early-type (O or B) companions (typically mass of $M_{\rm p} > 10M_{\odot}$), while the spectral type of the optical star (in general $M_{\rm p} < 1M_{\odot}$) in LMXBs is later than A. The classification of this companion star closely relate to the mode of mass-transfer mechanism and the environment surrounding the X-ray source.

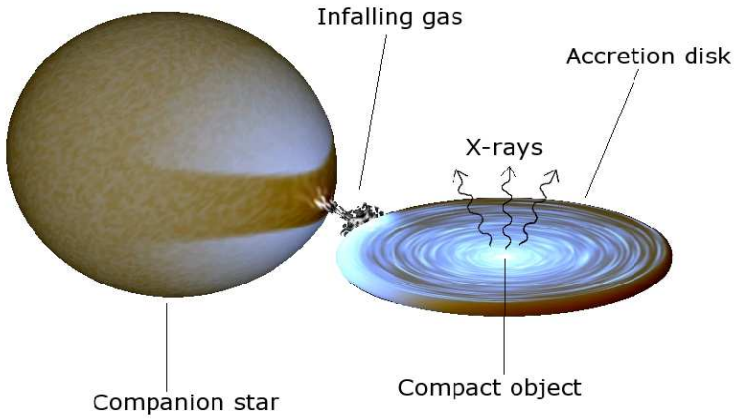

Figure 2.1: A schematic view of an X-ray binary (Klochkov 2007).

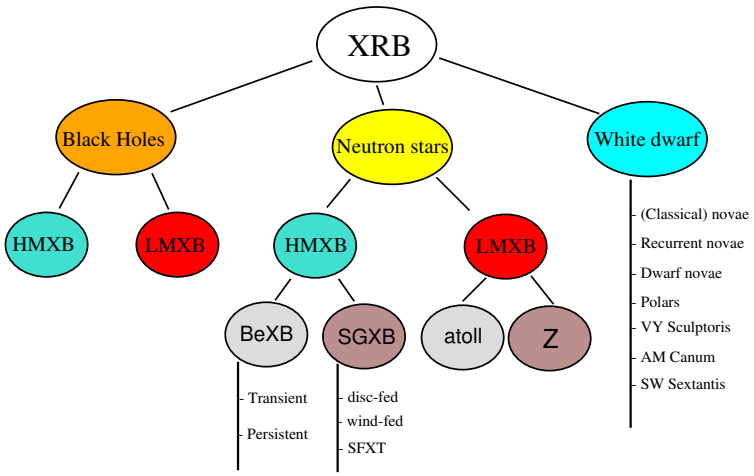

Figure 2.2: Classification of X-ray binaries (Reig 2011).

2.1.2 Accretion in Binary System

One of the most efficient energy sources is known as an accretion onto a compact star, where the gravitational energy is efficiently converted to kinetic or thermal energy. The X-ray binaries are powered by this mechanism. If a particle falls onto a compact object with a mass M_* and a radius R_* from an infinite distance along a radial direction, the velocity at r from the center of the compact object is represented by a free fall velocity, given by

$$v_{\rm ff}(r) = \sqrt{\frac{2GM_*}{r}}, \tag{2.1}$$

where G is the gravitational constant. Assuming that all the kinetic energy liberated is converted to radiation at the surface of the star, the total luminosity, $L_{\rm acc}$, can be given by

$$L_{\rm acc} = \frac{1}{2}\dot{M}v_{\rm ff}(R_*)^2 = \frac{GM_*\dot{M}}{R_*}, \tag{2.2}$$

where $\dot{M}$ is the steady accretion rate (in mass per unit time). For a modest mass transfer rate of $\dot{M} \sim 10^{17}$ g s^{-1}, one expects a luminosity of 10^{37} ergs s^{-1}. If it emits thermally from an area of a few times the size of the compact object, this radiation must predominantly fall in the X-ray band ($\sim$1 keV). Higher characteristic temperatures occur when the NS has a strong magnetic field that funnels all accreting matter onto two small areas near its poles, or when for some reason the emission is (partially) non-thermal.

The liberated accreted energy $L_{\rm acc}$ is sometimes expressed in a unit of its Eddington luminosity $L_{\rm edd}$. Assuming spherical symmetry, fully ionized accreted matter consisting of only hydrogen, and a steady accretion, $L_{\rm edd}$ represents the maximum possible luminosity, above which a star starts blowing away its outer layers by radiation pressure. $L_{\rm edd}$ can be derived by equating the gravitational force exerted by a star to the radiation force by fully

ionized hydrogen plasma, and is given by

$$L_{\rm edd} = \frac{4\pi G M_* m_{\rm p} c}{\sigma_{\rm T}} \sim 1.3 \times 10^{38} \left(\frac{M_*}{M_\odot}\right) \ {\rm ergs\,s^{-1}}, \tag{2.3}$$

where $m_{\rm p}$ is the proton mass ($m_{\rm p} = 1.7 \times 10^{-24}$ g), and $\sigma_{\rm T}$ is the Thomson scattering cross section ($\sigma_{\rm T} = 6.7 \times 10^{-25}$ cm^2).

Mass transfer from the companion star to the compact star takes place by different mechanisms according to some physical properties of binary system. In the HMXBs, the matter from the companion star generally accretes through stellar wind or equatorial disk. On the other hand, in the LMXBs, mass transfer occurs through the inner Lagrange point– the point where sum of gravitational forces and centrifugal force equals to zero. In the following section, we provide description of the different aspects of accreting mechanisms.

2.1.2.1 Roche lobe overflow

A star with certain mass and radius consists of spherical equipotential surfaces around it. By the presence of second star, the equipotential surfaces of a star appear no longer symmetric. They distort from spherical geometry and represent by a combined effective potential of both the stars, known as the Roche potential. The Roche potential is given by

$$\Phi_{\rm R}(\boldsymbol{r}) = -\frac{GM_1}{|\boldsymbol{r} - \boldsymbol{r}_1|} - \frac{GM_2}{|\boldsymbol{r} - \boldsymbol{r}_2|} - \frac{1}{2}|\boldsymbol{\omega} \times \boldsymbol{r}|^2, \tag{2.4}$$

where M_1 and M_2 are the masses of two stars, $\boldsymbol{r}_1$ and $\boldsymbol{r}_2$ are the position vectors of its centers, and $\boldsymbol{\omega}$ is the orbital angular velocity vector (Frank et al. 2002). The first and second terms are the gravitational potential, and the third one is the centrifugal potential. Close to each star, the potential is dominated by the gravitational potential of the star making the equipotential plane almost spherical. Figure 2.3 shows sections in the orbital plane of equipotential surfaces of $\Phi_{\rm R}$. The some extremum points are called the Lagrange points, where the net force on a test particle cancel out, and the number of them is five. It can be seen that the lobes of both the stars are connected at a point called first Lagrange point L_1. This equipotential surface is called Roche lobe. By some reasons, one of the stars in the binary system may increase in radius, or the binary separation may shrink and then one star fills its own Roche lobe. Then the gravitational attraction force of the compact star can gradually remove material from the companion star and the mass transfer occurs via the Lagrange point $\rm L_1$ (Frank et al. 2002; Longair 2011). Such type of mass transfer mechanism is known as "Roche-lobe overflow" and is applicable to systems where accretion disk are formed especially in LMXBs and in a few HMXBs.

If the matter in-falling on the compact object has sufficient specific angular momentum J, it will form a rotationally flattened disk around the compact object referred as the accretion disk. Assuming that the local circular velocity of the accreting matter can be approximated by Keplerian, the specific angular momentum J at the radius r is given by

$$J = \Omega_{\rm K} r^2 = \sqrt{G M_* r}, \tag{2.5}$$

where $\Omega_{\rm K} = \sqrt{GM_*/r^3}$ is an angular velocity at the radius of r. This formula can be rewrote for a radius,

$$R_{\rm circ} = \frac{J^2}{GM_*}. \tag{2.6}$$

Here $R_{\rm circ}$ is the circularization radius for the matter with specific angular moment J. If the accretion matter satisfies this condition, which means that the matter has an adequate angular momentum, the Keplerian accretion disk can be formed.

The estimation of circularization radius can also constrain the upper limit of the disk size. In other words, this relates to a distance where the disk begins to form. For the accretion via the Roche lobe overflow in LMXB system, the circularization radius can be simply described as

$$R_{\rm circ} \sim 3.5 \times 10^9 \left(\frac{M_{\rm p}}{M_\odot}\right) \left(\frac{P_{\rm orb}}{1\ {\rm hr}}\right)\ {\rm cm}, \tag{2.7}$$

where, $P_{\rm orb}$ is the orbital period of binary system and $M_{\rm p}$ is the mass of companion star (Frank et al. 2002). As it can be clearly seen, the $R_{\rm circ}$ is sufficiently larger than the size of compact object for both NSs and white dwarfs (10^6 and 10^9 cm respectively). Therefore an accretion disk is always expected to form during the process of Roche-lobe overflow.

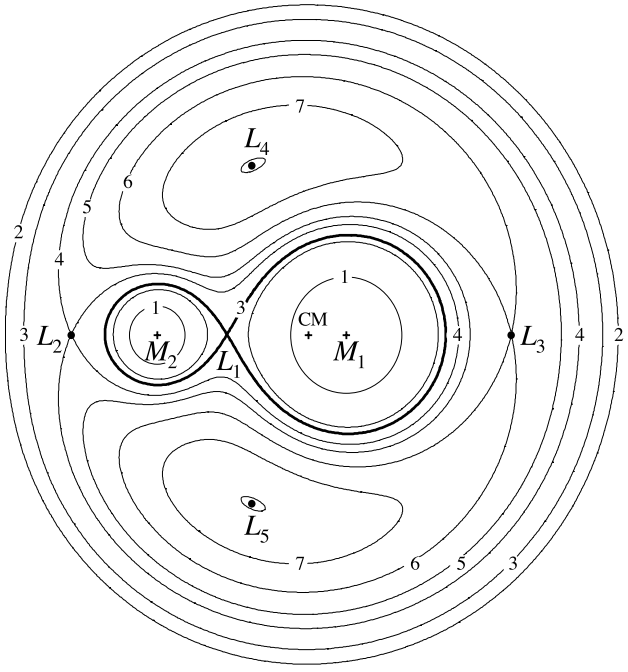

Figure 2.3: Sections in the orbital plane of the Roche equipotentials $\Phi_{\rm R}$=constant, for a binary system with mass ratio $q = M_2/M_1 = 0.25$ (Frank et al. 2002). Shown are the centre of mass and Lagrange points L_1–L_5. The equipotentials are labelled 1–7 in order of increasing $\Phi_{\rm R}$.

2.1.2.2 Capture from the Stellar Wind

Significant amount of the stellar mass of the companion may be ejected in the form of a stellar wind, during its life, and a fraction of this material be captured gravitationally by the compact object. Foregoing accretion mechanism is called "stellar wind accretion" and is usually applicable to the HMXBs (Bondi & Hoyle 1944; Davidson & Ostriker 1973). They are very luminous in nature and hence most of the first sources to be discovered like Vela X-1 fall in this category.

Mass loss rate from these early type companions are between 10^{-8}–10^{-6} $M_\odot$ yr^{-1} and are in the form of intense, supersonic stellar winds. This wind velocity greatly exceeds the sound velocity (c_s) the local medium given by $c_\mathrm{s} \sim 10\left(\frac{T}{10^4\,\mathrm{K}}\right)$ km s^{-1}. The accreting gas as a result is not in the form of hydrostatic equilibrium. In general only a small fraction of the wind is accreted, in contrast to the Roche lobe overflow case where almost all the mass is captured by the accreting component. A compact object with mass M_* and moving with relative velocity v_rel through a medium with sound speed c_s will gravitationally capture matter along a roughly cylindrical region with its axis along the relative wind direction (Davidson & Ostriker 1973; Lamb et al. 1973). The radius R_acc of the cylinder also called the accretion radius or gravitational capture radius is given by

$$R_\mathrm{acc} = \frac{2GM_*}{v_\mathrm{rel}^2 + c_\mathrm{s}^2}, \tag{2.8}$$

where $v_\mathrm{rel}^2 = v_\mathrm{wind}^2 + v_\mathrm{orb}^2$, v_orb^2 is an orbital velocity of the compact object, and v_wind is a stellar wind velocity (see Bondi & Hoyle 1944; Blondin et al. 1990). In most cases, $c_\mathrm{s} \ll v_\mathrm{rel}$ and the term of c_s^2 can be neglected. Since v_wind is of the order of 1000–2000 km s^{-1} and v_orb is considerably lower, R_acc is estimated as $\sim 10^{10}$ cm. The mass accretion rate $\dot{M}$ is described with R_acc, v_wind, and density of the wind ρ_wind as

$$\dot{M} = \pi R_\mathrm{acc}^2 \rho_\mathrm{wind} v_\mathrm{wind}. \tag{2.9}$$

Since the stellar winds are generally inhomogeneous, ρ_wind and $\dot{M}$ fluctuate largely. These therefore make the compact object with massive companion highly time variable in X-ray.

For the case of the stellar wind accretion, the specific angular momentum J is given by

$$J = \frac{1}{4}\Omega_\mathrm{orb}(R_\mathrm{acc})^2, \tag{2.10}$$

where Ω_orb is the orbital angular velocity. Following Frank et al. (2002), the circularization radius for the stellar wind accretion can be derived to be

$$R_\mathrm{circ} \sim 1.3 \times 10^6 \left(\frac{M_\mathrm{p}}{M_\odot}\right)^{1/3} \left(\frac{P_\mathrm{orb}}{10\,\mathrm{d}}\right)^{2/3} \mathrm{cm}. \tag{2.11}$$

For $M_\mathrm{p} = 10 M_\odot$, this is greater than the size of the compact object in case of NSs or white dwarfs. So in case of the stellar wind accretion, accretion disks may be formed (Boerner et al. 1987), but are small in size. Anyway, it is difficult to decide whether the disk formation condition (Equation 2.6) is satisfied.

2.1.2.3 Mass accretion from the equatorial disk

Mass loss from the equatorial disk is the mechanism of mass transfer for HMXBs with B-emission companion stars (Be stars), which is a dwarf, sub-giant or giant O/Be star (luminosity class Ⅲ–V; Reig 2011). So, Be/X-ray binary (BeXB) is a subclass of HMXBs. In these binary systems, the Be companion star rapidly rotates, shows, at irregular time intervals, outbursts of equatorial mass ejection which produce a rotating ring of gas around the star, giving rise to hydrogen emission lines in the optical spectrum. These systems typically have a large orbital period, moderate eccentricity, and being a non-supergiant system, the Be star lies deep within the Roche lobe. The abrupt accretion of matter onto the NS occurs while passing through the circumstellar disk of the Be companion. The ejected matter from the equatorial disk is captured at a distance $R_{\rm acc}$ from the NS as in the case of wind-fed HMXBs and the same description can be assumed to the first approximation.

Strong X-ray outbursts triggered by such the abrupt mass accretion are often observed from these system (Okazaki & Negueruela 2001). During such outbursts, the X-ray emission can be transiently enhanced by a large factor. Most BeXBs are transient sources and display two types of outbursts, such as (i) short, periodic (according to orbital period of binary system), less luminous Type I outbursts ($\leqslant 10^{36}$–10^{37} ergs s^{-1}), lasting for a few days, occurring at the phase of the periastron passage; and (ii) giant, longer, Type Ⅱ outbursts ($L_{\rm X} \geqslant 10^{37}$ ergs s^{-1}), lasting for several weeks to months, occurring when a large fraction of matter is accreted from the disk of Be star no showing any clear orbital dependence. Type Ⅱ outbursts are sometimes followed by smaller recurrent Type I outbursts. It also shows a persistent low luminosity X-ray emission during quiescence (Negueruela et al. 1998).

2.2 Accretion-Powered X-ray Pulsars

This thesis aims at studying the matter surrounding the highly magnetized NSs through emission lines and the absorption features found in their X-ray spectra. Following sections, we describe the properties of the X-ray binaries especially containing a strongly magnetized NS and a normal stellar companion as a mass donor, so called "accretion-powered pulsar".

2.2.1 General Picture

The first discovered accretion-powered pulsar is Centaurus X-3 (Cen X-3) in 1971 (Giacconi et al. 1971) with the *Uhuru* satellite. Cen X-3 exhibits a pulsed variation with a period of 4.84 s only in the X-ray flux. In the accretion-powered pulsar, since the NS has a strong magnetic field, typically 10^{12} G, the accretion flow will be disrupted at some distance from the NS by the magnetic field, and channeled to the magnetic poles of the NS, where most of X-rays originate from the conversion of gravitational potential energy into kinetic or thermal energy with a shock wave heating as described in § 2.1.2. If the magnetic poles are displaced with respect to the rotational axis of the NS, the observed X-ray flux will be modulated with the spin period of the NS, leading to the phenomenon of X-ray pulsating (Lamb et al. 1973). The X-ray pulsation is a common feature among the accretion-powered pulsar, therefore, the accretion-powered pulsars are also called APXPs or just "X-ray pulsars". About 110 APXPs are now known, having a wide range of pulse periods from a few milli-seconds to several hours. Some sources with the stable accretion are persistently bright in X-ray, which have been well investigated since the early age of the cosmic X-ray observations which started in 1962 (Giacconi et al. 1962), while others remain in their quiescent state for most of the time, and can be observed only during short episodes (outbursts) of high X-ray luminosity (so called transient sources).

The APXPs are astrophysical laboratories for testing accretion dynamics and the physical mechanisms in extreme conditions that are realized in the vicinity of NSs, at the site of X-ray emission. An X-ray study is the only way to investigate the physical information and process about the NS, accreting matter and its surrounding environment.

2.2.2 Accretion in X-ray Pulsars

The magnetic field strength at the surface of NS is typically about 10^{12} G. The strong magnetic fields play a crucial role in governing the dynamics of gas flow around the compact object (Pringle & Rees 1972). Because of the strong magnetic field, the accretion matter cannot form the accretion disk in vicinity of the NS. Its boundary is determined by the balance between the magnetic pressure and the ram pressure of the in-falling matter, we call such a boundary the Alfvén surface (Lamb et al. 1973). In term of the Keplerian gas velocity $v(r_{\rm A})$ and density $\rho(r_{\rm A})$ at radius of the Alfvén surface, $r_{\rm A}$, from the center of the NS, the balance is given by

$$p_{\rm mag} = p_{\rm ram} \Leftrightarrow \frac{B(r_{\rm A})^2}{8\pi} = \frac{1}{2}\rho(r_{\rm A})v(r_{\rm A})^2, \tag{2.12}$$

where the dipole magnetic field, $B(r)$, in the magnetic equator plane, is estimated to the magnetic dipole moment μ as $B(r) = \mu r^{-3}$. Assuming free fall condition and spherically symmetric steady accretion flow, the velocity is given as Equation 2.1 and the density is described as

$$\rho(r) = \frac{\dot{M}}{4\pi v(r) \cdot r^2}. \tag{2.13}$$

Using Equation 2.12 and 2.13, Alfvén radius, $r_{\rm A}$, (Lamb et al. 1973; Elsner & Lamb 1977) can be derived to be

$$r_{\rm A} = \left(\frac{\mu^4}{2GM_* \dot{M}^2} \right)^{1/7}, \tag{2.14}$$

and substituting Equation 2.2 into Equation 2.14 yields

$$r_{\rm A} = \left(\frac{\mu^4 GM_*}{2L_{\rm acc}^2 R_*^2} \right)^{1/7}. \tag{2.15}$$

Considering typical luminosity and mass of NS, we obtain

$$r_{\rm A} = 3.5 \times 10^8 \left(\frac{M_*}{M_\odot} \right)^{1/7} \left(\frac{R_*}{10^6 \text{ cm}} \right)^{-2/7} \left(\frac{\mu}{10^{30} \text{ G cm}^{-3}} \right)^{4/7} \left(\frac{L_{\rm acc}}{10^{37} \text{ ergs s}^{-1}} \right)^{-2/7} \text{ cm}. \tag{2.16}$$

The typical value of the $r_{\rm A}$ becomes $\sim 10^8$ cm (1000 km). Within the $r_{\rm A}$, the accreting matter falls along the magnetic field lines toward the magnetic poles of the NS, therefore the inner boundary of the accretion disk is determined by the Alfvén radius. Then it is expected to form a plasma layer at the Alfvén surface, which is called the Alfvén shell (Basko 1980).

Due to spinning of the NS, magnetosphere also rotates with the same velocity. The co-rotation radius $r_{\rm co}$ is defined at the position where centrifugal force balances the gravity, in other words, where the angular velocity of magnetosphere, $r\Omega_{\rm spin}$, is equal to the Keplerian velocity and is given as;

$$r_{\rm co} = \left(\frac{GM_*}{\Omega_{\rm spin}^2} \right)^{1/3}. \tag{2.17}$$

This radius is important in order to investigate the accretion regimes in NSs. When the angular velocity of the NS is smaller than the disk Keplerian velocity at the Alfvén radius, namely $r_{\rm A} < r_{\rm co}$, the matter is allowed to accrete along the magnetic field onto the NS. On the other hand, when NS rotates faster than the Keplerian velocity at the Alfvén radius, i.e., $r_{\rm A} > r_{\rm co}$, a centrifugal barrier arises which prevents mass accretion onto the NS and ceases X-ray emission. This mechanism is known as propeller effect (Illarionov & Sunyaev 1975).

The structure of the accretion flow, along the magnetic field lines onto the NS surface, is also controlled by the mass accretion rate, and hence the X-ray luminosity. Due to these variations, three major luminosity regimes can be considered for the pulsars which are being discussed here in detail.

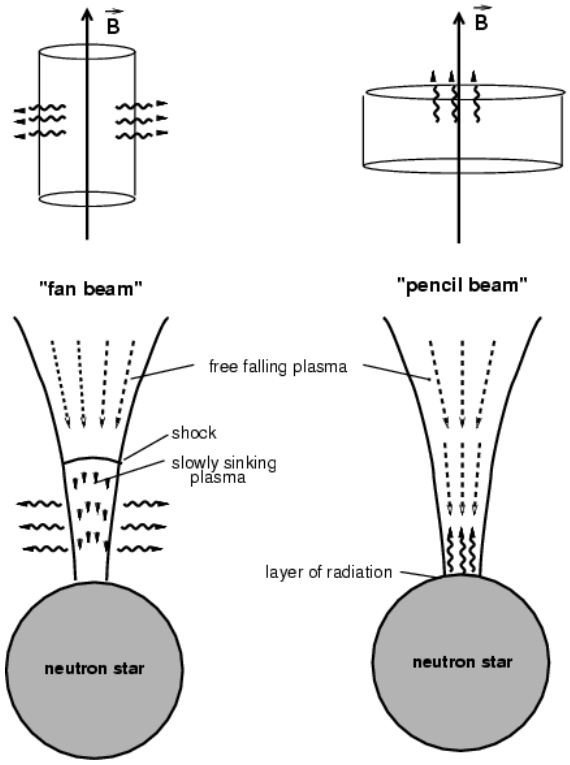

Figure 2.4: Emission beam patterns from the poles of the NS. For high accretion rate, a radiation dominated shock is formed in the column. Photons below the shock region escape from the side of the wall in form of fan beam pattern (left panel). The pencil beam pattern is formed in case of low accretion rate where photons propagate vertically along the accretion column (right panel). Figure is taken from Schönherr et al. (2007).

At low accretion rate ($L_{\rm X} = 10^{34}$–10^{35} ergs s^{-1}), the accreting matter is almost free to fall until hydrodynamical shock halts the plasma closer to the surface of NS. The gas is decelerated in shock region via Coulomb interactions before reaching the surface (Langer & Rappaport 1982). A hot spot formed at poles produces X-ray emissions that escape vertically along the accretion column. The observed emission pattern is known as pencil-beam, as shown in right side of Figure 2.4.

If accretion rate of NS increases such that luminosity is in the order of $L_{\rm X} = 10^{35}$–10^{37} ergs s^{-1}, a radiation dominated shock is expected to form in the accretion column (Figure 2.4). Thermal photons emitted from the hot spot gets up-scattered by inverse Compton scattering by hot electrons in the accretion column. The radiation which is emitted below the shock region diffuse through the side-walls of the accretion column in fan beam. X-ray photons above the shock region, however, move upward in the column in pencil-beam pattern. This results a mixture of pencil and fan beam patterns for the pulsar in this luminosity regime (Blum & Kraus 2000). Close to the surface of NS, the gas sinks slowly and decelerates again via Coulomb interactions before settling (Nelson et al. 1993). The shock or emission region can drift in the accretion column depending on accretion rate.

For very high luminosity of $L_{\rm X} = 10^{37}$–10^{38} ergs s^{-1}, accreting gas looses its energy in

radiation dominated shock and decelerates completely via radiation field below the shock region (Basko & Sunyaev 1976). In this luminosity regime, shock can drift upwards in accretion column with increasing accretion rate. X-rays are emitted only through the side walls of optically thick column in pure fan beam pattern, as shown in left panel of Figure 2.4.

2.2.3 X-ray Spectra

APXPs are some of the most powerful sources of X-ray band in our Galaxy. Their luminosities lies within 10^{33}–10^{35} ergs s^{-1} during quiescence, and can even rise up to 10^{38} ergs s^{-1} during the active state, and they radiate this energy in a broad energy range of 0.1–100 keV. This broadband nature of the energy spectrum originates from multiple and complicated processes which occur near the NS surface, where the in-falling and accreting matter is brought to rest and the X-ray are emitted by conversion of the gravitational potential energy to heat energy. The theory of X-ray pulsar spectral formation was originally proposed by Davidson & Ostriker (1973), as a scenario where most of the in-falling matter accreted to the NS passes through a radiation dominated shock region (Basko & Sunyaev 1976), and settles on the two poles of the NS forming dense "thermal mounds" just above the NS surface and an accretion column of the plasma above it, which is decelerated by the radiation pressure of the X-ray emission from the NS. The mound being optically thick emits mostly blackbody photons which are further up-scattered and Comptonized by the in-falling plasma and diffuse and escape through the walls of the accretion column (Barnard & Arons 1981; Nagel 1981a;b; Meszaros & Nagel 1985a;b; Brainerd & Meszaros 1991). The escaping photons carry away the kinetic energy of the plasma hence allowing it to come to rest on the NS surface. These photons undergo further scattering and reprocessing either in the accretion mound or column or the circumstellar material of the binary system as it reaches our line of sight. As a result of this, signatures of various processes that occur near the NS are also imprinted on the observed X-ray spectra included rich information. One of the most important processes in this regard is the reprocessing of the X-rays either by the circumstellar matter or the accretion disk. Depending on the density, elemental abundance and ionization state of the reprocessing region, emission line features of e.g., iron, silicon, oxygen, and neon, are often observed (e.g., White et al. 1983; Inoue 1985; Nagase 1989). Another important process is the resonant scattering by electrons, where the resonance levels are quantized into Landau levels in the presence of high magnetic fields. This resonances produce cyclotron resonance scattering features (CRSFs), which are broad absorption like features found in the energy spectrum. These features have been found in more than 17 accretion-powered pulsars (Mihara 1995; Coburn et al. 2002).

The energy spectrum of APXPs, thus, present to us a bonanza of features in a broad energy band starting from the very low energy reprocessed emission ($\lesssim 1$ keV) to the high energy Comptonized photons. The complete modeling of the energy spectrum should include various continuum emission, absorption, and scattering processes, including Comptonization, and CRSFs, and various emission and absorption lines.

2.2.3.1 Theoretical models of Spectral Formation

The X-ray spectra of APXPs are characterized by a low energy turnover of the power-law representing an un-saturated Planck spectrum, and a high energy cutoff at 20–30 keV. Other features like the CRSFs and the iron lines are superposed on it. There have been several previous attempts to calculate the X-ray spectra of APXPs (e.g., Yahel 1980; Nagel 1981b;a; Meszaros & Nagel 1985a;b; Klein et al. 1996). However, their calculations based on static or dynamic theoretical models have generally yielded results that do not agree very well with the observed X-ray spectra. Becker & Wolff (2005a;b) took a step forward by proposing a new model of spectral formation by introducing "bulk-motion Comptonization" of the seed photons produced in the accretion mound due to collisions with the rapidly in-falling plasma in the accretion column. Although the resultant spectrum is characterized by a power-law along with a low energy turnover, it lacks the high energy cutoff feature in the spectra. Becker & Wolff (2007) improved the model by including the effect of "Thermal Comptonization" along with the bulk-motion Comptonization, so as to reproduced a flatter spectrum with a high energy quasi exponential cutoff feature in its spectra. This model successfully reproduced the spectra of some bright X-ray pulsars like Cen X-3, Hercules X-1 (Her X-1) and SMC X-1 and more recently for 4U 0115+63 (Ferrigno et al. 2009). A Monte Carlo modeling of the accretion flow onto NS in a strong magnetic field (10^{12} G), which are both in geometrically constraining the flow into an accretion column and in modifying the cross section, was developed by Odaka et al. (2014). In this Monte Carlo modeling, bulk-motion Comptonization of the in-falling material as well as thermal Comptonization is also treaded. They applied this Monte Carlo model to the data of an APXP in HMXB, Vela X-1, observed by *Suzaku* and successfully explained the observed spectra over a wide range of mass accretion rates. Further several theoretical works about emission from the accretion column have been reported (Farinelli et al. 2012; 2016; West et al. 2017a;b). Nevertheless, a complete model for X-ray spectral formation in APXPs incorporating all the physical processes is still awaited. In the absence of this, it is a common trend to model the broadband energy spectrum phenomenologically by combination of multiple components.

2.2.3.2 Phenomenological Spectral Model

Phenomenological models usually consist of a power-law with quasi exponential high energy cutoffs of various functional forms, although the resulting model parameters are often difficult to relate to the physical mechanisms of the source. The most widely used models are a power-law with a high energy exponential cutoff (White et al. 1983; Coburn et al. 2002). A combination of two power-laws with different photon indices but common cutoff energy value called the Negative and Positive power-laws with an Exponential cutoff model (NPEX model; Mihara 1995; Makishima et al. 1999) also is used. A thermal Comptonization model is another model which describes the spectra of these sources well. To describe the low energy turnover apart from the intrinsic low energy cutoff, additional absorption column density of neutral matter along our line of sight or a local absorption component like a partial covering absorber (Endo et al. 2000) is sometimes used.

An additional absorption edge component may be used to represent a feature due to an

extra photoelectric absorption, for example by over abundant element or by ionized materials. A blackbody component with a temperature $kT < 1$ keV may also be used to describe the low energy excess, often observed in sources with low column density or absorbing material. Aside from this, a blackbody component with high temperature $kT > 1$ keV is used to represent the spectra of APXPs with simple continuum model such as exponential cutoff power-law model. A blackbody component associated with a continuum model was also reported in several X-ray pulsars such as EXO 2030+375 (Reig & Coe 1999), RX J0440.9+4431 (Ferrigno et al. 2013), GX 1+4 (Yoshida et al. 2017), and Swift J0243.6+6124 (Jaisawal et al. 2018). Although these blackbody component may not associate to a real physical emission prosess, we expect that the blackbody component may be the intrinsic emission which is originated from base of the accretion column. In addition to the continuum, Gaussian or Lorentzian multiplicative profiles are used to represent the CRSF. The details of these and other phenomenological spectral continuum models, which are often used, are given below. They are all part of the XSPEC package in HEASOFT either as a standard or a local model.

- **Power-law with high-energy cutoff model**
  The functional form of the power-law with high-energy cutoff model is as follows: $I(E)$ can be expressed as

$$I(E) = \begin{cases} AE^{-\Gamma} & (E < E_{\rm c}) \\ AE^{-\Gamma} \exp\left(\frac{E_{\rm c}-E}{E_{\rm f}}\right) & (E \geqslant E_{\rm c}), \end{cases} \tag{2.18}$$

  where Γ is a photon index, A is a normalization of power-law in photon per unit time, unit area, and unit energy, $E_{\rm c}$ is a cutoff energy and $E_{\rm f}$ is a folding energy. This model has been used extensively to effectively describe the continuum spectrum of many sources (White et al. 1983). However this suffers a disadvantage by the abrupt break at $E_{\rm c}$, which may give an artifactual hump at the cutoff energy (Makishima et al. 1990). This model also corresponds to "`powerlaw×highecut`" in XSPEC expression.

- **Power-law with Fermi-Dirac cutoff model**
  This model was introduced to improve the disadvantage of power-law with high-energy cutoff model by Tanaka (1986) given as

$$I(E) = AE^{-\Gamma} \times \frac{1}{1 + \exp\left(\frac{E-E_{\rm c}}{E_{\rm f}}\right)}. \tag{2.19}$$

  Apparent similarity to the Fermi-Dirac distribution function is responsible for its name, although Equation 2.19 is purely empirical. This model also corresponds to "`powerlaw×fdcut`" in XSPEC expression.

- **Exponential cutoff power-law model**
  This is a limiting case of the power-law with high-energy cutoff model in case of cutoff energy $E_{\rm c}$ approaching to 0. $I(E)$ can be expressed as

$$I(E) = AE^{-\Gamma} \exp\left(\frac{E}{E_{\rm f}}\right). \tag{2.20}$$

This model is expressed as "`cutoffpl`" in XSPEC.

- **Negative and Positive power-laws with EXponetial cutoff model**
  The functional form of this model is as follows:

$$I(E) = \left(A_{\rm n}E^{-\Gamma_{\rm n}} + A_{\rm p}E^{+\Gamma_{\rm p}}\right)\exp\left(\frac{E}{kT}\right), \tag{2.21}$$

  where $A_{\rm n}$, $A_{\rm p}$, $\Gamma_{\rm n}(>0)$, $\Gamma_{\rm p}(>0)$ and T are positive parameters and k is the Boltzmann constant. Thus, the model consists of Negative and Positive power-laws with a common EXponential cutoff factor, and is called NPEX model (Mihara 1995; Makishima et al. 1999). The NPEX continuum has been constructed by a physical picture of the emission mechanism. The NPEX continuum has been constructed by a physical picture of the emission mechanism and approximates a photon number spectrum for an unsaturated thermal Comptonization in a plasma of temperature T. At low energies, it reduces to the ordinary power-law with negative slope. As the energy increases, the positive power-law term becomes progressively dominant, so that the model can take a concave curvature on a log-log plot. At $E \sim kT$, the positive power-law term simulates the Wien hump in the Comptonized radiation, especially when $\Gamma_{\rm p} = 2.0$. This model is therefore sometimes used to reproduce the spectra of APXPs. In this thesis, the photon index of the positive power-law $\Gamma_{\rm p}$ is frozen to 2.0. This model is expressed as "`cutoffpl+cutoffpl`" with the common folding energy in XSPEC.

- **Broken power-law model**
  $I(E)$ of broken power-law can be expressed as

$$I(E) = \begin{cases} AE^{-\Gamma_1} & (E < E_{\rm b}) \\ AE^{\Gamma_2-\Gamma_1}E^{-\Gamma_2} & (E \geqslant E_{\rm b}), \end{cases} \tag{2.22}$$

  where $E_{\rm b}$ is a break energy, Γ_1, Γ_2 are photon indexes for $E < E_{\rm b}$ and $E \geqslant E_{\rm b}$, respectively. This model is sometimes used to represent the X-ray spectra of APXPs (e.g., dal Fiume et al. 1998; Masetti et al. 2004) and is expressed as "`bknpower`" in XSPEC.

- **Thermal Comptonization model**
  This is an analytic model describing Comptonization of soft photons in a hot plasma (Titarchuk 1994). It has parameters, the seed blackbody temperature, the electron temperature, and the optical depth, for fitting and it is valid for both optically thin and thick regions. There is an additional parameter, by which we can select the geometry of the Comptonizing region, from either a disk or a sphere. In this thesis, we assumed a disk geometry, which is the closest to the expected approximation for the accretion column geometry. This model also corresponds to "`compTT`" in XSPEC expression.

- **For absorption edge**
  Photoelectric absorption cross section of element above the energy where an absorption

edge accrue is roughly reduced in inversely proportional to the cube of the photon energy regardless of the ionization state of element. The approximate model of absorption edge, therefore, is given as

$$M(E) = \begin{cases} 1 & (E < E_{\rm c}) \\ \exp\left(-\tau\left(\frac{E}{E_{\rm c}}\right)^{-3}\right) & (E \geqslant E_{\rm c}) \end{cases} \tag{2.23}$$

where $E_{\rm c}$ is a threshold energy, and τ is an absorption depth at the threshold energy. This model is used to be multiplied by the continuum spectrum and corresponds to "`edge`" in XSPEC expression.

- **For CRSF**
  Model components for CRSF presented here are used to be multiplied by the continuum spectrum.
  - **Gaussian profile**
    This component has the form of

$$S(E) = \exp\left(-\frac{\tau}{\sqrt{2\pi}\sigma}\exp\left(\frac{(E-E_{\rm cycl})^2}{2\sigma^2}\right)\right), \tag{2.24}$$

    with $E_{\rm cycl}$, and σ being a cyclotron energy, and a width of line, and is expressed as "`gabs`" in XSPEC.
  - **Lorentzian profile**
    This component is given as

$$S(E) = \exp\left(-\frac{DE^2}{(E-E_{\rm cycl})^2 + W^2} \times \left(\frac{W}{E_{\rm cycl}}\right)^2\right), \tag{2.25}$$

    with D, and W being depth, and width of the resonance (e.g., Clark et al. 1990; Makishima et al. 1999), and is expressed as "`cyclabs`" in XSPEC.

2.2.4 Emission Line

In general, in addition to the continuum spectral component, we observe X-ray emission and absorption lines, absorption edges, and reflections in spectra of APXPs which are attributable to the X-ray source and its vicinity and are reflective of physical properties of elements in the plasma. These spectral components are utilized to prove the environments with regard to the X-ray source, its vicinity, and its surrounding matter. Measuring parameters of the emission lines and the absorption edges in spectra of APXPs, we intend to investigate the physical state and environment of the X-ray source and its vicinity.

As described in § 2.2.3, APXPs show iron emission lines in their spectra. In general, there are two mechanisms for the emission of iron lines. One is fluorescence and the other case is emission due to collisions by particles. Interaction of a photon or free electron with

an atom or ion may lead to ionization (former is called photo-ionization and later is called collisional-ionization). In particular when an electron from one of the inner shells is removed by a photoelectric absorption, the resulting ion has a vacancy in its atomic structure and is unstable. Fluorescence occurs to stabilize the ion again, in which one of the electrons from the outer shells makes a radiative transition in order to occupy the vacancy and the emitted photon has an energy corresponding to the energy difference between the initial and final discrete states. Since there is auto-ionization through the Auger process, which is other possible process to fill the vacancy, the fluorescence does occur with probability that a vacancy will be filled by a radiative transition, so-called the fluorescence yield. As a typical example, a K-shell vacancy of neutral iron has $\varepsilon_{\rm Fe} = 0.34$ (Kaastra & Mewe 1993).

The energy of emission line and absorption edge are the indicator of the ionization state of ion as given in Figure 2.5 for iron. If the collisional ionization is negligible small and ionization is dominated by photoionization, ionization state is determined by the balance of photoionization and recombination rates, which are determined by the incident X-ray flux and the density of the plasma, respectively. Then, the effect of photoionization is usually evaluated by so-called ionization parameter ξ written as

$$\xi \equiv \frac{L}{nr^2}, \tag{2.26}$$

where L is an illuminating X-ray luminosity, n is a number density of the gas (usually represented by a density of atoms) and r is a distance between the X-ray source and the gas (Tarter et al. 1969). The ionization parameter ξ determines the fraction of ionized ions.

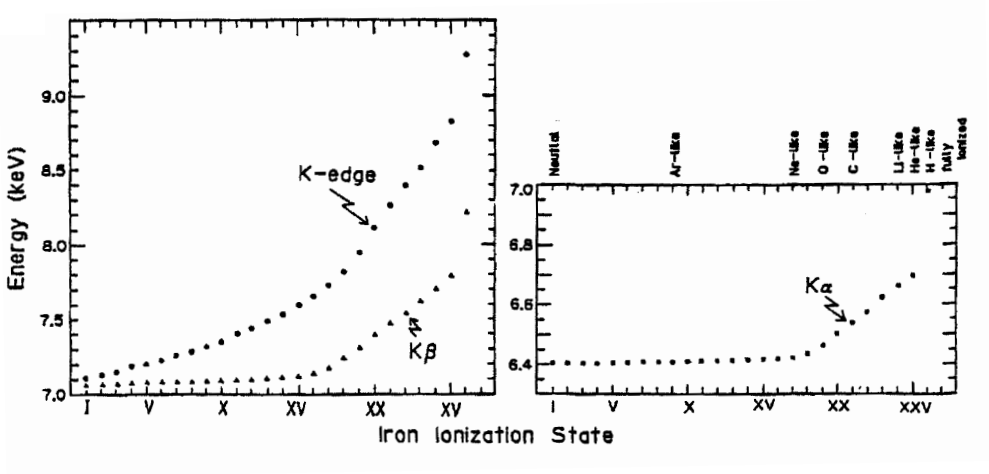

Figure 2.5: Energy of iron K_β emission line and absorption K-edge (left), and K_α emission line (right) as function of the ionization degree (Makishima 1986).

Emission lines, especially the iron line at 6.4 keV, are ubiquitous among X-ray pulsars. There usually exists a proportionality between the line flux and the continuum flux with energies above the ionization energy (Ohashi et al. 1984; Leahy et al. 1989; Naik & Paul 2003; Jaisawal & Naik 2014). It is also known that the equivalent width (EW) of line is

found to relate to the absorption column density (Ohashi et al. 1984; Makino et al. 1985; Makishima 1986; Kotani et al. 1999; Endo et al. 2002; Fürst et al. 2011b). In addition, the energies of these iron lines are usually observed at 6.4 keV, probably from neutral iron. These results indicate that the iron lines from APXPs are produced through the fluorescence of illumination of continuum X-rays with energies above the ionization energy from the NSs by neutral of low-ionized material (Koyama 1985; Inoue 1985; Makino et al. 1985; Makishima 1986; Nagase 1989). Although APXPs show emission lines from highly ionized iron as well as neutral iron lines, studying them is beyond the scope of this thesis.

A detailed investigation of these emission lines should be necessary for diagnostics of their emission mechanism. Identification of emission lines (ionization state of elements) and observed changes in line parameters with time and source luminosity provide important information on the line emitting regions. Possible sites of fluorescence may be (i) stellar wind from the companion star (White et al. 1983; Sako et al. 2002; Wojdowski et al. 2003); (ii) accreting matter around the Alfvén shell (Pravdo et al. 1977; Basko 1980; White et al. 1983; Inoue 1985; Ebisawa et al. 1996; Kohmura et al. 2001); (iii) accretion wake (Choi et al. 1996; Watanabe et al. 2006); (iv) accretion disk or its inner edge (Ebisawa et al. 1996; Endo et al. 2000; Vrtilek et al. 2005); (v) surface or photosphere of companion star (Watanabe et al. 2006); probably (vi) accretion flow at the region very close to NS forming a column (Endo et al. 2002; Asami et al. 2014); or some combination of these locations. Among of these, however the photosphere or the surface of companion star has been ruled out as a major line emission site, because the expected solid angle subtended at the NS is too small to explain the observed EW (Bai 1980; Basko 1978; Hatchett & Weaver 1977), which should exhibit a strong orbital dependence in contrast to the orbital independence that is observed (Pravdo et al. 1977). In this sense, a thorough investigation of fluorescence lines in the spectra of APXPs can provide information to study the surrounding wind regions or the interaction between the magnetic field and the accreting matter onto the NSs.

Absorption edges of iron are often observed in association with the iron emission lines, whose origin has been considered to the same of the fluorescence lines of neutral iron based on the ionization state estimated with energies of the edge (Makishima 1986; Ebisawa et al. 1996; Watanabe et al. 2006). These absorption edge feature in the X-ray spectrum are also interesting tool for studying the surrounding matter, especially being present between the observer and the X-ray sources.

Time variation of iron lines gives us more information. In APXPs, the emission line flux sometimes indicates variability depending of pulse phase, but sometimes it is found to have no pulse phase dependency (Ohashi et al. 1984; Paul et al. 2002; Lei et al. 2009; Suchy et al. 2012). Iron K_α line of Her X-1 shows a flux modulation with its spin period of 2.3 s (Choi et al. 1994; Zane et al. 2004; Vasco et al. 2013). Zane et al. (2004) and Choi et al. (1994) reported that the intensity modulation of the emission line is roughly represented by a sinusoidal function whose bottom phase corresponds to the peak phase of the pulse shape of the hard X-ray continuum. Choi et al. (1994) proposed that, since the iron line flux variations over the pulse phase is consistent with the soft X-ray behavior presented by McCray et al. (1982), the reprocessed iron line and the soft X-ray emission originate from the same place as predicted by McCray et al. (1982), i.e., Alfvén shell. But Vasco et al. (2013) reported the drastic disappearance of the iron line flux around the peak phase of

the pulse shape of the hard X-ray continuum and speculated a hollow cone geometry for the accretion column. Cen X-3 is another X-ray pulsar, which has the spin period of 4.8 s. Day et al. (1993) reported the line flux modulations as a function of the pulse phase, whose peak is shifted by roughly half a cycle with respect to the main peak of the continuum pulse above 7.1 keV. They proposed Alfvén shell as a possible candidate for the origin of the iron line with a mechanism of back illumination proposed by Warner et al. (1972), where the reprocessed emission is enhanced without increasing the continuum flux. Leahy & Matsuoka (1990) reported that the iron line pulsations of GX 301-2, whose spin period is ∼700 s, were possibly detected in *Tenma* observation though at marginal significance. On the other hand, Suchy et al. (2012) reported results from a *Suzaku* observation, and they argued that the line flux did not change significantly throughout the pulse phase and concluded that the iron fluorescence region was greater than ∼700 lt-s ($\sim 2 \times 10^{13}$ cm) from the NS, although there is a tendency toward higher fluxes around phase 0.6–1.0, where the pulse profile of the continuum X-rays shows the second peak, with an amplitude of ∼10%. Vela X-1 is an X-ray pulsar in HMXB system with ∼280 s spin period indicated a sinusoidal modulation of about 10% at half-amplitude in the iron line flux during the dip interval in *Ginga* observation (Choi et al. 1996). Choi et al. (1996) interprets that the iron line flux modulation is produced by the distribution of the reprocessing matter which is not completely spherically symmetric and not isotropic around the NS and proposes the accretion wake (Blondin et al. 1990), which is located at a distance of 10^{11} cm from the NS, as a possible reprocessing site. Other X-ray pulsars with longer spin periods, 4U 1538-522 ($P_{\rm spin}$ =530 s) and 4U 1909+07 ($P_{\rm spin}$ =605 s) were detected pulse phase modulation of iron line with *Suzaku* (Hemphill et al. 2014; Fürst et al. 2012). In 4U 1538-522 and 4U 1909+07, the pulse phase modulations of line flux indicate significant phase lags to the pulse profile of continuum with ∼350 s and ∼120 s for 4U 1538-522 and 4U 1909+07, respectively (Hemphill et al. 2014; Fürst et al. 2012). If we assume that the iron emission peaks due to the light from the peak of the pulse of continuum in above cases, these would imply that iron line emitting region is at distance 10^{12}–10^{13} cm from the X-ray sources. As seen above, studying with pulse phase dependent spectroscopy is expected to provide the additional constraint of size or geometry in reprocessing region.

2.2.5 Classification of X-ray Pulsars

As shown in Figure 2.2, X-ray binaries with NS are divided broadly into two categories, HMXB and LMXB, according to the nature of the companion. The accretion mechanism of NS in X-ray binaries is often closely related to these categories.

Depending on the nature of the companion, HMXBs are typically divided (see Corbet 1986) into two groups: Supergiant X-ray binaries (SGXBs) and BeXBs (see § 2.1.2.3). Historically, the SGXBs are also subdivided into two groups according to the dominant mode of mass transfer: Roche lobe overflow or the stellar wind accretion (Bildsten et al. 1997).

In SGXBs, a NS is usually fed by direct accretion from the relatively dense wind from companion (stellar wind accretion; see § 2.1.2.2), with little angular momentum transfer (see Waters & van Kerkwijk 1989). Wind-fed systems are normally persistent X-ray sources with X-ray luminosities of the order of 10^{35}–10^{36} ergs s^{-1}. If mass transfer occurs via Roche lobe overflow, then the X-ray emission is highly enhanced reaching to $L_{\rm X}$ ∼10^{38} ergs s^{-1} and an

accretion disk is formed around the NS. At present, there is known only one disk-fed SGXB in the Galaxy (Cen X-3) and three in total (SMC X-1 and LMC X-4), while there are about a few tens of wind-fed SGXBs. Orbits in disk-fed systems are circularized and it has been spun up to short spin periods ($P_{\rm spin} \lesssim 10$ s) of the NS, while wind-fed systems are with little angular momentum transfer and spin periods of NSs in its system are rather long, $P_{\rm spin} \gtrsim 100$ s. In the wind-fed systems, orbital periods of these systems are typically $P_{\rm orb} \lesssim 15$ d, and some orbits are almost circular (Corbet & Mukai 2002), but finite eccentricities have been measured for several systems, some of them rather high (e.g., $e = 0.17$ for 4U 1538-522; Clark 2000).

The different classes of HMXBs and thus the different types of mass transfer, can be recognized in a so-called Corbet diagram (Corbet 1984; 1986), which displays NS binaries on a plane of binary orbital period $P_{\rm orb}$ and NS spin period $P_{\rm spin}$. As shown in Figure 2.6, SGXBs exhibit no or a weak negative correlation, while BeXBs show a positive correlation in this diagram. Disk-fed SGXBs (blue triangles) show short orbital periods and short spin periods and display a negative correlation in the $P_{\rm orb}$-$P_{\rm spin}$ diagram. The most likely mass transfer mechanism of the system with a small orbital separation and an evolved companion is the Roche lobe overflow. On the other hand, wind-fed SGXBs (violet triangles) show long spin periods and short orbital periods, occupying a more or less flat region in the $P_{\rm orb}$-$P_{\rm spin}$ diagram. Three systems prevent the region from being a horizontal line. OAO 1657-415 with an orbital period of 10.4 d and a pulse period of 37.1 s, occupies an intermediate region between sources, which might be with mass transfer via a stellar wind and Roche lobe overflow (Chakrabarty et al. 1993). 4U 0114+65 and 4U 2206+54, which are categorized as a slow rotator, are located above the region of wind-fed SGXBs. The Be systems (yellow filled circles) display a positive correlation between orbital period and spin period. This can be interpreted as that the NSs is further away from the donor star in systems with a long orbital period and it is sampling a weaker portion of the circumstellar disk (Waters & van Kerkwijk 1989). Other systems show anomalous behavior, such as SAX J2103.5+4545 whose X-ray properties are similar to those of wind-fed systems but whose optical/infrared emission resemble that of BeXB (Reig et al. 2010). Its unusual orbital period of 12.68 d and pulse period of 358 s (Camero Arranz et al. 2007) place it among the wind-fed supergiants group in the Corbet diagram. SAX J0635.2+0533 (Kaaret et al. 1999; 2000) is also a peculiar system of BeXBs. This source has very short spin period of 34 ms, which leads to break away from the BeXBs group in the Corbet diagram.

Among the low-mass companion stars we find white dwarfs, late-type main-sequence stars, A-type stars and F–G-type sub-giants. The approximation to the radius of Roche lobe $R_{\rm lobe}$ is given by Eggleton (1983) with the mass ratio $q = M_*/M_{\rm p}$ as

$$R_{\rm lobe} = \frac{0.49q^{2/3}}{0.6q^{2/3} + \ln\left(1 + q^{1/3}\right)} \left(\frac{G\left(M_{\rm p} + M_*\right) P_{\rm orb}}{4\pi^2}\right)^{1/3}. \tag{2.27}$$

Substituting their typical values for LMXBs, $M_* = 1.4M_\odot$, $M_{\rm p} = 0.5M_\odot$, and $P_{\rm orb}$ =10 hr, Equation 2.27 gives $R_{\rm lobe} \sim 0.8R_\odot$, which is less than the radius of late-type main-sequence stars (Cox 2000). In LMXBs, therefore the companion star fills the Roche lobe and its outer layer overflow from the Roche lobe as it evolves. In LMXB, therefore the companion star

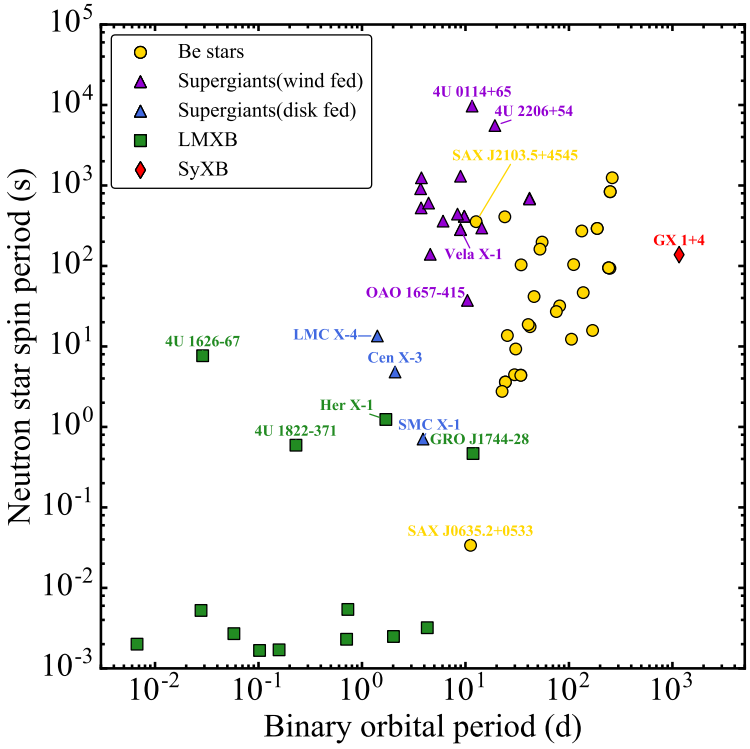

Figure 2.6: $P_{\rm orb}$–$P_{\rm spin}$ diagram (so-called Corbet diagram) of NS binary pulsars. BeXB pulsars (yellow filled circles), SGXB pulsars in disk-fed system (blue filled triangles), and wind-fed(violet filled triangles), LMXBs (green filled squares; only X-ray pulsars), and SyXB pulsar (red filled diamond) are shown from the catalogs (Liu et al. 2006; 2007; Bodaghee et al. 2007).

fills the Roche lobe and its outer layer overflows from the Roche lobe as it evolves. And they are considered to form an accretion disk around the NS.

Generally, LMXBs are old systems from the life times of the stars. In contrast with HMXBs, they mostly contain NSs with decayed magnetic field strengths, $B < 10^{10}$ G, since NSs in such systems should be old. In fact, among more than 180 known LMXBs (Liu et al. 2007), a few sources are known to have NSs with strong magnetic fields (Nagase 1989). Several indirect pieces of evidence support their weak-field nature: the X-ray pulsations have been detected from a minor fraction of LMXB, with very short period of $P_{\rm spin}$ ∼10 ms. Such short periods are close to those of "millisecond radio pulsars", which are believed to be very old systems (e.g., Manchester 1995), located at the bottom-left corner of Figure 2.6.

In LMXBs, a few objects, Her X-1, 4U 1626-67, 4U 1822-37, GRO J1744-28, GX 1+4, and 4U 1954+31 have strong magnetic field exceptionally (B >10^{12} G). The three of the six, Her X-1, 4U 1626-67, and 4U 1822-37 are persistent sources while GRO J1744-28 is a transient. Especially, magnetic field strength of Her X-1, 4U 1626-67, and 4U 1822-37 have been measured with CRSF. Their features including spin period and X-ray spectra are similar to those of APXPs in HMXBs. Their spin periods are typically $P_{\rm spin}$ ∼1 s and much longer

than 10 ms, typical spin period of LMXBs. GRO J1744-28, which is an unusually hard X-ray source and sometimes exhibits X-ray bursts, was discovered by *CGRO* in 1995 and its pulsation was detected at 0.467 s (Finger et al. 1996a). From the *CGRO* observation, an only spin period and its derivative were measured, and its magnetic field strength was estimated as $B = 2\text{–}6 \times 10^{11}$ G (Finger et al. 1996a), which is stronger than those of typical LMXBs, although its expected CRSF has not been detected.

Companions of GX 1+4 and 4U 1954+31 are M-type giant stars, and the binaries including them are categorized to be symbiotic X-ray binaries (SyXBs; Masetti et al. 2006). SyXBs are X-ray emitting binaries consisting of NSs and evolved (e.g., M-type) low-mass giants, latter having mass-loss rate close to those of high-mass stars, which is extremely rare population in LMXBs, since only five firm SyXB cases and some candidates are known involving GX 1+4 and 4U 1954+31 (Enoto et al. 2014). Two SyXBs, GX 1+4 and 4U 1954+31 show pulse period of $\sim$160 s and $\sim$20000 s, respectively, which are much longer than those of persistent sources and GRO J1744-28. They are considered to involve strongly magnetized NSs more then 10^{13} G (Makishima et al. 1988; Enoto et al. 2014), and different from other LMXBs because Roche-lobe is unfilled by M-giant star in SyXBs (Hinkle et al. 2006). Their X-ray spectra are very hard, extending to high energies, say several 100 keV, like other APXPs in HMXBs. In the system, accretions to NS may be caused by the stellar wind accretion described in § 2.1.2.2 and they behave in a similar way to APXPs in HMXBs.

On the Corbet diagram of Figure 2.6, these six sources in LMXBs are located close to other APXPs, far from typical LMXBs, although 4U 1954+31 is not plotted since its orbital period has not been derived yet. Therefore, we deal with the five object, Her X-1, 4U 1626-67, 4U 1822-37, GX 1+4 and 4U 1954+31 behaving similarly to APXPs in HMXB to our sample.

Chapter 3

Instrument

Contents

In this chapter, we review an astronomical satellite used in this thesis, i.e., *Suzaku* satellite. Its basic properties, X-ray optics, and the onboard instruments are described.

3.1 Overview of Suzaku Satellite

The *Suzaku* satellite is a joint mission between Japan and United States for the X-ray astronomy (Figure 3.1). It was successfully launched on July 10, 2005, from the Uchinoura Space Center (USC) of the Japan Aerospace Exploration Agency (JAXA). The spacecraft orbits around the Earth once in ∼96 min at ∼570 km altitude with an inclination angle of ∼31°. The weight and the length of the spacecraft is ∼1.7 tons and ∼6.5 m, respectively. The electric power is ∼1700 W and ∼660 W for total and scientific instruments, respectively. The pointing accuracy of the spacecraft is $\sim 0.2'$. The fixed solar panels onboard the spacecraft constrain the pointing direction of the telescope to be 65–110° from the Sun. Most targets are occulted by the Earth once in an orbit during the observations. In addition, scientific observations are not possible during the South Atlantic Anomaly (SAA) passages. Therefore, the average observing efficiency is ∼45%. For transient and unpredictable targets, *Suzaku* is prepared to perform Target of Opportunity (ToO) observations. The observation is typically conducted within a few days. More details of *Suzaku* can be found in the *Suzaku* Technical Description[1], the *Suzaku* Data Reduction Guide[2], and the official web page[3].

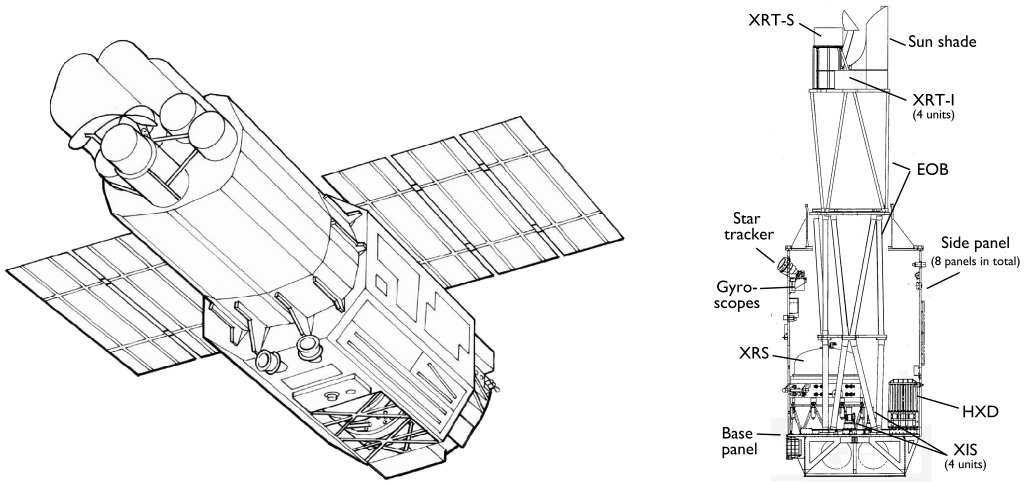

Figure 3.1: Schematic view of the *Suzaku* satellite (Mitsuda et al. 2007).

Suzaku has mirror assemblies and three scientific instruments for X-ray observations (Mitsuda et al. 2007); the X-Ray Spectrometer (XRS; Kelley et al. 2007), the X-ray Imaging Spectrometer (XIS; Koyama et al. 2007), and the Hard X-ray Detector (HXD; Takahashi

[1] `https://heasarc.gsfc.nasa.gov/docs/suzaku/prop_tools/suzaku_td/`
[2] `https://heasarc.gsfc.nasa.gov/docs/suzaku/analysis/abc/abc.html`
[3] `http://www.astro.isas.jaxa.jp/suzaku/`

et al. 2007; Kokubun et al. 2007). The XRS became not operational by a thermal short between helium and neon tanks one month after the launch. However, simultaneous observations of the XIS and the HXD provide high signal-to-noise ratio spectroscopy in broad energy band with a moderate energy resolution and a low background level.

3.2 X-ray Telescope

3.2.1 Performance and Calibration

3.2.1.1 Mirror Assembly

The mirror assembly of *Suzaku* is composed of five light-weight X-Ray Telescope (XRT; Serlemitsos et al. 2007) modules (Figure 3.2). Four of them (XRT-I0, 1, 2, and 3) are dedicated for the four XIS sensors, while the remaining one (XRT-S) for the XRS. All are grazing-incidence mirrors. Each XRT is composed of closely nested 175 thin-foil mirrors, which are conical approximation of the Wolter-I type geometry (Figure 3.3). The focal length, the inner and outer diameters of the XRT-I are respectively ∼4.8 m, ∼0.1 m, and ∼0.4 m. A large number of reflectors in each module provides a large collecting efficiency with a moderate imaging capability in the energy range of ∼0.2–12 keV.

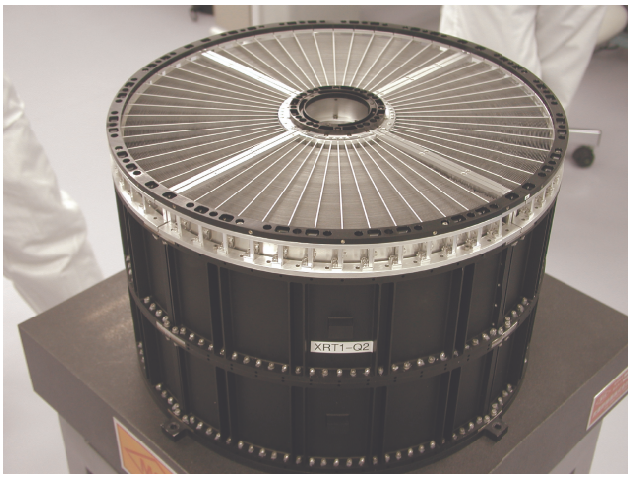

Figure 3.2: Picture of an XRT module onboard *Suzaku* (Serlemitsos et al. 2007).

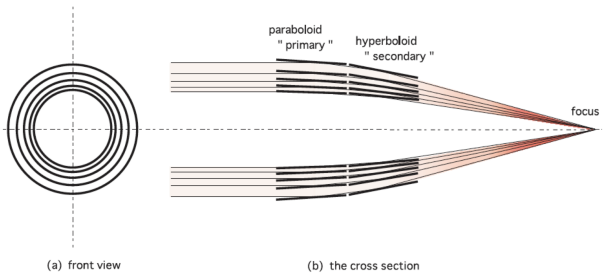

Figure 3.3: Schematic view of the Wolter-I type mirror (Mori et al. 2005)

3.2.1.2 Effective Area

The on-axis effective areas convolved with the transmissions of the thermal shield and the optical blocking filter, and with the detector quantum efficiency are shown in Figure 3.4. The effective area for off-axis incident X-rays is smaller than that for on-axis X-rays because off-axis X-rays are partially obscured by neighbor mirror shells. This "vignetting" effect is prominent at high energy. A maximum incident angle for full-reflection is smaller for higher energy X-rays than for lower ones. The off-axis angle dependences of the effective area for the soft (3–6 keV) and the hard (8–10 keV) bands are shown in Figure 3.5. The effective area decreases as increasing off-axis angle depending on the photon energy. It can be calculated based on Monte Carlo simulation (Ishisaki et al. 2007), and are tabulated as a function of incident X-ray energy, which is called an ancillary response file.

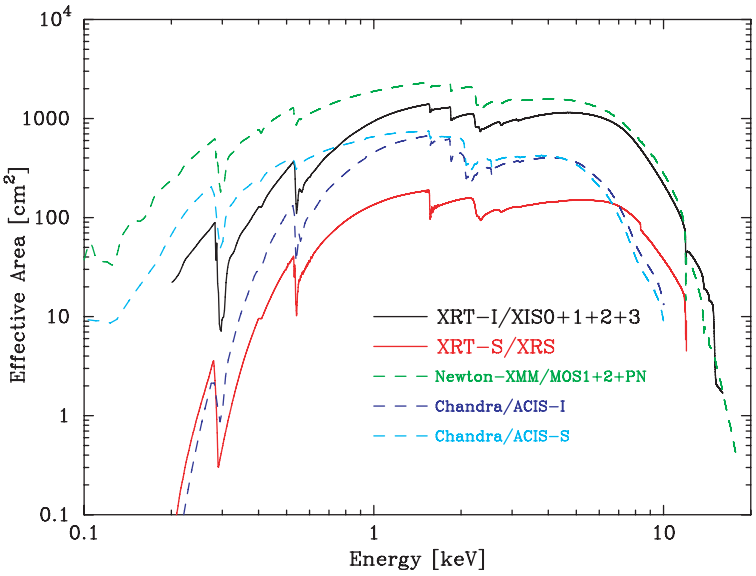

Figure 3.4: Total effective area of the four XRT modules combined with transmissions of the thermal shield and the optical blocking filter, and with the quantum efficiency of the CCD detectors (Serlemitsos et al. 2007). Those of *XMM-Newton* and *Chandra* are shown for comparison.

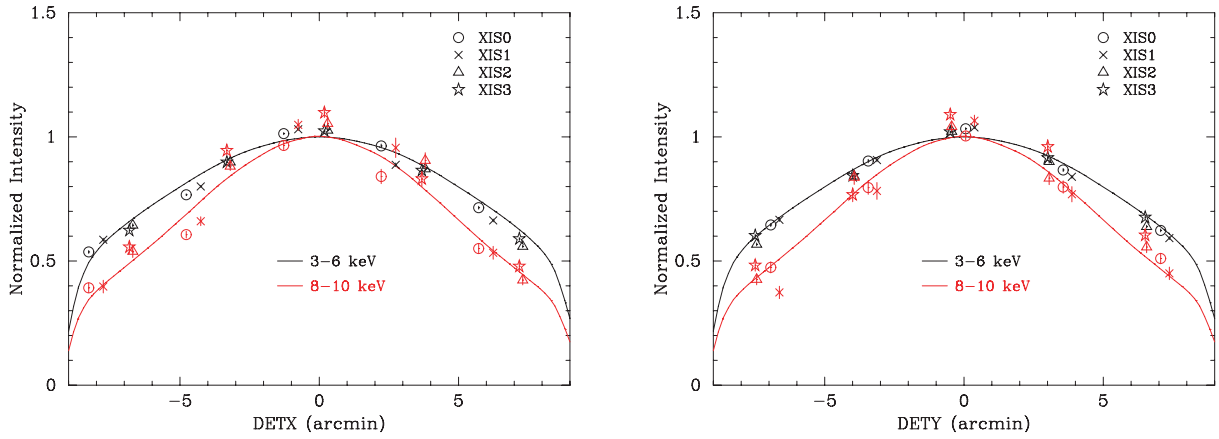

Figure 3.5: Off-axis angle dependence of the XRT modules along DETX (left) and DETY (right) axes in the 3–6 keV (black) and the 8–10 keV (red) energy band (Serlemitsos et al. 2007). Models and in-flight calibration data are shown with the solid lines and symbols, respectively.

3.2.1.3 Angular Resolution

Half power diameter (HPD) is the diameter of a circle which contains a half of the total flux of the focused X-rays from a point source. HPD is a standard value to evaluate the imaging capability. The XRT has an energy-independent HPD of $\sim 1'.8$–$2'.3$. Point spread function (PSF) is an intensity profile over the detector surface by a monochromatic X-ray point-like source at the infinity. In general, the sharpness of images is evaluated by the full width of half maximum (FWHM) and the encircled energy radius of the PSF. Encircled energy function (EEF) is an integration of PSF and shows the ratio of the flux of the enclosed circle to the total flux of a point source. A typical X-ray image, the PSF, and EEF of each XRT-I module are summarized in Figure 3.6. Each XRT is made of four sections ("quadrant"; see Figure 3.2). Since the spaces between the quadrants are dead areas, point source images appear to be a cross.

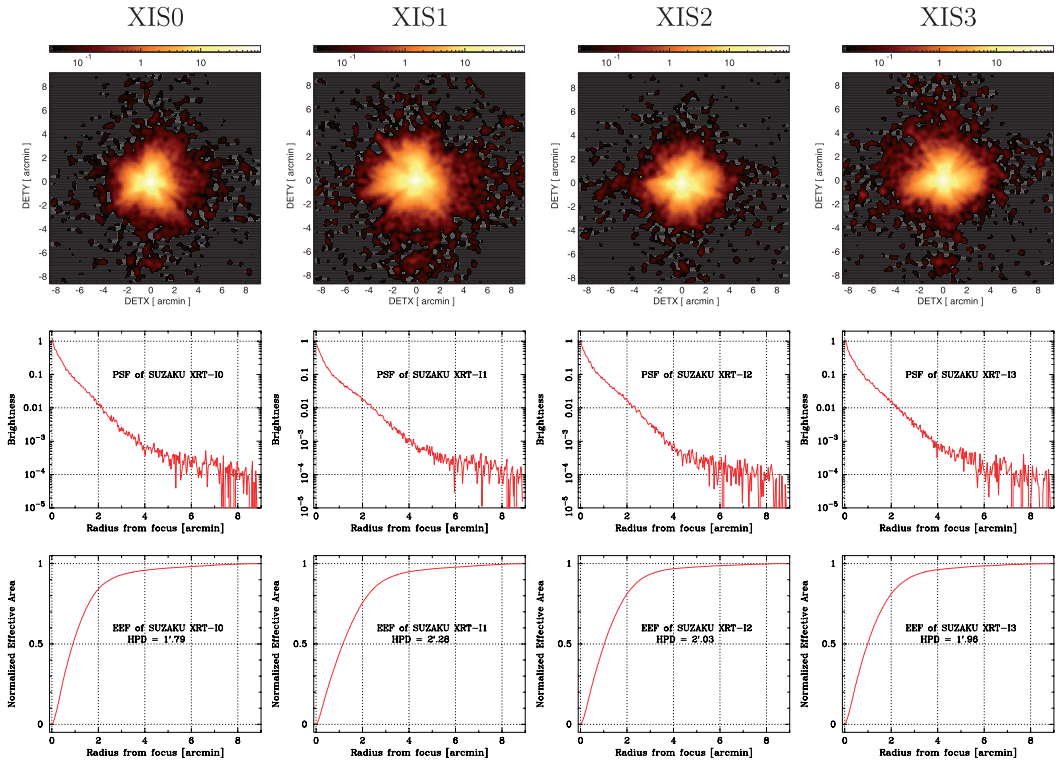

Figure 3.6: Typical X-ray image, the PSF, and the EEF of each XRT-I module at the focal plane (Serlemitsos et al. 2007).

Tightly nested structures increases the possibility of reflection other than the normal double reflection within the telescope structure. Because of these unexpected incidences, X-ray of bright sources outside the field of view reaches the focal plane. This is called stray light and it has been a large problem for nested X-ray telescopes (e.g., *ASCA*/XRT). In the case of *Suzaku*/XRT, front-mounted pre-collimators are installed and decrease the stray light by one order compared with that of *ASCA* (Mori et al. 2005).

3.2.1.4 Alignment Accuracy

When the satellite points a target for the XIS, its image is found at the focal position on each XIS sensor. The focal positions are located close to the detector center with a deviation of ∼0.3 mm from each other (Figure 3.7). On the other hand, the maximum effective area is achieved to observe a target along the optical axis, which are expected for the XRT to scatter in an angular range of ∼1′ (Figure 3.7).

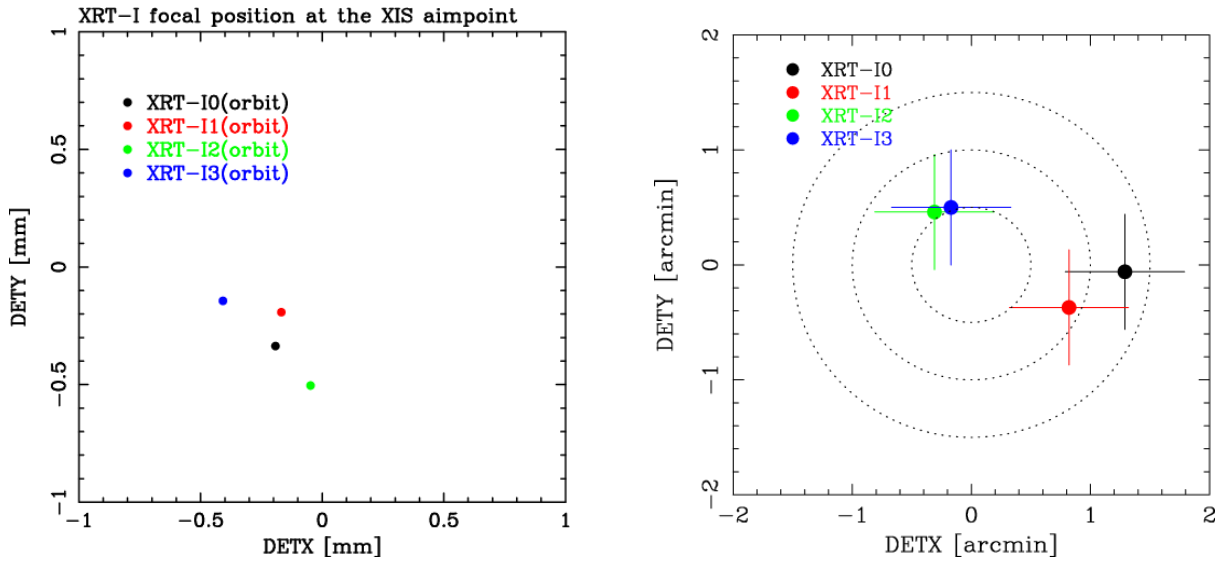

Figure 3.7: Positions of the focus (left) and the optical axis (right) in each XRT-I module (reprinted from the *Suzaku* Technical Description). In the right panel, the image on each XIS detector becomes brightest when a target star is placed at the position of the corresponding cross. The dotted circles are drawn every 30′ in radius from the default position for the XIS.

The optical axis of the HXD deviates from that of the XIS by ∼5′ in the negative DETX direction. When the satellite points a target for the XIS, the effective area of the HXD is reduced to ∼93% of the value at its optical axis. In contrast, when the satellite points a target for the HXD, the effective area of the XIS is ∼88% of the value at its optical axis.

3.3 X-ray Imaging Spectrometer

3.3.1 Overview

The XIS is equipped with four silicon X-ray Charge Coupled Devices (CCDs) at the foci of the four XRTs (Figure 3.8), which are named XIS 0, 1, 2, and 3. The combination of XRTs and XISs provides X-ray imaging-spectroscopic capability with a moderate energy resolution in the ∼0.2–12 keV energy range. The design parameters and the basic performance of the XIS are summarized in Table 3.1 at section 3.5. More details can be found in e.g., Koyama et al. (2007).

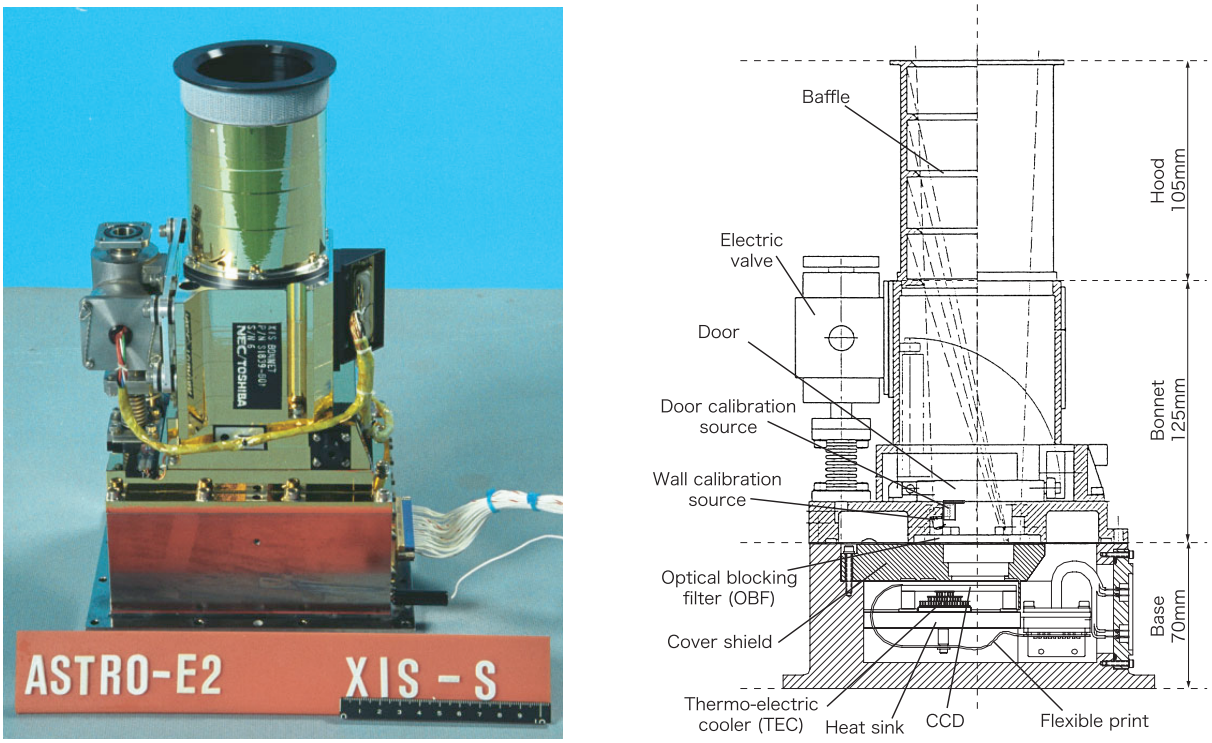

Figure 3.8: Picture and cross section of the XIS onboard *Suzaku* (Koyama et al. 2007).

The X-ray CCDs consist of a gate structure, an insulator, and a depletion layer. The XIS is Metal Oxide Semiconductor (MOS) type CCD, in which the gate structure, the insulator, and the depletion layer consist of Metal (polysilicon), Oxide (SiO_2), and Semiconductor (silicon), respectively. The XIS is operated in a photon-counting mode, similar to that used in the *ASCA*/SIS, *Chandra*/ACIS, *XMM-Newton*/EPIC and *Hitomi*/SXI. In general, the X-ray CCDs operate by converting an incident X-ray photon into an electron charge cloud by the photoelectric effect in the depletion layer. The electron cloud on each pixel is transferred into the output transistor of the gate structure. The amount of electrons is proportional to the energies of the incoming photons. The surface of the chip with the gate structure is called the "front side". X-ray CCDs are categorized as a front-illuminated (FI) or a back-illuminated (BI) chips based on the direction of incoming photons. The FI CCD detects

X-ray photons that pass through its gate structures, i.e., from the front side. Conversely, the BI CCD receives photons from "back" side, or the side without the gate structures. For the X-ray observations, Optical and UV photons are reduced by the Optical Blocking Filters (OBFs) in front of the CCDs. The charges are transferred from an imaging area to a frame store area after the exposure, and then read out into a serial register in the normal operation.

A schematic view of the CCD chip is shown in Figure 3.9. Each XIS sensor has a single CCD chip with an array of 1024×1024 picture elements ("pixels"), and covers an $18' \times 18'$ field of view (FoV) at the focal plane of the XRT. Each pixel is 24 μm square, and the size of the CCD is 25 mm$\times$25 mm. The CCD chip consists of four segments (A, B, C, and D) with 256×1024 pixels each of which has a readout node. Two radioactive sources of ^{55}Fe illuminate two corners of each CCD for in-flight calibration. One of the sensors, XIS 1, uses a BI CCD, while the other three use a FI CCD.

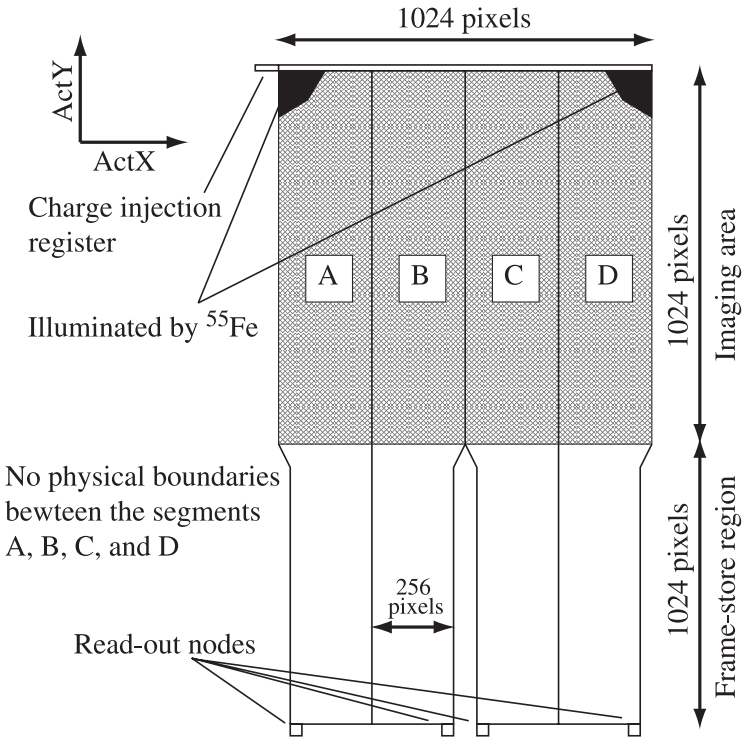

Figure 3.9: Schematic view of a CCD chip in the XIS (Koyama et al. 2007).

3.3.2 Performance and Calibration

3.3.2.1 Effective Energy Range

The effective energy range and the quantum efficiency highly depend on the structure of the CCD chips, i.e. FI CCD or BI CCD. Because of the additional photo-electric absorption at the gate structure, the low-energy quantum detection efficiency (QDE) of the FI CCD is rather limited, while FI CCD provides a low background observation. In contrast, the BI CCD retains a high QDE even in a sub-keV energy band because of the absence of the gate structure on the photon-detection side. However, the BI CCD tends to have a slightly thinner depletion layer, and the QDE is therefore slightly lower in the high energy band. Accordingly, XIS 0, 2, and 3 of FI CCD are sensitive in the 0.4–12 keV energy range, and XIS 1 of BI CCD is sensitive in the 0.2–12 keV energy range. The quantum efficiency is calibrated for each sensor (Figure 3.10), which is used to generate the redistribution matrix function (RMF; Ishisaki et al. 2007).

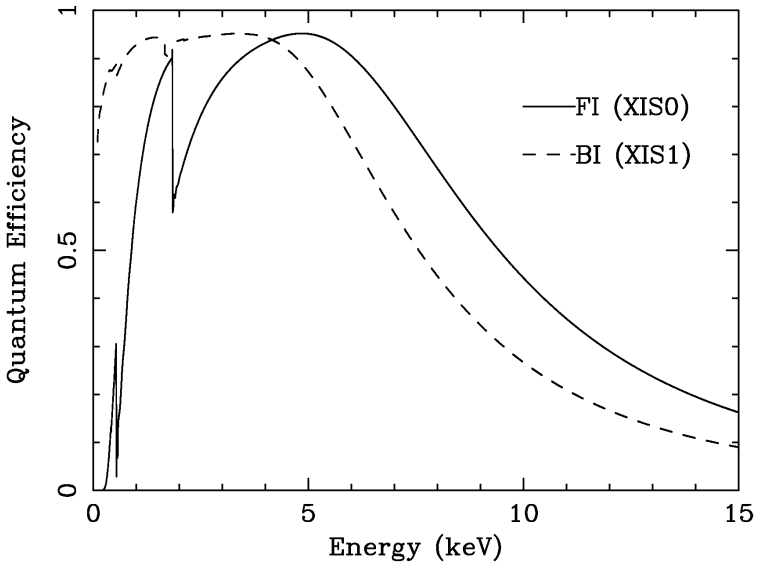

Figure 3.10: Quantum efficiency of the CCD chips in the XIS as a function of incident photon energy (Koyama et al. 2007). The FI (XIS 0) and the BI (XIS 1) CCDs are indicated with the solid and dashed lines, respectively.

3.3.2.2 Energy Resolution and Scale

The performance of the CCD chips is gradually degraded in space due to charge traps in pixels damaged by cosmic-ray radiation (e.g., Nakajima et al. 2008). One of the unique features of the XIS is the capability to inject sacrificial electrons in the imaging area to fill the charge traps while observing. It prevents charges by X-rays from being captured by the traps, and makes them almost harmless. This method is called the spaced-row charge injection (SCI) and the SCI has been adopted as a standard method in the XIS (Uchiyama et al. 2009). The SCI is applied for almost all observations since October 2006 to cope with the increase of the radiation damage (Uchiyama et al. 2009). The charge transfer efficiency (CTE) and the energy resolution were rejuvenated owing to the SCI. The degradation of the energy resolution is shown in Figure 3.11. The absolute energy scale is accurate to $\lesssim$0.2% and $\lesssim$5 eV at 5.9 keV and below 1 keV, respectively. They are also called into account in the RMF for the XIS (Ishisaki et al. 2007). The charge injection capability is also used to measure the CTE of each CCD column in the case of the no-SCI mode (Nakajima et al. 2008; Ozawa et al. 2009).

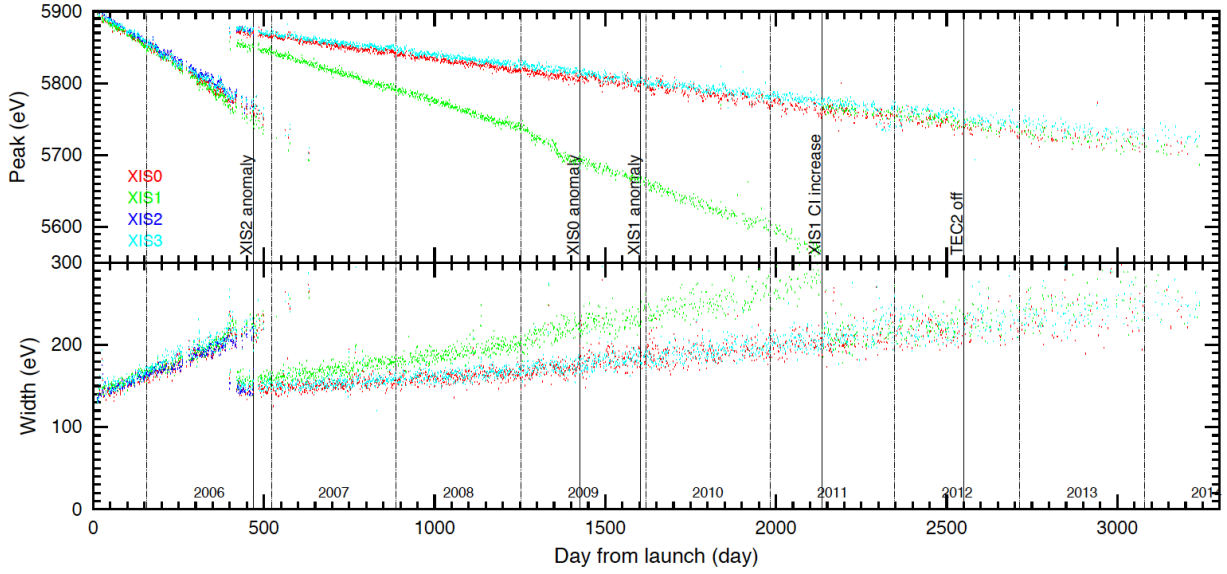

Figure 3.11: Trend of the energy resolution in the XIS with and without the SCI technique (reprinted from the *Suzaku* Technical Description).

3.3.2.3 Background Events

Two major sources of background for the XIS are the non X-ray background (NXB) and the cosmic X-ray background (CXB). The NXB is caused by interactions between cosmic-ray particles and the satellite. The intensity of the NXB depends on the strength of the geomagnetic field at the position of the spacecraft, which is called the cut-off rigidity (COR). A typical NXB spectrum of each XIS sensor is shown in Figure 3.12, which is accumulated from observations pointed toward the night-Earth. In contrast, the intensity of the CXB depends on the target positions. In our observations of APXPs, the background intensity can be estimated from off-source regions within the same CCD.

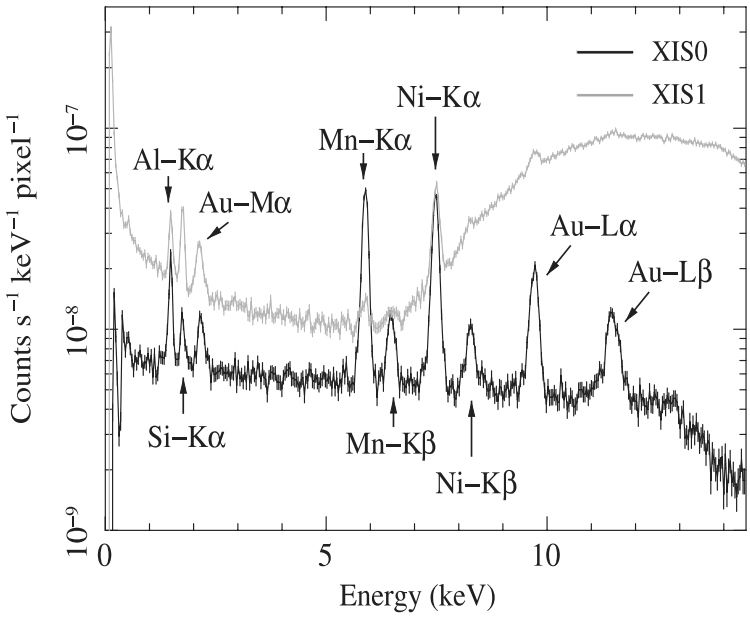

Figure 3.12: Typical NXB spectra of the XIS 0 (black) and the XIS 1(gray) (Tawa et al. 2008).

3.3.3 Systematic Observational Effects and their Mitigation

3.3.3.1 Photon Pile-Up

The XIS is essentially a position-sensitive integrating instrument, with a nominal interval of 8 s between readouts. If more than one photon strikes the same CCD pixel, or one of its immediate neighbors during the integration time, electron signals cannot be correctly detected as independent photons. Once this effect occurs, both images and spectra are distorted. This is called a photon pile-up, which is potentially a big problem for the integrating instrument particularly in observations of bright targets. A pile-up fraction highly depends on a source flux, the PSF of the telescope, and a readout method of the CCD detector. However, the modest angular resolution of the *Suzaku*/XRT is an advantage to avoid pile-up, and the pile-up does not usually come up when observing an object extended more than the point spread function of the XRT. We can prevent the pile-up by reducing the snap exposure time by selecting a clock mode with some options. Figure 3.13 shows the range of the incident count rate that we can observe without the pile-up. Other strategy to mitigate the effects of pile-up is to only use events from the outskirts of the PSF, where the incoming rate per pixel is substantially smaller than in the center. This is called the annulus extraction method and is discussed in detail in Yamada et al. (2012).

3.3.3.2 Self Charge Filling

In principle, charge traps can be filled not only by artificially injected charges, but also by charges created by X-ray events. This effect is called Self Charge Filling (SCF) effect. Apparent in observations of some very bright sources is demonstrated by Todoroki et al. (2012), and they proposed a correction method of the SCF effect. Even if XIS is operated with the SCI, the SCF effect can be seen. Yoshida et al. (2017) shows an apparently inconsistent energy scale of XIS 1 data compared to those of XIS 0 and 3 in the observation conducted the SCI, since the events for XIS 0 and 3 were well recovered from the degradation of the CTE with the SCI performed with 2 keV equivalent electrons for three XIS sensor, though it was insufficient for XIS 1. However, this effect is not included in the calibration. It may be encountered that a better energy resolution than the RMF indicate.

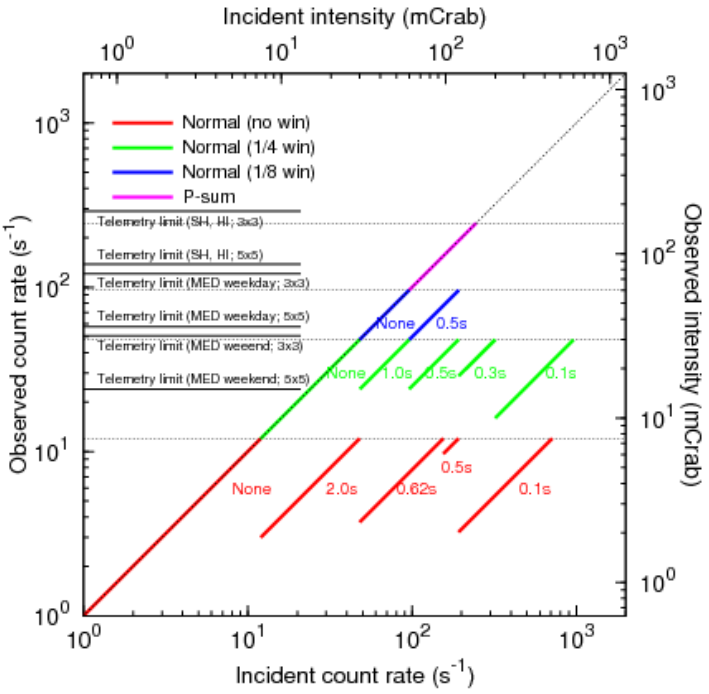

Figure 3.13: Incident versus observed count rates of a point source for the XIS detector (reprinted from the *Suzaku* Technical Description). The ratio of the two gives the observing efficiency. The thick colored lines show the range below the pile-up limit for a given window option (defined by the figure legend) and burst option (defined by the time values indicated in the figure).

3.3.4 Operation

There are two different kinds of on-board data processing modes. The clock modes, describing how the CCD clocks are driven, determine the exposure time, the exposure region, and the time resolution. The clock modes are determined by a program loaded into the analog electronics. The editing modes specify how detected events are edited, and determine the format of the XIS data telemetry. The editing modes are determined by the digital electronics. In principle, each XIS sensor can be operated with different mode combinations.

The clocking mode specifies how the CCD pixels are read out. Each clocking mode has its own μ-code, a pattern of voltage clocking for exposure and charge transfer. It enables full read, partial read, or stacked read. With a partial or stacked read, a higher pile-up limit and timing resolution can be achieved at a sacrifice of observing efficiency and imaging information. There are two major types of clocking mode in the XIS, the Normal and the Parallel-sum (P-sum) mode presented below.

- **Normal mode** is for timed-exposure readout. It can be combined with a window option (partial readout in space), a burst option (partial readout in time), or both (partial readout in both space and time). If neither the window nor burst option is specified, a frame time is 8 s, and all pixels are read out every 8 s. Furthermore, the two options which can be used in combination with the normal mode are described blow.

  - **Burst option** is for partial readout in time. In the b s ($b = 2.0, 0.62, 0.5, 0.1$ s) burst mode, all pixels are read out, but the effective exposure time is limited to b s. During 8 s of exposure time, events detected in the first $(8 - b)$ s are transferred and discarded without being recorded. Events detected in the remaining b s are transferred and recorded.
  - **Window option** is for partial readout in space. In the $1/w$ ($w = 4, 8$) window mode, the central $1024/w$ pixels are read out in the vertical direction and the entire pixels are read out in the horizontal direction, yielding a $1024 \times 1024/w$ pixel image. The exposure time is $8/w$ s.

- **P-sum mode** is for stacked readout. The pulse height from 128 rows are stacked into a single row along the vertical direction. Charge is transferred continuously, thus the spatial information along the vertical direction is lost and replaced with the arrival time information. The arrival time is ticked at a 7.8 ms resolution. This is smeared by the point spread function with a HPD of $2'$, which is equivalent to 0.9 s.

  The P-sum clocking mode is in principle available for all FI sensors. However, because it is severely affected by leaked charge in areas damaged by micrometeorite hits, the P-sum clocking support was terminated for the XIS 2 and XIS 0. Therefore, it is currently available only for the XIS 3. Observers using the P-sum clocking mode for the XIS 3 need to use a Normal clocking mode for the other sensors.

3.4 Hard X-ray Detector

3.4.1 Overview

The HXD is a non-imaging collimated instrument sensitive in the 10–600 keV energy range (Figure 3.14). The sensor consists of 16 well-type main units and surrounding 20 scintillators for active anti-coincidence shielding. Thanks to the active anti-coincidence shields, a narrow field of view, and stable as well as low background environment in a low Earth orbit, unprecedented sensitivity is archived in the hard X-ray band. The design parameters and the basic performance are summarized in Table 3.1 in § 3.5. More details can be found in e.g., Takahashi et al. (2007) and Kokubun et al. (2007).

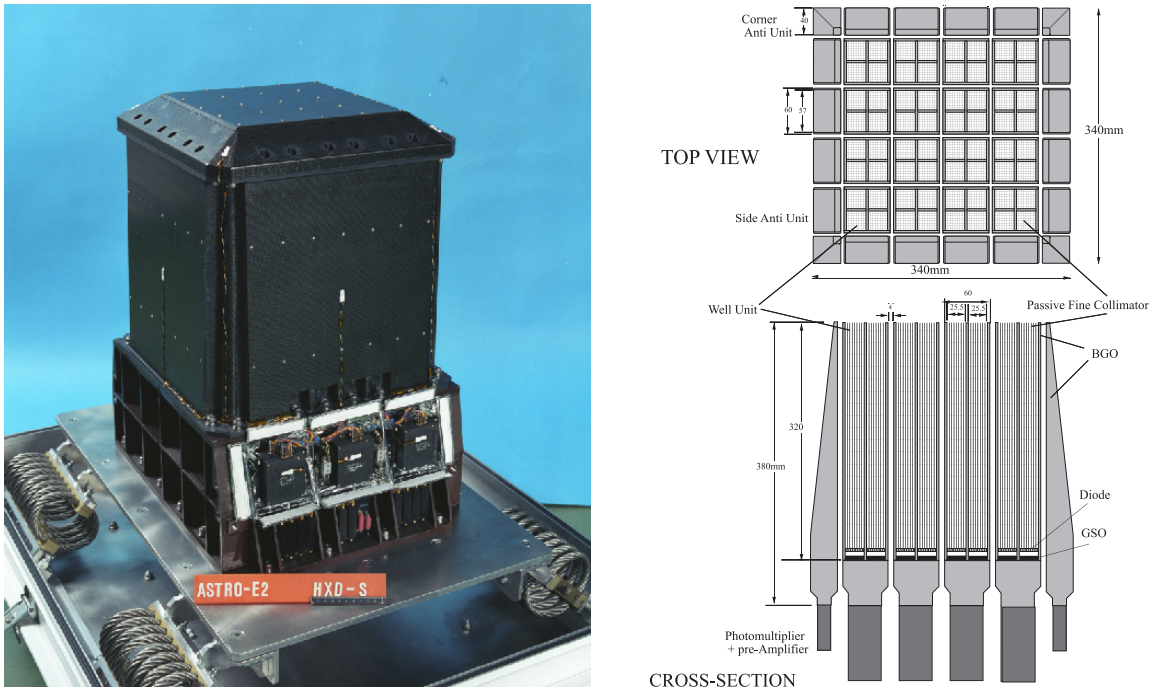

Figure 3.14: Picture, top view, and cross section of the HXD onboard*Suzaku* (Takahashi et al. 2007).

The well-type units and the anti-coincidence shields have a compound-eye configuration to increase an effective area. The array configuration of the sensor units is shown in Figure 3.15.

Each well-type unit consists of two independent sensors: the gadolinium silicate (GSO) / bismuth germanate (BGO) phoswich counters and the silicon PIN diodes. A schematic view of the well-type unit is shown in Figure 3.16. Each detector forms a 2×2 array with a layered structure at the bottom of the well. The lower energy response is provided by the PIN, which is located in front of the GSO and the BGO scintillators. The PIN has sensitivity in the $\sim$10–70 keV energy range, and gradually becomes transparent to higher

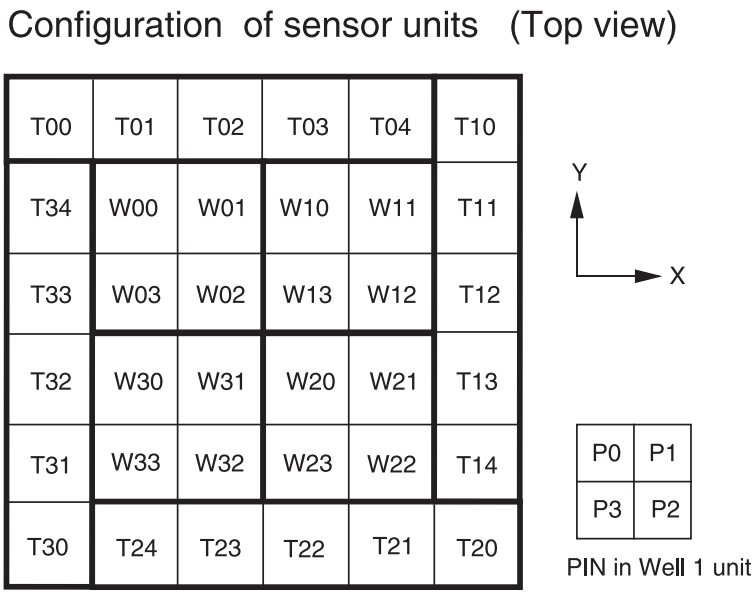

Figure 3.15: Array configuration and numbering of the sensor units in the HXD (Takahashi et al. 2007). The 16 well-type units and the surrounding 20 scintillators are identified from W00 to W33 and from T00 to T34, respectively.

energy photons. The transparent photons are detected with the GSO scintillators located in the middle layer, which has sensitivity in the 40–600 keV energy range. The bottom layer is the BGO scintillators, which work as a veto counter for both PIN and GSO detectors. Additionally, in order to reduce contamination from irrelevant emission, passive shields, called "fine collimators", are inserted in each well-type unit above the PIN. The scintillator signals are read out by photomultiplier tube (PMT) glued to the well unit BGO.

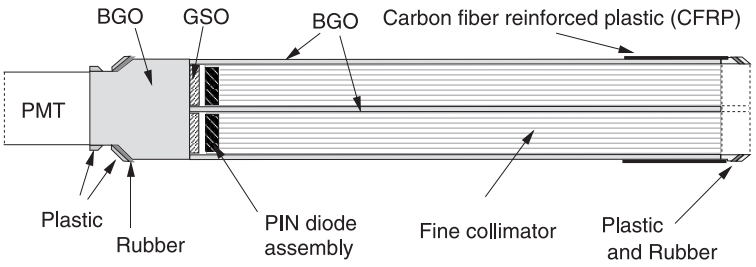

Figure 3.16: Schematic view of the well-type unit of HXD (Takahashi et al. 2007).

3.4.2 Performance and Calibration

3.4.2.1 Effective Area

The total effective area is shown in Figure 3.17. The values are convolved with the detector responses and with the photon absorption of the layered materials in front of the devices. Both the PIN and the GSO scintillators cover the ∼40–70 keV energy range. The HXD features an effective area of ∼160 cm^2 at 20 keV, and ∼260 cm^2 at 100 keV (Figure 3.17).

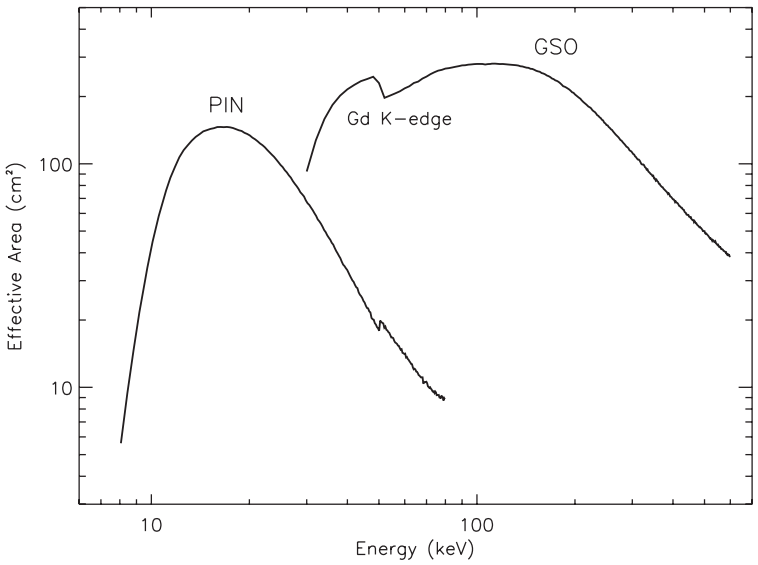

Figure 3.17: Total effective areas of the PIN and the GSO scintillators. The values are convolved with the detector responses and with the photon absorption of the layered materials in front of the devices (Takahashi et al. 2007).

3.4.2.2 Angular Resolution

With a combination of the surrounding BGO veto counters and the fine collimators, the angular response and the FoV highly depend on incoming photon energies. The low energy photons below ∼100 keV where the fine collimator is opaque to X-rays are restricted to a $\sim 34' \times 34'$ in FWHM square FoV with the passive fine collimators. For high energy photons above ∼100 keV, the fine collimator becomes gradually transparent, the FoV is $\sim 4.^{\circ}5 \times 4.^{\circ}5$ in FWHM square opening, defined by the BGO well. Figure 3.18(a) shows the calculation of the energy dependence of the angular response. The measured angular response with gamma-ray lines from radio isotope sources located at a limited distance is shown in Figure 3.18(b) for different energies. The results agree well with the calculated response shown in Figure 3.18(a).

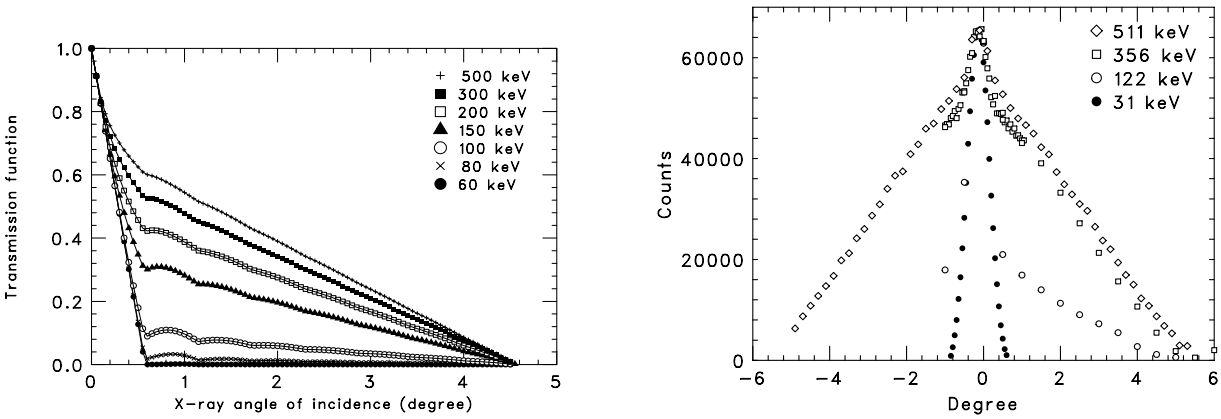

(a) (b)

Figure 3.18: (a) Calculated angular transmission of the well-type counter, including the effects of ideal fine colimators (Takahashi et al. 2007). (b) Angular responses of the well-type units measured with radio isotope sources at a finite distance (Takahashi et al. 2007).

3.4.2.3 Energy Response

The energy response of HXD-PIN have been constructed for individually for the 64 PIN diodes, through Monte Calro simulations using GEANT4 toolkit. The bias voltage on-board and low energy threshold in the ground processing of various subsets of HXD-PIN units have been adjusted since launch to reduce noise events. This changes the characteristics of these PIN units in several discrete steps.

The energy response of HXD-GSO was also produced using GEANT4, in the same way as that of HXD-PIN. However, there is an apparent change in the energy scale of HXD-GSO. Recently, the in-orbit calibration of HXD-GSO is improved by Yamada et al. (2011). They updated the data processing, the response, and the auxiliary files of HXD-GSO.

3.4.2.4 Background Events

The HXD is designed to achieve an extremely low background level in operation. Most of the NXB for the PIN is considered to be caused by interactions between cosmic-ray particles and surrounding materials. A typical NXB for the PIN measured in orbit is shown in Figure 3.19(a). In addition, almost no long-term variation of the NXB of the PIN was confirmed during the first three years in operation, thanks to the small amount of activation in silicon. In contrast, as shown in Figure 3.19(b), a significant long-term increase caused by in-orbit activation has been observed for the NXB of the HXD-GSO, especially during the early phase of the mission. The GSO scintillators emit a certain amount of high energy particles and photons by themselves, because it is exposed to heavy cosmic-ray particles and activated, and background level becomes gradually high after launch. The background spectrum of the HXD-GSO thus contains several activation peaks, with intensities exponentially increasing with their half-lives.

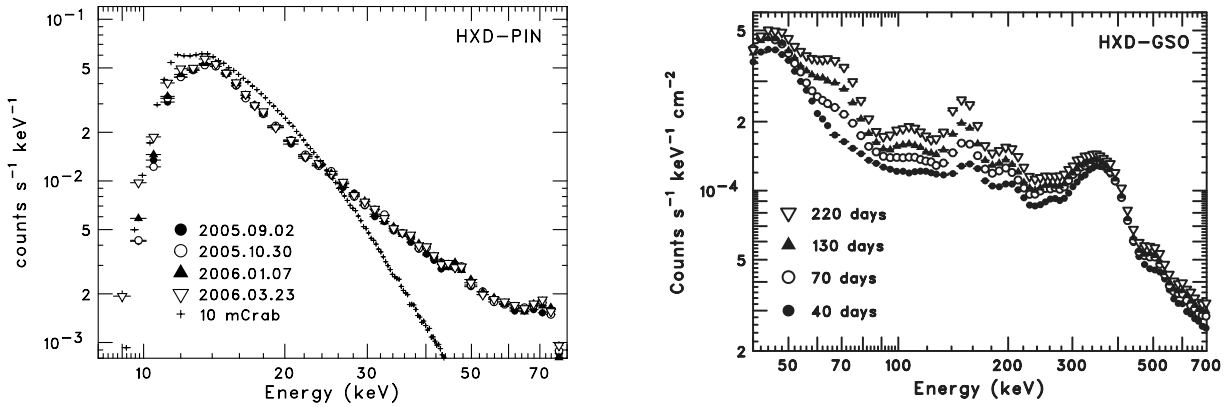

(a) (b)

Figure 3.19: (a) Comparison of the NXB spectra during the first three years (Kokubun et al. 2007). (b) Evolution of the averaged GSO-NXB spectra during the first half year after the launch. (Kokubun et al. 2007).

Figure 3.20 illustrates the comparison between detector backgrounds of several hard X-ray missions. The lowest background level per effective area is achieved by HXD in an energy range of 12–70 and 150–500 keV. The in-orbit sensitivity of the experiment can be roughly estimated by comparing the background level with celestial source intensities indicated by dotted lines. Below 30 keV, the level is smaller than 10 mCrab, which means a sensitivity better than 0.3 mCrab can be obtained, if an accuracy of 3% is achieved in the background modeling.

Since the long-term variation of NXB for both HXD-PIN and HXD-GSO can be expected to be stable, the main uncertainties of the background come from temporal and spectral short-term variations. A significant short-term variability is seen in the NXB with a peak-to-peak amplitude of a factor of 3, which highly depends on the cut-off rigidity (COR) over the orbit (Figure 3.21(a)). Since the COR affects the flux of incoming primary cosmic-ray particles, most of the NXB of HXD-PIN is considered to originate in the secondary

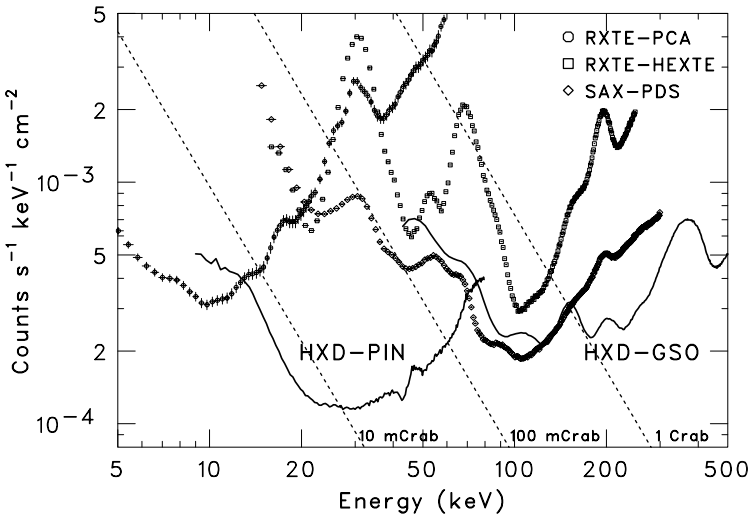

Figure 3.20: In-orbit detector background of HXD-PIN and HXD-GSO, averaged over 2005 August to 2006 March and normalized by individual effective areas (Kokubun et al. 2007). For a comparison, those of the *RXTE*/PCA, *RXTE*/HEXTE, and *BeppoSAX*/PDS are also shown. The dotted lines indicate 1 Crab, 100 mCrab, and 10 mCrab intensities.

emission produced by interactions between cosmic-ray particles and materials surrounding the detector. During this temporal variation of the NXB of HXD-PIN, its spectral shape also changes slightly (Kokubun et al. 2007). In case of the NXB of HXD-GSO the temporal variation differs for different energy bands, as shown in the right panel of Figure 3.21(b). In the lowest energy range a rapid decline after the SAA passage is clearly observed, in addition to a similar anti-correlation with the COR. All these temporal and spectral behaviors have to be properly handled in the background modeling.

As the HXD is a non-imaging instrument, the limiting sensitivity heavily depends on the reproducibility of background estimation. Its instantaneous background can be estimated from separate off-source observations or models. The NXB is caused by activations, neutron reactions and a small leakage of the CXB and earth albedo gamma-rays. Since the orbital environment in view of cosmic-ray changes with the COR as well as the SAA, the NXB itself is time variable. The *Suzaku* HXD team provides the NXB models for each observation, based on the real data obtained within the earth occultation, sorted with a few major orbital parameters (Fukazawa et al. 2009). Reproducibilities at a 90% confidence level are better than 5% for HXD-PIN and 2% for HXD-GSO, respectively. More details and the latest background models are available at the official webpages[4].

[4]HXD-PIN `https://heasarc.gsfc.nasa.gov/docs/suzaku/analysis/pinbgd.html`; HXD-GSO `https://heasarc.gsfc.nasa.gov/docs/suzaku/analysis/gsobgd2012.html`

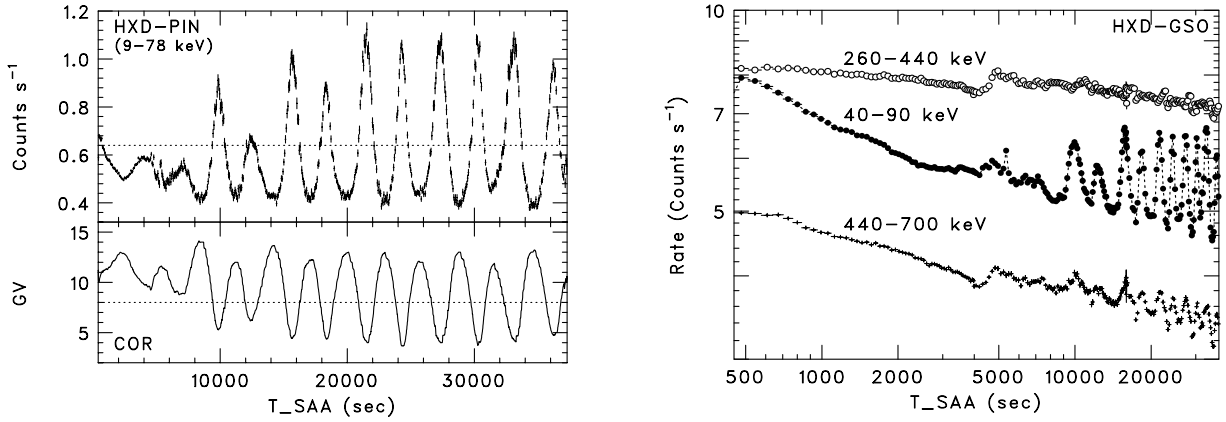

(a) (b)

Figure 3.21: Short-term variability of the NXB (Kokubun et al. 2007). (a) The upper panel shows a light curve of the NXB of HXD-PIN folded with an elapsed time from the SAA in the 9–78 keV energy range. The lower panel shows the corresponding COR values. (b) Light curves of the NXB of HXD-GSO in 40–90, 260–440, and 440–700 keV, folded with an elapsed time from the SAA.

3.5 Summary of the Mission

The design parameters and the orbital information of the *Suzaku* spacecraft are summarized in Table 3.1.

Table 3.1: Details of the *Suzaku* mission (Mitsuda et al. 2007).

	Parameter	Value
Spacecraft	Orbit apogee	∼568 km
	Orbital period	∼96 m
	Observing efficiency	∼45 %
XRT [a]	Focal length	4.75 m
	Substrate	Aluminium (152 μm)
	Reflector	Gold ($\lesssim$0.1 μm)
	Number of reflectors	175
	Inner diameter	118 mm
	Outer diameter	399 mm
	Incident angle	0.°18–0.°60
	Effective area (1.5 keV)	440 cm^2
	Effective area (8 keV)	250 cm^2
	Plate scale	0.′724 mm^{-1}
	FoV (1.5 keV)	∼17′
	FoV (8 keV)	∼13′
	Angular resolution	∼2′ (HPD)
XIS [a]	FoV	17.8′×17.8′
	Bandpass	0.2–12 keV
	Pixel grid	1024×1024
	Energy resolution (6 keV)	∼130 eV (FWHM)
	Effective area (1.5 keV)	∼340 cm^2 (FI), ∼390 cm^2 (BI)
	Effective area (8 keV)	∼150 cm^2 (FI), ∼100 cm^2 (BI)
	Timing resolution	8 s
HXD [a]	FoV ($\gtrsim$100 keV)	4.5°×4.5°
	FoV ($\lesssim$100 keV)	34′×34′
	Bandpass (PIN)	10–70 keV
	Bandpass (GSO)	40–600 keV
	Energy resolution (PIN)	∼4.0 keV (FWHM)
	Energy resolution (GSO)	$\sim 7.6/\sqrt{E_{\rm MeV}}$ % (FWHM)
	Effective area (20 keV)	∼160 cm^2
	Effective area (100 keV)	∼260 cm^2
	Timing resolution	61 μs

[a] Details of the XRT, the XIS, and the HXD are respectively described in § 3.2, 3.3, and 3.4.

Chapter 4

Observations

Contents

Until the end of observational operation in 2015, more than 30 APXPs have been observed with *Suzaku*, more than 60 times in total. All of the acquired data are available in archive. The present thesis utilizes 34 available data sets among them, after excluding data sets, an exposure time of which is short ($<$ 10 ks) or a target source in which was faint ($<$ 0.5 counts s^{-1} with each XIS). Individual observations lasted typically for $\sim$1 to $\sim$2 days, depending on the objective. However, the orbit of *Suzaku* is almost circular with an altitude is of $\sim$570 km. Therefore, the line of sight of *Suzaku* is interrupted by the earth, typically for $\sim$30% of each orbit ($\sim$ 30 min; so called earth occultation). In addition, data acquisition must be stopped when the satellite pass through SAA (see § 3.1). Thus, the net exposures are reduced to roughly $\sim$50% of the gross duration time of observation, and the data suffers periodic gaps. We, in § 4.1 describe the data reduction procedure, and how those data sets have been acquired in § 4.2. In latter section, since the observation strategy differs among BeXB pulsar, SGXB pulsar and LMXB pulsar, these three classes are described separately.

4.1 Data Reduction

All the archived *Suzaku* data of our samples were analyzed by using HEASARC software version 6.19. We reprocessed the XIS and the HXD data using the FTOOLS task, `aepipeline` with the latest calibration database and the standard screening criteria. The XIS data acquired in the normal mode (parts of them were operated with the window option and the burst option, see Table 4.1–4.3). Some observations were performed with the P-sum mode. Their energy resolution is significantly worse than that in the normal mode due to applicable neither the SCI nor a CTE correction and their calibration accuracy for spectral analysis is not as good as that for the normal mode. Hence, we did not use the XIS data acquired in the P-sum mode. As for the HXD, the HXD-PIN data were utilized in all samples, while HXD-GSO data were used in a part of them, which has high intensity in hard X-rays.

The on-source and background XIS events were extracted from a circular region of $3'$ radius and an annulus with the inner radius of $4'$ and outer radius $7'$ centered at the source position, respectively. If the pile-up effect occurred in data of a XIS detector, we excluded events in a central region of the on-source circle to reduce the effect of pile-up less than 1% with an estimation following Yamada et al. (2012). The redistribution matrix files and ancillary response files for XISs were generated by using `xisrmfgen` and `xissimarfgen` routines (Ishisaki et al. 2007), respectively.

We used tuned (LCFITDT) NXB models (Fukazawa et al. 2009) to get the NXB events for HXD-PIN and HXD-GSO. From the HXD-PIN data, we subtracted the NXB and an expected contribution of CXB with a spectral shape given by Boldt & Leiter (1987). From the HXD-GSO data, we subtracted only the NXB, as the expected contribution of CXB is negligible. In our analysis, response files released between 2008 January and 2011 June were used for HXD-PIN data selecting suitable one to each observation, whereas response and effective area files released in 2010 May were used for HXD-GSO data.

4.2 Light Curves

For timing analysis, we applied barycentric correction to the arrival times of individual photons using the `aebarycen` task of FTOOLS (Terada et al. 2008). As for HXD events, dead-time corrections were applied using FTOOLS task `hxddtcor`. After barycentric and dead-time corrections, we conducted a farther correction of the binary motion, when the orbital parameters have been derived in a system. The used orbital parameters are listed in Table 4.4. Light curves were extracted from the XIS event data in range of 0.5–10 keV with minimum available time resolution attributed to XIS operation mode (i.e. window option). Data from all operated XISs are added together and obtained a single light curve for XISs. We also created light curves in range of 12–70 keV from HXD-PIN events data with a resolution of 1 s. The hardness ratios (HRs) of the HXD-PIN light curves to those of XISs were calculated. Figure 4.2–4.23, 4.30, 4.31, and 4.33–4.38 show background-subtracted light curves of XIS (upper panel) and HXD-PIN (middle panel) with a bin-time of the pulsar spin period or its harmonic value, respectively. The calculated HRs are also shown in the lowest panel in each figure.

4.2.1 BeXB Pulsars

As described in § 2.1.2.3, BeXB pulsars show periodic X-ray outbursts with the orbital period, $P_{\rm orb}$, which occur around the periastron phase and remain in quiescence when the NSs are away from their periastron phases. So far six BeXB pulsars have been observed with *Suzaku* on fourteen occasions in total, of which ten were ToO observations to catch the top of an X-ray outburst. Most of these ToO observations were triggered by alerts from the operating X-ray all sky monitors, *RXTE*, *Swift*, and MAXI. In Figure 4.1, we show long term, one-day binned light curves of these BeXBs obtained by *RXTE*/ASM (Levine et al. 1996), *Swift*/BAT (Barthelmy et al. 2005; Krimm et al. 2013), and MAXI/GSC (Mihara et al. 2011; Sugizaki et al. 2011) can be downloaded from ASM web page[1], BAT Transient Monitor page[2], and MAXI home page [3], respectively. The times of *Suzaku* observations are indicated by dashed lines in the figures. Details of these observations are summarized in Tables 4.1.

As indicated with star symbols in Table 4.1, eleven observations of six objects have been conducted during X-ray outbursts. Four (GX 304-1, EXO 2030+375, GRO J1008-57, and Cep X-4) of the six objects were observed twice or three times during outbursts. In all of those observations, the XIS were operated with the 1/4 window option, to avoid pile-up effects and to realize a better time resolution (2 s), which are required for phase-resolved study of these bright sources like BeXB pulsars in the outbursts.

[1] `http://xte.mit.edu/asmlc/ASM.html`
[2] `https://swift.gsfc.nasa.gov/results/transients/`
[3] `http://maxi.riken.jp/top/index.html`

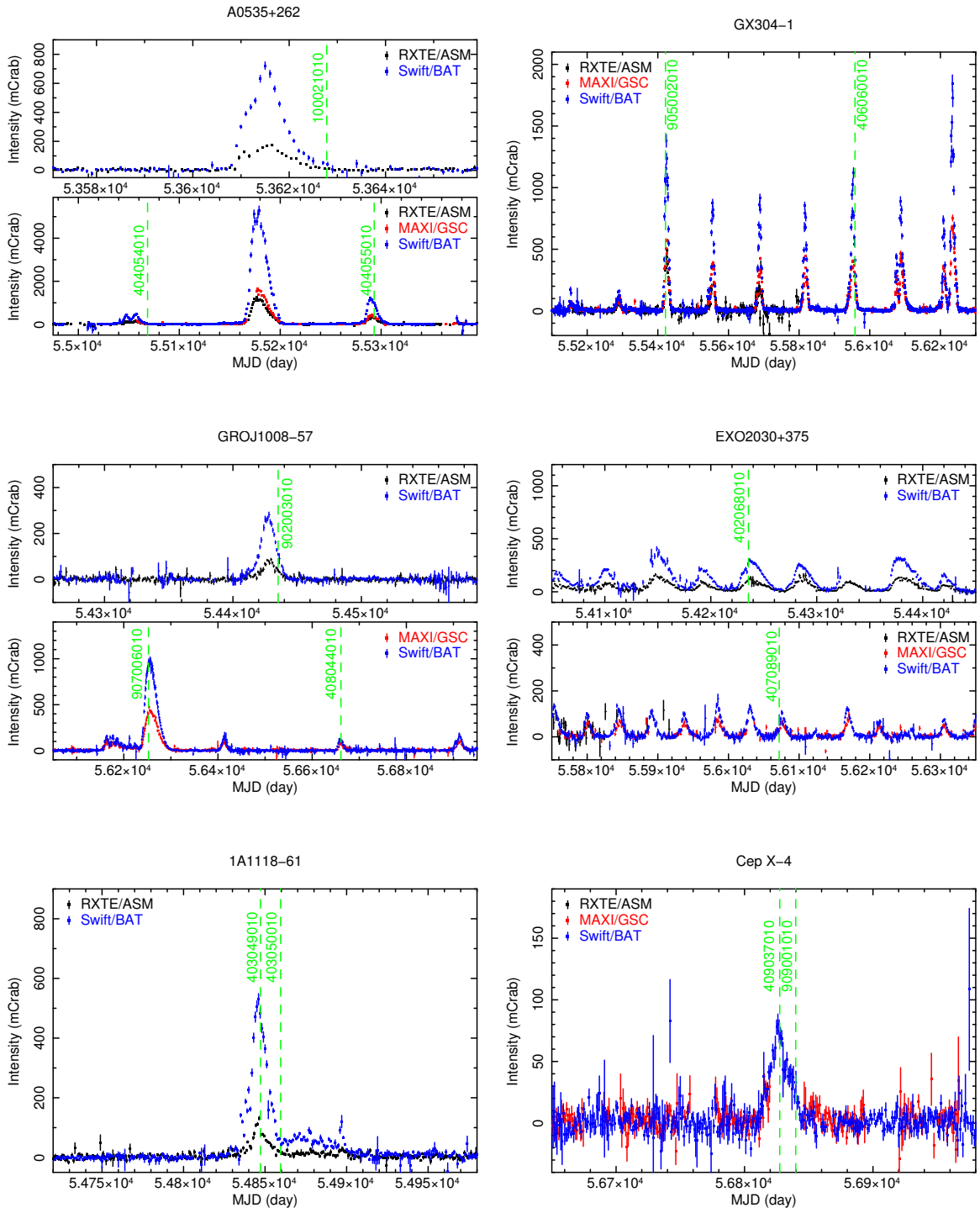

Figure 4.1: Long-term light curves of BeXB pulsars obtained from *RXTE*/ASM (1.5–12 keV; with black), MAXI/GSC (2.0–20 keV; with red) and *Swift*/BAT (15–50 keV;blue) around the *Suzaku* observation. The fluxes are expressed in "Crab unit". *Suzaku* observations are indicated by dashed green lines. The source names are indicated above each panel.

Table 4.1: *Suzaku* observation list of BeXB pulsars.

Source[a]	ObsID[b]	Date(UT) START	Date(UT) END	Duration(ks)[c]	Aim[d]	XIS operation[e] CLK	XIS operation[e] WIN
A 0535+262	100021010	2005-09-14 13:40	2005-09-15 01:00	40.8	XIS	normal	1/4
	404054010	2009-08-24 23:06	2009-08-26 03:50	103.4	HXD	1.0 s burst	1/4
	404055010⋆	2010-04-06 12:03	2010-04-07 16:52	103.7	HXD	0.1 s burst	1/4
GX 304-1	905002010⋆	2010-08-13 16:18	2010-08-13 23:00	24.1	HXD	0.5 s burst	1/4
	406060010⋆	2012-01-31 10:29	2012-02-02 04:00	149.5	XIS	0.5 s burst	1/4
GRO J1008-57	902003010⋆	2007-11-30 11:32	2007-12-01 19:15	114.2	XIS	1.0 s burst(XIS 0)	1/4
						normal(XIS 1,3)	1/4
	907006010⋆	2012-11-20 14:44	2012-11-22 05:21	139.0	XIS	0.3 s burst	1/4
	408044010⋆	2014-01-03 15:42	2014-01-04 14:09	80.8	XIS	1.0 s burst	1/4
EXO 2030+375	402068010⋆	2007-05-14 20:37	2007-05-16 03:45	112.1	HXD	1.0 s burst	1/4
	407089010⋆	2012-05-23 20:12	2012-05-25 18:57	168.3	XIS	normal	1/4
1A 1118-61	403049010⋆	2009-01-15 12:20	2009-01-16 21:40	120.0	HXD	1.0 s burst	1/4
	403050010	2009-01-28 05:37	2009-01-28 21:25	56.9	HXD	1.0 s burst	1/4
Cep X-4	409037010⋆	2014-06-18 20:49	2014-06-20 00:52	100.9	XIS	normal	1/4
	909001010⋆	2014-07-01 05:00	2014-07-02 14:00	118.8	XIS	normal	1/4

Notes.
[a] Preceding *Suzaku* studies: A 0535+262 (Terada et al. 2006; Naik et al. 2008; Caballero et al. 2013; Maitra & Paul 2013a), GX 304-1 (Yamamoto et al. 2011; Jaisawal et al. 2016), GRO J1008-57 (Naik et al. 2011b; Kühnel et al. 2013; Yamamoto et al. 2014; Bellm et al. 2014), EXO 2030+375 (Naik et al. 2013; Naik & Jaisawal 2015), 1A 1118-61 (Suchy et al. 2011; Maitra et al. 2012), Cep X-4 (Jaisawal & Naik 2015)
[b] The ObsIDs marked with star symbol are the observations during the X-ray outburst.
[c] On-source time.
[d] Nominal pointing position (XIS or HXD) in the observations; see Mitsuda et al. (2007).
[e] Clock mode and window option of XIS.

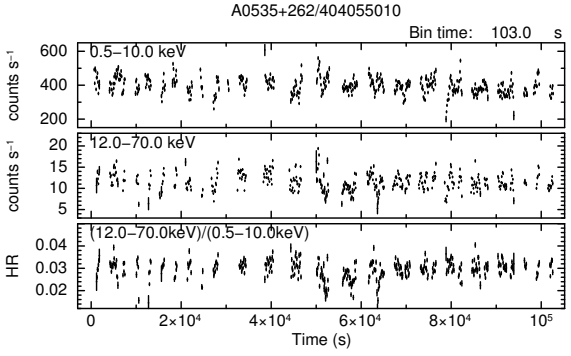

Figure 4.2: Background-subtracted, XIS (0.5-10 keV) and HXD-PIN (12-70 keV) light curves of A 0535+262 (ObsID=404055010) with 103 s time bins are shown in top and middle panels, respectively. Lower panel represent the hardness between two light curves.

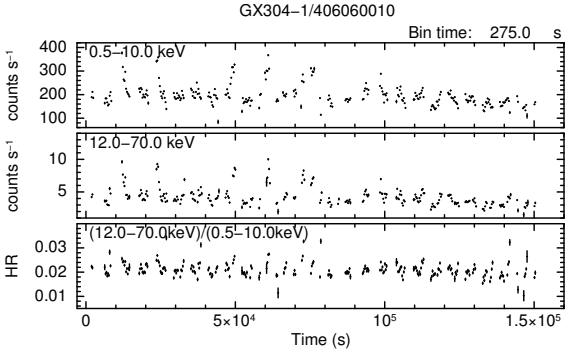

Figure 4.3: The same as Figure 4.2 but light curves and HR of GX 304-1 (ObsID=406060010) with 60 s time bins.

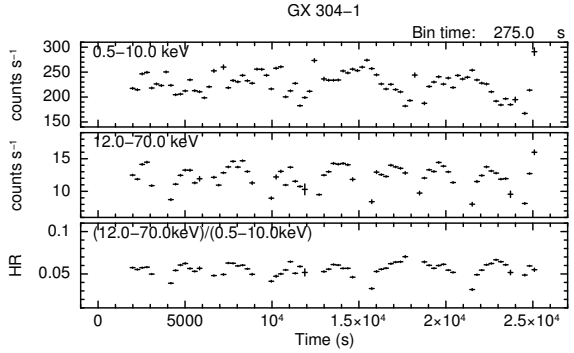

Figure 4.4: The same as Figure 4.2 but light curves and HR of GX 304-1 (ObsID=905002010) with 60 s time bins.

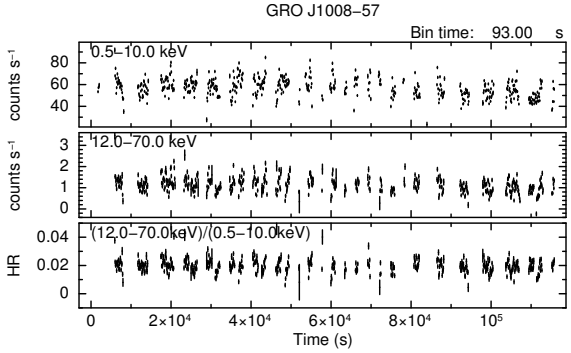

Figure 4.5: The same as Figure 4.2 but light curves and HR of GRO J1008-57 (ObsID=902003010) with 60 s time bins.

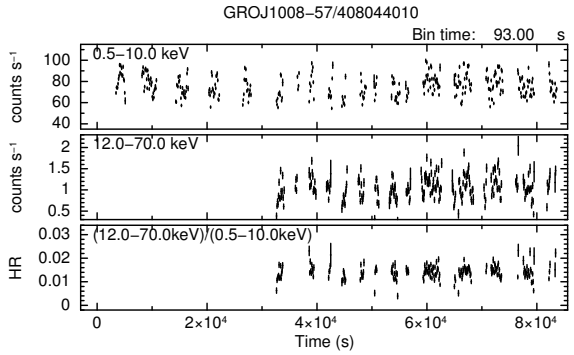

Figure 4.6: The same as Figure 4.2 but light curves and HR of GRO J1008-57 (ObsID=408044010) with 60 s time bins.

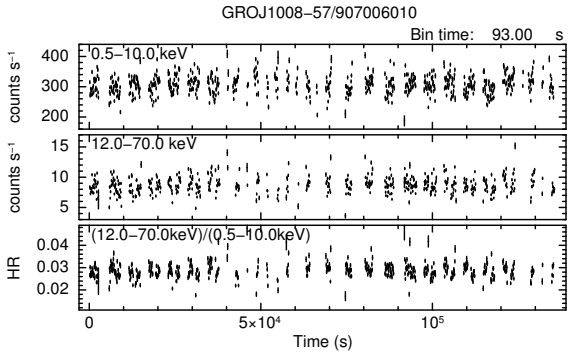

Figure 4.7: The same as Figure 4.2 but light curves and HR of GRO J1008-57 (ObsID=907006010) with 60 s time bins.

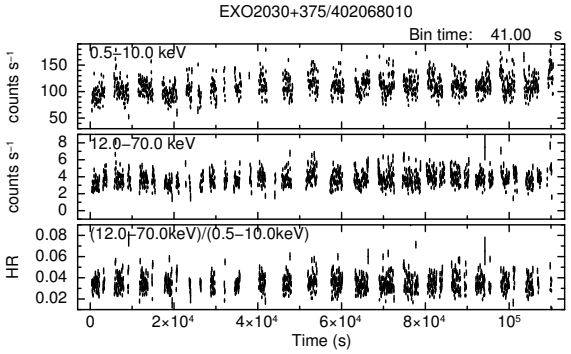

Figure 4.8: The same as Figure 4.2 but light curves and HR of EXO 2030+375 (ObsID=402068010) with 60 s time bins.

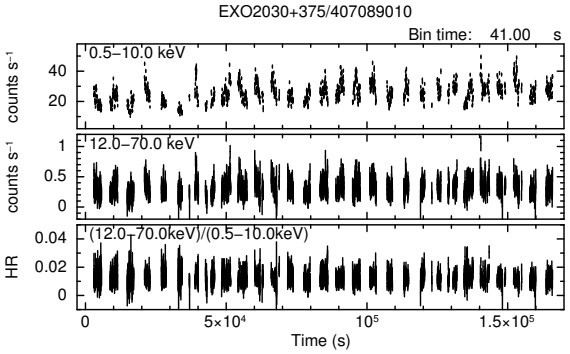

Figure 4.9: The same as Figure 4.2 but light curves and HR of EXO 2030+375 (ObsID=407089010) with 60 s time bins.

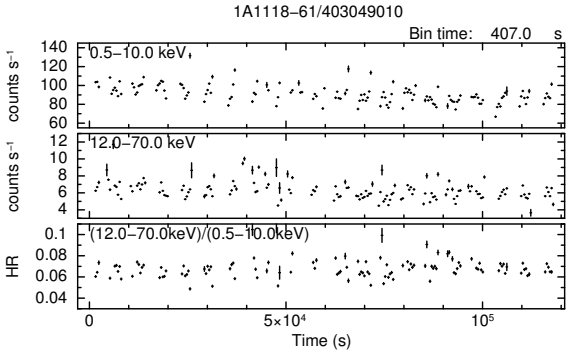

Figure 4.10: The same as Figure 4.2 but light curves and HR of 1A 1118-61 (ObsID=403049010) with 407 s time bins.

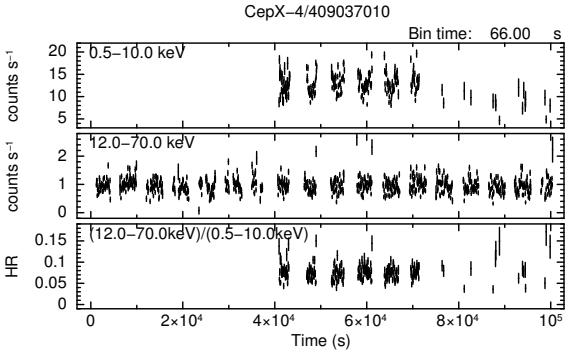

Figure 4.11: The same as Figure 4.2 but light curves and HR of Cep X-4 (ObsID=409037010) with 66 s time bins.

The extracted light curves of XISs and HXD-PIN and calculated HRs derived from the observation in the X-ray outbursts are shown in Figures 4.2–4.12. Part of these observations utilized the XIS burst option with various snap times (see Table 4.1), to further reduce pile-up effects under high count rates. Although there are several data points with a low and high count rate, there is no trend of any gradual intensity change in BeXB pulsars light curves in contrast to SGXBs (§ 4.2.2). Since the BeXB pulsars in our sample have pulse periods of $P_{\rm spin}$ = 40–700 s, the time resolutions of the XIS (2.0 s) and HXD (67 μs) are enough to resolve the pulses of BeXB pulsars. As already reported by previous works using the same *Suzaku* data, spectra of these objects were obtained by the XIS and HXD-PIN with good statistics. In addition, most of them were bright enough to detect with HXD-GSO and allow a construction of broadband spectra (1–100 keV).

Four BeXB pulsars were also observed in quiescence, namely, in orbital phases far away from the periastron, or when the overall activity was rather low. These are A 0535+262, 1A 1118-61, and X 0331+53. As shown in Figure 4.1, three sources, except for X 0331+53,

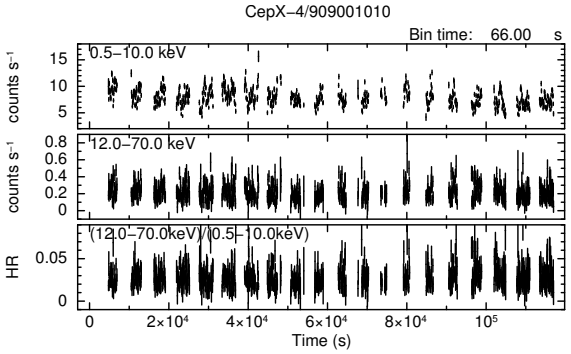

Figure 4.12: The same as Figure 4.2 but light curves and HR of Cep X-4 (ObsID=909001010) with 66 s time bins.

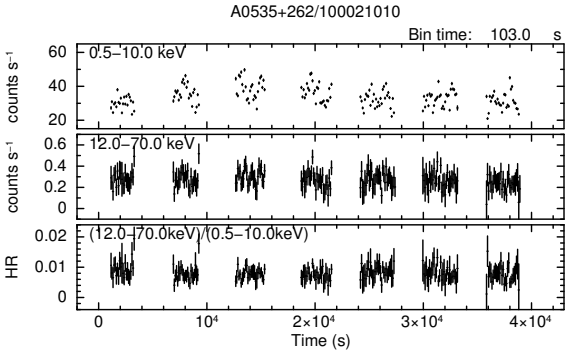

Figure 4.13: The same as Figure 4.2 but light curves and HR of A 0535+262 (ObsID=100021010) with 60 s time bins.

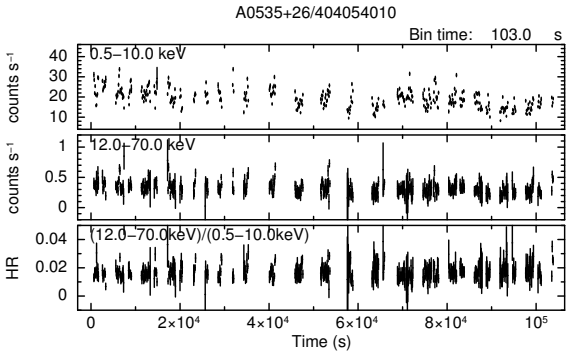

Figure 4.14: The same as Figure 4.2 but light curves and HR of A 0535+262 (ObsID=404054010) with 60 s time bins.

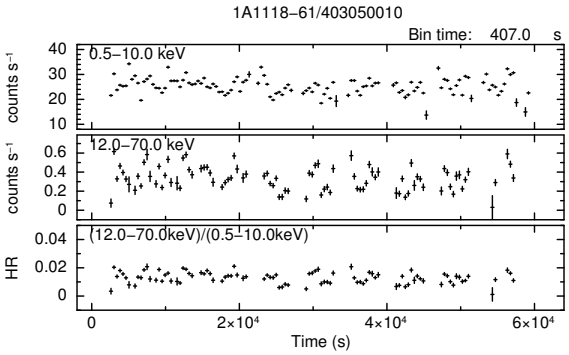

Figure 4.15: The same as Figure 4.2 but light curves and HR of 1A 1118-61 (ObsID=403050010) with 407 s time bins.

were detected in quiescence in addition to the outburst observations, when they were two orders of magnitude fainter than in outbursts. Their light curves and HRs in *Suzaku* observations are shown in Figures 4.13–4.15. Although X 0331+53 was observed in a minor outburst and was detected with the XIS, it was not detected with HXD-PIN. Therefore, this data set is excluded from the present study.

4.2.2 SGXB Pulsars

As stated in § 2.2.5, SGXB pulsars compose another major subclass of HMXB, which is NS with OB type supergiant primary. As described in § 2.1.2.2, these objects show rapid flares randomly, while BeXB pulsars produce periodic outbursts (see § 4.2.1). Twelve SGXB pulsars were selected among those observed by *Suzaku*, as summarized in Table 4.2.

Table 4.2: *Suzaku* observation list of SGXB pulsars.

Source[a]	ObsID	Date(UT) START	Date(UT) END	Duration(ks)[b]	Aim[c]	XIS operation[d] CLK	XIS operation[d] WIN
OAO 1657-415	406011010	2011-09-26 09:34	2011-09-28 16:00	195.9	XIS	normal	1/4
4U 1909+07	405073010	2010-11-02 16:53	2010-11-03 10:24	63.1	XIS	normal	1/4
4U 1907+097	401057010	2006-05-02 06:11	2006-05-03 17:34	127.4	XIS	normal	1/4
	402067010	2007-04-19 10:03	2007-04-21 06:16	159.2	HXD	normal	full
4U 1538-522	407068010	2012-08-10 00:04	2012-08-10 17:38	63.2	XIS	normal	1/4
4U 0114+65	406017010	2011-07-21 10:20	2011-07-22 22:41	130.9	XIS	normal	1/4
4U 2206+54	402069010	2007-05-16 03:53	2007-05-17 19:30	142.6	HXD	normal	1/4
IGR J16393-4643	404056010	2010-03-12 23:40	2010-03-14 10:49	126.5	XIS	normal	full
GX 301-2	403044010	2008-08-25 13:15	2008-08-26 00:05	39.0	HXD	normal	1/4
	403044020	2009-01-05 10:33	2009-01-07 01:00	138.4	HXD	normal	1/4
Vela X-1	403045010	2008-06-17 04:45	2008-06-18 21:42	147.4	XIS	normal	1/4
Cen X-3	403046010	2008-12-08 06:55	2008-12-10 05:00	165.9	HXD	1.0 s burst	1/4
LMC X-4	702036020	2008-04-05 13:15	2008-04-06 07:20	65.1	XIS	normal	1/8
	702037010	2008-02-11 00:42	2008-02-11 14:30	49.7	XIS	normal	1/8
	702038010	2008-01-15 08:39	2008-01-15 19:00	37.3	XIS	normal	1/8
SMC X-1	706030010	2011-04-07 20:45	2011-04-08 05:52	32.8	XIS	normal(XIS 0,1)	1/4
						p-sum(XIS 3)	full
	706030020	2011-04-18 06:08	2011-04-18 16:56	38.8	XIS	normal(XIS 0,1)	1/4
						p-sum(XIS 3)	full
	706030030	2011-04-22 15:34	2011-04-23 02:40	39.9	XIS	normal(XIS 0,1)	full
						p-sum(XIS 3)	full
	706030040	2011-05-10 00:28	2011-05-10 09:45	33.4	XIS	normal(XIS 0,1)	full
						p-sum(XIS 3)	full
	706030050	2011-05-25 02:02	2011-05-25 16:11	50.9	XIS	normal(XIS 0,1)	1/4
						p-sum(XIS 3)	full
	706030060	2011-06-28 14:17	2011-06-29 02:18	43.3	XIS	normal(XIS 0,1)	full
						p-sum(XIS 3)	full
	706030070	2011-09-21 04:07	2011-09-21 15:41	41.6	XIS	normal(XIS 0,1)	1/4
						p-sum(XIS 3)	full
	706030080	2011-11-10 01:50	2011-11-10 14:50	46.8	XIS	normal(XIS 0,1)	1/4
						p-sum(XIS 3)	full
	706030090	2011-12-12 21:33	2011-12-13 06:30	32.2	XIS	normal(XIS 0,1)	full
						p-sum(XIS 3)	full
	706030100	2012-03-19 06:14	2012-03-19 20:17	50.6	XIS	normal(XIS 0,1)	full
						p-sum(XIS 3)	full

Notes.
[a] Preceding *Suzaku* studies: OAO 1657-415 (Pradhan et al. 2014; Jaisawal & Naik 2014), GX 301-2 (Suchy et al. 2012), 4U 1909+07 (Fürst et al. 2012; Jaisawal et al. 2013), 4U 1907+097 (Rivers et al. 2010; Maitra & Paul 2013a), 4U 1538-522 (Hemphill et al. 2014; 2016), 4U 0114+65 (Pradhan et al. 2015), 4U 2206+54 (Finger et al. 2010), Vela X-1 (Doroshenko et al. 2011; Odaka et al. 2013; Maitra & Paul 2013b), Cen X-3 (Naik et al. 2011a), LMC X-4 (Hung et al. 2010)
[b] On-source time.
[c] Nominal pointing position (XIS or HXD) in the observations; see Mitsuda et al. (2007).
[d] Clock mode and window option of XIS.

Objects in this class have been discovered by the oldest satellite, namely *Uhuru* satellite. Most of them are located in our galaxy (< 8 kpc), while LMC X-4 and SMC X-1 are in the Large Magellanic Cloud (~ 50 kpc) and, the Small Magellanic Cloud (~ 60 kpc), respectively. As described in § 2.2.5, their orbital periods are typically $\lesssim 15$ d, shorter than those of BeXB

pulsars. The NSs are close to the companion stars and they are usually luminous, because they persistently capture a large amount of stellar wind from the companion stars. Thus, their observations do not need to be triggered by other all sky monitors, and hence their observation have never been conducted as a ToO. Particularly, GX 301-2 exhibits a behavior similar to BeXB pulsars pulsars in the variability of X-ray flux averaged over multiple orbits, although GX 301-2 is not classified as a BeXB pulsar since its optical emission line has never been detected. In Figure 4.16, we show a long-term variability of the X-ray intensity of GX 301-2 with *RXTE*/ASM and *Swift*/BAT around the *Suzaku* observations. With a large eccentricity of 0.46 (Koh et al. 1997), shortly before the periastron passage, the X-ray intensity increases drastically. LMC X-4 and SMC X-1 exhibit a long-term periodicity originated in neither NS spin nor orbital motion of the binary system. Figure 4.17 shows long-term X-ray light curves of LMC X-4 and SMC X-1 obtained from *RXTE*/ASM and *Swift*/BAT around the *Suzaku* observations. The long-term (super-orbital) period of LMC X-4 and SMC X-1 are ~ 30 d and ~ 60 d, respectively (Lang et al. 1981; Gruber & Rothschild 1984). These periodic variations are thought to be caused by a precessing accretion disk that periodically obscures the NS. *Suzaku* observed LMC X-4 as well as SMC X-1 at several times, covering various super-orbital phases. However, we chose one of them, when the sources were in high X-ray flux state (XIS count rate of 6 counts s^{-1} for LMC X-4, of 21 counts s^{-1} for SMC X-1), since study of the dependency on super-orbital period is out of our scope.

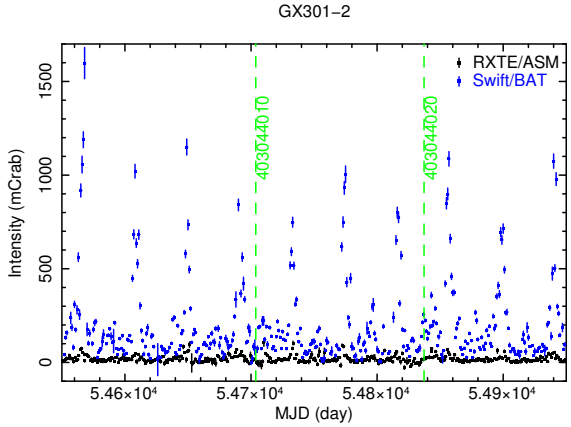

Figure 4.16: The same as Figure 4.1 but long-term light curve of GX 301-2.

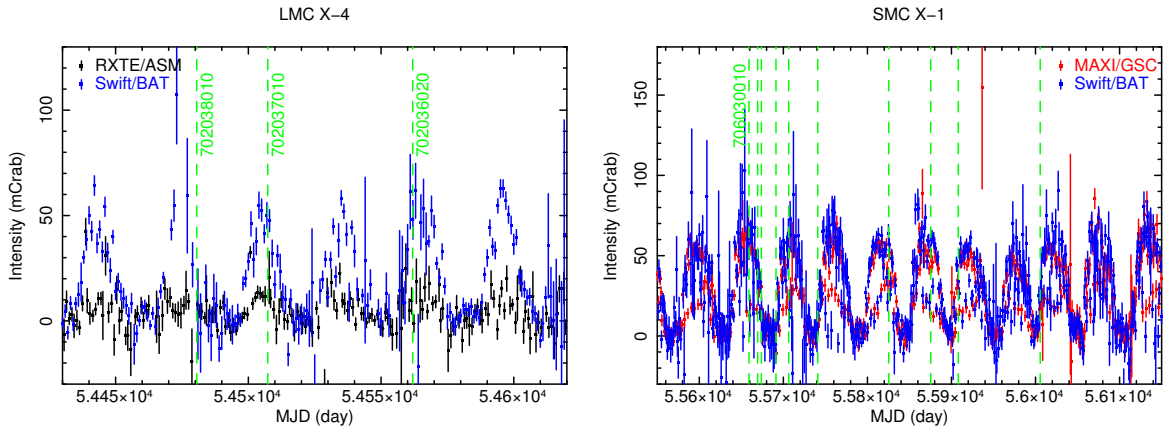

Figure 4.17: The same as Figure 4.1 but long-term light curves of LMC X-4 (left) and SMC X-1 (right).

In observations of SGXB pulsars, the XIS was mostly operated utilizing the 1/4 window option for the same reason for the BeXB pulsars. The pulse periods of the NS are typically $\sim$ 100 s, which are long enough to resolve the pulse shape with the 1/4 window option. In addition to their longer pulse periods, the sources are lower luminous than BeXB pulsars in their outbursts, so that the 1/4 window option is sufficient to prevent pile-up effects. Since Cen X-3 is a one of the brightest X-ray source and the relatively fast rotator ($P_{\rm spin}$ = 4.8 s) among them, the XISs were operated in 1 s burst clock mode in its observation. In the observations of LMC X-4, the 1/8 window option was adopted because it has a relatively short pulse period ($P_{\rm spin}$ $\sim$ 13 s). In the case of SMC X-1, its pulse period is too short ($P_{\rm spin}$ $\sim$ 0.7 s) for usual XIS window option, so that XIS 3 was operated in the P-sum mode.

In Figures 4.18–4.31, we show background subtracted light curves of several SGXB pulsars obtained by the XIS and HXD-PIN along with their HRs. As we can see in the figures, these sources exhibit rapid and violent variability. Individual pulses of some sources (e.g., 4U 0114+65 and 4U 2206+54) with long pulse periods are visible in Figure 4.23 and 4.24. The XIS intensities of Vela X-1, OAO 1657-415, and Cen X-3 varied by 1–2 order of magnitudes, while those of LMC X-4 and SMC X-1 were almost constant. In the light curves of Cen X-3, eclipses can be seen with the *Suzaku* observation covering nearly one orbital period (2.1 d) (Naik et al. 2011a), whereas OAO 1657-415 and Vela X-1 exhibited low-intensity episodes in the *Suzaku* observations as shown in Figure 4.18 and 4.28. The hardness of some sources also changed by a factor 5–10, implying significant spectral changes.

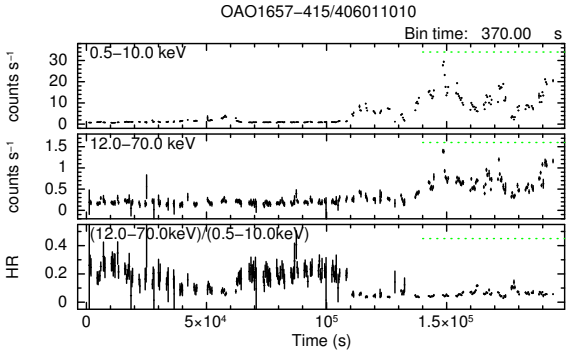

Figure 4.18: The same as Figure 4.2 but light curves and HR of OAO 1657-415 (ObsID=406011010) with 370 s time bins. The horizontal green-dotted line in each the panel show the duration of the high intensity period selected for time-resolving analysis in § 5.3.

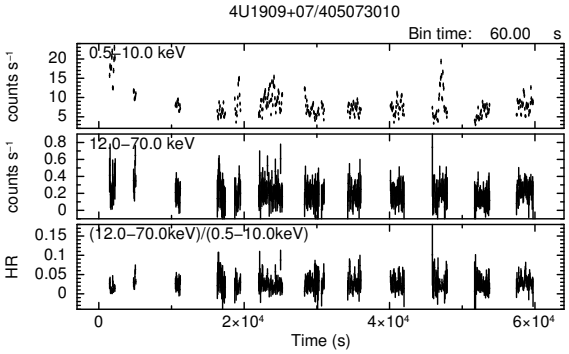

Figure 4.19: The same as Figure 4.2 but light curves and HR of 4U 1909+07 (ObsID=405073010) with 60 s time bins.

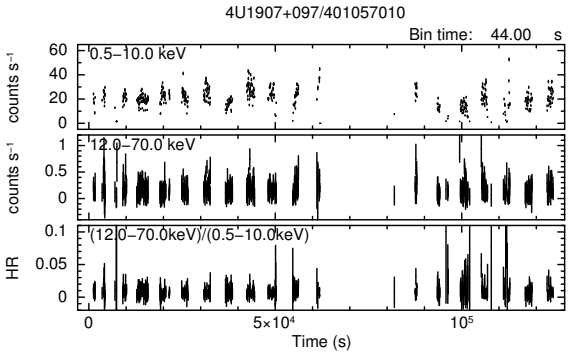

Figure 4.20: The same as Figure 4.2 but light curves and HR of 4U 1907+097 (ObsID=401057010) with 44 s time bins.

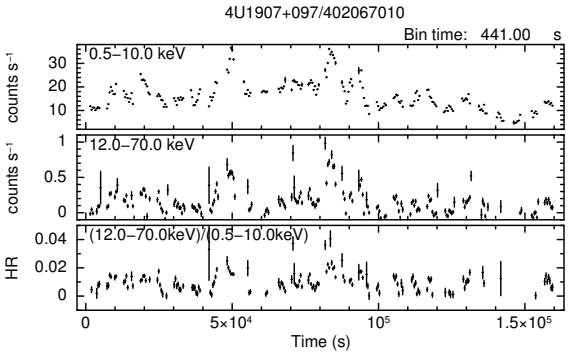

Figure 4.21: The same as Figure 4.2 but light curves and HR of 4U 1907+097 (ObsID=402067010) with 441 s time bins.

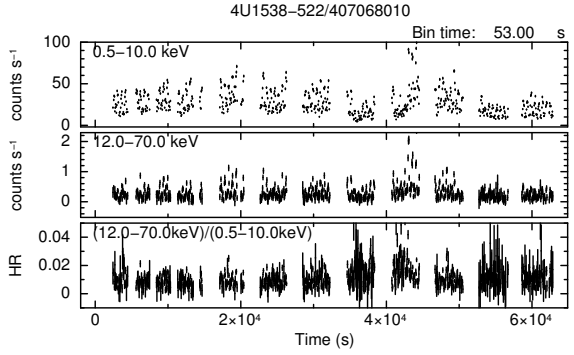

Figure 4.22: The same as Figure 4.2 but light curves and HR of 4U 1538-522 (ObsID=407068010) with 53 s time bins.

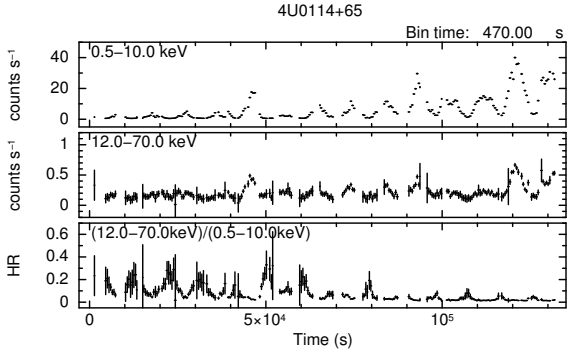

Figure 4.23: The same as Figure 4.2 but light curves and HR of 4U 0114+65 (ObsID=406017010) with 908 s time bins.

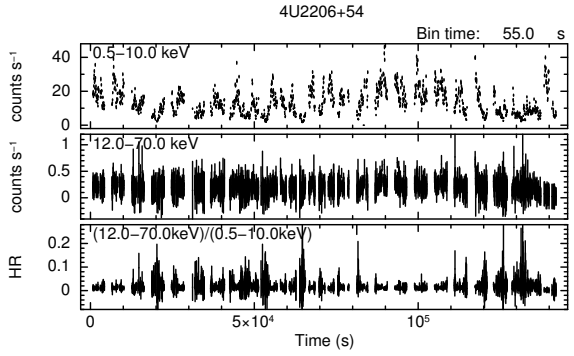

Figure 4.24: The same as Figure 4.2 but light curves and HR of 4U 2206+54 (ObsID=402069010) with 53 s time bins.

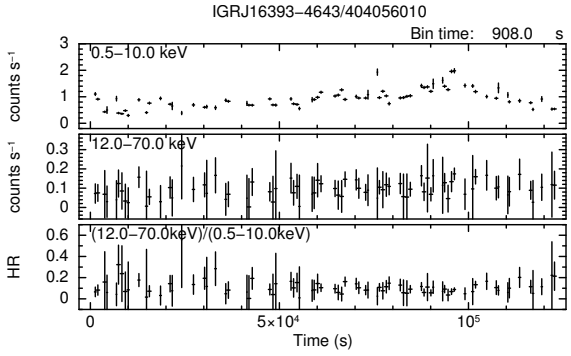

Figure 4.25: The same as Figure 4.2 but light curves and HR of IGR J16393-4643 (ObsID=404056010) with 908 s time bins.

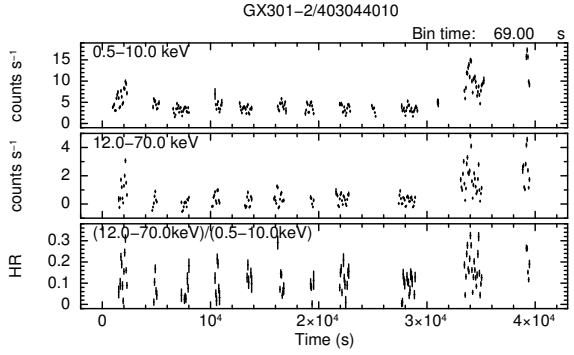

Figure 4.26: The same as Figure 4.2 but light curves and HR of GX 301-2 (ObsID=403044010) with 69 s time bins.

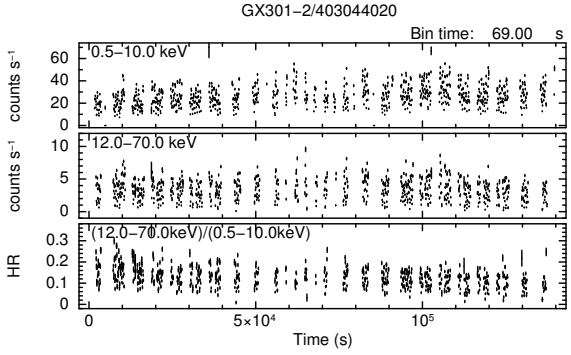

Figure 4.27: The same as Figure 4.2 but light curves and HR of GX 301-2 (ObsID=403044020) with 69 s time bins.

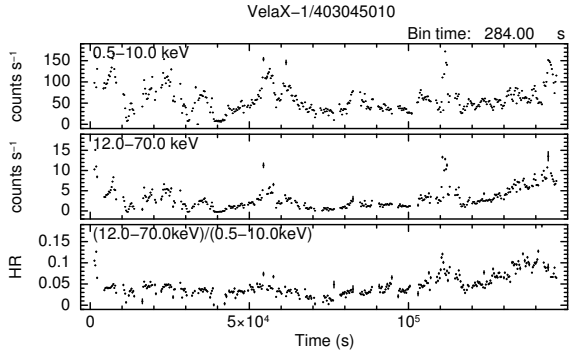

Figure 4.28: The same as Figure 4.2 but light curves and HR of Vela X-1 (ObsID=403045010) with 264 s time bins.

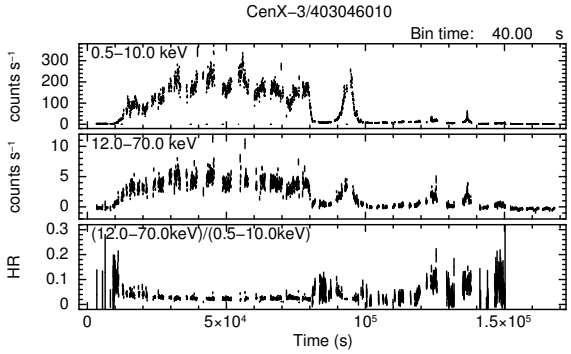

Figure 4.29: The same as Figure 4.2 but light curves and HR of Cen X-3 (ObsID=403046010) with 40 s time bins.

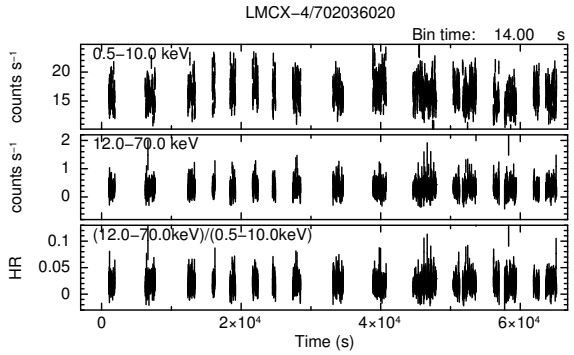

Figure 4.30: The same as Figure 4.2 but light curves and HR of LMC X-4 (ObsID=702036020) with 60 s time bins.

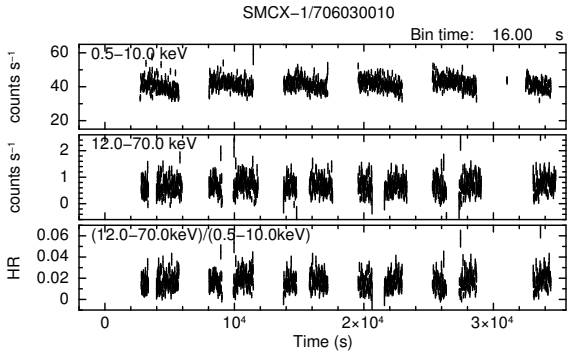

Figure 4.31: The same as Figure 4.2 but light curves and HR of SMC X-1 (ObsID=706030010) with 60 s time bins.

4.2.3 LMXB Pulsars

X-ray pulsations are seldom detected from LMXBs (§ 2.2.5), and if any we found very short period ($P_{\rm spin}$ is somewhere between a few ms and a few tens ms). As a result, they locate on the lower side of the Corbet diagram (see Figure 2.6). Only six exceptional LMXBs have spin period of > 0.1 s. The six objects are Her X-1, 4U 1626-67, 4U 1822-37, GRO J1744-28, GX 1+4, and 4U 1954+31, which are placed away from typical LMXBs in the Corbet diagram, although 4U 1954+31 is not exhibited in the Corbet diagram (Figure 2.6) since its orbital period has not been derived. We utilized the *Suzaku* observational data of five objects among the six by excluding GRO J1744-28 because of its short exposure time of XIS (4 ks). Table 4.3 gives information of used *Suzaku* data of LMXB pulsars.

Table 4.3: *Suzaku* observation list of LMXB pulsars.

Source[a]	ObsID	Date(UT)		Duration(ks)[b]	Aim[c]	XIS operation[d]	
		START	END			CLK	WIN
Her X-1	100035010	2005-10-05 15:28	2005-10-06 10:25	68.2	XIS	normal	1/8
	101001010	2006-03-29 18:24	2006-03-30 15:22	75.5	HXD	normal(XIS 0,1,2,3)	1/4
						p-sum(XIS 0,2,3)[e]	full
	102024010	2008-02-21 15:03	2008-02-22 11:40	74.2	XIS	0.1 s burst	full
	405058010	2010-09-28 18:47	2010-09-29 05:40	39.2	HXD	normal(XIS 0,1)	1/4
						p-sum(XIS 3)	full
	405058020	2010-09-28 18:47	2010-09-29 05:40	39.2	HXD	normal(XIS 0,1)	1/4
						p-sum(XIS 3)	full
	405058030	2010-09-22 00:00	2010-09-22 10:47	38.8	HXD	normal(XIS 0,1)	1/4
						p-sum(XIS 3)	full
	405058040	2010-09-22 19:02	2010-09-23 05:55	39.1	HXD	normal(XIS 0,1)	1/4
						p-sum(XIS 3)	full
	407051010	2012-09-19 08:29	2012-09-20 00:43	58.4	XIS	normal	1/4
	407051020	2012-09-22 04:20	2012-09-22 18:45	51.9	XIS	normal	1/4
	407051030	2012-09-24 10:21	2012-09-25 01:32	54.6	XIS	normal	1/4
4U 1822-37	401051010	2006-10-02 10:57	2006-10-03 12:27	91.8	XIS	normal	1/4(XIS 0,1)
						normal	full(XIS 2,3)
4U 1626-67	400015010	2006-03-09 01:18	2006-03-11 19:38	238.8	XIS	normal	1/8
	405044010	2010-09-06 12:58	2010-09-07 05:42	60.2	XIS	normal	1/4
GX 1+4	405077010	2010-10-02 06:43	2010-10-04 12:20	193.0	HXD	normal	1/4
4U 1954+31	907005010	2012-11-01 02:39	2012-11-02 12:02	120.1	XIS	normal	full

Notes.
[a] Preceding *Suzaku* studies: Her X-1 (Enoto et al. 2008; Asami et al. 2014; Staubert et al. 2014), 4U 1626-67 (Iwakiri et al. 2012; Camero-Arranz et al. 2012), 4U 1822-37 (Sasano et al. 2014), GX 1+4 (Yoshida et al. 2017), 4U 1954+31 (Enoto et al. 2014)
[b] On-source time.
[c] Nominal pointing position (XIS or HXD) in the observations; see Mitsuda et al. (2007).
[d] Clock mode and window option of XIS.
[e] The p-sum mode was operated in a part of the observation.

Since Her X-1, 4U 1626-67, and 4U 1822-37 possess a short spin period, their observations require relatively high time resolution. Therefore, the XIS was operated in the modes exercise high time resolution (e.g. P-sum mode) in some of these observations (see Table 4.3). Three persistent sources are considered to have accretion disks like typical LMXBs. As shown in Figure 4.32, Her X-1 shows long time variability with a 35 d period, which is usually thought to be ascribed to disk precession as being similar to LMC X-4 and SMC X-1. Actually, as shown in Figure 4.32, *Suzaku* observed various intensity states of Her X-1 at different phases of the 35 d cycles. We selected one in March 2006 of these observations, which was conducted "main on" phase of 35 d cycles, when the source exhibits the high X-ray flux. The light

curve of Her X-1 obtained from the selected *Suzaku* observation are shown in Figure 4.33. The observation of 4U 1822-37 covered about four its orbital cycles ($P_{\rm orb}$ =5.57 hr), in which periodic narrow dips were observed as shown in Figure 4.34. 4U 1626-67 was observed two times with *Suzaku* and there is no notable time variability in both observations (Figures 4.35 and 4.36).

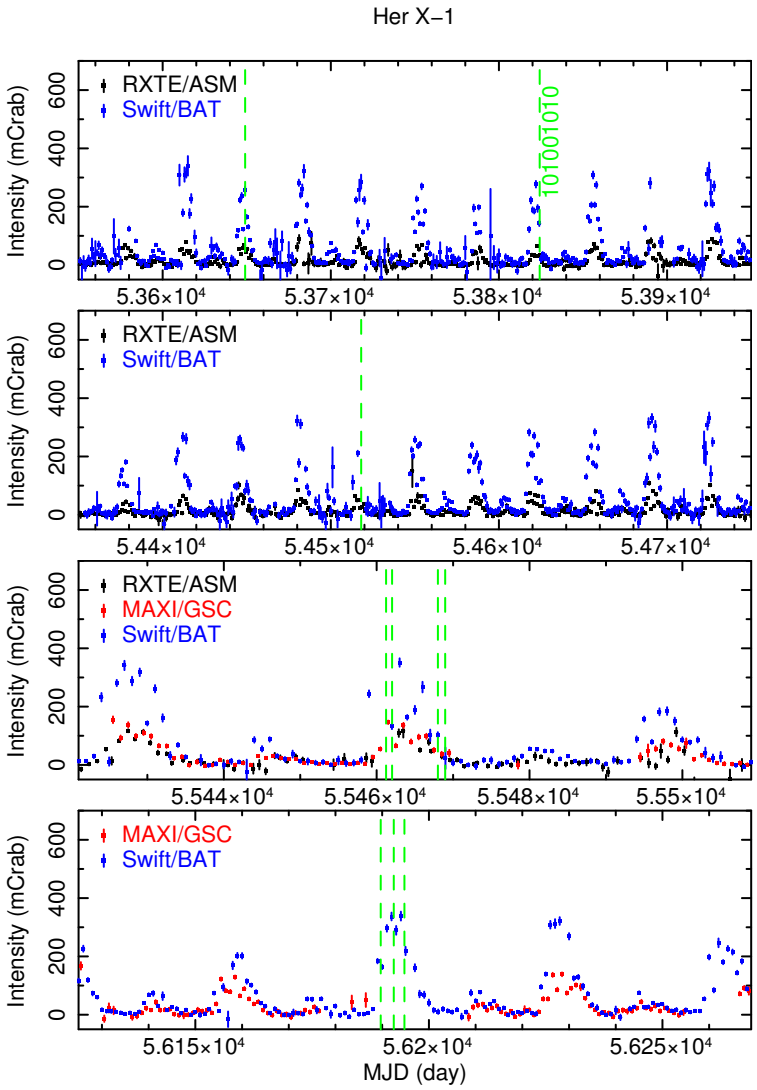

Figure 4.32: The same as Figure 4.1 but long-term light curves of Her X-1.

In the *Suzaku* observations of the two SyXBs (GX 1+4 and 4U 1954+31; see § 2.2.5), the XISs were operated with the 1/4 window option. Figures 4.37 and 4.38 show their light curves and HRs obtained on these occasions. Although there are several data points with a low count rate in the light curve of GX 1+4, there is no trend of any gradual intensity change during the *Suzaku* observation. The Suzaku observation of 4U 1954+31 was performed as a ToO after a brightening detected by MAXI monitoring. The light curve of 4U 1954+31 obtained from this observation shows violent time variability like SGXB pulsars. The HR of both objects was roughly constant during the observations, though their errors are large.

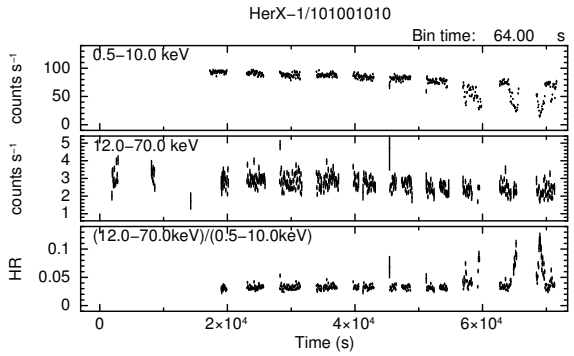

Figure 4.33: The same as Figure 4.2 but light curves and HR of Her X-1 (ObsID=101001010) with 64 s time bins.

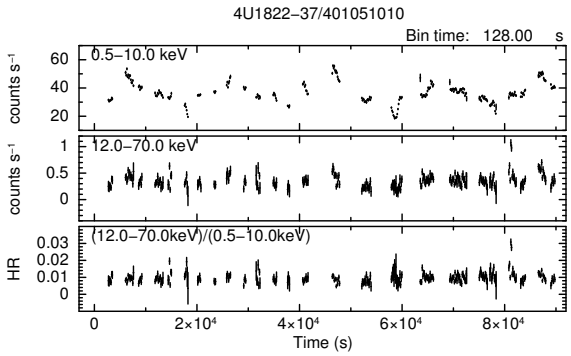

Figure 4.34: The same as Figure 4.2 but light curves and HR of 4U 1822-37 (ObsID=401051010) with 16 s time bins.

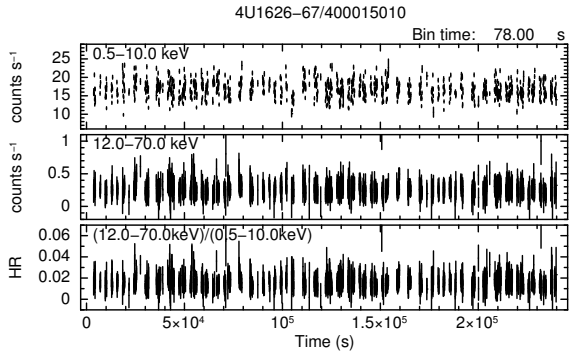

Figure 4.35: The same as Figure 4.2 but light curves and HR of 4U 1626-67 (ObsID=400015010) with 78 s time bins.

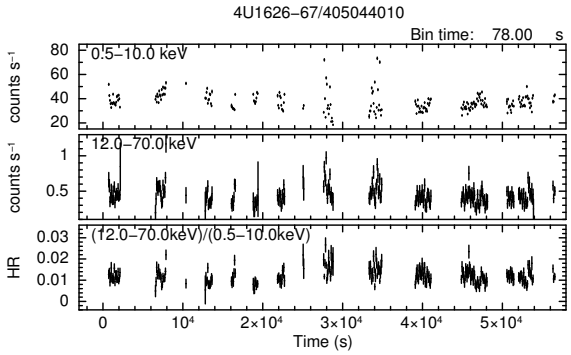

Figure 4.36: The same as Figure 4.2 but light curves and HR of 4U 1626-67 (ObsID=405044010) with 78 s time bins.

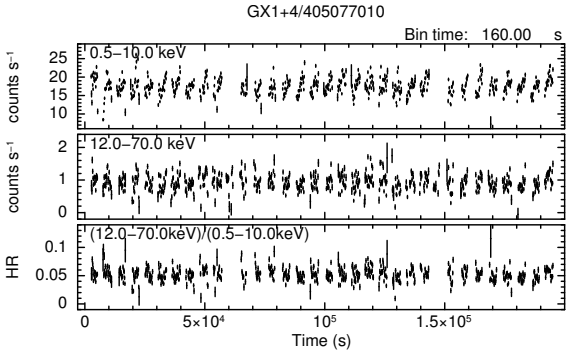

Figure 4.37: The same as Figure 4.2 but light curves and HR of GX 1+4 (ObsID=405077010) with 160 s time bins.

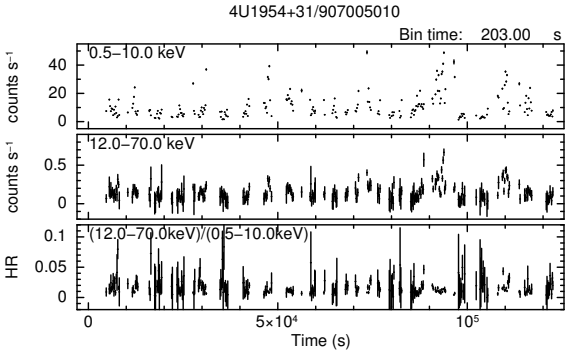

Figure 4.38: The same as Figure 4.2 but light curves and HR of 4U 1954+31 (ObsID=907005010) with 203 s time bins.

4.3 Summary of Selected Sources

The source parameters of our APXP samples are summarized in Table 4.4.

Table 4.4: Parameters of selected sources.

Source	Counterpart	$P_{\rm spin}$[a]	Orbital paramters[b]					D[c]	Remarks[d]	References[e]
			$P_{\rm orb}$	$a_{\rm x}\sin i$	e	ω	$T_{\rm epoch}$			
SMC X-1	B0 Ib	0.708	3.892	53.48	4.0×10^{-5} [f]	···	42836.18[g]	60[h]	SGXB/D	1,2
	···									
4U 1822-37	low-mass	0.5924	0.23	···	···	···	···	2.5	LMXB	3,4,5
	(V691 CrA)									
Her X-1	A8–F0	1.24	1.700	13.183	4.2×10^{-4}	96	46359.87[g]	6.6	LMXB	6,7,8
	(HZ Her)									
Cen X-3	O6–7 III	4.82	2.09	39.661	0[i]	0[i]	50506.79[g]	5.7	SGXB/D	9,10,11
	(V779 Cen)									
4U 1626-67	low-mass dwarf	7.66	0.0292	0.0013[j]	···	···	···	8	LMXB	12,13
	(Kz TrA)									
LMC X-4	O8 III	13.5	1.40	26.3	0.006	···	51110.86[g]	50[h]	SGXB/D	2,14
	···									
OAO 1657-415	Ofpe/WNL	38.22	10.447	106.157	0.1075	92.7	52298.0[g]	7.1	SGXB/W?	15,16,17,18
	···									
EXO 2030+375	B0e	41.3	46.0	248	0.41	212	53308.5[k]	7.1	BeXB	19,20,21,22
	···									
Cep X-4	B1–2 Ve	66.3	···	···	···	···	···	5.9	BeXB	23,24
	···									
GRO J1008-57	B0e	93.7	249.5	530	0.68	334	54424.7[k]	5.8	BeXB	25,26,27,24
	···									
A 0535+262	O9.7 IIIe	103.5	110.3	267	0.47	130	49169.0[k]	2.1	BeXB	28,29
	(HDE 245770)									
GX 1+4	M5 III	150	1161	···	···	···	···	4.3	LMXB	30,31
	(V2116 Oph)									
GX 304-1	B0.7 Ve	272	132.19	498	0.524	123	55425.02[k]	2.4	BeXB	32,33,34
	···									
Vela X-1	B0.5 Ib	283.5	8.964	113.89	0.0898	152.6	52974.00[g]	1.9	SGXB/W	35,36,37,38
	(HD 77581)									
1A 1118-61	O9.5 IV–Ve	405.6	24.0	54.85	0[i]	0[i]	54845.37[g]	5.2	BeXB	39,40,41,24
	(Wray 793)									
4U 1907+097	O8–O9 Ia	440.341	8.375	83	0.28	330	50134.8[g]	5	SGXB/W	42,43
	···									
4U 1538-522	B0.2 Ia	530	3.728	53.1	0.18	40	52851.3[g]	2.9	SGXB/W	44,45,46,47
	(QV Nor)									
4U 1909+07	O7.5–O9.5 If	604.66	4.4007	47.83	0[i]	0[i]	51870.1[g]	7	SGXB/W?	48,49
	···									
GX 301-2	B1 Ia+	680	41.498	368.3	0.462	310.4	48802.8[k]	3	SGXB/W	50,51,52,53,54
	(Wray 977)									
IGR J16393-4643	OB?	912	3.7	43	0[i]	0[i]	53654.98[g]	10	SGXB	55,56,57,58
	···									
4U 2206+54	O9.5 V	5560	19.25	···	···	···	···	6.4	HMXB/W	59,60,61
	(BD +53° 2790)									
4U 0114+65	B1 Ia	9720	11.598	7.33	0.18	51	51825.3[k]	7.2	SGXB/W	62,63
	(LS I+65 010)									
4U 1954+31	M4–5 III	18320	···	···	···	···	···	1.7	LMXB	64
	···									

NOTES.

[a] Spin period (s).

[b] $P_{\rm orb}$, $a_{\rm x}\sin i$, e, ω, and $T_{\rm epoch}$ are orbital period (d), projected semimajor axis (lt-s), eccentricity, longitude of periastron (deg), orbital epoch (MJD), respectively.

[c] Distance to source from the observer (kpc).

[d] HMXB: High-mass X-ray binary, SGXB: Supergiant X-ray binary, BeXB: Be X-ray binary, LMXB: Low-mass X-ray binary, D: dominant mass-transfer via disk-fed system W: dominant mass-transfer via wind-fed system

[e] (1) van der Meer et al. (2007); (2) Wojdowski et al. (1998); (3) Burderi et al. (2010); (4) Liu et al. (2007); (5) Mason & Cordova (1982); (6) Anderson et al. (1994); (7) Staubert et al. (2009); (8) Reynolds et al. (1997);(9) Raichur & Paul (2010); (10) Ash et al. (1999); (11) Thompson & Rothschild (2009);(12) Chakrabarty (1998); (13) Levine et al. (1988); (14) Levine et al. (2000); (15) White & Pravdo (1979); (16) Jenke et al. (2012); (17) Mason et al. (2009); (18) Audley et al. (2006);(19) Motch & Janot-Pacheco (1987); (20) Coe et al. (1988); (21) Wilson et al. (2008); (22) Wilson et al. (2002); (23) Bonnet-Bidaud & Mouchet (1998); (24) Riquelme et al. (2012);(25) Coe et al. (1994); (26) Coe et al. (2007); (27) Kühnel et al. (2013);(28) Steele et al. (1998); (29) Finger et al. (1996b); (30) Chakrabarty & Roche (1997); (31) Hinkle et al. (2006); (32) Mason et al. (1978); (33) Sugizaki et al. (2015); (34) Parkes et al. (1980);(35) Morgan et al. (1955); (36) Bildsten et al. (1997); (37) Kreykenbohm et al. (2008); (38) Sadakane et al. (1985); (39) Staubert et al. (2011); (40) Ives et al. (1975); (41) Janot-Pacheco et al. (1981); (42) in 't Zand et al. (1998); (43) Cox et al. (2005); (44) Parkes et al. (1978); (45) Makishima et al. (1987); (46) Mukherjee et al. (2006); (47) Reynolds et al. (1992); (48) Levine et al. (2004); (49) Morel & Grosdidier (2005); (50) Jones et al. (1974); (51) Kaper et al. (1995); (52) Kaper et al. (2006); (53) White et al. (1976); (54) Koh et al. (1997); (55) Bodaghee et al. (2012); (56) Thompson et al. (2006); (57) Nespoli et al. (2010); (58) Bodaghee et al. (2006); (59) Blay et al. (2006); (60) Reig et al. (2009); (61) Corbet et al. (2007); (62) Reig et al. (1996); (63) Grundstrom et al. (2007); (64) Corbet et al. (2008);

[f] An Upper limit in 2σ confidence level.

[g] The epoch of 90° mean orbital longitude (i.e. superior conjunction of the neutron star).

[h] Assuming a distance of 50 kpc for LMC and 60 kpc for SMC.

[i] The orbital parameters were estimated assuming circular orbit.

[j] An Upper limit in 3σ confidence level.

[k] The epoch of periastron passage.

Chapter 5

Data Analysis and Results

Contents

5.1 Phase-averaged Analysis

In the following analyses, we performed phase-averaged spectroscopic analyses of all the archived *Suzaku* data of selected sources, by focusing on emission lines and their related features.

5.1.1 Phase-averaged Spectra

As described in section § 4.1, we obtained on-source and background spectra, response matrices and effective area files for corresponding detectors. Background subtracted and phase-averaged spectra, of each observation, are shown in Figure 5.1(A)–5.34(A). Expected background spectra for the HXD-PIN and HXD-GSO, together with typical systematic uncertainty of the NXB modeling, are also plotted in the same figures. Typical repeatability of the NXB modeling for HXD-PIN is about 5%. We utilized the energy range where it is less than about 10% of the signal in phase-averaged (§ 5.1.2) and resolved (§ 5.2.3) spectral fitting. For all observations, we can use the data up to ∼40 keV considering above restrictions of energy range. Several of our sample spectra show significant detection of the signals above 70 keV with the HXD-GSO, after the subtraction of background.

In order to grasp the basic properties of the pulsar among all our sample spectra in a model-independent way, we first calculated spectral ratios of the phase-averaged spectra to a power-law model with a photon index of 2.0. The resultant spectral ratios are shown in Figure 5.1(B)–5.34(B). Inset panels, Figure 5.1(C)–5.34(C) show expanded view of the spectral ratio around the iron lines. Emission lines around 6.4 keV significantly appear in almost all the spectral ratios. In particular, K-shell emission lines and absorption edge of almost neutral iron ions are prominent in the spectra of OAO 1657-415, GX 301-2, Vela X-1, Cen X-3, 4U 1822-37, and GX 1+4 without any spectral model fitting. On the other hands, ionized lines can be seen at somewhat higher energies than that of neutral line in the spectra of GRO J1008-57, EXO 2030+375, Cen X-3, SMC X-1, Her X-1, 4U 1822-37, and 4U 1626-67. Owing to the wide band coverage of the *Suzaku* spectra, CRSFs were detected from several sources in our samples. New discovery of CRSFs with *Suzaku* observations have been reported from GX 304-1, GRO J1008-57, and 4U 1822-37 at 54 keV, 76 keV, and 33 keV, respectively (Yamamoto et al. 2011; 2014; Sasano et al. 2014), as well as a marginal detection of CRSF from 4U 1909+07 at 44 keV (Jaisawal et al. 2013). The CRSFs of A 0535+262, 1A 1118-61, Cep X-4, 4U 1907+097, 4U 1538-522, GX 301-2, Vela X-1, Cen X-3, Her X-1, and 4U 1626-67, were previously reported their confirmation with the *Suzaku* observations (Terada et al. 2006; Suchy et al. 2011; Jaisawal & Naik 2015; Rivers et al. 2010; Hemphill et al. 2014; Suchy et al. 2012; Doroshenko et al. 2011; Naik et al. 2011a; Enoto et al. 2008; Iwakiri et al. 2012). The detection of the harmonic features, in the spectra of Vela X-1, Her X-1, and Cep X-4, has been also reported (Doroshenko et al. 2011; Enoto et al. 2008; Jaisawal & Naik 2015). Iwakiri et al. (2012) studied with same *Suzaku* observation and found an evidence of cyclotron emission at a particular pulse phase. The other sources in our sample (e.g., OAO 1657-415, LMC X-4, SMC X-1, GX 1+4, 4U 1954+31) do not show clear CRSFs, and hence their magnetic field strengths remain to be unknown.

5.1.2 Modeling of Broadband Spectra

In this section, we describe model fitting analysis of the phase-averaged spectra obtained from XISs, HXD-PIN and HXD-GSO observation of the APXPs, as shown in previous section. After the subtraction of appropriate background, the spectra obtained by the two or three kinds of detectors are simultaneously fitted by models, described below, using the XSPEC version 12.9 package. Data in the 1.7–1.9 and 2.2–2.4 keV energy ranges were ignored for the spectral fitting because of the presence of Si and Au edge features, precision of calibration of which is not enough comparing to statistical uncertainty. We also ignored data below 1 keV, where X-ray signals are weak in most of the objects, except for LMC X-4, SMC X-1, Her X-1, 4U 1822-37 and 4U 1626-67, whose spectra show distinct soft X-ray emission below 1 keV. We also omitted the 10–15 keV energy band of the HXD-PIN data because of calibration uncertainty of the temperature-dependent electrical noise. In cases of OAO 1657-415, GX 301-2, IGR J16393-4643 and GX 1+4, we used only 2–10 keV data for FI CCDs. Because they show strong low energy absorption (more than $N_{\rm H}$ =10^{22} H atoms cm^{-2}) as seen in Figure 5.15, 5.23, 5.24, 5.22, and 5.33, the detected events below 2 keV are dominated by the "low energy tail" component (Matsumoto et al. 2006), which is characteristic of the instruments and is not well calibrated (Suchy et al. 2012). The cross-normalizations of XIS detectors were set to be free to cope with their calibration uncertainty of the effective area, whereas the cross normalizations between XIS and HXD were fixed at 1.16 and 1.18 for "XIS nominal" and "HXD nominal" observation, respectively, following the recommendation in the *Suzaku* ABC guide.

In our phase-averaged spectroscopy, a typical X-ray spectral model $f(E)$ is as;

$$f(E) = \exp\left(-\sigma(E)N_{\rm H}\right)\left(I(E) + G(E)\right), \tag{5.1}$$

where $\sigma(E)$ is photoelectric absorption cross section, $N_{\rm H}$ is an equivalent hydrogen column density, $I(E)$ is a continuum spectrum and $G(E)$ is Gaussian function for the emission lines. Mainly according to preceding *Suzaku* studies (see Table 4.1, 4.2 and 4.3), we tried several empirical models (see § 2.2.3.2) to represent a broadband continuum $I(E)$ of APXPs of our samples. The best-fit continuum models to describe the phase-averaged spectra are listed in Table 5.1.

Several spectra, of mainly BeXB pulsars, show noticeable curvature in their XIS spectra and have much poorer fits. We thus modify the model for these spectra by applying a partial covering intrinsic absorption component of the form;

$$f(E) = \exp\left(-\sigma(E)N_{\rm H1}\right)\left(f_{\rm pc} * \exp\left(-\sigma(E)N_{\rm H2} + (1 - f_{\rm pc})\right)\left(I(E) + G(E)\right)\right), \tag{5.2}$$

where $N_{\rm H1}$ and $N_{\rm H2}$ describe the line of sight and partial covering intrinsic absorption equivalent hydrogen column density, and $f_{\rm pc}$ is the partial covering fraction, respectively. In this model, one absorption component absorbs the entire spectrum, whereas the other component absorbs the spectrum partially. This model is known as the partial covering absorption model, which is often described as two different power-law component with the same photon index but different normalizations, being absorbed by different column densities. This model has been used to represent X-ray spectra of APXPs (e.g., Her X-1—Endo et al. 2000; GX 301-2—Mukherjee & Paul 2004; Suchy et al. 2012; 4U 1538-522—Hemphill et al. 2014; Vela X-1—Maitra & Paul 2013b; Fürst et al. 2014; Cen X-3—Naik et al. 2011a; 1A 1118-61—Maitra

et al. 2012; GRO J1008-57—Naik et al. 2011b; Yamamoto et al. 2014; EXO 2030+375—Naik et al. 2013; GX 304-1—Jaisawal et al. 2016). In this model, the partial covering absorption is often interpreted to be caused by dense and clumpy material localized to the pulsar, in addition to the fully coved absorption of extrinsic material, such as galactic absorption. These clumps manifest themselves in two ways in the X-rays: as partially covering, variable absorption, and through a highly variable accretion rate. For other example, the existence of clumps in the stellar wind of GX 301-2 was indicated by several authors (Kreykenbohm et al. 2004; Mukherjee & Paul 2004; Suchy et al. 2012), which were modeled using the partial covering absorption in addition to fully covered photoelectric absorption of the smooth stellar wind.

In spectra of A 0535+262, GX 304-1, GRO J1008-57 (ObsID=907006010), 1A 1118-61, Cep X-4, 4U 1907+097, 4U 1538-522, IGR J16393-4643, GX 301-2, Vela X-1, Cen X-3, Her X-1, 4U 1822-37, and 4U 1626-67, there are broad absorption-like features typically around 15–50 keV in the residuals, which indicated presences of the CRSF. Then, we modified the spectral model by multiplying a CRSF component onto the continuum model, describing as;

$$f(E) = \exp\left(-\sigma(E)N_{\rm H}\right)\left(I(E) * S(E) + G(E)\right), \tag{5.3}$$

where $S(E)$ is the CRSF component. The CRSFs in each spectrum were modeled using `gabs` or `cyclabs` in XSPEC (see Table 5.1). In addition, local excesses (soft excess, 10 keV bump feature, broad 1 keV emission, and Fe broad line), were found in the residuals of several X-ray source spectra and we added an additional component to represent them. The model components composing of the best-fit model of phase-averaged broadband spectra are listed in Table 5.1.

For the model of the photoelectric absorption and partial covering absorption, `TBnew` and `TBnew_pcf` in XSPEC are used respectively. We assume the elemental abundances of Wilms et al. (2000), and the photoelectric absorption cross sections of Verner et al. (1996), which are the proper interstellar medium (ISM) abundances and cross sections to use the `TBnew` and `TBnew_pcf` models. For the parameters of the emission lines, the widths of iron K_α lines are kept to be free, except for GX 304-1 (ObsID=905002010), Cep X-4 (ObsID=409037010), OAO 1657-415, Vela X-1, SMC X-1, LMC X-4, 4U 2206+54, and 4U 1626-67, whose iron K_α line width was fixed to 0 eV, because they were not able to be constrained due to the poor statistics. On the other hands, some sources show sufficiently narrow line, so the their widths were fixed to be 0 eV in our phase-averaged fitting. X-ray continuum and emission line component models were multiplied by the same absorption column density of matter along the line of sight. In some object (4U 1907+097, Vela X-1 and GX 1+4), we noticed absorption-edge-like residuals of data from a model around 7 keV. We fitted this edge-like feature by allowing the Fe abundance of the absorber relative to ISM, $Z_{\rm Fe}$, to vary, and values of $Z_{\rm Fe}$ near 3–5 in 4U 1907+097, ~ 14 in Vela X-1 and ~ 1.4 in GX 1+4 were typically obtained.

Figure 5.35–5.68 show results of the phase-averaged spectral fitting of our sample APXPs and obtained parameters of iron K_α emission line are listed in Table 5.2. The equivalent hydrogen column densities estimated with fully and partially covering absorption model are given in Table 5.2. From these results, we calculated absorption-corrected X-ray photon

fluxes $F_{\rm s}$ and $F_{\rm h}$ defined in 4.0–7.1 keV and 7.1–10.0 keV, respectively, using the `cpflux` model in XSPEC. Hardness ratio (HR) was defined as $\eta \equiv F_{\rm h}/F_{\rm s}$, which indicates roughly a slope of the spectrum of the source around the iron K-edge. Calculated HR are given in Table 5.2. We calculated X-ray luminosities in a range of 0.5–100 keV assuming the source distances listed in Table 4.4 and derived values are also summarized in Table 5.2.

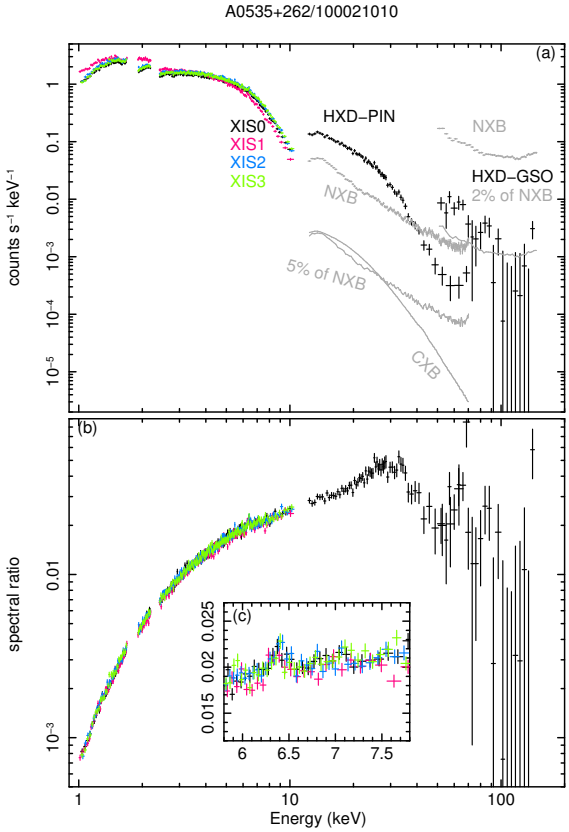

Figure 5.1: (a) Phase-averaged, background-subtracted XISs (below 10 keV) and HXD (above 15 keV) spectra of A 0535+262 (ObsID=100021010) in count rate space. The expected NXB spectra, their typical repeatability of the NXB modeling, and modeled CXB are also plotted. (b) Spectral ratio of the data to a power-law model with an index of 2.0. The inset panel (c) shows an expanded view around the iron lines.

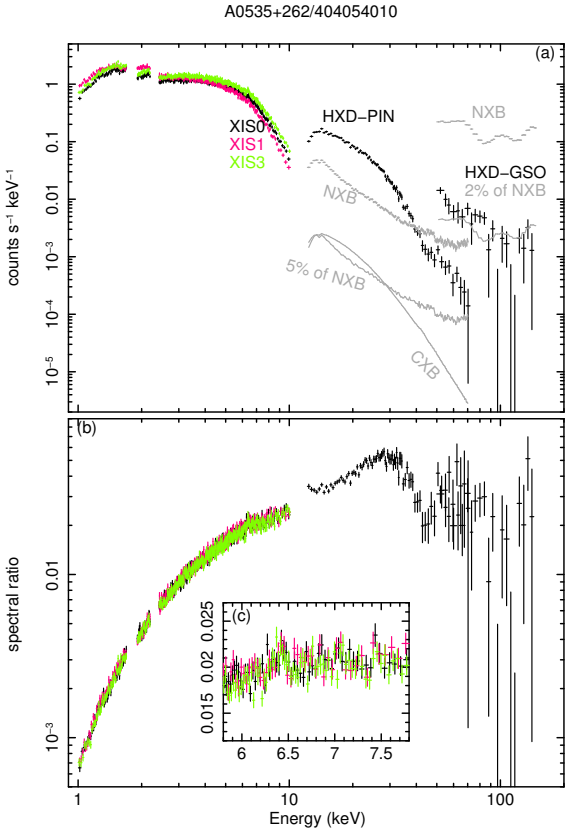

Figure 5.2: The same as Figure 5.1, but phase-averaged, background-subtracted spectra of A 0535+262 (ObsID=404054010).

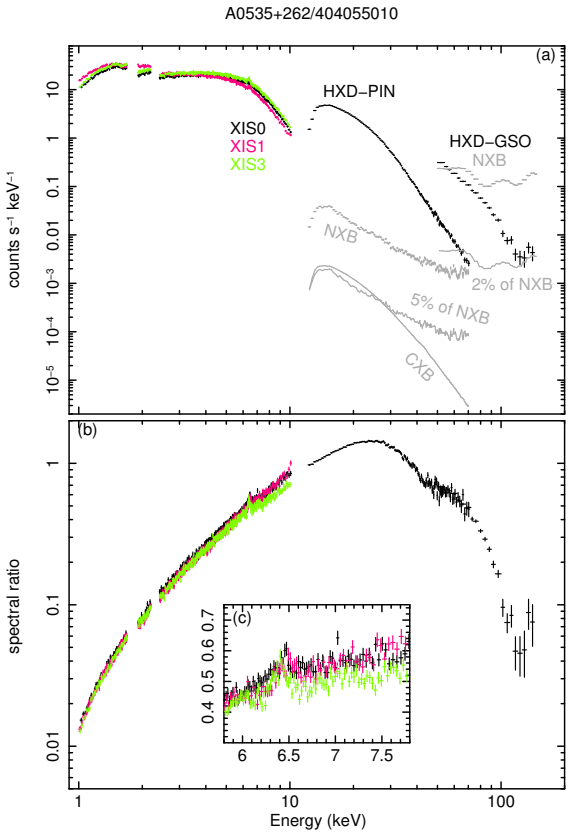

Figure 5.3: The same as Figure 5.1, but phase-averaged, background-subtracted spectra of A 0535+262 (ObsID=404055010).

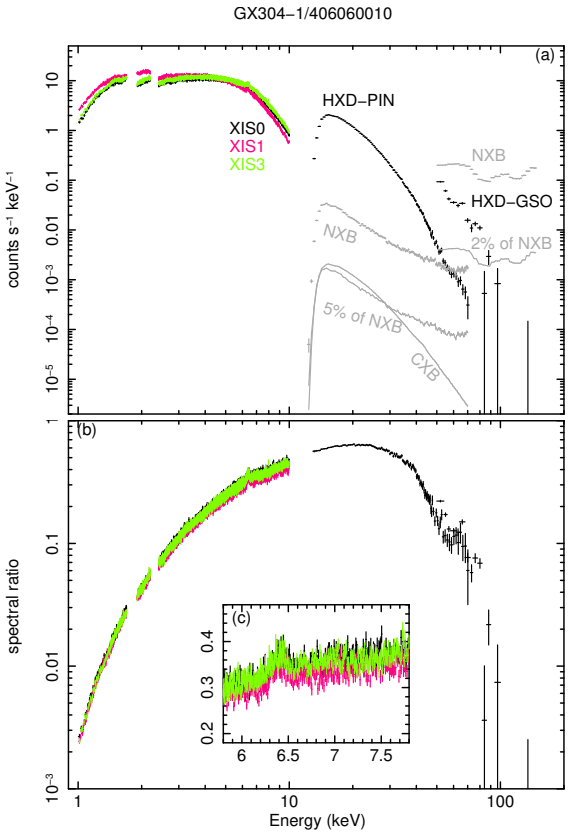

Figure 5.4: The same as Figure 5.1, but phase-averaged, background-subtracted spectra of GX 304-1 (ObsID=406060010).

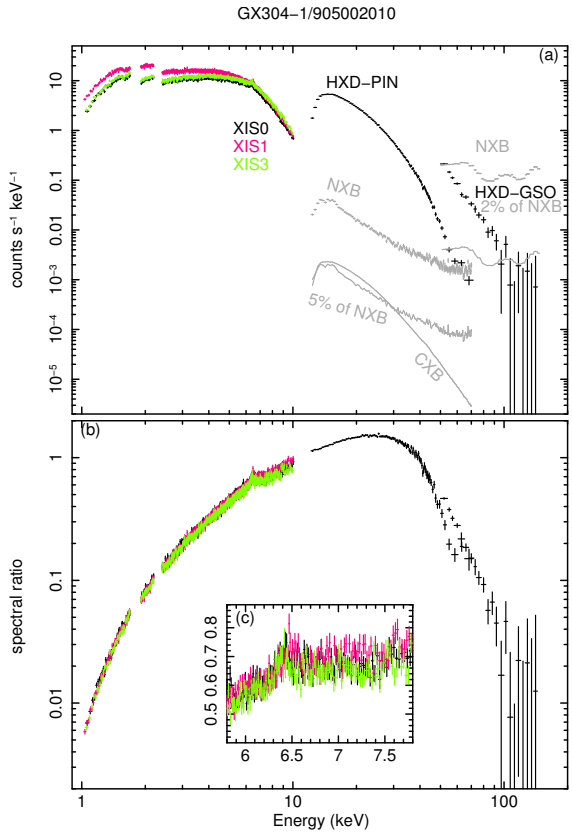

Figure 5.5: The same as Figure 5.1, but phase-averaged, background-subtracted spectra of GX 304-1 (ObsID=905002010).

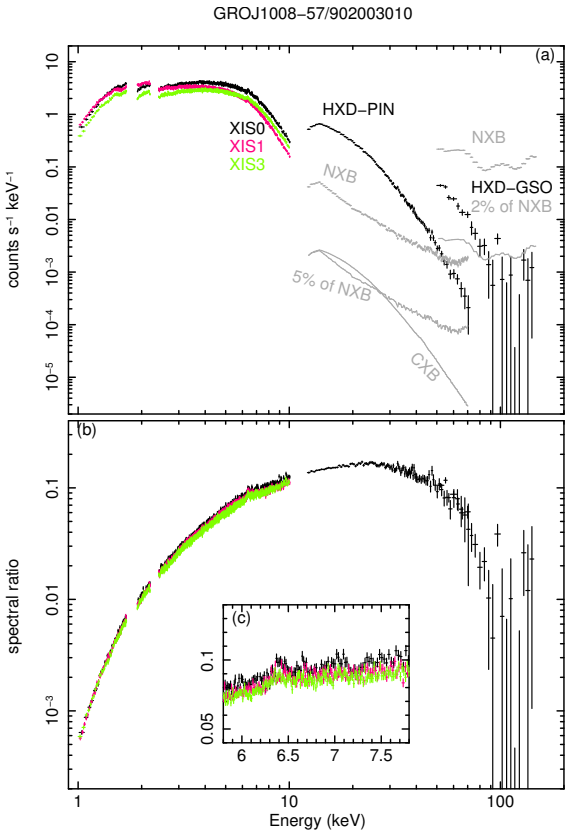

Figure 5.6: The same as Figure 5.1, but phase-averaged, background-subtracted spectra of GRO J1008-57 (ObsID=902003010).

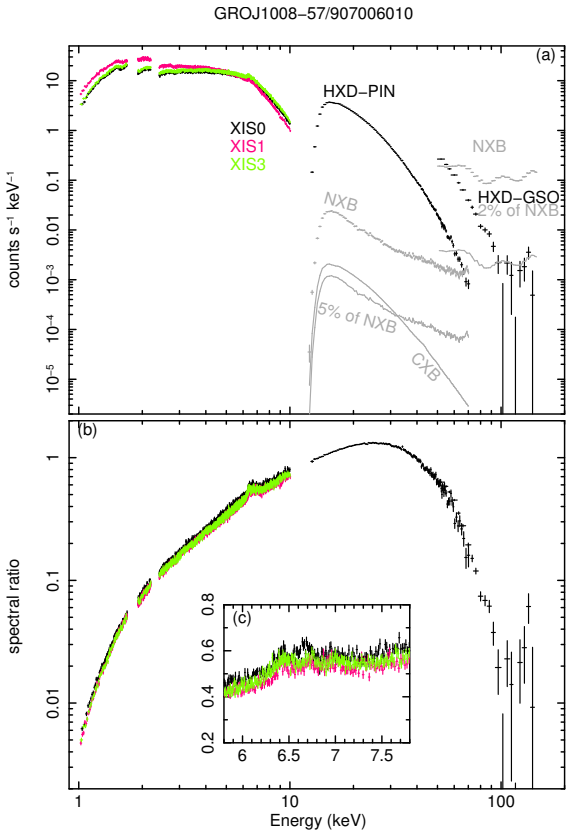

Figure 5.7: The same as Figure 5.1, but phase-averaged, background-subtracted spectra of GRO J1008-57 (ObsID=907006010).

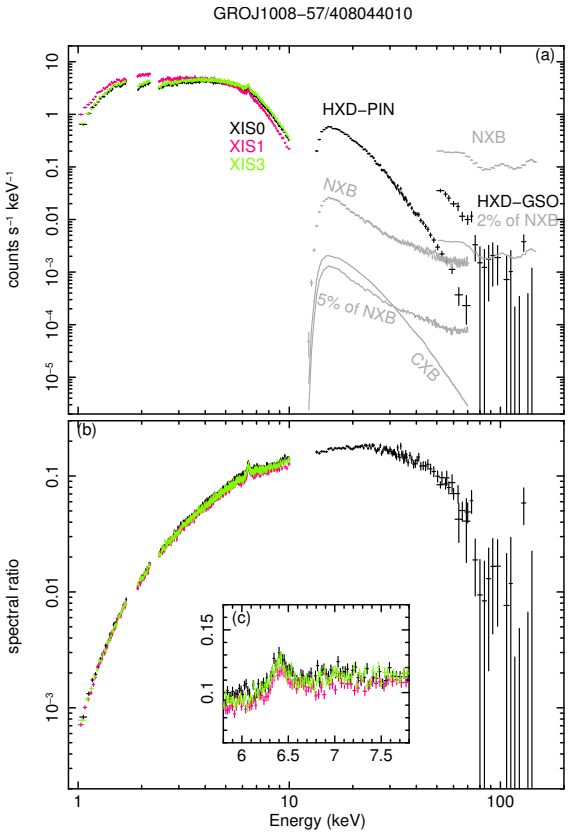

Figure 5.8: The same as Figure 5.1, but phase-averaged, background-subtracted spectra of GRO J1008-57 (ObsID=408044010).

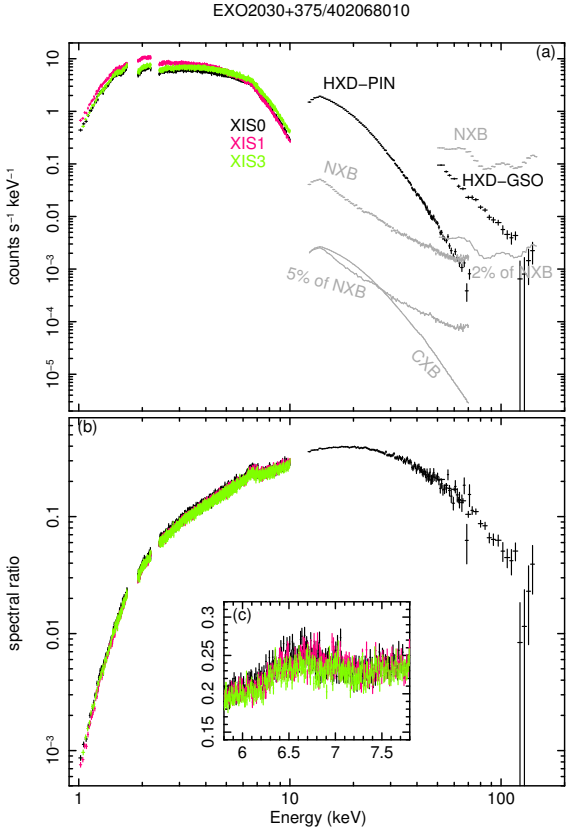

Figure 5.9: The same as Figure 5.1, but phase-averaged, background-subtracted spectra of EXO 2030+375 (ObsID=402068010).

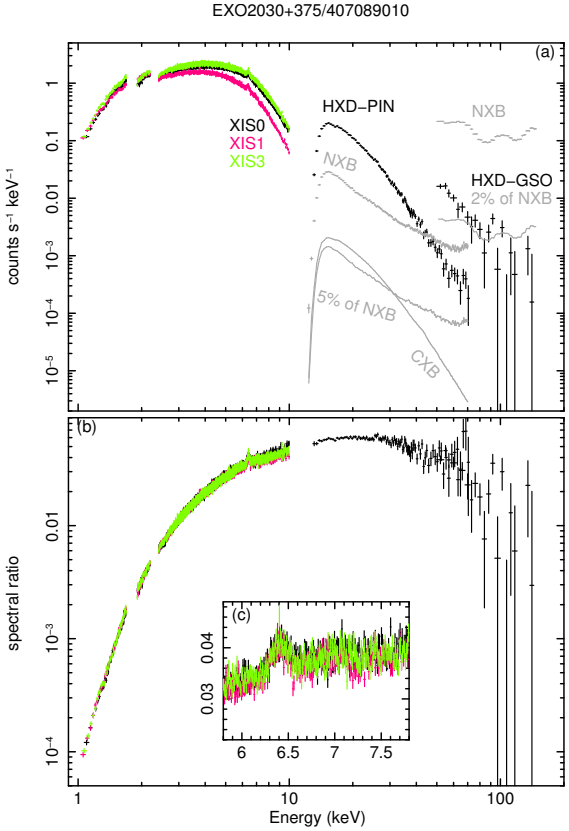

Figure 5.10: The same as Figure 5.1, but phase-averaged, background-subtracted spectra of EXO 2030+375 (ObsID=407089010).

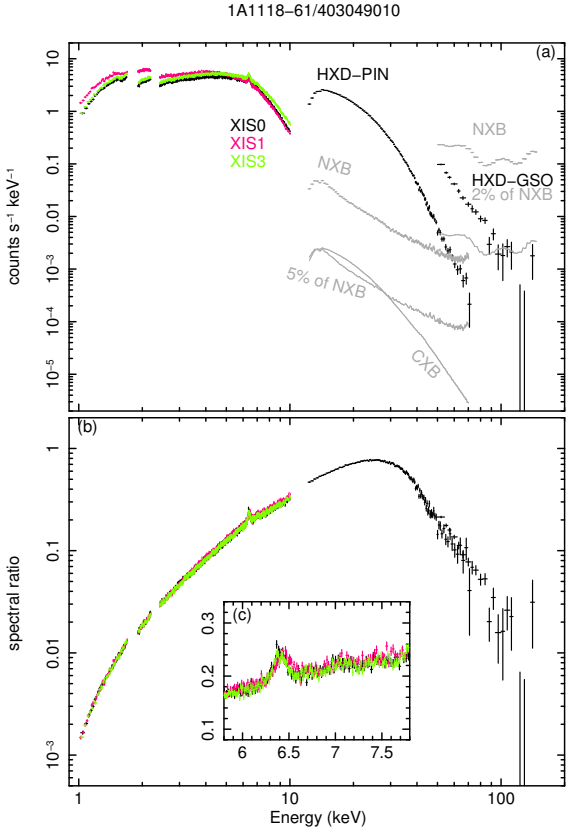

Figure 5.11: The same as Figure 5.1, but phase-averaged, background-subtracted spectra of 1A 1118-61 (ObsID=403049010).

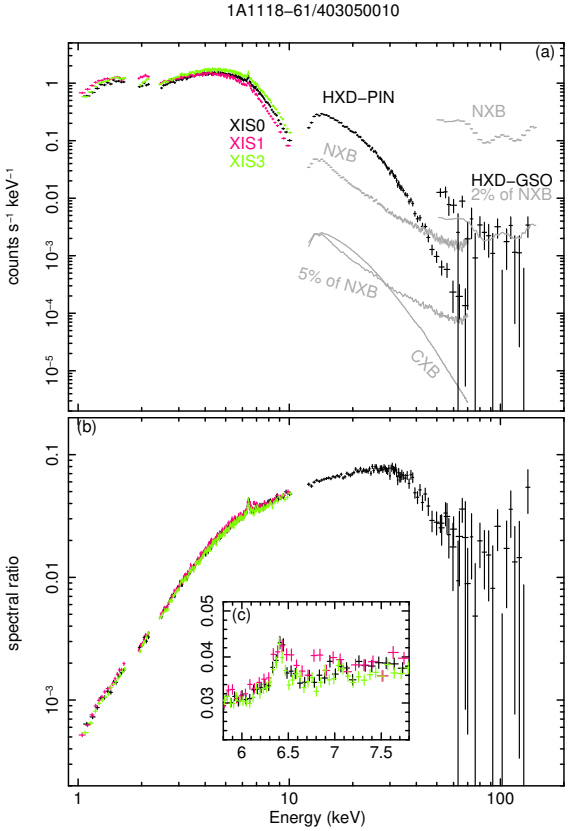

Figure 5.12: The same as Figure 5.1, but phase-averaged, background-subtracted spectra of 1A 1118-61 (ObsID=403050010).

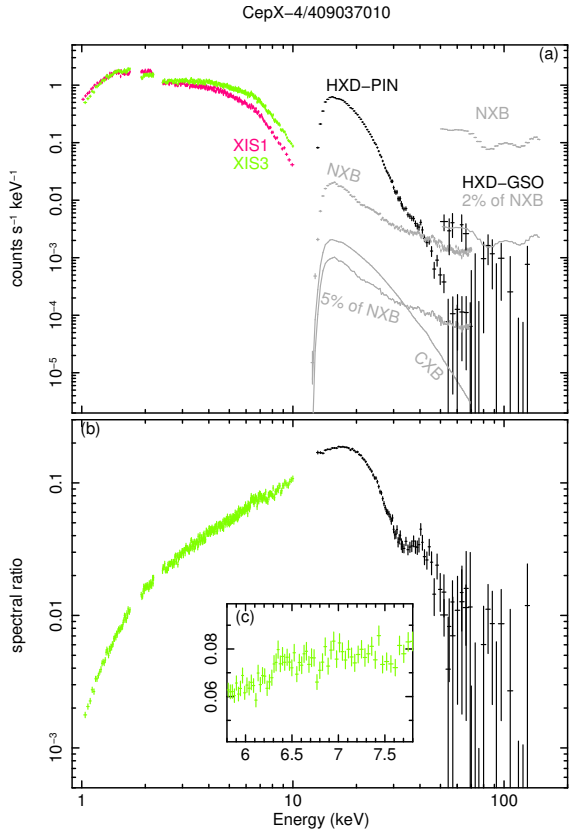

Figure 5.13: The same as Figure 5.1, but phase-averaged, background-subtracted spectra of Cep X-4 (ObsID=409037010).

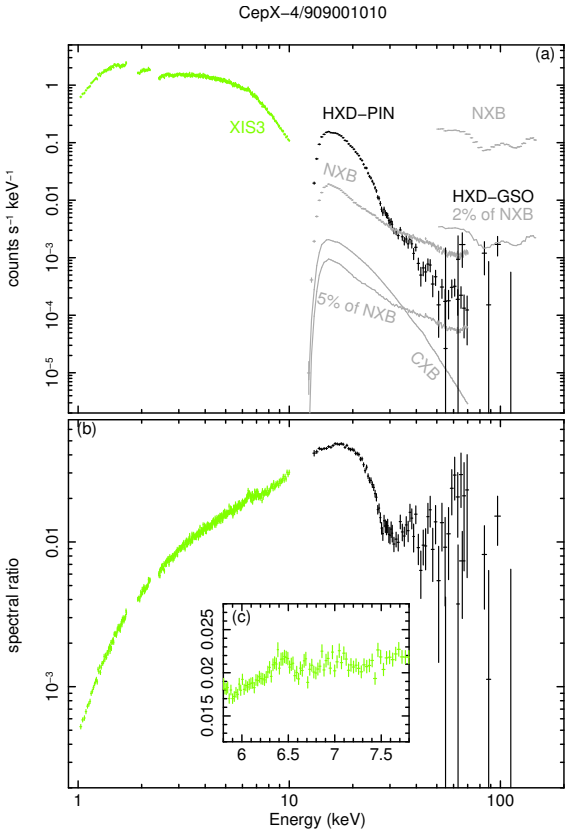

Figure 5.14: The same as Figure 5.1, but phase-averaged, background-subtracted spectra of Cep X-4 (ObsID=909001010).

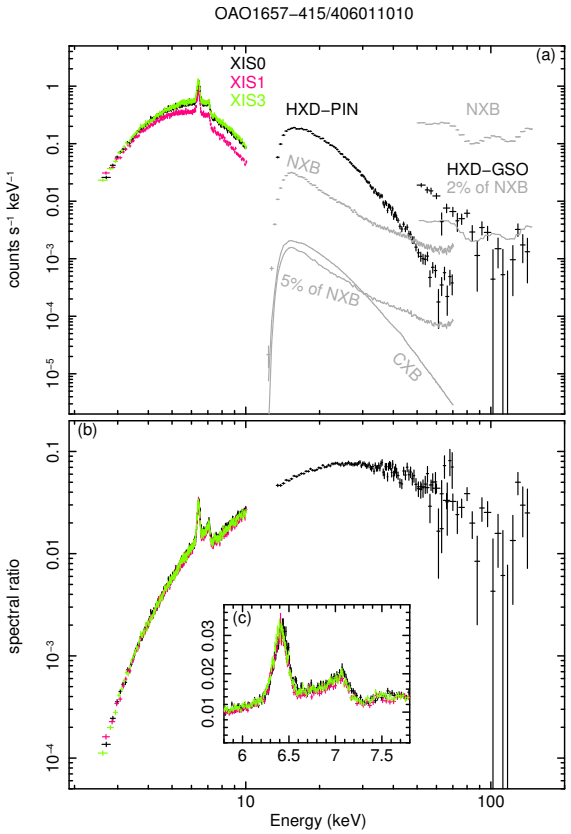

Figure 5.15: The same as Figure 5.1, but phase-averaged, background-subtracted spectra of OAO 1657-415 (ObsID=406011010).

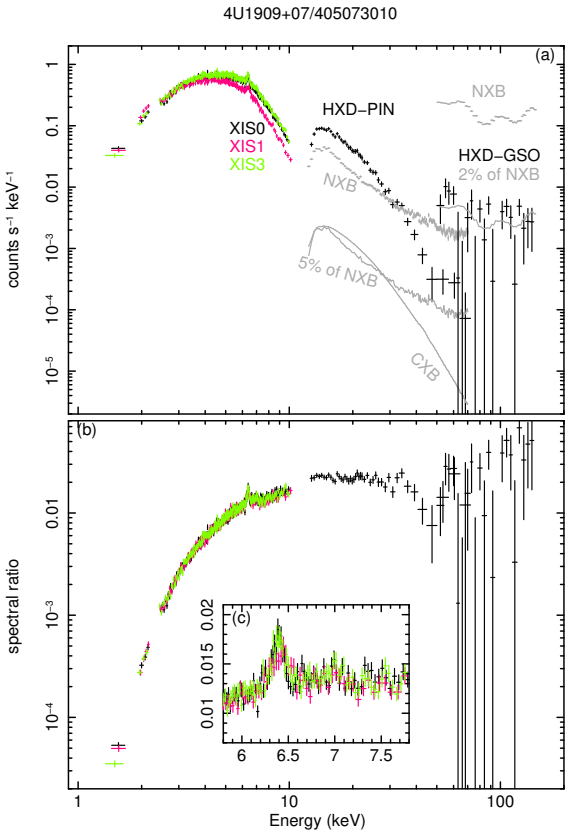

Figure 5.16: The same as Figure 5.1, but phase-averaged, background-subtracted spectra of 4U 1909+07 (ObsID=405073010).

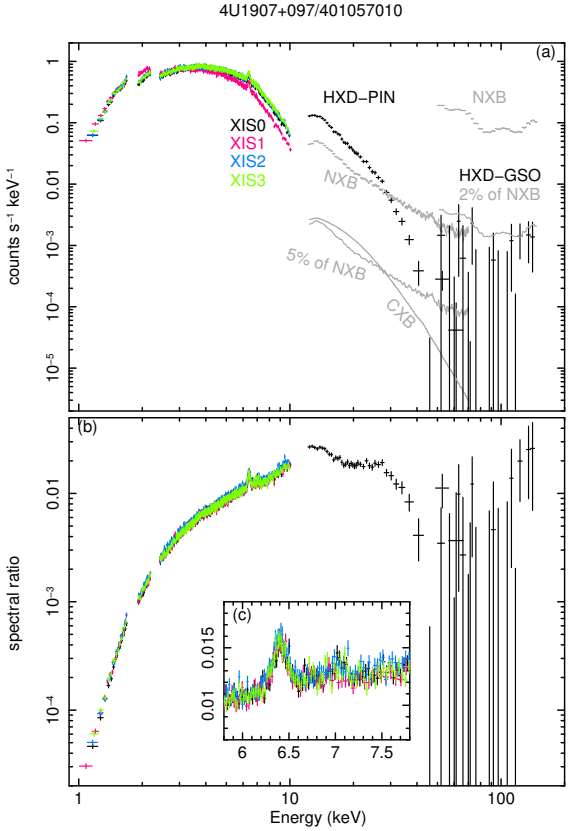

Figure 5.17: The same as Figure 5.1, but phase-averaged, background-subtracted spectra of 4U 1907+097 (ObsID=401057010).

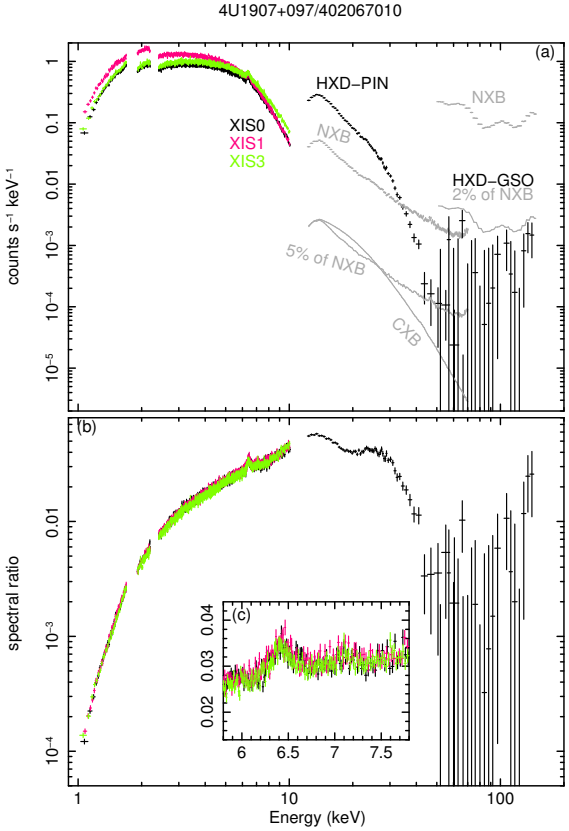

Figure 5.18: The same as Figure 5.1, but phase-averaged, background-subtracted spectra of 4U 1907+097 (ObsID=402067010).

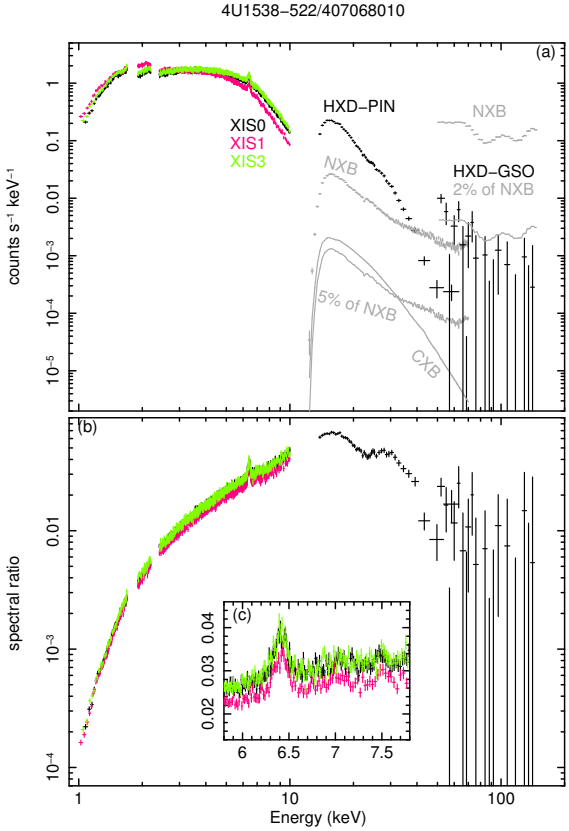

Figure 5.19: The same as Figure 5.1, but phase-averaged, background-subtracted spectra of 4U 1538-522 (ObsID=407068010).

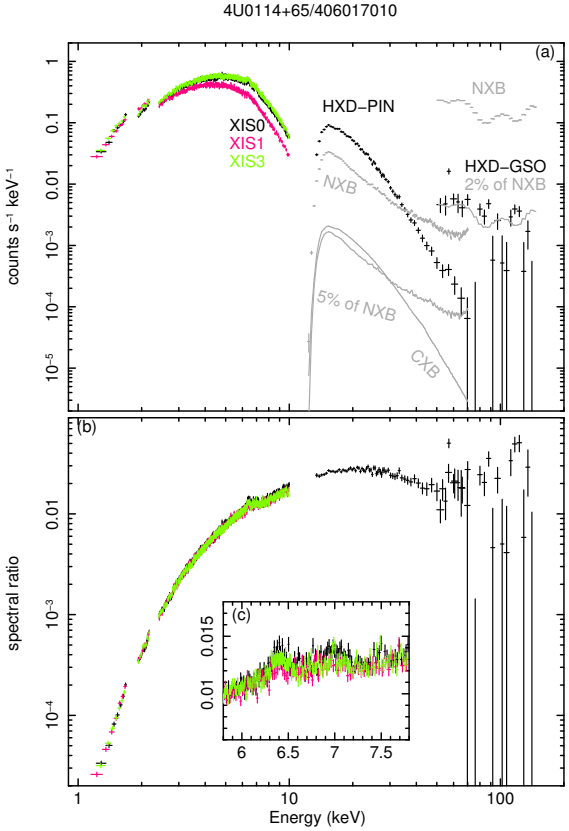

Figure 5.20: The same as Figure 5.1, but phase-averaged, background-subtracted spectra of 4U 0114+65 (ObsID=406017010).

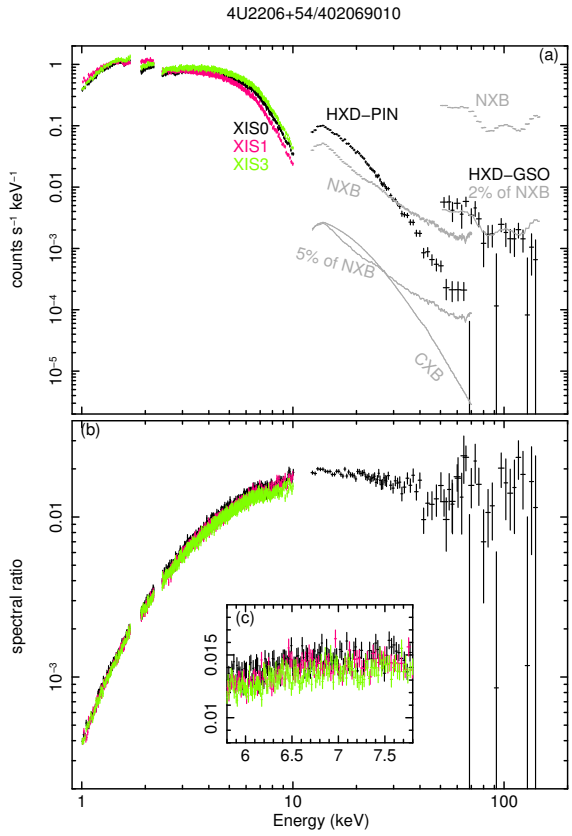

Figure 5.21: The same as Figure 5.1, but phase-averaged, background-subtracted spectra of 4U 2206+54 (ObsID=402069010).

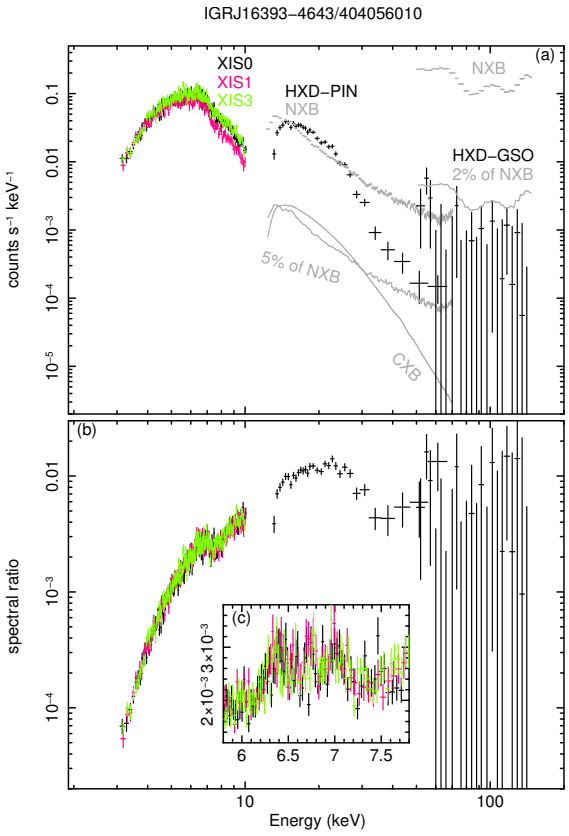

Figure 5.22: The same as Figure 5.1, but phase-averaged, background-subtracted spectra of IGR J16393-4643 (ObsID=404056010).

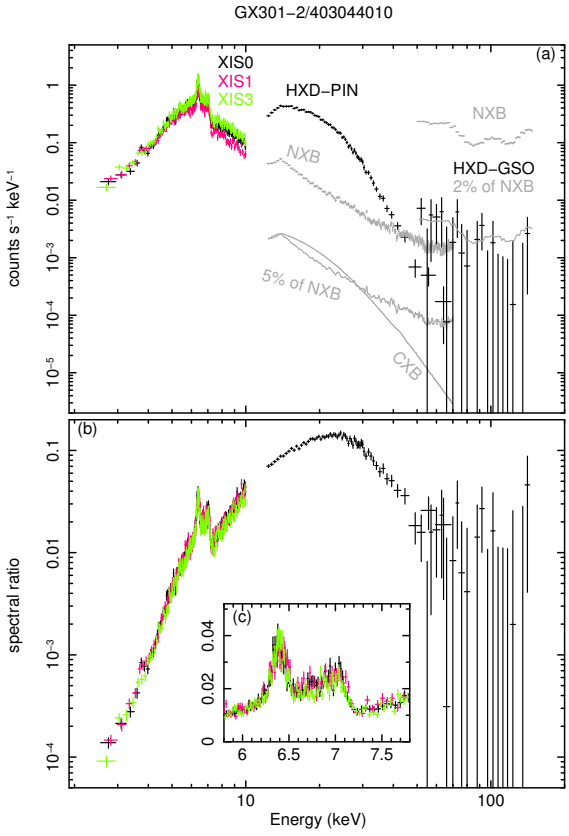

Figure 5.23: The same as Figure 5.1, but phase-averaged, background-subtracted spectra of GX 301-2 (ObsID=403044010).

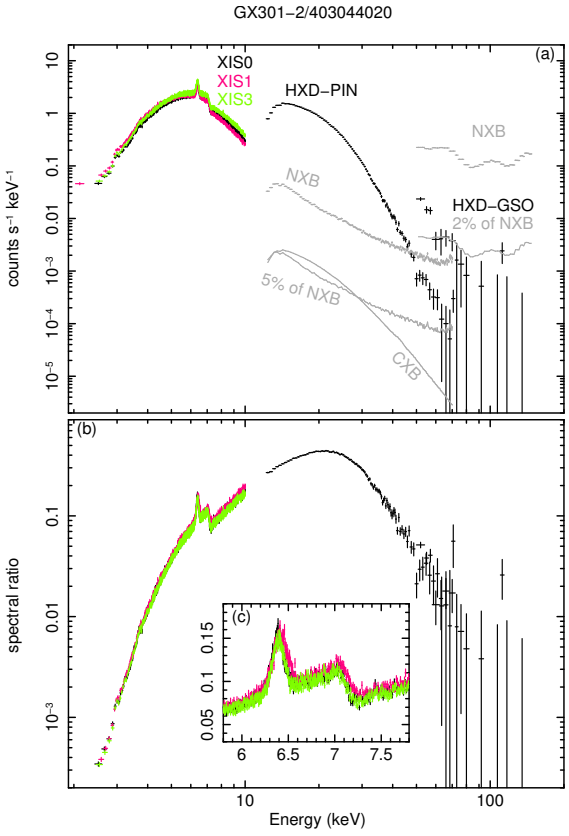

Figure 5.24: The same as Figure 5.1, but phase-averaged, background-subtracted spectra of GX 301-2 (ObsID=403044020).

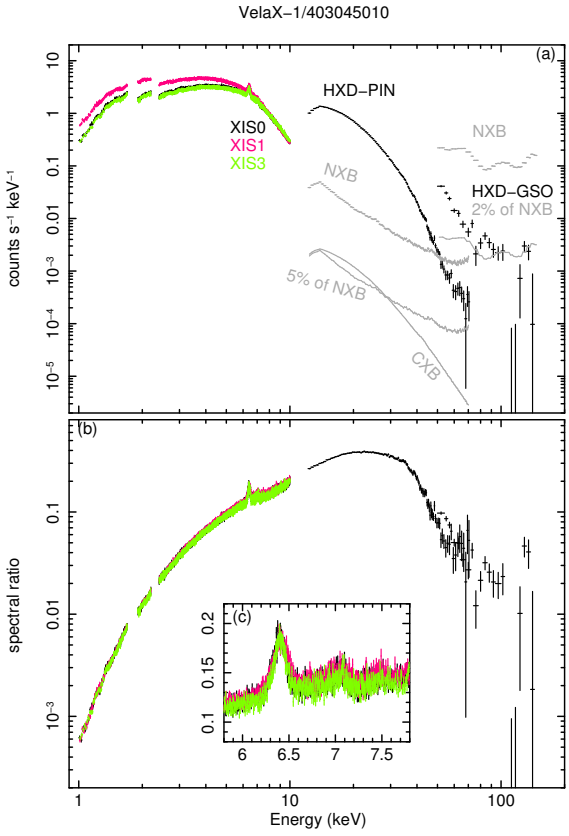

Figure 5.25: The same as Figure 5.1, but phase-averaged, background-subtracted spectra of Vela X-1 (ObsID=403045010).

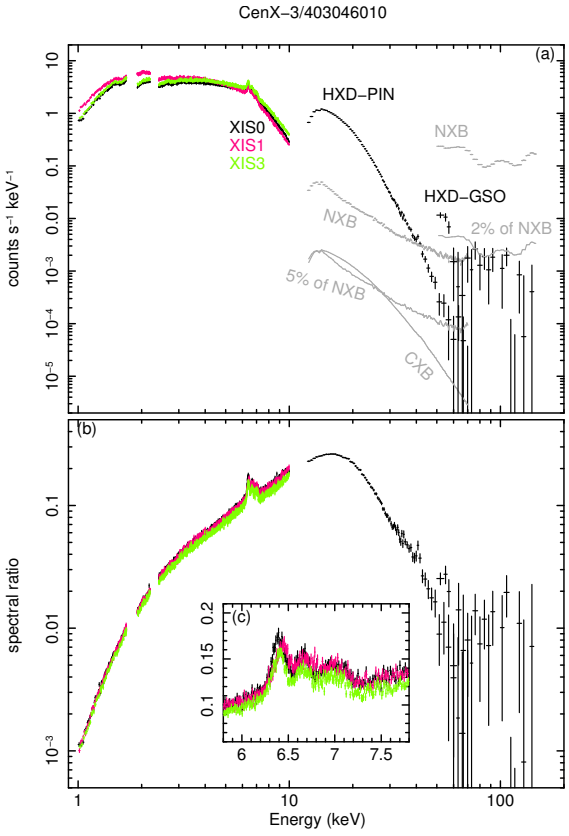

Figure 5.26: The same as Figure 5.1, but phase-averaged, background-subtracted spectra of Cen X-3 (ObsID=403046010).

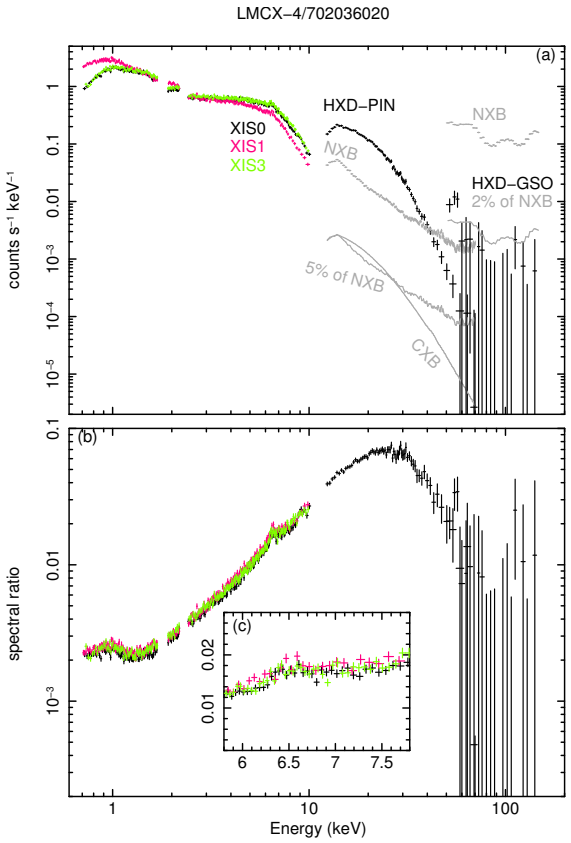

Figure 5.27: The same as Figure 5.1, but phase-averaged, background-subtracted spectra of LMC X-4 (ObsID=702036020).

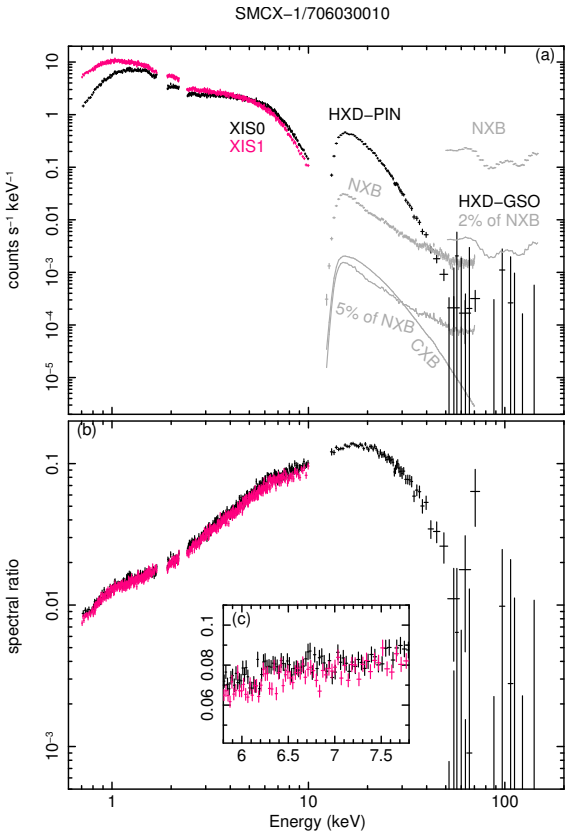

Figure 5.28: The same as Figure 5.1, but phase-averaged, background-subtracted spectra of SMC X-1 (ObsID=706030010).

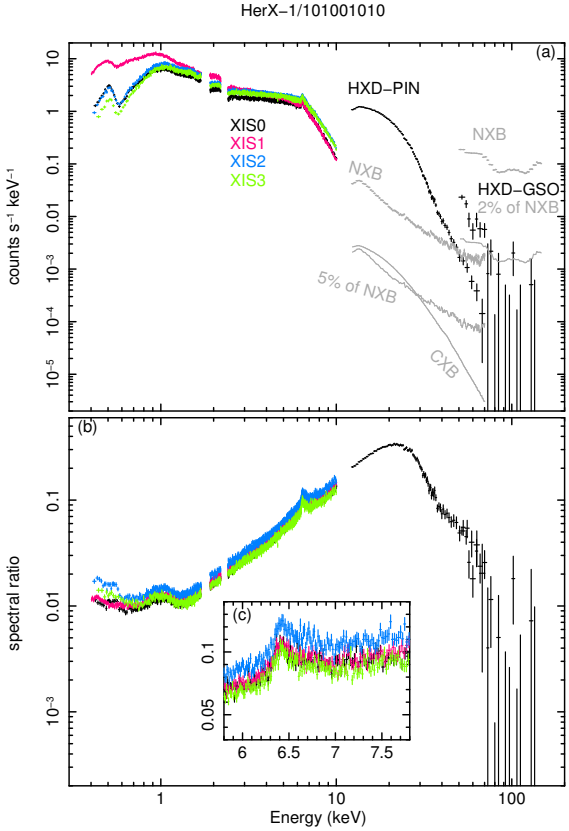

Figure 5.29: The same as Figure 5.1, but phase-averaged, background-subtracted spectra of Her X-1 (ObsID=101001010).

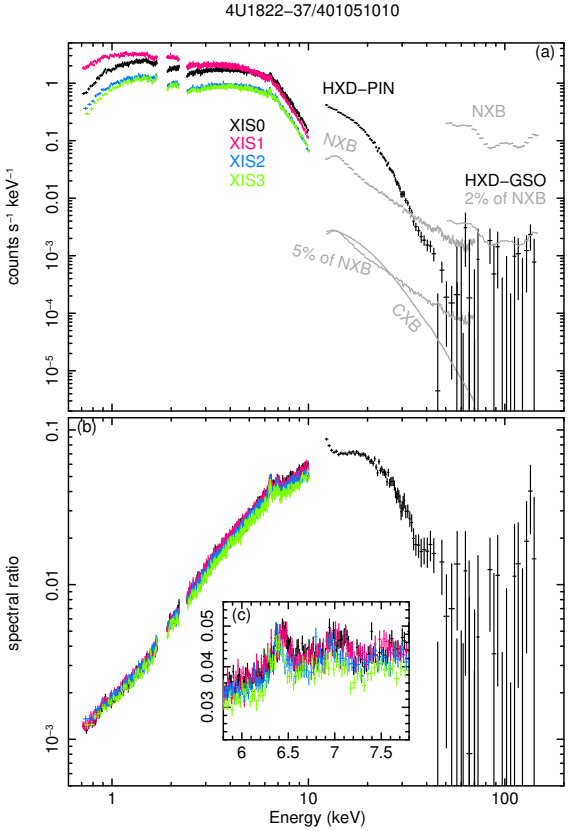

Figure 5.30: The same as Figure 5.1, but phase-averaged, background-subtracted spectra of 4U 1822-37 (ObsID=401051010).

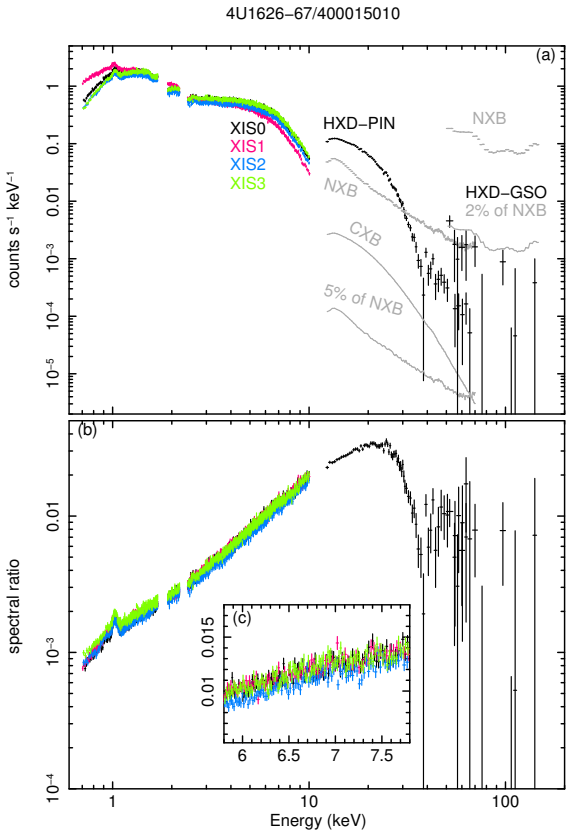

Figure 5.31: The same as Figure 5.1, but phase-averaged, background-subtracted spectra of 4U 1626-67 (ObsID=400015010).

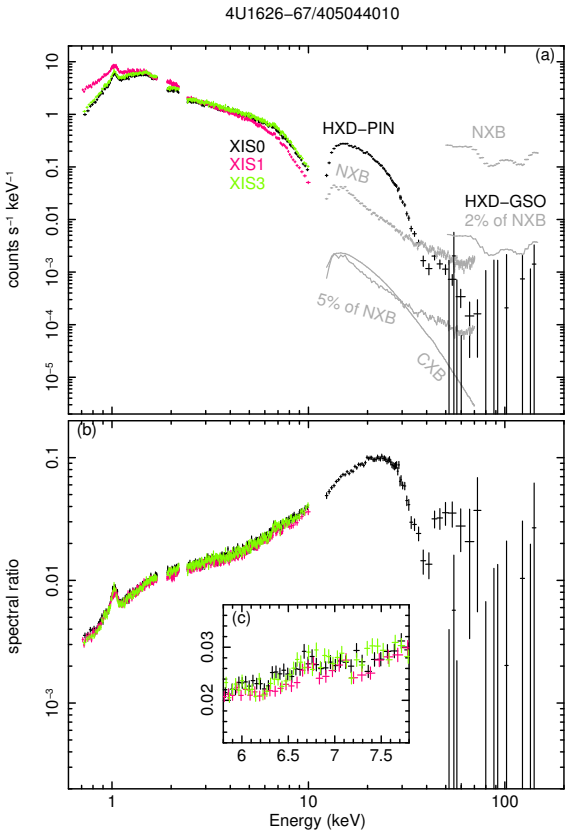

Figure 5.32: The same as Figure 5.1, but phase-averaged, background-subtracted spectra of 4U 1626-67 (ObsID=405044010).

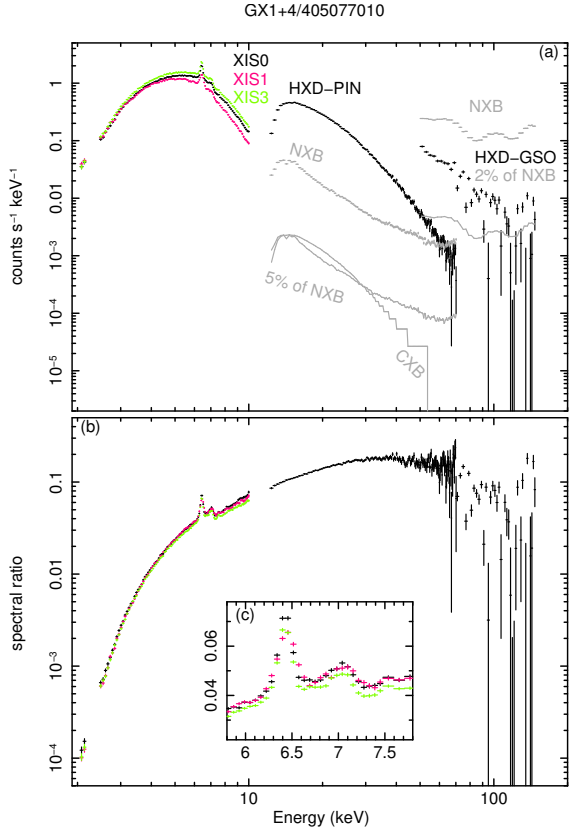

Figure 5.33: The same as Figure 5.1, but phase-averaged, background-subtracted spectra of GX 1+4 (ObsID=405077010).

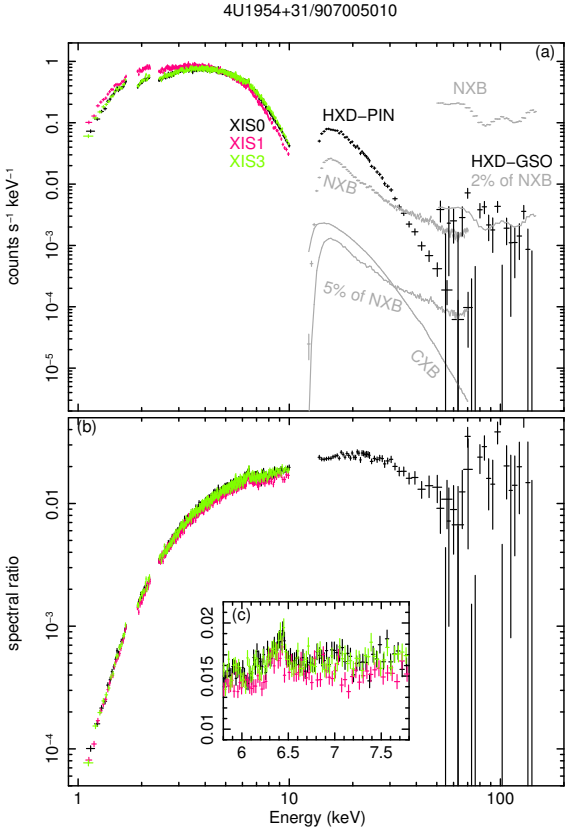

Figure 5.34: The same as Figure 5.1, but phase-averaged, background-subtracted spectra of 4U 1954+31 (ObsID=907005010).

Table 5.1: List of applied spectral model components representing the phase-averaged spectra in *Suzaku* observation of our sample APXPs.

Source	ObsID	Comtinuum[a]	PCA[b]	CRSF[c]	Emission Lines[d]	Additional Components[e]
			BeXB Pulsars			
A 0535+262	100021010	A:NPEX	O	`cyclabs`	Fe K_α	···
A 0535+262	404054010	A:NPEX	O	`cyclabs`	Fe K_α	···
A 0535+262	404055010	A:NPEX	O	`cyclabs`	Fe K_α	···
GX 304-1	406060010	A:NPEX	O	`cyclabs`	Fe K_α, Fe K_β	···
GX 304-1	905002010	A:NPEX	O	`cyclabs`	Fe K_α, Fe K_β	···
GRO J1008-57	902003010	A:NPEX	O	···	Fe K_α, Fe He_α, Fe K_β	soft excess
GRO J1008-57	907006010	A:NPEX	O	`cyclabs`	Fe K_α, Fe He_α, Fe K_β	soft excess
GRO J1008-57	408044010	A:NPEX	O	···	Fe K_α, Fe K_β	soft excess
EXO 2030+375	402068010	A:NPEX	O	···	Fe K_α, Fe He_α	···
EXO 2030+375	407089010	A:NPEX	O	···	Fe K_α	···
1A 1118-61	403049010	F:`compTT`	O	`gabs`	Fe K_α, Fe K_β	soft excess
1A 1118-61	403050010	F:`compTT`	O	`gabs`	Fe K_α, Fe K_β	soft excess
Cep X-4	409037010	A:NPEX	O	`cyclabs`	Fe K_α, Fe K_β	···
Cep X-4	909001010	A:NPEX	O	`cyclabs`	Fe K_α, Fe K_β	···
			SGXB Pulsars			
OAO 1657-415	406011010	D:BB+CPL	O	···	Fe K_α, Fe K_β, Ni K_α	···
4U 1909+07	405073010	C:CPL	O	···	Fe K_α, Fe K_β	···
4U 1907+097	401057010	F:`compTT`	X	`cyclabs`	Fe K_α, Fe K_β	10 keV bump feature
4U 1907+097	402067010	F:`compTT`	X	`cyclabs`	Fe K_α, Fe K_β	10 keV bump feature
4U 1538-522	407068010	B:FPL	O	`gabs`	Fe K_α, Fe K_β	···
4U 0114+65	406017010	D:BB+CPL	O	···	Fe K_α, Fe K_β	···
4U 2206+54	402069010	E:BB+BPL	X	···	Fe K_α, Fe He_α	···
IGR J16393-4643	404056010	B:FPL	X	`cyclabs`	Fe K_α, Fe K_β	···
GX 301-2	403044010	B:FPL	O	`gabs`	Fe K_α, Fe K_β	···
GX 301-2	403044020	B:FPL	O	`gabs`	Ar K_α, Ca K_α, Cr K_α	···
					Fe K_α, Fe K_β, Ni K_α	
Vela X-1	403045010	A:NPEX	O	`cyclabs`	Fe K_α, Fe K_β, Ni K_α	···
Cen X-3	403046010	A:NPEX	O	`gabs`	Fe K_α,Fe K_β	10 keV bump feature
					Fe He_α, Fe Ly_α	6.5 keV broad line
LMC X-4	702036020	A:NPEX	X	···	Ne He_α, Fe K_α	soft excess
						Fe broad line
SMC X-1	706030010	A:NPEX	X	···	Fe K_α, Fe He_α	soft excess
			LMXB Pulsars			
Her X-1	101001010	A:NPEX	X	`cyclabs`	Fe K_α, Fe He_α	broad 1 keV emission
						soft excess, Fe broad line
4U 1822-37	401051010	D:BB+CPL	X	···	Fe K_α, Fe He_α, Fe Ly_α	···
4U 1626-67	400015010	A:NPEX	X	`cyclabs`	Ne He_α, Ne Ly_α	soft excess
					Fe K_α, Fe He_α, Fe Ly_α	
4U 1626-67	405044010	A:NPEX	X	`cyclabs`	Ne He_α, Ne Ly_α	soft excess
					Fe K_α, Fe He_α, Fe Ly_α	
GX 1+4	405077010	D:BB+CPL	X	···	Fe K_α, Fe K_β, Ni K_α	···
4U 1954+31	907005010	F:`compTT`	X	···	Fe K_α	···

Notes.

[a] Applied continuum model to fit the X-ray broadband spectra. NPEX, BB, CPL, BPL and FPL represent negative and positive exponential cutoff power-law, blackbody, exponential cutoff power-law, broken power-law and power-law multiplied Fermi-Dirac cutoff, respectively. The photoelectric-absorption (`TBnew`) is included in all the spectral models. In our fitting with `compTT` continuum model, a disk geometry was assumed.

[b] Partial covering photoelectric absorption. O and X mean that the fitting model includes the partial covering absorption component or not.

[c] The component to represent a cyclotron resonance scattering feature in the X-ray spectrum.

[d] Emission line component included in the fitting model.

[e] Additional component to the fitting model. Soft excess (Hickox et al. 2004; Hung et al. 2010; Suchy et al. 2011; Yamamoto et al. 2014; Asami et al. 2014; Camero-Arranz et al. 2012) was modeled by blackbody. 10 keV bump feature (Mihara 1995; Coburn et al. 2002; Rivers et al. 2010), broad 1 keV emission (Endo et al. 2000; Asami et al. 2014) and Fe broad line (Hung et al. 2010; Asami et al. 2014) were represented by a Gaussian function, respectively.

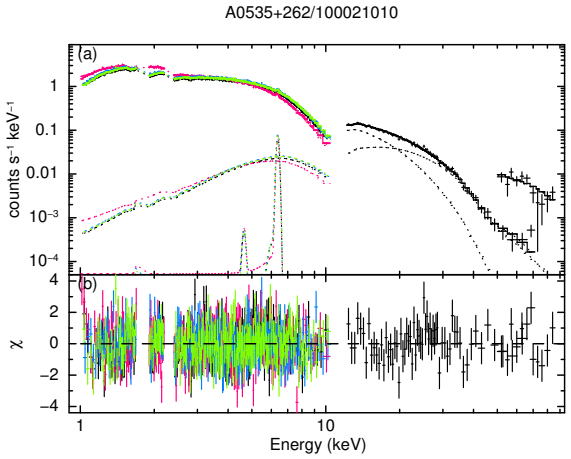

Figure 5.35: Phase-averaged fitting result of *Suzaku* observational data of A 0535+262 (ObsID=100021010). (a) Phase-averaged, background-subtracted spectra obtained with XISs (XIS 0; black, XIS 1; red, XIS 2; blue, XIS 3; green), HXD-PIN and HXD-GSO (above 15 keV; plotted in black color) onboard *Suzaku*. The best-fit model is also plotted in same panel (see Table 5.1). (b) Residuals of data from the best-fit model which were divided by its error. Different colors correspond to the same ones in panel (a).

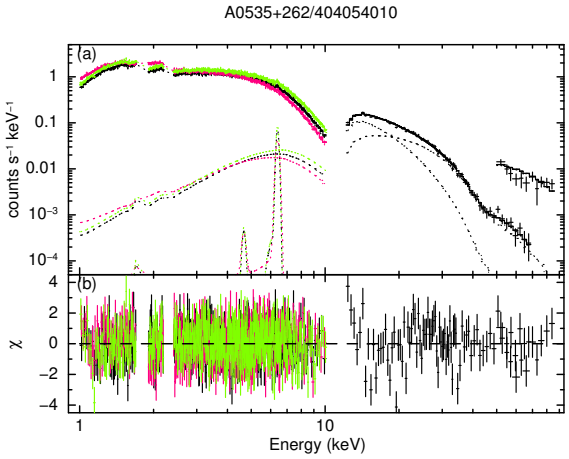

Figure 5.36: The same as Figure 5.35, but phase-averaged fitting result of A 0535+262 (ObsID=404054010).

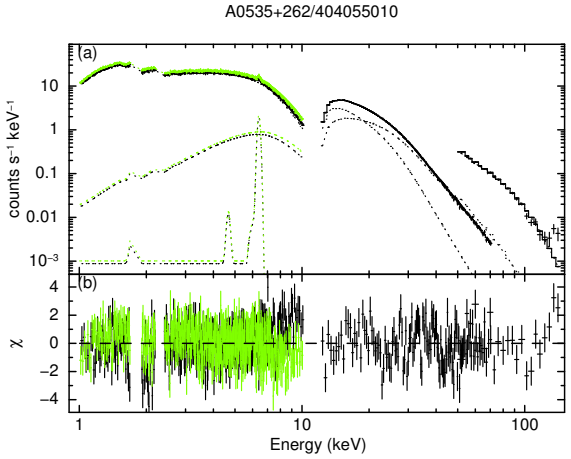

Figure 5.37: The same as Figure 5.35, but phase-averaged fitting result of A 0535+262 (ObsID=404055010).

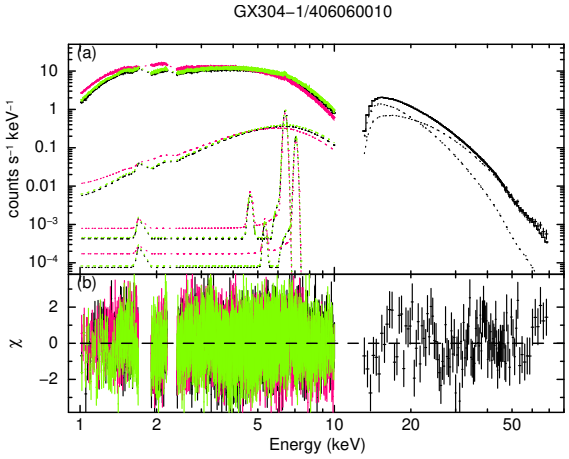

Figure 5.38: The same as Figure 5.35, but phase-averaged fitting result of GX 304-1 (ObsID=406060010).

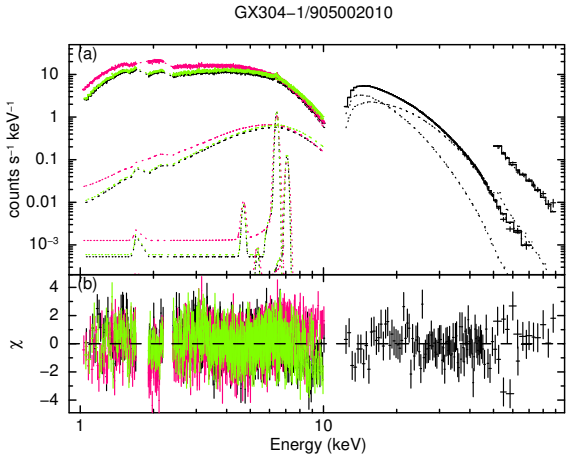

Figure 5.39: The same as Figure 5.35, but phase-averaged fitting result of GX 304-1 (ObsID=905002010).

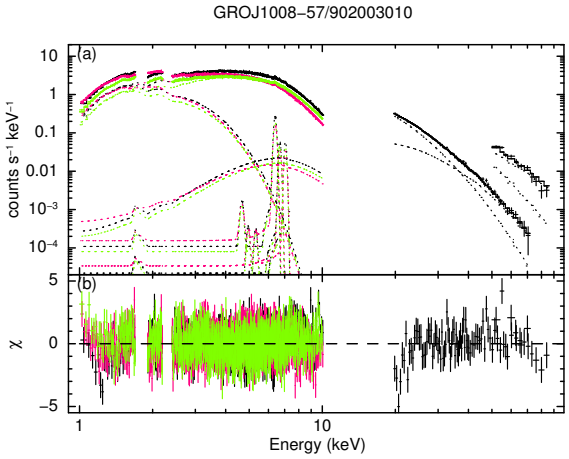

Figure 5.40: The same as Figure 5.35, but phase-averaged fitting result of GRO J1008-57 (ObsID=902003010).

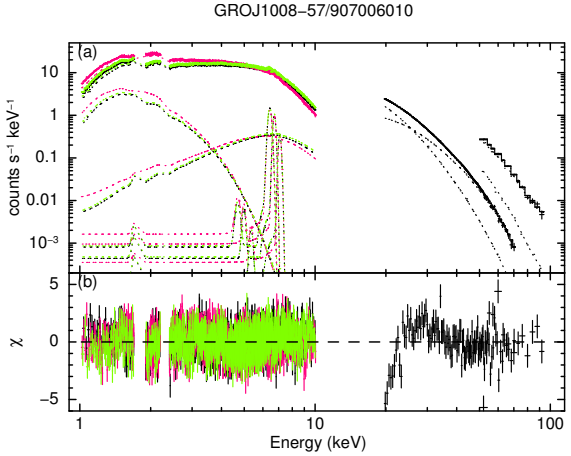

Figure 5.41: The same as Figure 5.35, but phase-averaged fitting result of GRO J1008-57 (ObsID=907006010).

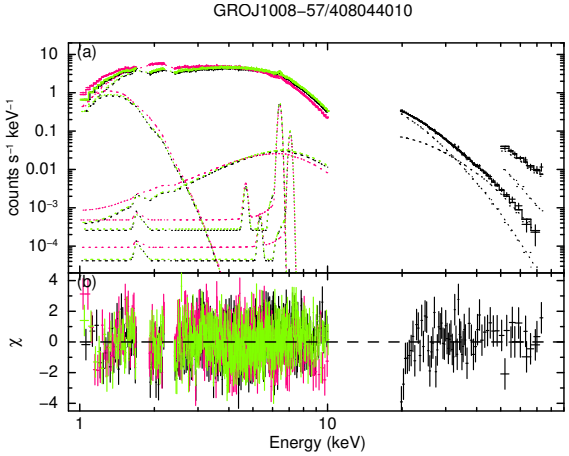

Figure 5.42: The same as Figure 5.35, but phase-averaged fitting result of GRO J1008-57 (ObsID=408044010).

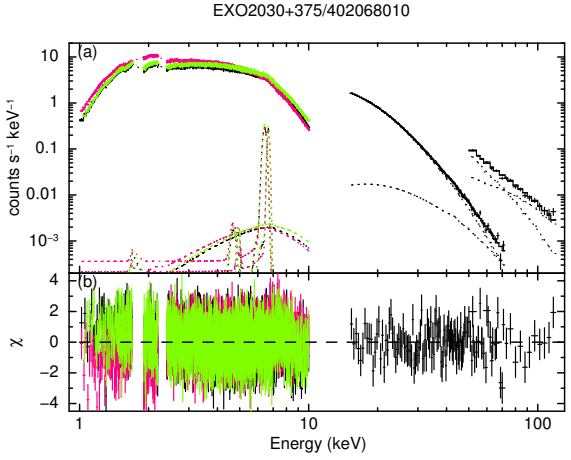

Figure 5.43: The same as Figure 5.35, but phase-averaged fitting result of EXO 2030+375 (ObsID=402068010).

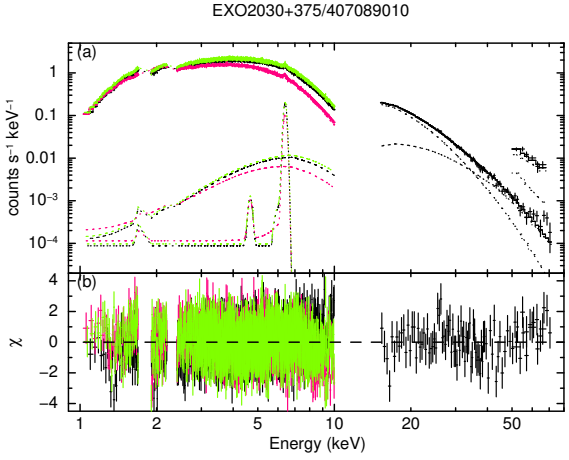

Figure 5.44: The same as Figure 5.35, but phase-averaged fitting result of EXO 2030+375 (ObsID=407089010).

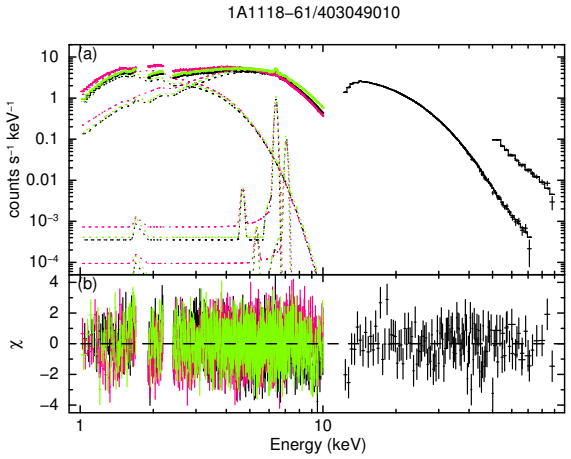

Figure 5.45: The same as Figure 5.35, but phase-averaged fitting result of 1A 1118-61 (ObsID=403049010).

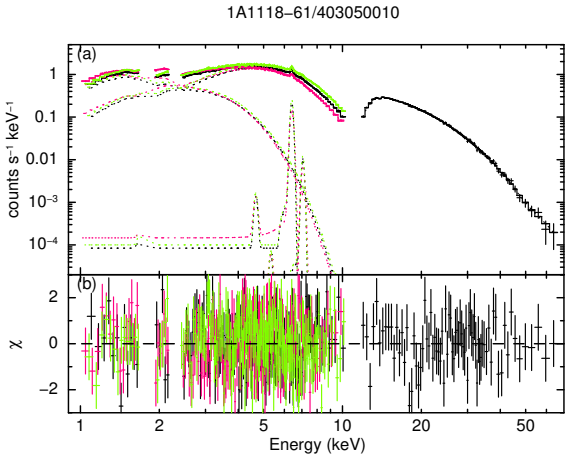

Figure 5.46: The same as Figure 5.35, but phase-averaged fitting result of 1A 1118-61 (ObsID=403050010).

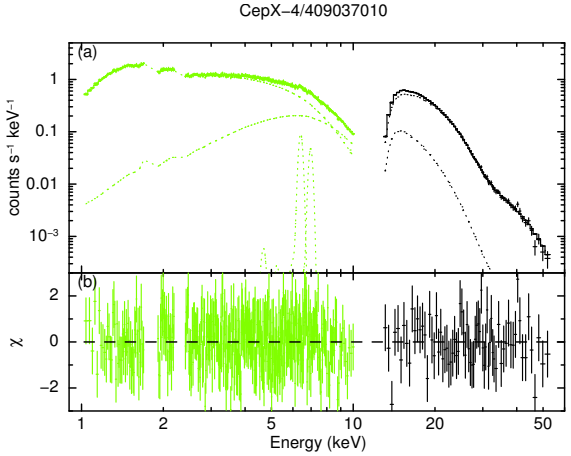

Figure 5.47: The same as Figure 5.35, but phase-averaged fitting result of Cep X-4 (ObsID=409037010).

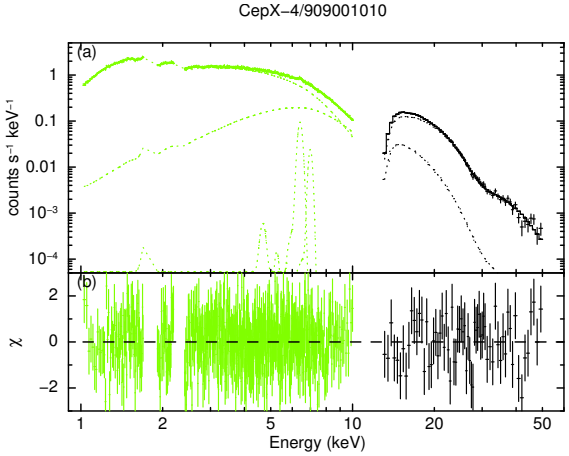

Figure 5.48: The same as Figure 5.35, but phase-averaged fitting result of Cep X-4 (ObsID=909001010).

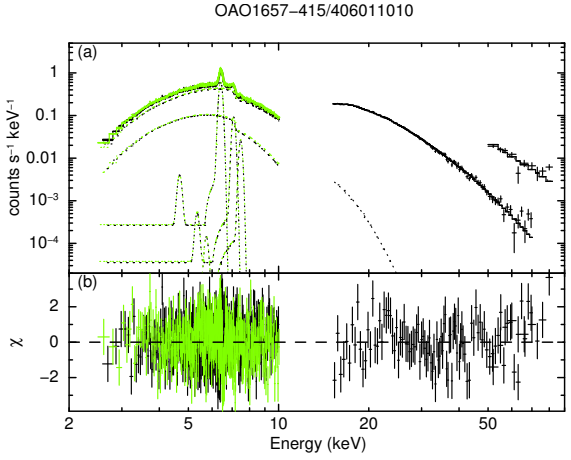

Figure 5.49: The same as Figure 5.35, but phase-averaged fitting result of OAO 1657-415 (ObsID=406011010).

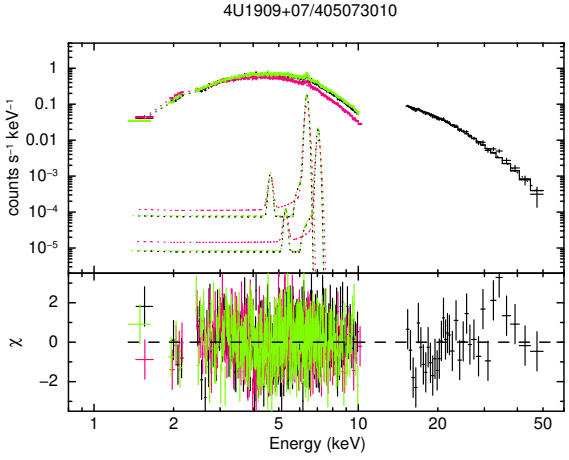

Figure 5.50: The same as Figure 5.35, but phase-averaged fitting result of 4U 1909+07 (ObsID=405073010).

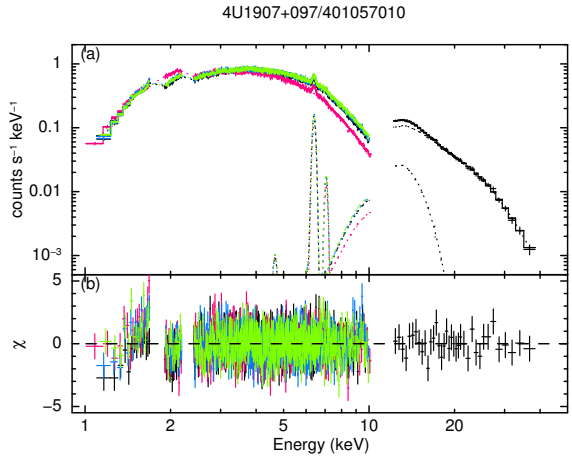

Figure 5.51: The same as Figure 5.35, but phase-averaged fitting result of 4U 1907+097 (ObsID=401057010).

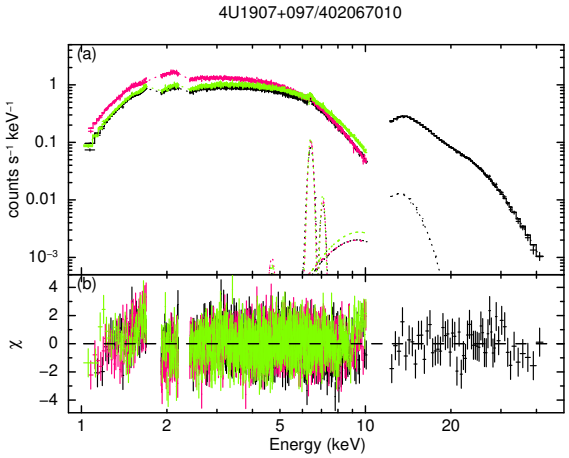

Figure 5.52: The same as Figure 5.35, but phase-averaged fitting result of 4U 1907+097 (ObsID=402067010).

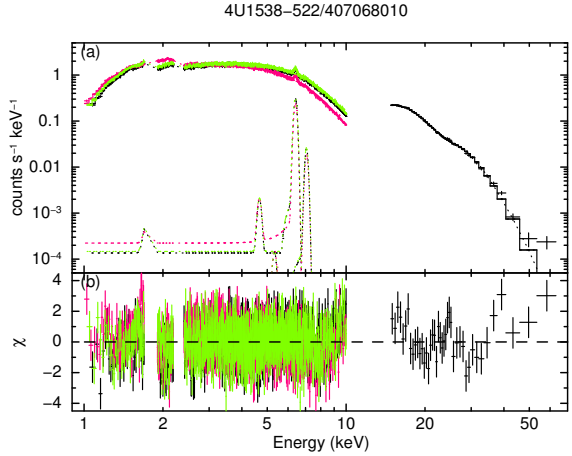

Figure 5.53: The same as Figure 5.35, but phase-averaged fitting result of 4U 1538-522 (ObsID=407068010).

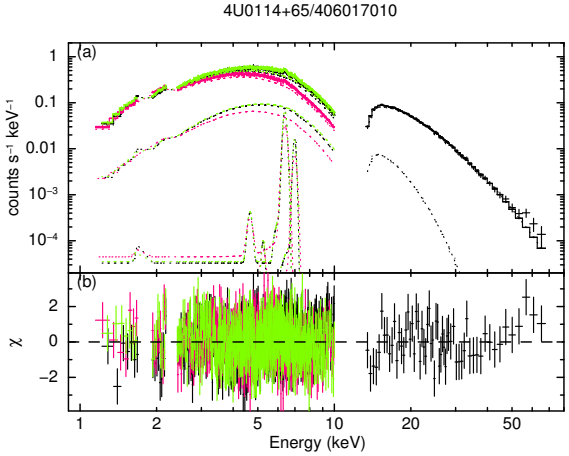

Figure 5.54: The same as Figure 5.35, but phase-averaged fitting result of 4U 0114+65 (ObsID=406017010).

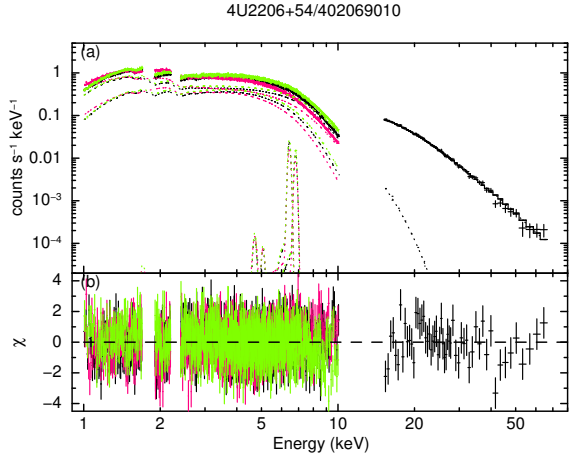

Figure 5.55: The same as Figure 5.35, but phase-averaged fitting result of 4U 2206+54 (ObsID=402069010).

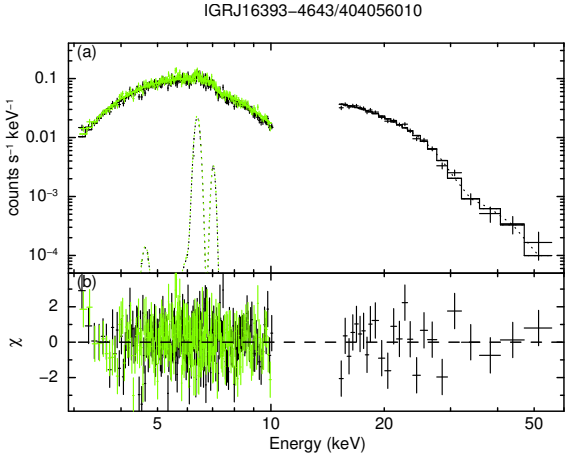

Figure 5.56: The same as Figure 5.35, but phase-averaged fitting result of IGR J16393-4643 (ObsID=404056010).

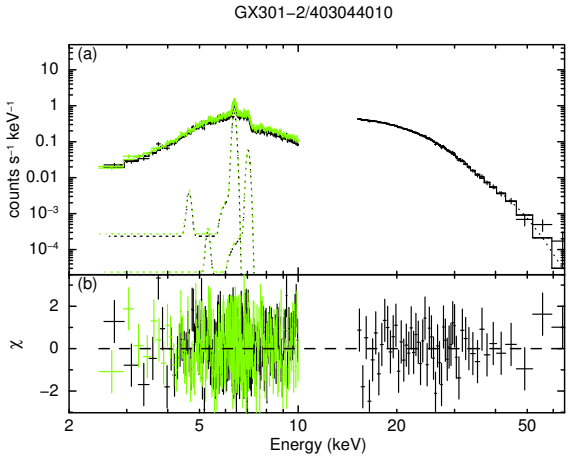

Figure 5.57: The same as Figure 5.35, but phase-averaged fitting result of GX 301-2 (ObsID=403044010).

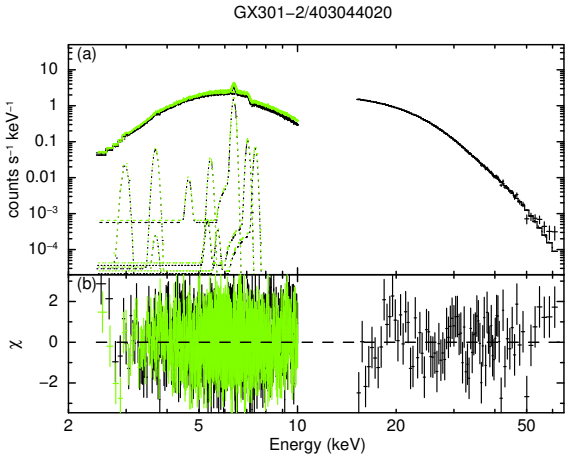

Figure 5.58: The same as Figure 5.35, but phase-averaged fitting result of GX 301-2 (ObsID=403044020).

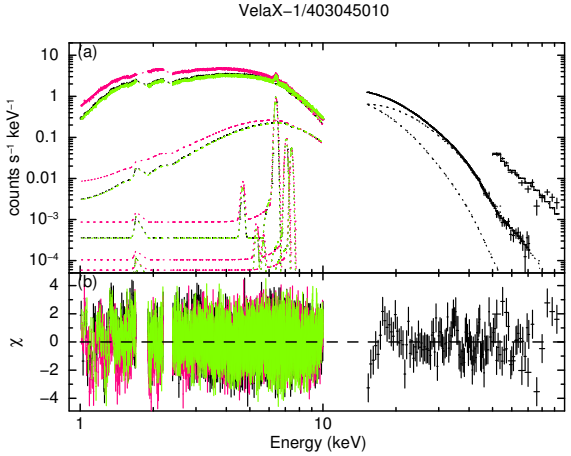

Figure 5.59: The same as Figure 5.35, but phase-averaged fitting result of Vela X-1 (ObsID=403045010).

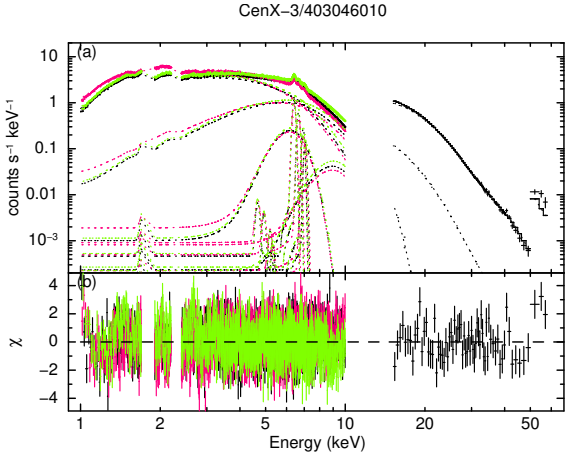

Figure 5.60: The same as Figure 5.35, but phase-averaged fitting result of Cen X-3 (ObsID=403046010).

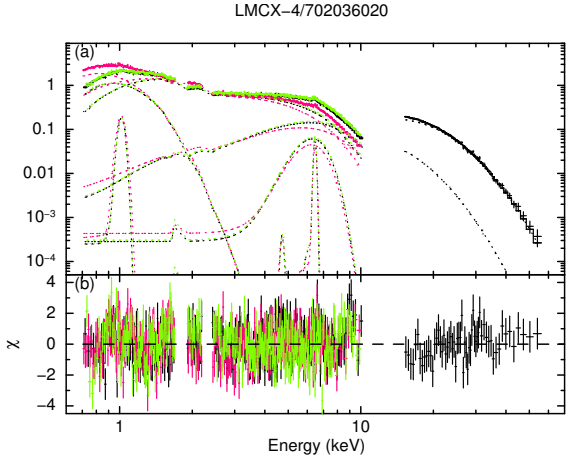

Figure 5.61: The same as Figure 5.35, but phase-averaged fitting result of LMC X-4 (ObsID=702036020).

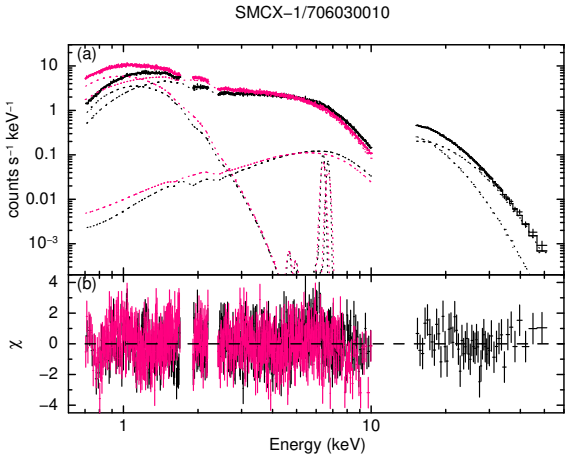

Figure 5.62: The same as Figure 5.35, but phase-averaged fitting result of SMC X-1 (ObsID=706030010).

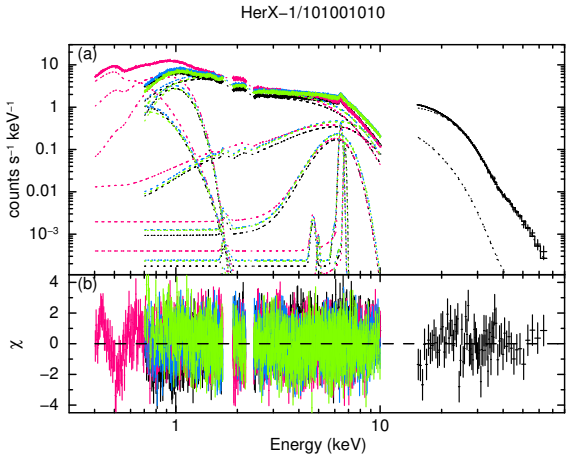

Figure 5.63: The same as Figure 5.35, but phase-averaged fitting result of Her X-1 (ObsID=101001010).

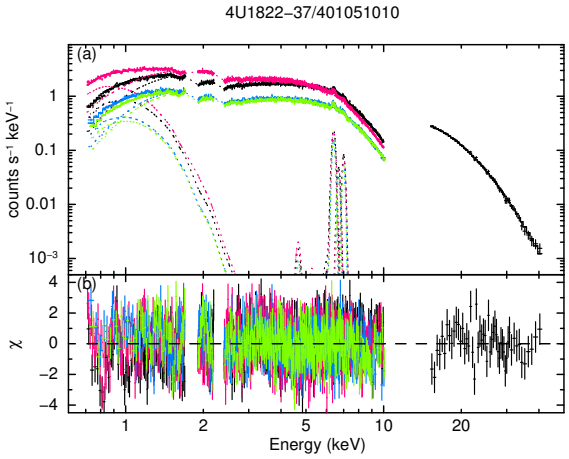

Figure 5.64: The same as Figure 5.35, but phase-averaged fitting result of 4U 1822-37 (ObsID=401051010).

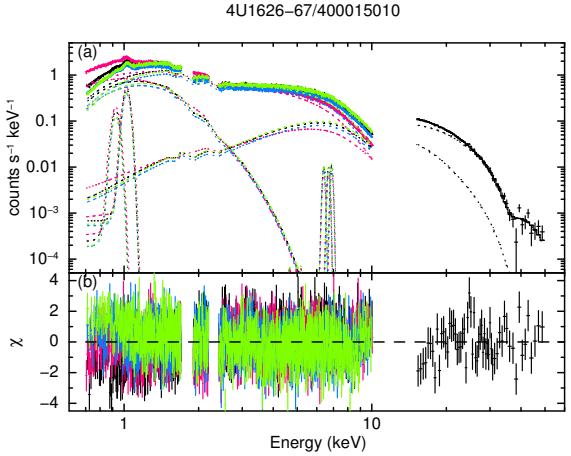

Figure 5.65: The same as Figure 5.35, but phase-averaged fitting result of 4U 1626-67 (ObsID=400015010).

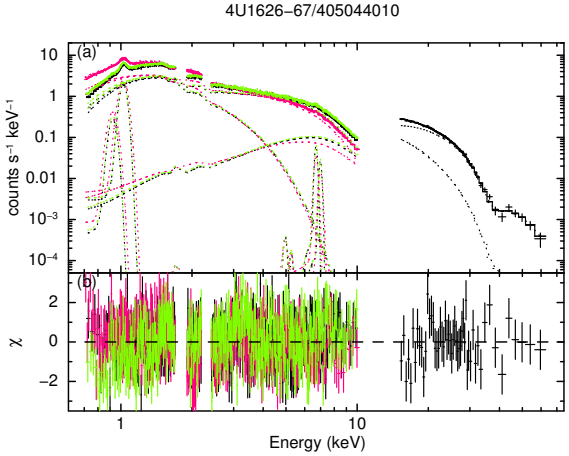

Figure 5.66: The same as Figure 5.35, but phase-averaged fitting result of 4U 1626-67 (ObsID=405044010).

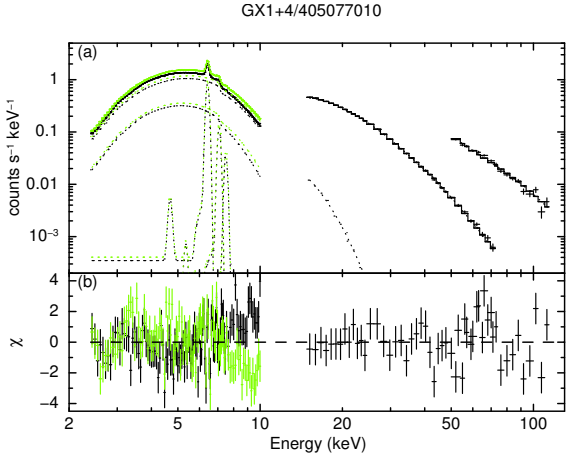

Figure 5.67: The same as Figure 5.35, but phase-averaged fitting result of GX 1+4 (ObsID=405077010).

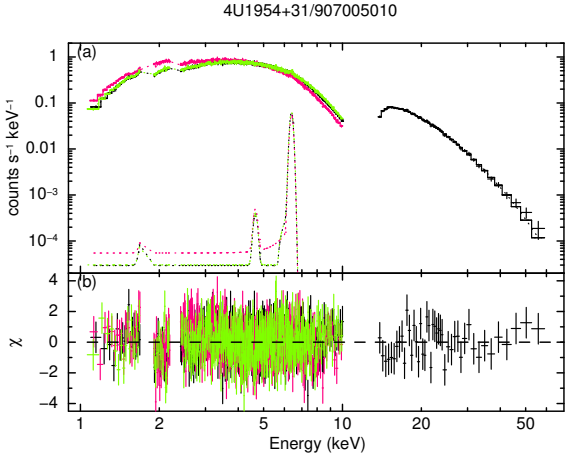

Figure 5.68: The same as Figure 5.35, but phase-averaged fitting result of 4U 1954+31 (ObsID=907005010).

Table 5.2: Best-fit spectral parameters obtained by fitting the phase-averaged spectra of *Suzaku* observation of our sample APXPs.

Source	ObsID	Model(χ^2/d.o.f.)[a]	$N_{\rm H1}$[b]	$N_{\rm H2}$[c]	$f_{\rm pc}$[d]	iron K_α line			Unabs.$F_{\rm x}$[i]	HR[j]	$L_{\rm x}$[k]
						E_{K_α}[e]	W_{K_α}[f]	I_{K_α}[g] eq.W_{K_α}[h]	$F_{\rm h}/F_{\rm s}$	$\eta = F_{\rm h}/F_{\rm s}$	
BeXB Pulsars											
A 0535+262	100021010	A(965.91/904)	0.93(2)	5.6(3)	0.35(1)	6.38(2)	< 0.06	0.07(1)	20 ± 4	6.96(2)/15.05(5)	0.463(2)	0.63(1)
A 0535+262	404054010	A(1371.06/1200)	0.91(3)	7.3(6)	0.37(1)	6.41(2)	< 0.3	0.08(2)	22 ± 6	7.04(3)/14.97(8)	0.470(3)	0.637(8)
A 0535+262	404055010	A(1330.14/987)	0.61(2)	15(2)	0.18(2)	6.41(1)	< 0.07	3.1(4)	34 ± 3	205.7(9)/352(2)	0.585(4)	16.59(4)
GX 304-1	406060010	A(4941.66/4690)	1.49(1)	9.0(4)	0.31(1)	6.407(7)	< 0.05	1.8(1)	29 ± 2	126.6(2)/240.6(6)	0.526(1)	10.27(2)
GX 304-1	905002010	A(2359.05/1907)	1.42(2)	21(1)	0.29(2)	6.42(1)	0.0(fixed)	4.0(3)	34 ± 2	257.4(8)/470(2)	0.548(3)	23.28(8)
GRO J1008-57	902003010	A(2492.43/2148)	1.83(3)	8.8(5)	0.69(3)	6.4(1)	< 0.06	0.34(4)	20 ± 1	34.00(7)/64.4(2)	0.528(2)	19.0(2)
GRO J1008-57	907006010	A(3179.56/2616)	1.53(4)	55(4)	0.22(2)	6.426(8)	0.06(2)	3.6(3)	37 ± 2	214(1)/377(4)	0.567(7)	128(3)
GRO J1008-57	408044010	A(1515.92/1244)	2.7(1)	26(3)	0.29(2)	6.415(7)	< 0.04	0.89(6)	46 ± 2	39.8(1)/78.1(4)	0.510(3)	22.6(2)
EXO 2030+375	402068010	A(4992.12/4348)	2.90(2)	92(6)	0.28(1)	6.43(2)	0.09(2)	1.0(2)	25 ± 3	97.9(9)/210(2)	0.466(6)	74.2(4)
EXO 2030+375	407089010	A(3700.78/3334)	2.88(4)	7.5(3)	0.49(1)	6.407(7)	0.03(2)	0.22(2)	34 ± 3	13.43(2)/27.29(7)	0.492(2)	10.50(7)
1A 1118-61	403049010	F(2203.70/1851)	1.24(2)	11.2(5)	0.68(2)	6.408(4)	< 0.02	1.70(7)	47 ± 2	88.3(3)/139.6(8)	0.632(4)	44.2(2)
1A 1118-61	403050010	F(601.87/561)	0.46(9)	11.0(8)	0.76(4)	6.409(9)	< 0.02	0.24(2)	39 ± 5	13.75(10)/26.0(3)	0.528(7)	5.88(8)
Cep X-4	409037010	A(426.41/434)	1.28(6)	14(4)	0.19(7)	6.41(3)	0.0(fixed)	0.4(1)	31 ± 15	28.4(3)/51.8(6)	0.547(9)	13.3(2)
Cep X-4	909001010	A(583.21/570)	1.24(4)	9(1)	0.30(4)	6.41(2)	< 0.1	0.12(3)	34 ± 12	7.57(7)/14.7(1)	0.515(6)	3.69(6)
SGXB Pulsars											
OAO 1657-415	406011010	D(1006.46/763)	26.0(8)	74(6)	0.62(2)	6.413(1)	0.0(fixed)	0.84(2)	254 ± 6	11.1(2)/19.7(6)	0.56(2)	9.7(1)
4U 1909+07	405073010	C(874.96/799)	7.7(6)	10(3)	0.6(1)	6.389(7)	< 0.03	0.18(1)	79 ± 3	5.09(5)/10.5(2)	0.48(1)	3.61(7)
4U 1907+097	401057010	F(1742.54/1591)	1.9(2)	···	···	6.403(5)	< 0.04	0.143(9)	66 ± 2	4.51(1)/8.16(2)	0.553(2)	1.30(1)
4U 1907+097	402067010	F(2354.98/2042)	1.3(1)	···	···	6.421(8)	< 0.05	0.27(2)	49 ± 2	11.53(3)/20.93(3)	0.551(2)	3.20(1)
4U 1538-522	407068010	B(2392.00/2059)	2.22(3)	6(1)	0.18(2)	6.407(3)	< 0.02	0.35(2)	66 ± 2	11.11(3)/20.28(8)	0.548(3)	1.26(1)
4U 0114+65	406017010	D(1485.08/1400)	3.6(2)	9.7(7)	0.66(2)	6.40(1)	0.05(3)	0.08(1)	37 ± 2	4.99(1)/8.70(4)	0.573(3)	3.86(6)
4U 2206+54	402069010	E(2334.80/2160)	0.68(3)	···	···	6.44(3)	0.0(fixed)	0.026(7)	10 ± 1	4.81(2)/9.97(2)	0.482(2)	2.72(4)
IGR J16393-4643	404056010	B(483.52/391)	38(2)	···	···	6.38(2)	< 0.1	0.039(9)	59 ± 10	1.44(2)/2.31(6)	0.62(2)	2.4(1)
GX 301-2	403044010	B(445.30/428)	16(3)	89(3)	0.97(1)	6.386(4)	< 0.02	0.84(5)	381 ± 18	20.2(6)/38(2)	0.54(3)	2.85(8)
GX 301-2	403044020	B(1948.31/1748)	31(2)	32(1)	0.79(5)	6.391(1)	0.0(fixed)	2.96(8)	182 ± 2	64.2(5)/117(1)	0.550(7)	8.51(5)
Vela X-1	403045010	A(6654.16/5729)	0.67(7)	8.6(2)	0.48(1)	6.403(1)	0.0(fixed)	1.89(3)	77 ± 1	53.80(5)/95.9(1)	0.561(1)	3.110(4)
Cen X-3	403046010	A(3625.17/2894)	1.51(5)	4.4(3)	0.51(2)	6.404(2)	0.027(8)	1.94(7)	84 ± 2	44.17(9)/75.5(1)	0.585(1)	17.62(4)
LMC X-4	702036020	A(891.85/755)	0.05(4)	···	···	6.46(4)	0.0(fixed)	0.07(2)	26 ± 4	5.76(3)/8.14(3)	0.708(4)	307(3)
SMC X-1	706030010	A(1359.67/1156)	0.10(2)	···	···	6.4(fixed)	0.0(fixed)	0.23(7)	17 ± 3	26.9(1)/50.7(1)	0.530(3)	1250(6)
LMXB Pulsars											
Her X-1	101001010	A(4061.19/3514)	< 0.001	···	···	6.434(6)	0.08(1)	1.10(9)	73 ± 2	30.51(5)/45.11(6)	0.676(1)	23.68(7)
4U 1822-37	401051010	D(2612.16/2195)	0.28(3)	···	···	6.406(7)	0.04(2)	0.34(3)	47 ± 2	14.34(3)/24.77(4)	0.579(2)	0.993(4)
4U 1626-67	400015010	A(3393.54/2911)	0.01(1)	···	···	6.4(fixed)	0.0(fixed)	0.010(5)	5 ± 1	4.51(1)/6.94(1)	0.650(2)	4.47(2)
4U 1626-67	405044010	A(1241.23/1122)	0.05(1)	···	···	6.4(fixed)	0.0(fixed)	< 0.02	< 6	9.48(4)/16.64(5)	0.570(3)	12.0(1)
GX 1+4	405077010	D(512.07/257)	18.6(3)	···	···	6.422(4)	< 0.007	1.37(2)	144 ± 2	20.70(5)/34.0(1)	0.608(3)	8.94(5)
4U 1954+31	907005010	F(1301.11/1206)	1.65(3)	···	···	6.39(1)	< 0.06	0.10(1)	34 ± 3	5.40(2)/11.79(3)	0.458(2)	0.202(2)

Notes. The statical errors given here are for 90% confidence level.

[a] Applied model to fit the X-ray broadband spectra; Model A: NPEX, Model B: power-law multiplied `fdcut` (FPL), Model C: exponential cutoff power-law (CPL), Model D: blackbody plus exponential cutoff power-law (BB+CPL), Model E: blackbody plus broken power-law (BB+BPL), Model F: `compTT`. The photoelectric-absorption (`TBnew`) is included in all the spectral models. The detail model representation are listed in Table 5.1

[b] Equivalent hydrogen column densities (10^{22} H atoms cm^{-2}) estimated from the fully covering photoelectric absorption model.

[c] Equivalent hydrogen column densities (10^{22} H atoms cm^{-2}) estimated from the partially covering photoelectric absorption model.

[d] Covering fraction of the the partial covering photoelectric absorption model.

[e] Center energy of iron K_α line in unit of keV.

[f] Width of iron K_α line in unit of keV.

[g] Flux of iron K_α line in unit of 10^{-3} photons s^{-1} cm^{-2}.

[h] Equivalent width of iron K_α line in unit of eV.

[i] $F_{\rm h}$, $F_{\rm s}$, Unabsorbed X-ray photon fluxes (10^{-3} photons s^{-1} cm^{-2}) in range of 7.1–10 keV and 4.0–7.1 keV.

[j] HR η, calculated from the two unabsorbed photon fluxes.

[k] X-ray luminosity (10^{36} ergs s^{-1}) in a range of 0.5–100 keV. The ambiguities of distance to source from the observer are not included.

5.2 Phase-resolved Analysis

5.2.1 Selection of Sources

Following section, we describe phase-resolved analyses with seven selected sources. Based on the results of phase-averaged spectral analysis, we selected OAO 1657-415, 4U 1909+07, 4U 1907+097, 4U 1538-522, GX 301-2, Vela X-1, and GX 1+4, which indicate large EW ($>$ 50 eV) of iron K_α line (see Table 5.2). They belong to SGXBs, except for GX 1+4 which is categorized to be the LMXBs, or the SyXB. We found that Her X-1 has the large EW of iron K_α line. However we exclude it from the selected sources for the phase-resolved analysis, since the spin period of Her X-1 is shorter than the time resolution of the XIS operated with normal clock mode. The data of GX 301-2 observed in 2008 (ObsID=403044010) were also not used for phase-resolved analysis because of its short effective exposure time ($\sim$ 10 ks).

5.2.2 Pulse Period Determination

To search for pulsations in the light curves of the selected samples for the phase-resolved analysis, we performed standard epoch folding analysis (Leahy 1987) on the XISs and HXD-PIN data for each observation with `efsearch` task of FTOOLS. Our analysis revealed consistent barycentric pulsation periods, for all the samples, with the expected values from previous reports as listed in Table 5.3. Using the estimated pulse periods and the epochs, we calculated pulse profiles by applying `efold` task of FTOOLS. Energy-divided pulse profiles, obtained from background subtracted light curves in 0.5–2.0 keV 2.0–4.0 keV, 4.0–7.0 keV, 7.0–12.0 keV (data from all operated XISs added together), and 12.0–20.0 keV (HXD-PIN) ranges, are shown in top to bottom panels of Figure 5.69–5.76. The HXD-PIN data have been corrected for the dead time.

Table 5.3: Revealed barycentric pulsation period of samples for phase-resolved spectral analysis obtained from HXD-PIN data in *Suzaku* observation.

Source	ObsID	P(s)[a]	Epoch[b]
OAO 1657-415	406011010	36.96(3)	55830.4
4U 1909+07	405073010	603.5(9)	55502.7
4U 1907+097	401057010	441.4(4)	53857.3
4U 1907+097	402067010	441.4(4)	54209.4
4U 1538-522	407068010	525.9(9)	56149.0
GX 301-2	403044020	685.5(6)	54836.4
Vela X-1	403045010	283.45(2)	54634.2
GX 1+4	405077010	159.94(2)	55471.3

Notes.
[a] Pulse period obtained from HXD-PIN and XISs data in range of 12.0–70.0 keV, 0.5–10.0 keV, respectively. Quoted errors are statistical 1σ level.
[b] Epoch to fold the light curves with individual pulse period in MJD.

Energy-divided folded light curve of OAO 1657-415 plotted in Figure 5.69 shows that the profiles do not show any significant energy dependency, although feature of profile below 2.0 keV is obscure due to its large absorption at low energy band. Fürst et al. (2011a; 2012) reported that the pulse profile of 4U 1909+07 changes between 8 and 20 keV from

a two-peaked to a single peaked profile. We confirmed the same energy-dependency of the pulse profile with the *Suzaku* observation (see Figure 5.70). Energy-divided pulse profiles of 4U 1907+097 derived from two *Suzaku* observations, shown in Figures 5.71 and 5.72, indicate no obvious difference from each other. Both profiles exhibit a double-peak. A dimming after first peak is shallower than another, which occurs after second peak. We found that the second peak of 0.5–2.0 keV band shows a significant phase lag of ~ 0.2 than that of high energy band.

The pulse profile of 4U 1538-522 can be found in Figure 5.73. We confirmed the same profile as that reported by Hemphill et al. (2014) with same observational data. The profile shows an intense main peak flowing a weak secondary peak. The main peak is double-peaked at lower energies, becoming narrower and a complex feature as energy increases.

Energy divided folded light curves of GX 301-2 in January 2009, show a double peak, which are peaked at ~ 0.0 and ~ 0.7 in phase. The peak around phase ~ 0.0 becomes intense in its relative intensity toward higher energies. These results have already been reported by Suchy et al. (2012) with same data.

In case of Vela X-1, its pulse profiles have complex energy dependent structures. There are five peaks in low energy pulse profiles, which merge to two peaks in high energy band. The dips around 0.3–0.4 and 0.8–0.9 in phase silts up as the energy becomes higher. These characteristics of pulse profile have already been published in Maitra & Paul (2013b).

A gradual change in the pulse profile as the energy change of GX 1+4 can be clearly seen in Figure 5.76. The width of the dip was found to be increasing with energy as pointed out by Naik et al. (2005). Apart from the dip, a small hump was also seen at phase $\sim$0.1 in 12.0–20.0 keV range pulse profile. These characteristics of pulse profile have already been reported by Yoshida et al. (2017) with same observational data.

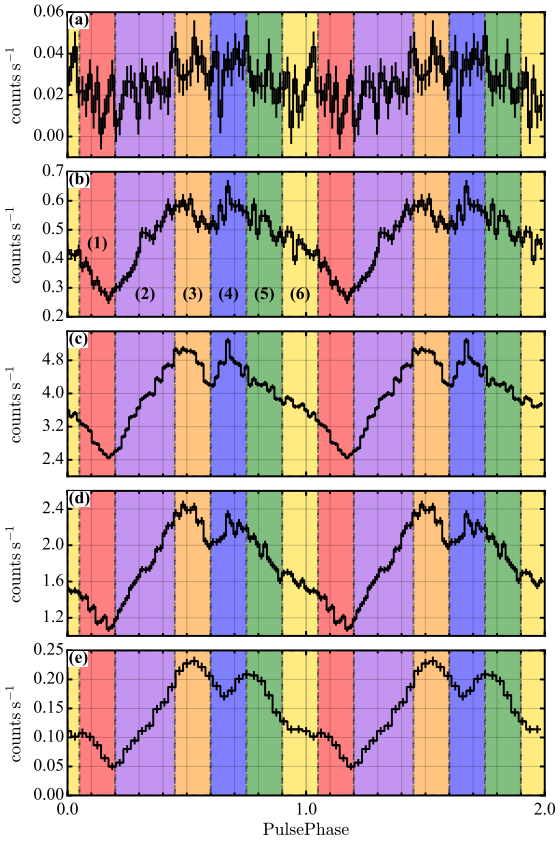

Figure 5.69: Energy-divided pulse profiles of OAO 1657-415 during whole observation. All the background subtracted data have been folded with a pulse period obtained with the *Suzaku*. From top to bottom panels ((a) to (e)), the energy bands are 0.5–2.0 keV, 2.0–4.0 keV, 4.0–7.0 keV, and 7.0–12.0 keV, with the XISs data summed of all the operating sensors, and 12.0–20.0 keV with the dead-time corrected HXD-PIN data. For phase-resolved spectroscopy described in § 5.2, the data are divided into six pulse phase intervals as indicated by quoted numbers and overlaying colors.

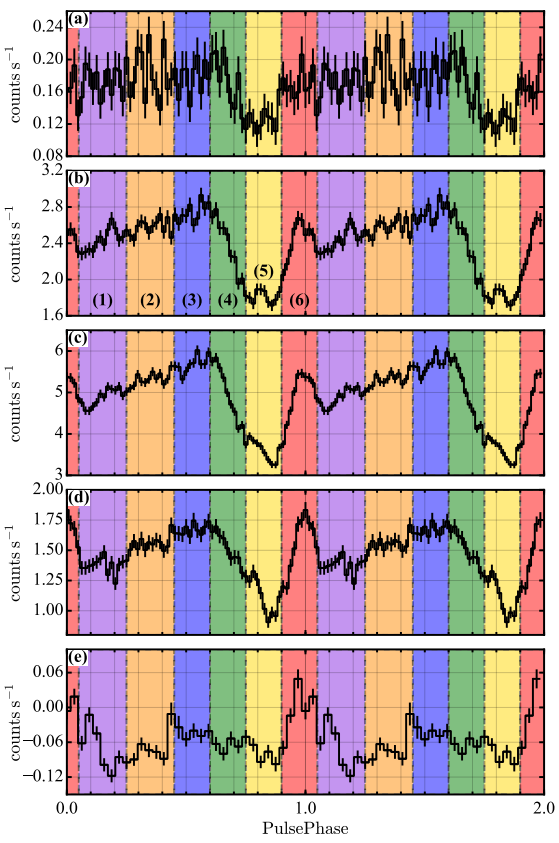

Figure 5.70: Same figure as Figure 5.69, but energy-divided pulse profiles of 4U 1909+07 during whole observation.

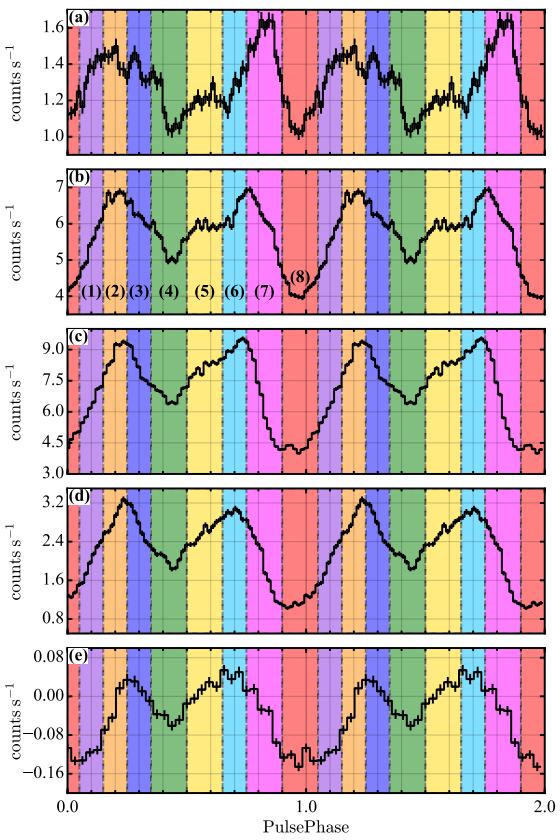

Figure 5.71: Same figure as Figure 5.69, but energy-divided pulse profiles of 4U 1907+097 (ObsID=401057010) during whole observation. For phase-resolved spectroscopy, the data are divided into eight pulse phase intervals as indicated by quoted numbers and overlaying colors.

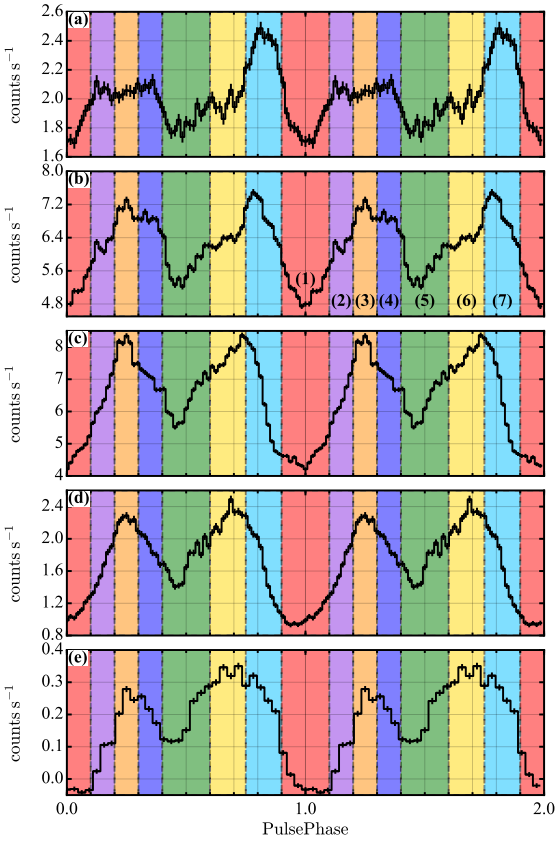

Figure 5.72: Same figure as Figure 5.69, but energy-divided pulse profile of 4U 1907+097 (ObsID=402067010) during whole observation. For phase-resolved spectroscopy, the data are divided into seven pulse phase intervals as indicated by quoted numbers and overlaying colors.

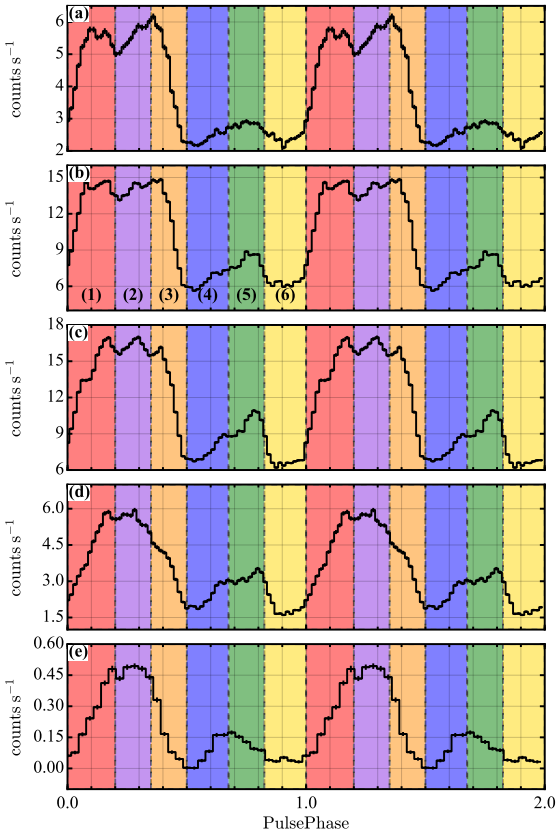

Figure 5.73: Same figure as Figure 5.69, but energy-divided pulse profiles of 4U 1538-522 during whole observation.

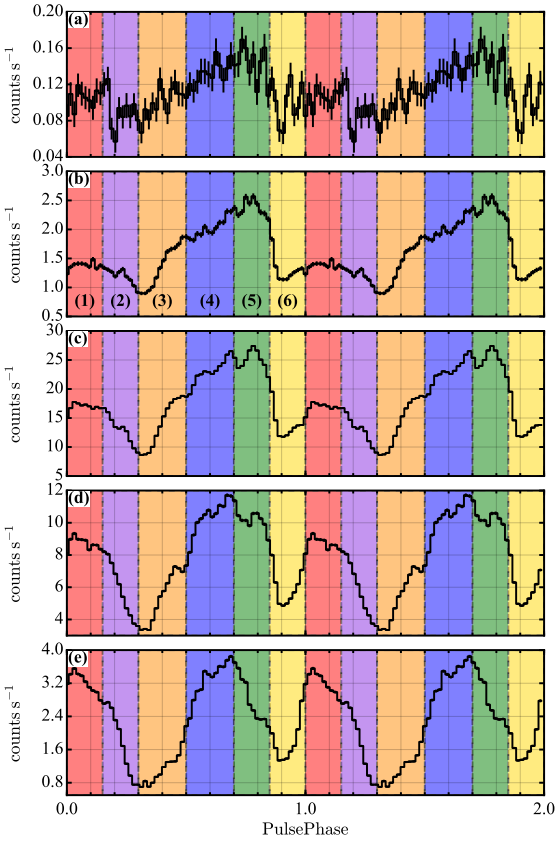

Figure 5.74: Same figure as Figure 5.69, but energy-divided pulse profiles of GX 301-2 (ObsID=403044020) during whole observation.

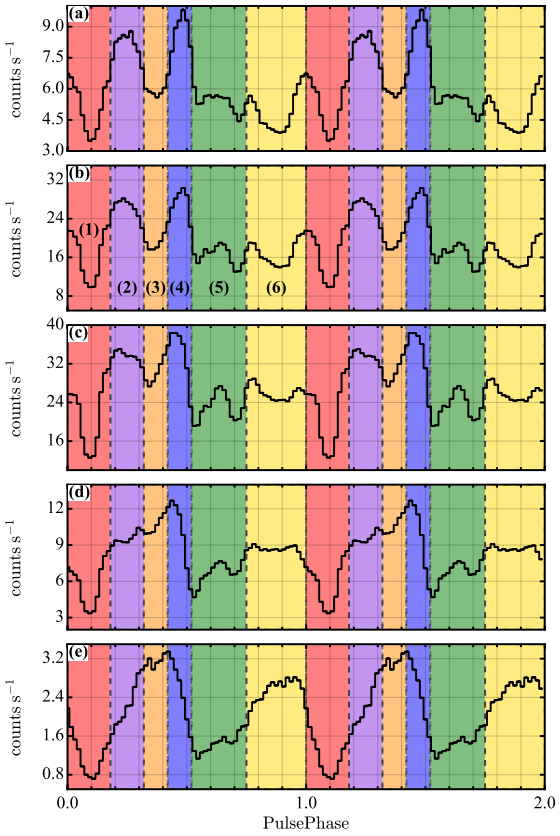

Figure 5.75: Same figure as Figure 5.69, but energy-divided pulse profiles of Vela X-1 during whole observation.

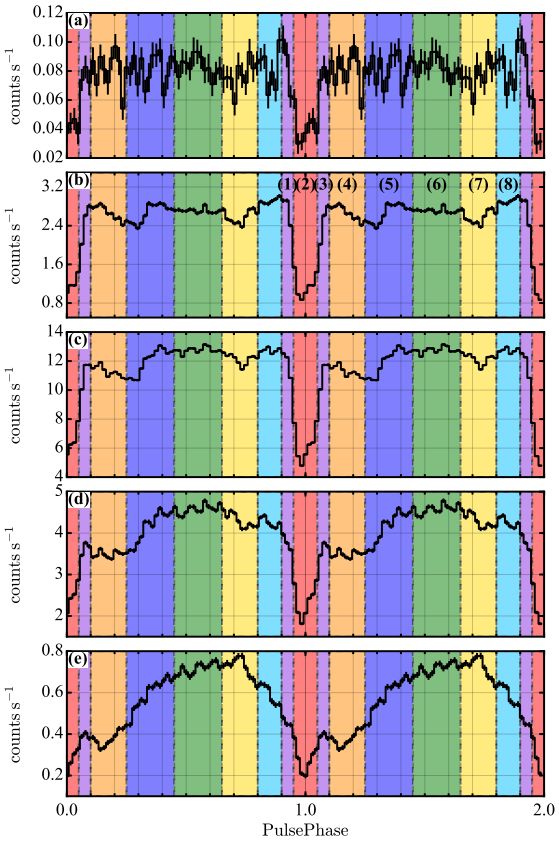

Figure 5.76: Same figure as Figure 5.69, but energy-divided pulse profile of GX 1+4 during whole observation. For phase-resolved spectroscopy, the data are divided into eight pulse phase intervals as indicated by quoted numbers and overlaying colors.

5.2.3 Spectral Fitting

To study the variation of the spectral shape according to the viewing angle onto the neutron star, i.e., the pulse phase, we divided the data into several phase bins, as indicated in Figure 5.69–5.76 with different colors. The bins were chosen to pick up various prominent features, e.g., the deep minimum and maximum peaks, as well as to retain a photon statistics sufficient to constrain the individual spectral parameters well. In case of GX 1+4, phase intervals 1 and 3 (marked in purple in the figure) were combined into one.

We fitted the broadband phase-resolved spectra with the same models as those used in the phase-averaged spectral fitting listed in Table 5.1. We found that the adopted model fitted all phase-resolved spectra well for the individual sources. In case of 4U 1907+097 and 4U 1538-522, a partial covering absorptions was not able to be significantly detected in some spectra due to the lower photon statistics, hence we only used a single photoelectric absorption. The 10 keV bump feature represented by Gaussian function, found in the phase-averaged spectra of 4U 1907+097, was unnecessary to express the phase-resolved spectra and we omitted from the fitting model. When phase-resolved spectra of 4U 1538-522 and GX 301-2 were fitted using the power-law with FDCO model, we fixed the cutoff energies at the best-fit value of the phase-averaged spectra, whereas the other parameters were remained to be free. In the fitting of 4U 1907+097, Vela X-1 and GX 1+4, Fe abundance of the absorber relative to ISM, $Z_{\rm Fe}$, was fixed at the value obtained from phase-averaged fitting.

The best-fit parameters of photoelectric absorption, $N_{\rm H}$, derived from broadband phase-resolved spectral fitting and calculated HR η, using best-fit phase-resolved spectral model are plotted as a function of the pulse phase in Figure 5.77–5.84. The folded light curves in the energy range of 0.5–7.1 keV and 7.1–12.0 keV are also shown in same figures. The photon index (of exponential cutoff power-law model, negative exponential cutoff power-law component in NPEX, and power-law with FDCO model) and the optical depth of the `compTT` model, derived from broadband phase-resolved spectral fitting, are also plotted on panel (A) in Figure 5.77–5.84 with blue markers. As seen in the figures, there are strong positive-correlations between the $N_{\rm H}$ and the photon index in 4U 1538-522, GX 301-2, Vela X-1, and GX 1+4, as well as negative-correlations between the $N_{\rm H}$ and the optical depth are shown in 4U 1907+097. These correlations suggest that the derived values influence on each other parameter and they are not physically meaningful values. For example, if the spectral shape is steep in the high energy band, the derived $N_{\rm H}$ value becomes high because the extrapolation to the low energy band of the steep spectra requires a large photoelectric absorption, without any evidence of justifying the extrapolation. If the $N_{\rm H}$ is a fake value, the K_α line intensity and the K-edge depth of the iron ions are also affected and we may derive wrong values.

For a robust analysis of the variation of emission lines and their related features with pulse phase without effects of low-energy absorption varying, we restricted the energy range to 5.8–7.8 keV for the spectral fitting. In this restricted region, the continuum can be fitted by a simple power-law model with an absorption edge so that we can deduce the edge parameter independently from the low-energy absorption. However, the large value of photoelectric absorption with $N_{\rm H}$ =10^{22}–10^{23} H atoms cm^{-2} affects the intensities of the emission lines, while variation of the hydrogen column density with pulse phase may lead

artificial variations in parameters of emission lines with pulse phase. So, we applied two model consisting of `powerlaw` × `edge` + `TBnew` × `gaussians` and `powerlaw` × `edge` + `gaussians` in XSPEC expression to fit the spectra in the restricted energy range. In some spectra, photoelectric absorption (`TBnew`) was required in the broadband fitting and then we applied the same amount of the absorption to the Gaussian functions for emission lines, but the values of equivalent hydrogen column density $N_{\rm H}$ were fixed at the values obtained from each phase-resolved broadband fitting. We fixed the ratios of the energies of the iron K_β and the iron K-edge to that of the iron K_α line at 1.103 and 1.119, respectively, in case of 4U 1909+07, 4U 1907+097, and 4U 1538-522. In the case of OAO 1657-415, GX 301-2, Vela X-1, and GX 1+4, the energy of the iron K-edge was allowed to vary, although the ratio of the energy of the iron K_β line to that of the iron K_α line at above value, because these sources show apparent absorption edge of iron in the spectra without any spectral model fitting. In our phase-resolved fitting, the widths of the emission lines were fixed to be narrow enough according to the results of the phase-averaged spectroscopy. Note that, for our broadband spectroscopy, we used only the FI CCDs in case of OAO 1657-415, GX 301-2, and GX 1+4, because of a discrepancy between the FI and BI CCDs in the low-energy region (below 3 keV). However, in the above-restricted narrow energy range, the discrepancy between the FI and BI CCDs is negligibly small. Therefore, we used data from all the CCDs for the analysis of emission lines and related features in all our samples.

Parameters obtained from our spectral fitting are plotted as function of pulse phase in Figure 5.77–5.84. The energies of the iron line were found to remain constant within their errors in all the sources. In Figures 5.77 (OAO 1657-415), 5.77 (GX 301-2), 5.77 (Vela X-1), and 5.77 (GX 1+4), the calculated ratios of energy of iron K-edge to that of the iron K_α line, which remained as a free parameter in their fitting, are plotted and we confirmed that the values are constant within their errors over pulse phase. Averaged values of the energy ratios of all of the four sources are in range of 1.117–1.122, which indicates ionization state of the iron is $\rm Fe_{II–III}$. Marginal increasing of energy of the iron K-edge at the phase when iron K-edge indicates the maximum depth in GX 1+4 is notable. We also confirmed that the assumed ratio of energy of iron K_α line to that of the iron K_β line in the fitting are consistent with this ionization state. Except for OAO 1657-415, enhancements of the equivalent width of the iron K_α line at the interval dimming of continuum flux were notable. Especially, in case of Vela X-1 and GX 1+4, these enhancements at narrow dip intervals are clear. In the Figure 5.78–5.84, we can find that the iron K_α line fluxes of 4U 1907+097, 4U 1909+07, 4U 1538-522, GX 301-2, Vela X-1, and GX 1+4 exhibit modulations with pulse phase. These iron line flux modulation in 4U 1907+097, 4U 1909+07, 4U 1538-522, and GX 1+4 with same *Suzaku* observations have been reported by Rivers et al. (2010), Fürst et al. (2012), Hemphill et al. (2014), and Yoshida et al. (2017), respectively, whereas in GX 301-2 Suchy et al. (2012) argued that the line flux did not change significantly throughout the pulse phase with the same Suzaku observation, although there is a tendency toward higher fluxes around phase 0.6–1.0, with an amplitude of ∼10%. The depths of the iron K-edge increase at the phase when the X-ray continuum fluxes become dim, such as the dip for all of 4U 1538-522, GX 301-2, Vela X-1, and GX 1+4.

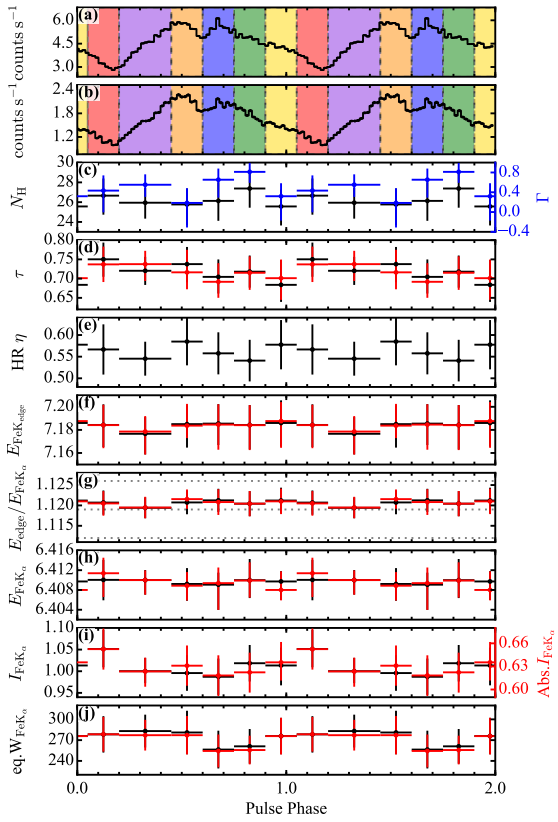

Figure 5.77: Results of phase-sliced spectroscopy in *Suzaku* data of OAO 1657-415 during whole observation. Energy resolved, back-ground subtracted epoch folded light curves of OAO 1657-415 in range of 0.5–7.1 keV (a) and 7.1–12.0 keV (b). The spectral parameters are also plotted as a function of pulse phase. The parameters shown in each of the panels are described as follows; (c) equivalent hydrogen column density $N_{\rm H}$ (in 10^{22} H atoms cm^{-2}) overlaid photon index of the exponential cutoff power-law component with blue, (d) depth of iron K-edge, (e) HR η, (f) energy ratios of the iron K$_\alpha$ line to the iron K-edge, (g) center energies of the iron K$_\alpha$ line (in keV), (h) absorbed (red) and unabsorbed (black) fluxes of the iron K$_\alpha$ line (in 10^{-3} photons s^{-1} cm^{-2}) (i) EW of the iron K$_\alpha$ line (in eV). The vertical axes on the right of (c) and (g) panels indicate the photon index of the exponential cutoff power-law component and absorbed iron K$_\alpha$ emission line respectively. Red-colored plots are the values obtained from the fitting without applying photoelectric absorption (`TBnew`) to the Gaussian functions. The horizontal gray dotted-lines in panel (f) indicate the energy ratios in cases of Fe$_{\rm I}$, Fe$_{\rm II}$, and Fe$_{\rm III}$ (in order from down to up in the panel). Two cycles are shown for clarity. The errors shown here are for 90% confidence limits.

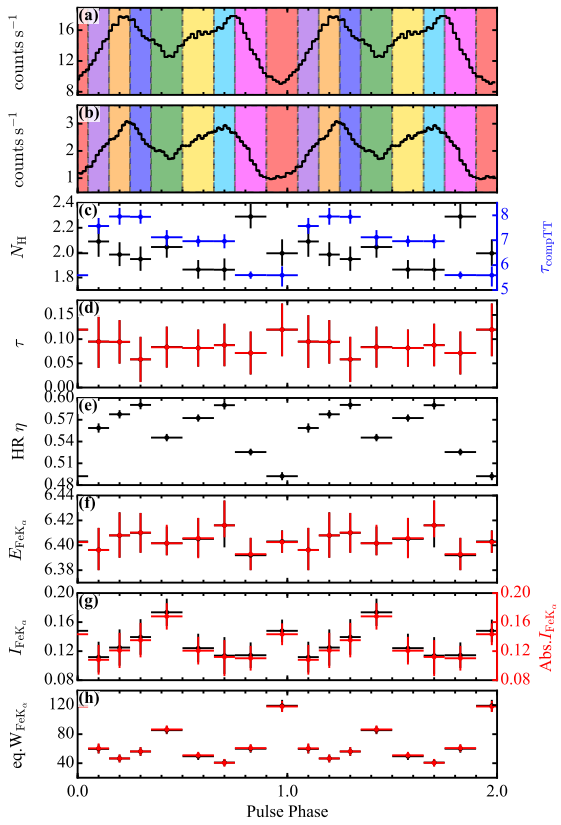

Figure 5.78: Results of phase-sliced spectroscopy in *Suzaku* data of 4U 1907+097 (ObsID=401057010) during whole observation. Energy resolved, back-ground subtracted epoch folded light curves of 4U 1907+097 in range of 0.5–7.1 keV (a) and 7.1–12.0 keV (b). The spectral parameters are also plotted as a function of pulse phase. The parameters shown in each of the panels are described as follows. (c) equivalent hydrogen column density $N_{\rm H}$ (in 10^{22} H atoms cm^{-2}) overlaid optical depth of the `compTT` with blue (d) depth of iron K-edge (e) HR η (f) center energies of the iron K$_\alpha$ line (in keV), (g) absorbed (red) and unabsorbed (black) fluxes of the iron K$_\alpha$ line (in 10^{-3} photons s^{-1} cm^{-2}) (h) EW of the iron K$_\alpha$ line (in eV). The vertical axes on the right of (c) and (g) panels indicate the optical depths of the `compTT` model and absorbed iron K$_\alpha$ emission line fluxes, respectively. Red-colored plots are the values obtained from the fitting without applying photoelectric absorption (`TBnew`) to the Gaussian functions. Two cycles are shown for clarity. The errors shown here are for 90% confidence limits.

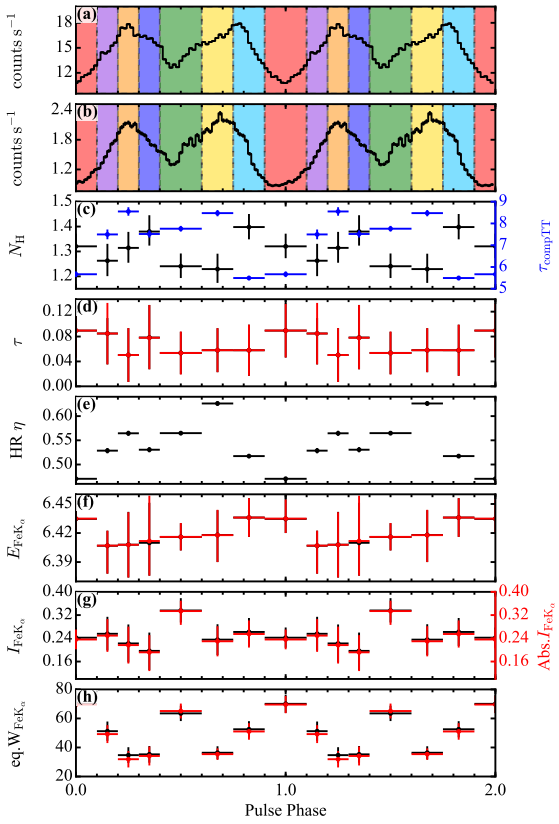

Figure 5.79: Same figure as Figure 5.78, but in *Suzaku* data of 4U 1907+097 (ObsID=402067010) during whole observation.

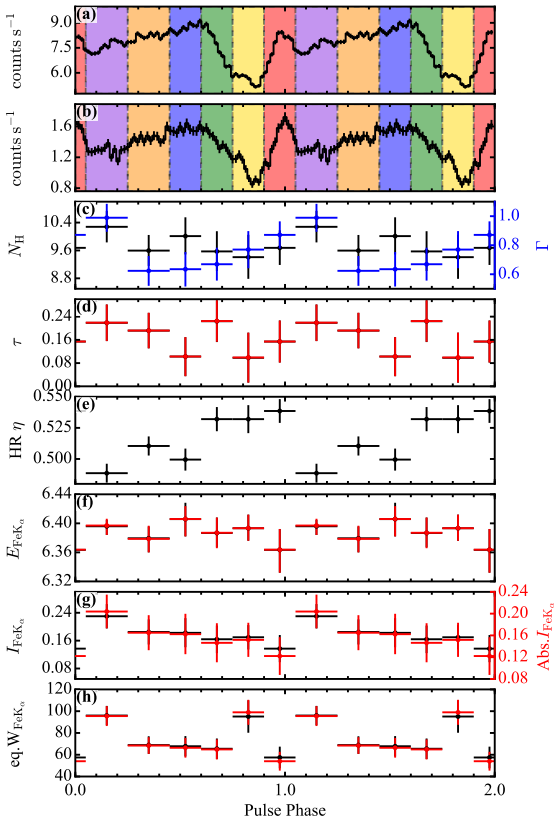

Figure 5.80: Same figure as Figure 5.78, but in *Suzaku* data of 4U 1909+07 during whole observation. The vertical axis on the right of (c) panel indicates the photon index of the exponential cutoff power-law component.

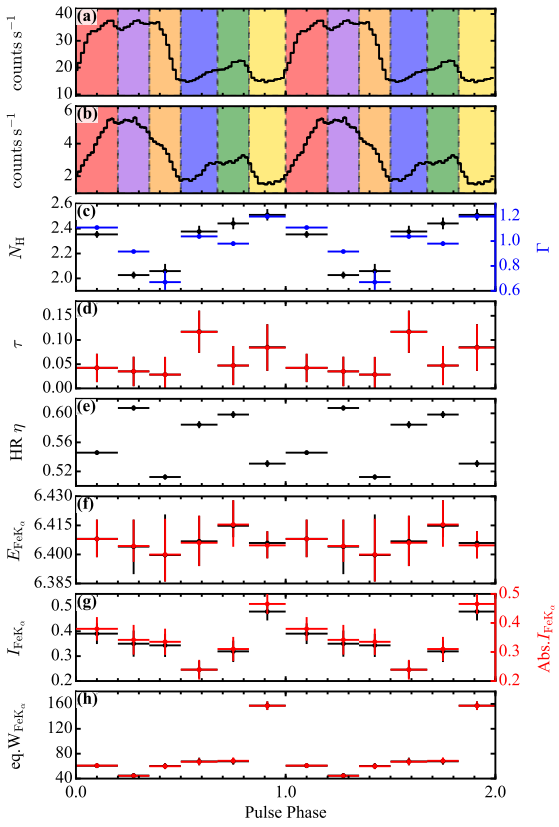

Figure 5.81: Same figure as Figure 5.78, but in *Suzaku* data of 4U 1538-522 during whole observation. The vertical axis on the right of (c) panel indicates the photon index of the power-law multiplied `fdcut` model.

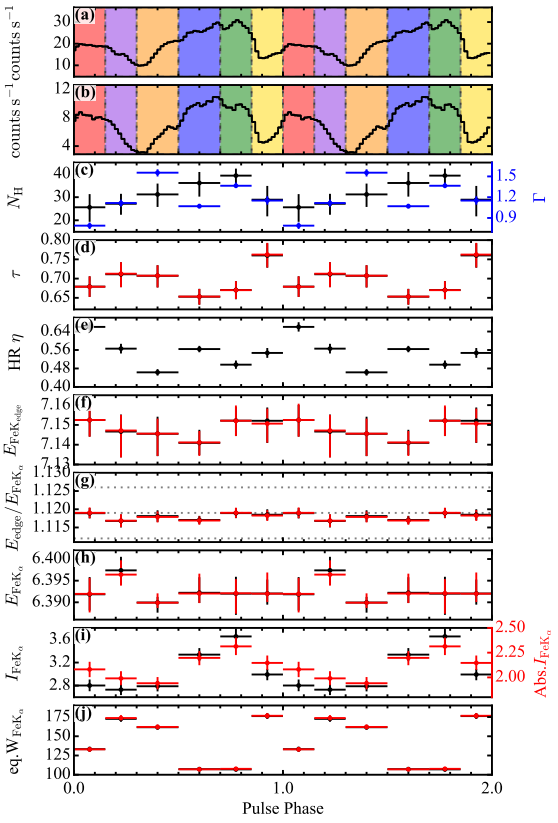

Figure 5.82: Same figure as Figure 5.77, but in *Suzaku* data of GX 301-2 (ObsID=403044020) during whole observation.

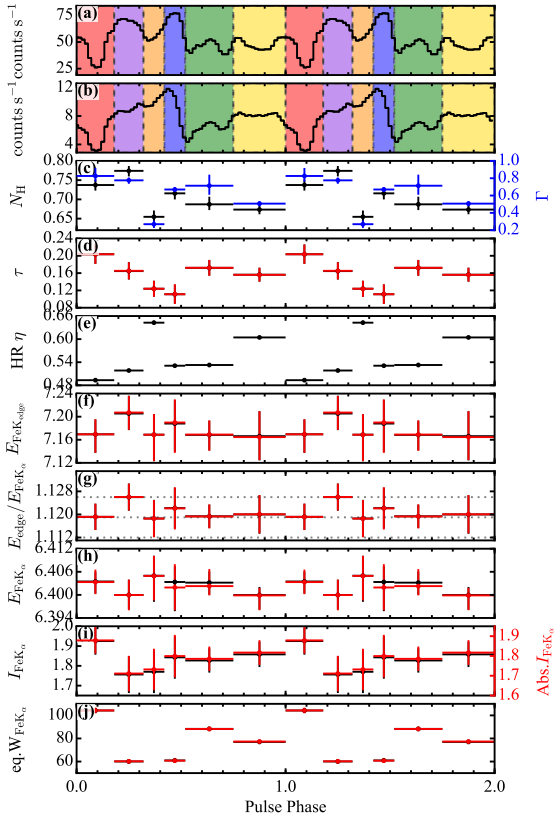

Figure 5.83: Same figure as Figure 5.77, but in *Suzaku* data of Vela X-1 during whole observation.

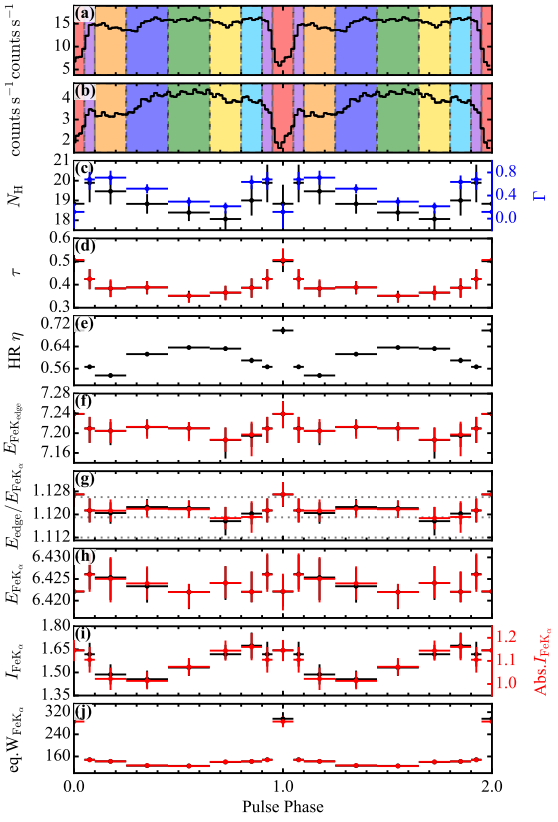

Figure 5.84: Same figure as Figure 5.77, but in *Suzaku* data of GX 1+4 during whole observation.

5.2.4 Investigating Statistical Significance of Variations

In some sources, modulations of the iron K_α line flux or the depth of iron K-edge can be seen in the figures as stated above. We performed χ^2 tests to investigate their significance of the modulation with pulse phase, and yielded χ^2 values and corresponding statistically significance with null hypothesis probabilities are summarized in Table 5.4. The results of above χ^2 test indicated that the modulation of line flux with pulse phase in GX 301-2, 4U 1538-522, 4U 1907+097, and GX 1+4 are statistically significant, while constant fittings to the depth of the iron K-edge in GX 301-2, Vela X-1, and GX 1+4 gave χ^2 values of 26, 36, and 44, for 5, 5, and 8 d.o.f., respectively, which clearly demonstrate the significance of the depth modulations with pulse phase.

Table 5.4: Results of χ^2 tests to investigate the modulation in the iron K_α line intensity and the depth of iron K-edge with pulse phase.

Source	ObsID	Statistically values					
		I_{FeK_α} [a]		Abs.I_{FeK_α} [b]		τ [c]	
		χ^2/d.o.f.	Probability	χ^2/d.o.f.	Probability	χ^2/d.o.f.	Probability
OAO 1657-415	406011010	4.45/5	4.86×10^{-1}	3.85/5	5.71×10^{-1}	2.45/5	7.46×10^{-1}
4U 1909+07	405073010	9.59/5	8.77×10^{-2}	9.44/5	9.28×10^{-2}	8.22/5	1.50×10^{-1}
4U 1907+097	401057010	23.35/7	1.48×10^{-3}	23.52/7	1.38×10^{-3}	2.49/7	9.30×10^{-1}
4U 1907+097	402067010	13.61/7	5.87×10^{-2}	13.72/7	5.64×10^{-2}	3.17/7	8.69×10^{-1}
4U 1538-522	407068010	62.65/5	$< 1 \times 10^{-10}$	64.93/5	$< 1 \times 10^{-10}$	9.56/5	8.28×10^{-2}
GX 301-2	403044020	133.70/5	$< 1 \times 10^{-10}$	46.43/5	7.41×10^{-9}	26.38/5	2.64×10^{-4}
Vela X-1	403045010	7.89/5	1.63×10^{-1}	7.86/5	1.64×10^{-1}	35.72/5	3.24×10^{-6}
GX 1+4	405077010	33.37/8	5.27×10^{-5}	34.92/8	2.76×10^{-5}	44.34/8	1.88×10^{-7}

Notes.
[a] The values for the flux of iron K_α line obtained from the fitting with model applied the photoelectric absorption (`TBnew`) to the Gaussian functions.
[b] The values for the flux of iron K_α line obtained from the fitting without applying photoelectric absorption (`TBnew`) to the Gaussian functions.
[c] The values for the depth of iron K-edge obtained from the fitting without applying photoelectric absorption (`TBnew`) to the Gaussian functions.

To further inspect the significance of the modulations in line flux and edge depth, we have made a direct comparison of the spectra extracted in the different phase bins. In Figure 5.85, we plotted phase-resolved spectra divided by a power-law model with photon index of 2.0 of GX 301-2, Vela X-1, and GX 1+4. In the same figure, the best-fit models are overlaid, which were obtained from phase-resolved fitting with the restricted range and also divided by the power-law model. For clarity, we selected two phase-resolved spectra so as to become the maximum difference of the depth. The spectral ratios clearly show the depth differences of the iron K-edge around 7.3 keV in all sources. Figure 5.86 shows phase-resolved spectra 4U 1907+097, 4U 1538-522, GX 301-2, and GX 1+4, which are the spectra after the best-fit continuum model derived from phase-averaged broadband fitting have been subtracted. In this figure, phase-resolved spectra of two phase bins, when the iron K_α emission line indicates maximum and minimum fluxes, are plotted. The flux differences of the iron K_α line can be seen obviously in all sources. For 4U 1907+097, 4U 1538-522, GX 301-2, and GX 1+4, we also calculate the iron line flux modulation amplitudes as $A = (I_{\mathrm{max}} - I_{\mathrm{min}})/(I_{\mathrm{max}} + I_{\mathrm{min}})$, where I_{max} and I_{min} are the maximum and minimum iron line fluxes and summarize them in Table 5.5.

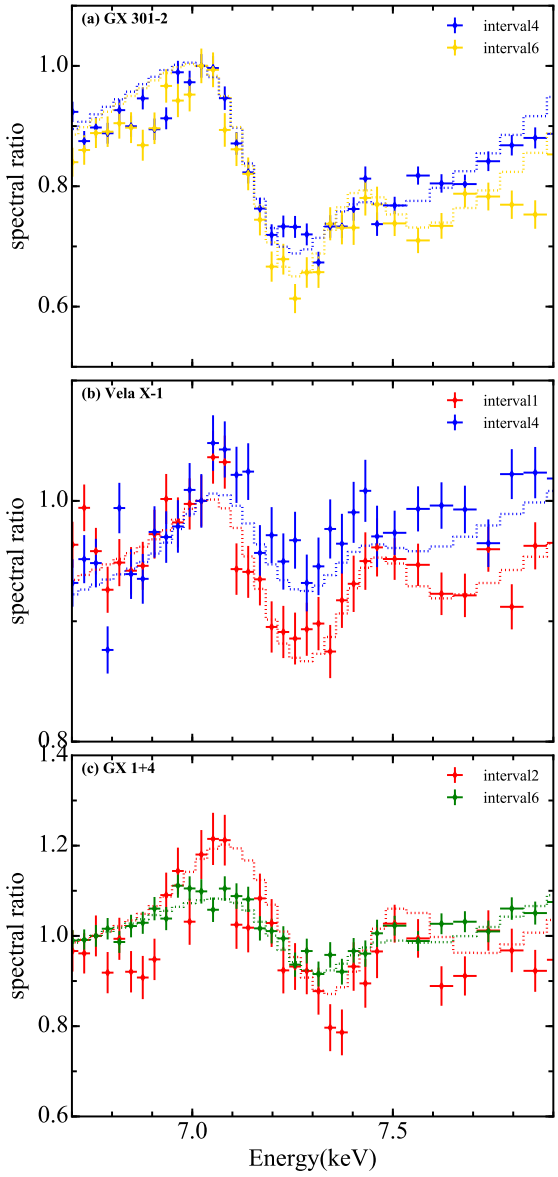

Figure 5.85: Ratios of phase-resolved spectra normalized by a power-law model with photon index of 2.0. Source names are indicated in each panel with quoted alphabets. Different colors in each panel correspond to the colors indicated in Figure 5.74 (GX 301-2), 5.75 (Vela X-1), and 5.76 (GX 1+4), respectively.

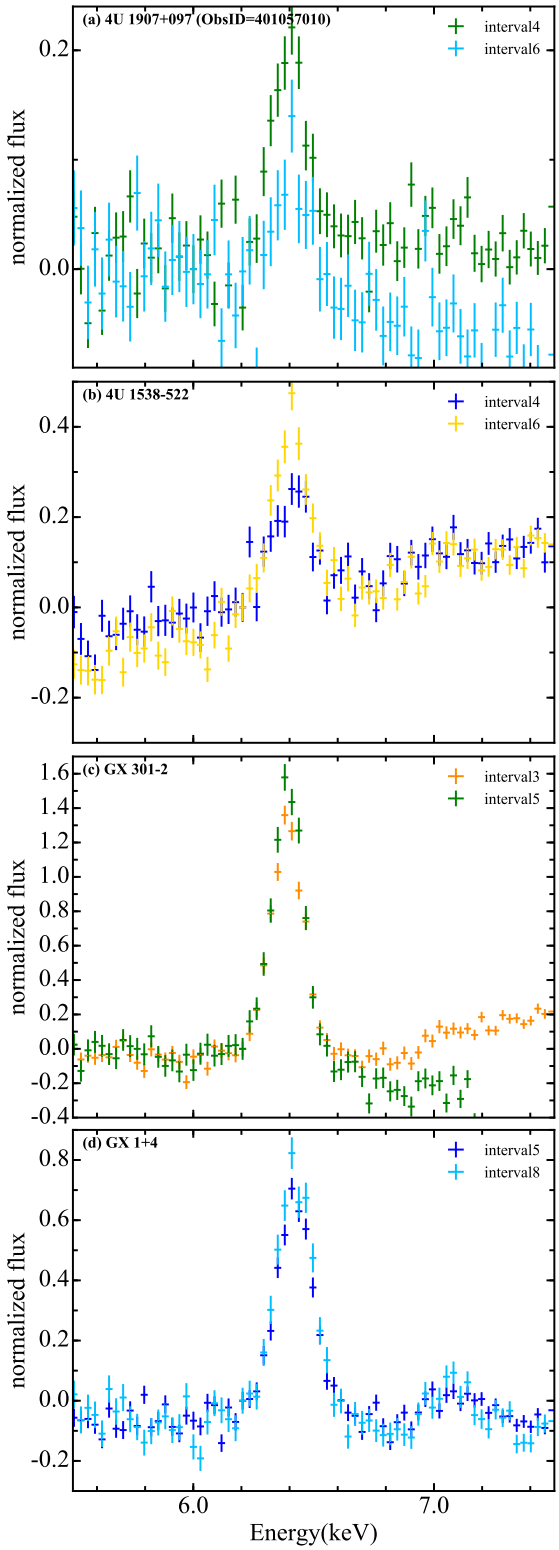

Figure 5.86: Phase-resolved spectra subtracted the best-fit continuum model of phase-averaged broadband fitting. Individual spectra are shown with offsets to make it easier to compare difference of each other. Source names are indicated in each panel with quoted alphabets. Difference colors in each panel correspond to the colors indicated in Figure 5.71 (4U 1907+097), 5.73 (4U 1538-522), 5.74 (GX 301-2), and 5.76 (GX 1+4), respectively.

Table 5.5: The amplitude of the iron line flux modulation with pulse phase.

Source	A^{a}
4U 1907+097	0.21 ± 0.09
4U 1538-522	0.31 ± 0.04
GX 301-2	0.13 ± 0.01
GX 1+4	0.07 ± 0.01

Notes.
[a] The errors are given here are for 1σ confidence limits.

In particular, we have also made a direct comparison of the spectra extracted above two pulse-phases to demonstrate the modulations of the depth of edge. Panels (a) of Figure 5.87–5.89 show spectral ratios between the two spectra, which show the maximum difference in depth of the edge. In the spectral ratios, edge features can be seen around 7.1 keV and excesses exhibit at 6.4 keV and 7.5 keV, which result from iron K_α line and nickel K_α line, respectively. The emission line at 6.4 keV in the spectral ratio can be represented by a Gaussian function in the model fitting, whereas it is difficult to reproduce the emission line at 7.5 keV in the spectral ratio due to the feature being obscure. However, the emission line at 7.5 keV prevents us from accurate estimation of the depth of the edge-like feature in the spectral ratio. We therefore fitted the spectral ratios in 5.0–8.4 keV range with both including and excluding the range around the emission line at 7.5 keV. In panels (b) of each the figures, the spectral ratios excluded the emission line at 7.5 keV are plotted. We employed following a liner function multiplied by $M(E)$ function representing the edge feature (e.g. `edge` in XSPEC; see Equation 2.23) as a model in the fitting of spectral ratio;

$$R(E) = (AE + B) \times M(E) + G(E), \tag{5.4}$$
$$M(E) = \begin{cases} 1 & (E < E_{\rm c}) \\ \exp\left(-D\left(\frac{E}{E_{\rm c}}\right)^{-3}\right) & (E \geqslant E_{\rm c}) \end{cases}$$

where A is a slope, B is an intercept, $G(E)$ is a Gaussian function to express the iron K_α line, energy, and D is a depth of the edge in spectral ratio. The parameter of D roughly corresponds to the difference of the iron K-edge depth between the two phase-resolved spectra. In our fitting of the spectral ratio, the edge energy was scanned from 7.11 to 7.50 keV with a step of 1 eV. The best-fit model obtained from fitting with each data set are plotted in panel (a) and (b), and residuals of each data-set from the best-fit model are plotted in panel (c) and (d) of the figures. In panel (e) and (f) of the figures, residuals of each data-set from the best-fit model, without the edge component, are also plotted, in which the residuals exhibit absorption edge features around 7.1 keV. The resultant χ^2 values and corresponding statistical significance with null hypothesis probabilities are summarized in Table 5.6. These values indicate improvements in the fitting of the spectral ratios with introducing the edge component in all of sources. The depths of edge feature D derived from the fitting of spectral ratio are listed in Table 5.6. For comparison, the maximum variation of the depth of iron

K-edge $\Delta\tau$ obtained from the phase-resolved spectral fitting are also listed in same table. In all sources, the values of $\Delta\tau$ are consistent with the values of D obtained from the fitting with ignoring the range contained the emission line at 7.5 keV within their errors.

Table 5.6: Results of fitting spectral ratios around iron K-edge.

Source	ObsID	Nickel [a]	without edge		with edge			$\Delta\tau$[b]
		K_α Line	χ^2/d.o.f.	Probability	χ^2/d.o.f.	Probability	D	($\tau_{\rm max} - \tau_{\rm min}$)
GX 301-2	403044020	I	98.43/53	1.51×10^{-4}	81.58/52	5.46×10^{-3}	0.06 ± 0.02	0.11 ± 0.02
		E	83.87/46	5.46×10^{-4}	59.16/45	7.65×10^{-2}	0.10 ± 0.02	
Vela X-1	403045010	I	90.68/53	9.77×10^{-4}	64.93/52	1.07×10^{-1}	0.06 ± 0.02	0.09 ± 0.01
		E	87.32/48	4.50×10^{-4}	58.78/47	1.16×10^{-1}	0.07 ± 0.02	
GX 1+4	405077010	I	93.91/53	4.56×10^{-4}	66.32/52	8.76×10^{-2}	0.12 ± 0.03	0.16 ± 0.04
		E	84.36/47	6.72×10^{-4}	48.46/46	3.74×10^{-1}	0.18 ± 0.03	

Notes.
[a] Handling of the data around the nickel line. I and E mean that the data in the energy range is included or not.
[b] Difference between two depths of the iron K-edge obtained from the spectral fitting of the two phase-resolved spectra which are used to calculate the spectral ratio.

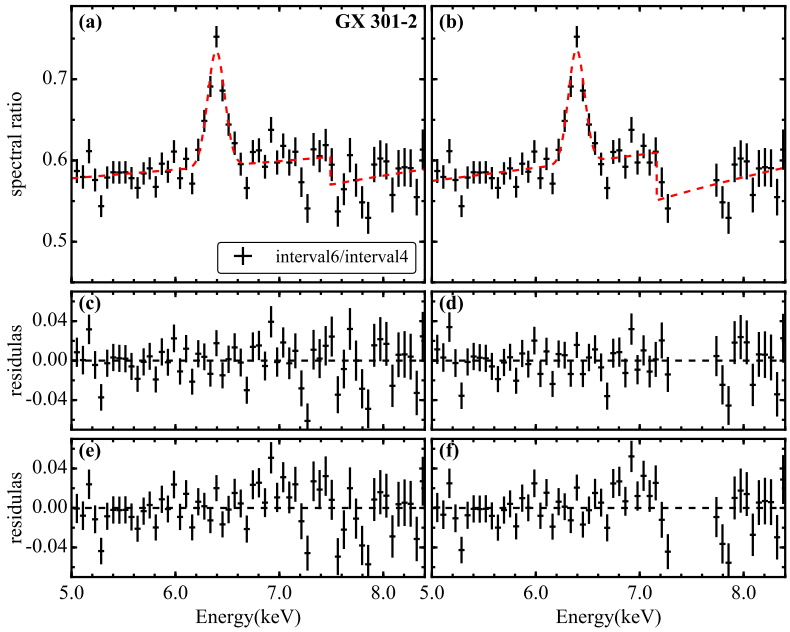

Figure 5.87: Spectral ratio between two phase-resolved spectra and results of the fitting of GX 301-2 (ObsID=403044020) with data during whole observation. (a) Spectral ratio between two phase-resolved spectra with best-fit model of Equation 5.4. (b) Same as panel (a), but data set is ignored the range around the emission line at 7.5 keV. (c)(d) Residuals from the best-fit model in panel (a) and (b), respectively. (e)(f) Same as panel (c) and (d), respectively, but the model is not employed the edge component.

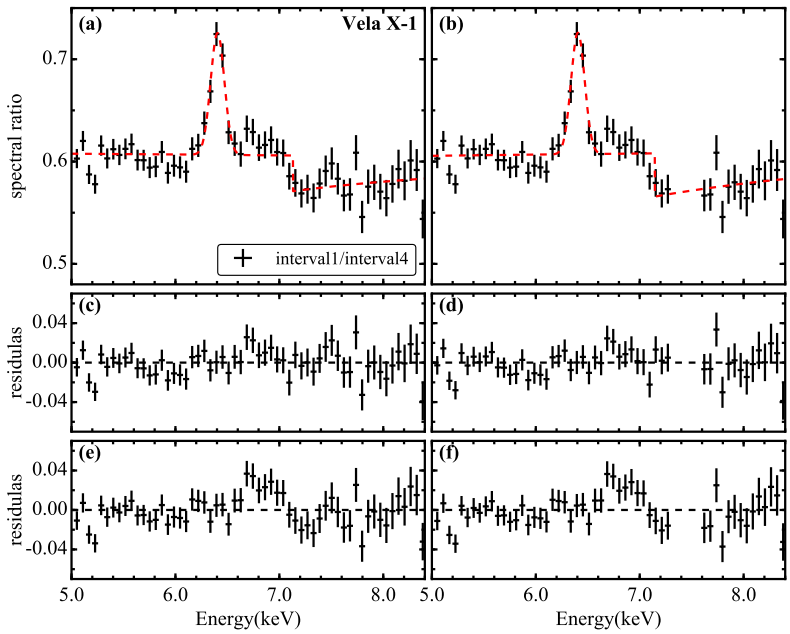

Figure 5.88: Same figure as Figure 5.87, but results of Vela X-1 with data during whole observation.

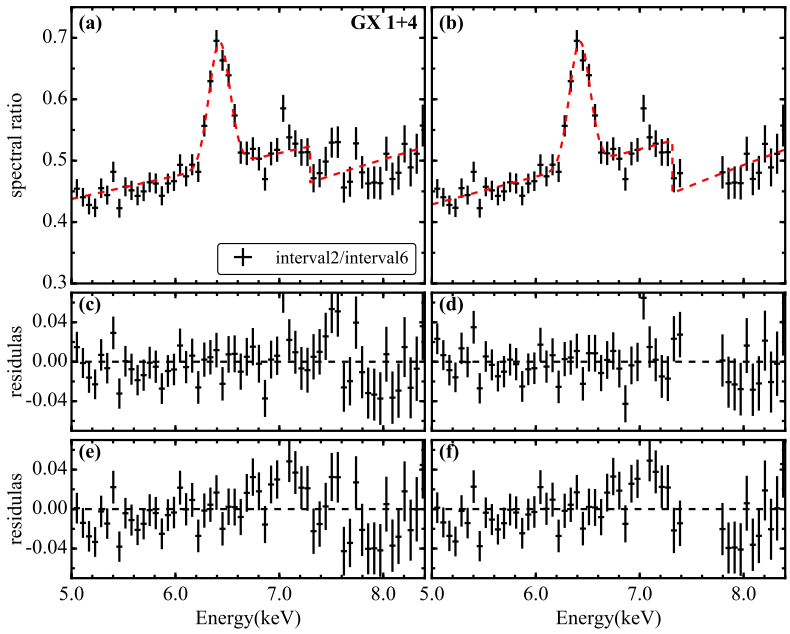

Figure 5.89: Same figure as Figure 5.87, but results of GX 1+4 with data during whole observation.

5.3 Phase-resolved Analysis with High Intensity State Data

In our phase-resolved analysis of OAO 1657-415 (see § 5.2.3), there is no significant modulations of line flux or depth of edge, where we used the spectra extracted from whole observation data. The light curve of OAO 1657-415 obtained from the *Suzaku* observation in Figure 4.18 shows prominent change in its intensity during the observation. The low intensity period lasted during the first $\sim 1.3 \times 10^5$ s, and subsequently the high intensity period followed for $\sim 6 \times 10^4$ s. If a pulse-phase modulation appears only in either the low intensity or the high intensity period and we analyze whole data as described above section, the modulation is diluted and we may miss the detection of the modulation. Therefore, we extracted events from the data obtained from last $\sim 5 \times 10^4$ seconds of the observation, when the source indicated high intensity. The selected time interval is indicated in Figure 4.18 by green-dotted horizontal lines.

5.3.1 Pulse Profiles

Using the events extracted from the XISs and HXD-PIN data in the high intensity period, we searched the pulsation with the epoch folding technique, and pulse period of $P = 36.96 \pm 0.03$ s at an epoch of 55830.43 MJD in this time interval was determined. The light curves derived from XISs and HXD-PIN in the selected high intensity period were folded with the determined pulse period. The epoch folded light curves subtracted appropriate background in 0.5–2.0 keV 2.0–4.0 keV, 4.0–7.0 keV, 7.0–12.0 keV (data from all operated XISs added together), and 12.0–20.0 keV (HXD-PIN) are shown in top to bottom panels of Figure 5.90.

The pulse profiles are roughly sinusoidal and very similar to the pulse profiles obtained from folding the light curve of whole observation (see Figure 5.69). However, amplitudes of 40–50% of the pulse profiles in all energy bands are larger than those obtained from whole observation, whose amplitudes are $\sim 30\%$ in all energy bands.

5.3.2 Spectral Parameter Variations with Pulse Phase

To study variations of spectral parameters along with the pulse period, the pulse profiles were divided into six bins, as indicated in Figure 5.90, and we extracted spectra in each phase bin from the data during the selected high intensity period. Only the XISs spectra are analyzed, because the HXD data are not statistically enough due to the short exposure time. We fitted the phase-resolved spectra, by restricting the energy range in 5.8–7.8 keV, with a model consisting of `powerlaw`×`edge`+`gaussians` in XSPEC expression. This spectral fitting is good enough to investigate variations with pulse phase of iron emission line and K-edge, in particular line flux and depth of absorption edge. However, as center energies of iron K_β and nickel K_α line were poorly constrained due to low effective exposure in each phase bin, the ratio of their energies were fixed to that of the iron K_α line at 1.103 and 1.168, respectively. The widths of the emission lines were fixed to be narrow enough, whereas the energy of the iron K-edge remained as a free parameter as the same in § 5.2.3. We show obtained

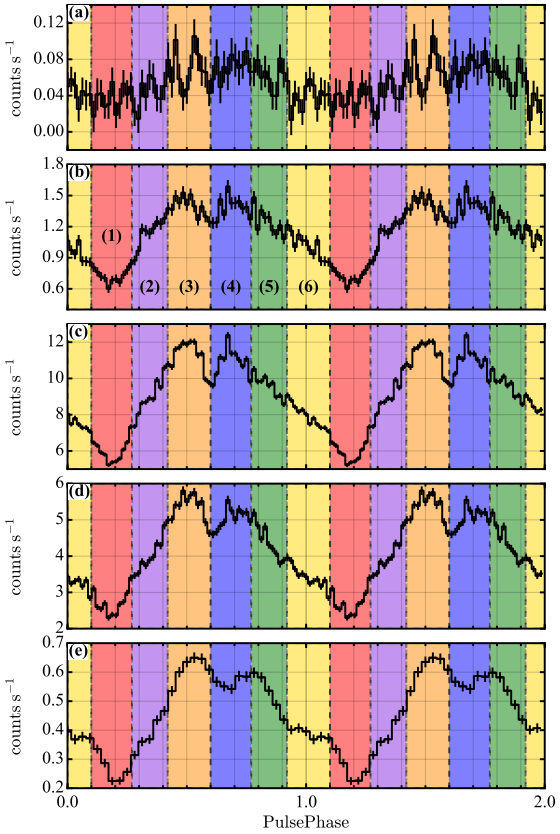

Figure 5.90: Same figure as Figure 5.69, but energy-divided pulse profiles during the selected time interval.

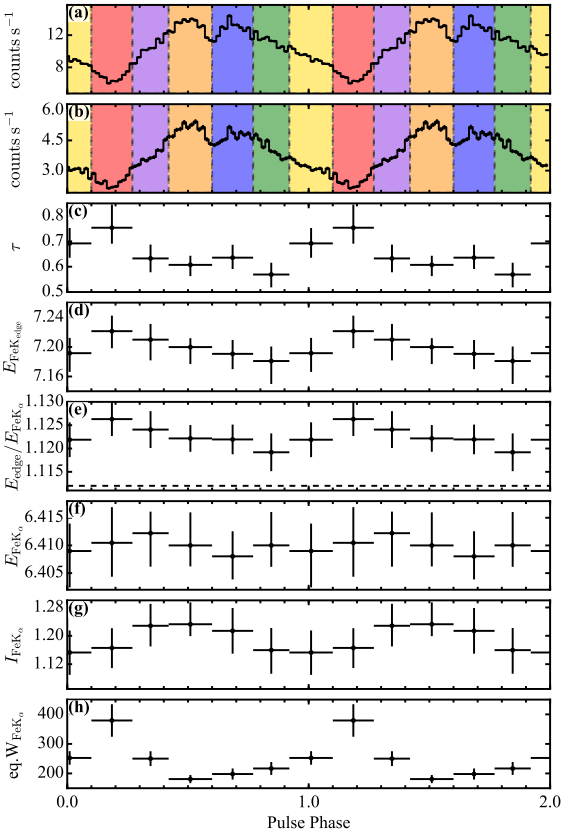

Figure 5.91: Results of phase-sliced spectroscopy in *Suzaku* data of OAO 1657-415 during selected time interval. Energy resolved, back-ground subtracted epoch folded light curves of OAO 1657-415 in range of 0.5–7.1 keV (a) and 7.1–12.0 keV (b). The spectral parameters are also plotted as a function of pulse phase. The parameters shown in each of the panels are described as follows. (c) depth of the iron K-edge (d) energy ratios of the iron K$_\alpha$ line to the iron K-edge (e) center energies of the iron K$_\alpha$ line (in keV), (f) absorbed fluxes of the iron K$_\alpha$ line (in 10^{-3} photons s^{-1} cm^{-2}) (g) EW of the iron K$_\alpha$ line (in eV). The horizontal gray dotted-lines in panel (d) indicate the energy ratios in cases of Fe$_{\mathrm{I}}$, Fe$_{\mathrm{II}}$, and Fe$_{\mathrm{III}}$ (in order from down to up in the panel). Two cycles are shown for clarity. The errors shown here are for 90% confidence limits.

spectral parameters of OAO 1657-415 with pulse phase in Figure 5.91. In Figure 5.91, the energies of the iron line were found to remain constant within their errors, while the energies of the iron K-edge seem to correlate with the depth of iron K-edge. The iron K_α line fluxes and the depth of iron K-edge exhibit modulations with pulse phase, although the errors are large. We performed χ^2 tests to investigate the significance of the their modulations. The obtained χ^2 values indicate statistical significance with null hypothesis probabilities summarized in Table 5.7. We found that modulation of the iron K-edge depth with pulse phase of OAO 1657-415 in the high intensity period is statistically significant.

Table 5.7: Results of χ^2 tests to investigate the modulation in the iron K_α line intensity and the depth of iron K-edge with pulse phase.

Source	ObsID	Statistically values			
		Abs.I_{FeK_α} [a]		τ [b]	
		χ^2/d.o.f.	Probability	χ^2/d.o.f.	Probability
OAO 1657-415	406011010	4.97/5	4.19×10^{-1}	18.10/5	2.83×10^{-3}

Notes.
[a] The values for the flux of iron K_α line obtained from the fitting without applying photoelectric absorption (`TBnew`) to the Gaussian functions.
[b] The values for the depth of iron K-edge obtained from the fitting without applying photoelectric absorption (`TBnew`) to the Gaussian functions.

To further inspect the significance of the modulation of edge depth with pulse period, we have made a direct comparison of the spectra extracted in the different phase bins. We divided the phase-resolved spectra of OAO 1657-415 in the selected high intensity period by a power-law model with photon index of 2.0. Figure 5.92 shows obtained two spectral ratios, where the optical depth shows maximum variation. In same figure, the best-fit models divided by the power-law model are overlaid, which were obtained from phase-resolved fitting with the restricted range. The depth differences of for the iron K-edge between two spectral ratios can be seen clearly around 7.4 keV.

In addition, to demonstrate the modulation of the depth of edge, we analyzed with a similar way in § 5.2.3. We calculated a spectral ratio between the spectra extracted above two pulse-phases as shown in panel (a) of Figure 5.93. Edge feature appears around 7.1 keV as well as emission lines at 6.4 keV and 7.5 keV. We fitted the spectral ratios in 5.0–8.4 keV range using the same model as in the case of analyses in § 5.2.3. To prevent the effect of the emission line at 7.5 keV, we also fitted the spectral ratios ignoring data in a range of 7.4–7.7 keV. In our fitting of the spectral ratio, the edge energy was scanned from 7.11 to 7.50 keV with a step of 1 eV. The best-fit models obtained from fitting are plotted in panel (a) and (b), and residuals from the best-fit model are plotted in panel (c) and (d). In panel (e) and (f), residuals from the best-fit model without applying the edge component are plotted, and we can see an absorption edge features around 7.2 keV in the residuals. The obtained χ^2 values and corresponding statistical significance with null hypothesis probabilities are summarized in Table 5.8. The results of above fittings clearly demonstrate the significance of difference in the depth between two phase bins. We also confirmed that the value of D (see § 5.2.3) derived from the fitting of spectral ratio are consistent with maximum variation of the depth of iron K-edge, $\Delta\tau$, obtained from the phase-resolved spectral fitting, which are listed in Table 5.8.

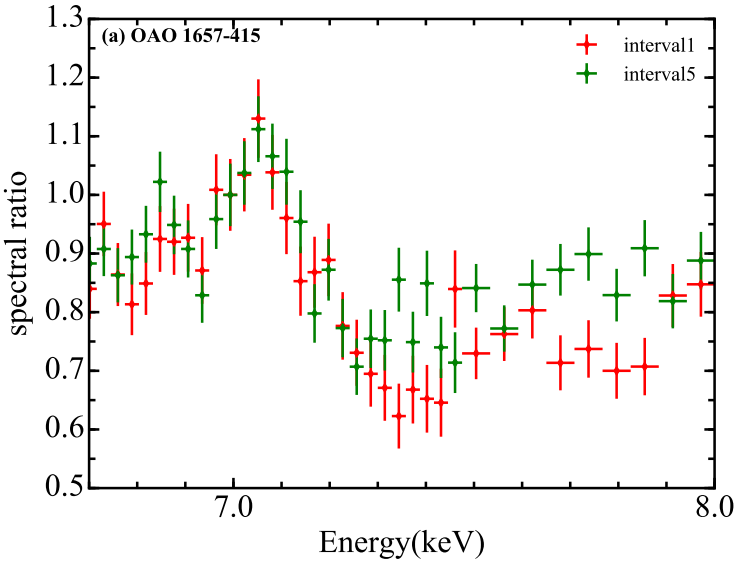

Figure 5.92: Ratios of phase-resolved spectra normalized by a power-law model with photon index of 2.0 of OAO 1657-415 during the selected time interval. Difference colors correspond to the colors indicated in Figure 5.90.

Table 5.8: Results of fitting spectral ratios around iron K-edge.

Source	ObsID	Nickel [a]	without edge		with edge			$\Delta\tau$ [b]
		K_α Line	χ^2/d.o.f.	Probability	χ^2/d.o.f.	Probability	D	($\tau_{\rm max} - \tau_{\rm min}$)
OAO 1657-415	403044020	I	100.33/96	3.61×10^{-1}	82.40/95	8.18×10^{-1}	0.11 ± 0.03	0.18 ± 0.05
		E	85.86/88	5.44×10^{-1}	63.13/87	9.75×10^{-1}	0.19 ± 0.03	

Notes.
[a] Handling of the data around the nickel line. I and E mean that the data in the energy range is included or not.
[b] Difference between two depths of the iron K-edge obtained from the spectral fitting of the two phase-resolved spectra which are used to calculate the spectral ratio.

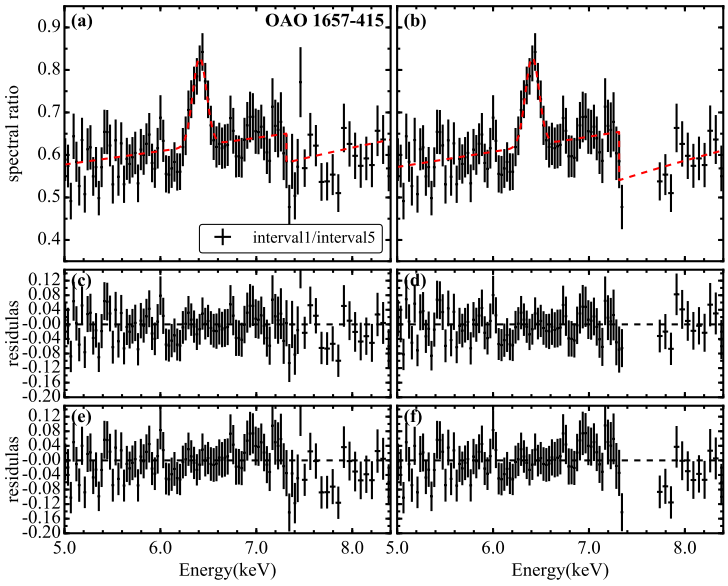

Figure 5.93: Same figure as Figure 5.87, but results of OAO 1657-415 with data during selected time interval.

Chapter 6

Discussion

Contents

6.1 Summary of the Results

We analyzed the observational data with *Suzaku* to study the origin of the emission lines and the absorption edges of iron in X-ray spectra of APXPs. The spectral properties, in particular the iron emission lines and their related features such as photoelectric absorption along the line of sight and spectral shape, were determined from phase-averaged spectra of X-ray pulsars. We also investigated the variations of the emission lines and the absorption edges of iron according to the pulsar spin phase with phase-resolved spectroscopy. The following results were obtained.

- From phase-averaged spectroscopy
  - We observed iron K-emission lines from all of sources of our samples, whose center energies were determined mostly to be 6.40–6.44 keV. This result indicates that the observed lines are coming from neutral or low ionized iron.
- From phase-resolved spectroscopy
  - Clear pulse phase modulations of the flux of the iron K_α emission line were detected with an amplitude of 21%, 31%, 13%, and 7% from 4U 1907+097, 4U 1538-522, GX 301-2 and GX 1+4, respectively.
  - We found that GX 301-2, Vela X-1, GX 1+4, and OAO 1657-415 indicate modulation of the depth of iron K-edge with pulse phase. A similar tendency was also seen for 4U 1538-522, though with poorly statistical significance.
  - For GX 301-2 and Vela X-1, energy ratios of iron K-edge to that of iron K_α line are constant over the pulse phase, which is consistent with ionization state of $Fe_{\text{II–III}}$, while those of GX 1+4 and OAO 1657-415 indicate marginal modulation.

As described in § 2.2.4, several APXPs have indicated variations of iron line flux depending on the pulse phase. However, no detection of variation of the absorption edge depth with the pulse phase in APXPs has been reported, and we present the first discovery of spin phase modulations of iron absorption edge depth from four APXPs, thanks to good photon statistics and high energy resolution of *Suzaku*. Undoubtedly, the variations of the iron emission line flux as well as ones of the iron absorption edge depth are intimately associated with both the structure of the matter surrounding the pulsar and the X-ray beam produced the NS. Based on the results as indicated above, we investigate the origin of emission line and absorption edge of iron and discuss distribution of matter surrounding the NS.

6.2 Nature of Iron Lines

6.2.1 Fluorescent Iron K-line Emission and its Emission Region

If emission mechanisms for the iron K_α emission line is fluorescence, we expect that their EWs are roughly proportional to iron column density, $N_{\rm Fe}$, and solid angle of the reprocessing matter viewed from the X-ray source, Ω. The EWs are also related to the ratio of the number of photons above the absorption edge to the intensity of the continuum at the line energy. This ratio is represented by the HR η, defined in § 5.1.2, or a spectral slope of the continuum around the line energy. To study the relation between the iron K_α emission line flux and the column density of the intervening gas as well as the spectral slope of the continuum, in Figure 6.1 the iron line flux in unit of EW was plotted against the equivalent hydrogen column density $N_{\rm H}$ (panel (a)) and HR η (panel (b)). The $N_{\rm H}$, derived from the low energy cutoff, is statistically well determined from the observed spectra and is thought to be proportional to $N_{\rm Fe}$.

The panel (a) of Figure 6.1 shows positive correlation between the EW and the equivalent hydrogen column density (hence $N_{\rm Fe}$) above $N_{\rm H} \sim 5 \times 10^{22}$ cm^{-2}, though several sources locate at the lower left corner of this diagram away from the others. On the other hands, any correlation between HR and EW is not obvious at first glance. However, if we focus on only BeXB pulsars (in color of yellow), their EW show possible positive correlation with HR.

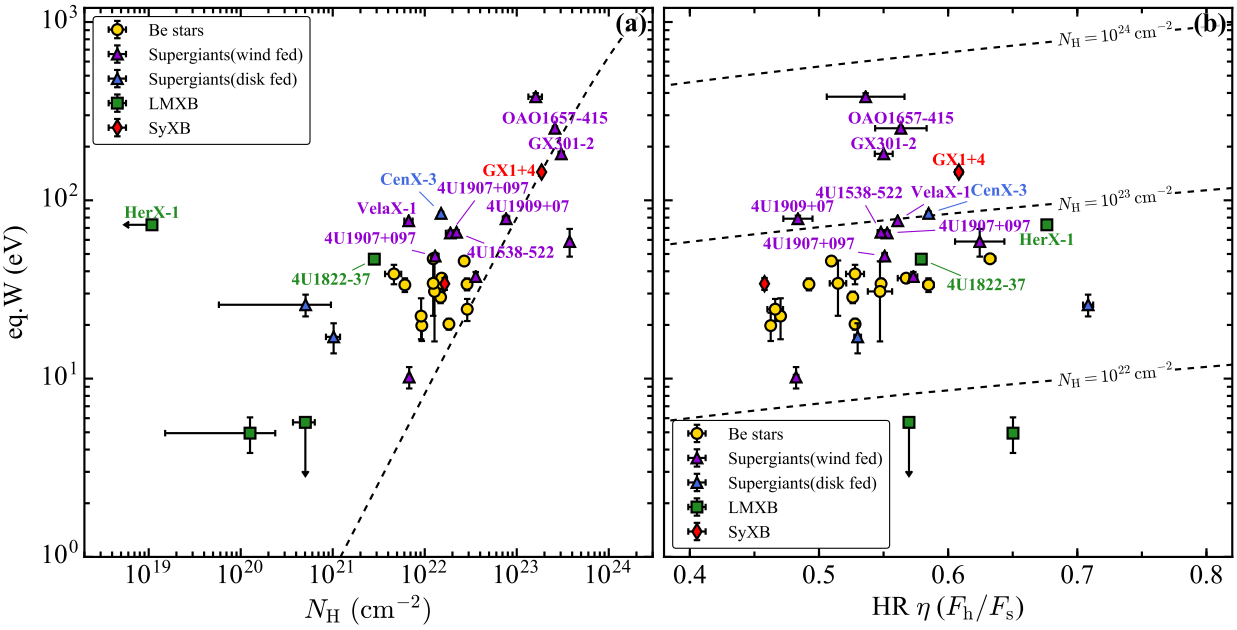

Figure 6.1: Panel (a) shows correlation between the EW of iron K_α line and the equivalent hydrogen column density ($N_{\rm H}$). Panel (b) is same as the panel (a), but plotted as a function of the HR η. The calculated model is indicated with dashed lines, respectively.

We discuss the relation, shown in Figure 6.1, of the EW of the iron K_α line against the hydrogen column density and the HR η, as followings. It is assumed that the observed X-ray spectrum consists of an X-ray continuum, $f(E)$, and an iron emission line with a flux of L, those are modified ones from the original emission, $I(E)$, due to a photoelectric absorption by a surrounding matter with a column density, N. Then, the expected X-ray spectral continuum, $f(E)$ and the line flux L, are represented by

$$f(E) = I(E) \cdot \exp\left(-\sigma(E)N\right) \tag{6.1}$$

$$L = \varepsilon_{\rm Fe}\frac{\Omega}{4\pi} \cdot \exp\left(-\sigma(E_{\rm line})N\right) \cdot \int_{E_{\rm edge}}^{\infty} I(E')\left(1 - \exp\left(-\sigma_{\rm Fe}(E)(E')N_{\rm Fe}\right)\right) dE' \tag{6.2}$$

where $E_{\rm line}$ and $E_{\rm edge}$ are energies of the K_α emission line and absorption K-edge of iron, respectively, and $\sigma(E)$ is the total photoelectric absorption cross section assuming the ISM abundance (Wilms et al. 2000), $\sigma_{\rm Fe}(E)$ is the photoelectric absorption cross section of neutral iron (Henke et al. 1993), N and $N_{\rm Fe}$ are representative column densities of the total matter and iron, respectively, $\varepsilon_{\rm Fe}$ (=0.34) is iron fluorescence yields for K-shell (Kaastra & Mewe 1993), and Ω is the solid angle of the X-ray source with respect to the reprocessing matter.

When an isotropically radiating X-ray source is spherically covered by neutral matters, that is $\Omega = 4\pi$, according to Makishima (1986), the expected EW of the fluorescent lines is expressed as;

$$EW = L/f(E_{\rm line}). \tag{6.3}$$

Given the incident continuum spectrum by $I(E) = AE^{-\Gamma}$ (Γ;photon index, A; normalization), calculated EW from Equation 6.3 is plotted with dashed line in panel (a) of Figure 6.1, as a function of $N_{\rm H}$ with Γ=1.1, which is utilized to calculate it by Inoue (1985). Dashed lines in panel (b) of Figure 6.1 show the EWs as function of HR η assuming $N_{\rm H}$ =10^{22}, 10^{23}, and 10^{24} cm^{-2}.

The prediction by the assumption with isotropic and uniform distribution is considered to correspond to the sources located on the dashed line in the panel (a) of Figure 6.1. This is consistent with the correlation in GX 301-2 obtained from *Tenma* and *ASCA* observations (Makino et al. 1985; Endo et al. 2002) and in GX 1+4 obtained from *Ginga* and *ASCA* observations (Kotani et al. 1999). From these results, we confirmed that the fluorescent is a plausible emission mechanism for observed iron lines, which were described by many authors (Ohashi et al. 1984; Makino et al. 1985; Koyama 1985; Inoue 1985; Makishima 1986).

However, we see that the some sources (e.g., Her X-1, Cen X-3, Vela X-1, 4U 1907+097, 4U 1822-37, and 4U 1538-522) indicate that their EWs remain several tens of electron volts, even when the line of sight $N_{\rm H}$ is very small. Several authors (Ohashi et al. 1984; Koyama 1985; Inoue 1985; Makishima 1986) have interpreted this as a situation that some thick matter with $N_{\rm H} \sim 10^{23}$ cm^{-2} must be present out of the line of sight. Koyama (1985) suggested another possibility that the X-ray intensity out of our line of sight is larger than that in our line of sight.

6.2.1.1 Homogeneous Matter

In this section, the distribution of the matter being the fluorescent region is discussed specifically. As a first step, we examine the reprocessing site based on the following simple assumption. We assume the matter in the fluorescent region is distributed homogeneously around the X-ray source. Furthermore we assume that the distance from the X-ray source r is comparable to the size of the matter δ (say the radius of the matter). A schematic picture is shown in Figure 6.2. By these assumptions, $N_{\rm Fe} = N_{\rm H} Z_{\rm Fe} \sim n\delta Z_{\rm Fe} \sim nr Z_{\rm Fe}$, is obtained. Then the ionization parameter can be rewritten as $\xi = \frac{L_{\rm X} Z_{\rm Fe}}{r N_{\rm Fe}}$. If the ionization state of the gas is determined, the distance of the fluorescent region from the X-ray source can be estimated by using the obtained values of the X-ray luminosity and the iron absorption column density. In particular, for 4U 1907+097, 4U 1538-522, GX 301-2 and GX 1+4, which exhibited iron line flux modulations with pulse phase, their energies of iron K_α line were found to be almost 6.4 keV and iron K-edge features in their broadband spectra were able to be represented by the absorption by neutral atoms. These results indicate the iron is in a state of neutral or lowly ionized. In addition, during the *Suzaku* observation of GX 1+4, the ionization state of iron atoms was determined to be $\rm Fe_{I–III}$ by Yoshida et al. (2017). We therefore assume that the ionization state of iron atoms in these sources are at most $\rm Fe_{I–III}$. This corresponds to a value of the ionization parameter ξ of less than 3.98 ($\log \xi < 0.6$) and 22.4 ($\log \xi < 1.35$) in the case of optically thin and thick plasma, respectively (Kallman & McCray 1982; their model 1 and 4). Since the optically thick case gives a laxer restriction on the ionization parameter ξ than the optically thin case, in the following discussion, unless otherwise specified, all restriction on the ionization parameter are given as $\xi < 22.4$. Using the value of this ionization parameter, the obtained iron column absorption densities and estimated X-ray luminosities, which are listed in Table 5.2, the distance of the fluorescent region to be more than $1–3 \times 10^{12}$ cm for 4U 1907+097, 4U 1538-522, GX 301-2 and GX 1+4.

The flux modulations of the fluorescent lines with the NS rotation were significantly detected from the several pulsars. Therefore, the flux modulation of the fluorescent lines emitted from such a large region should be explained, if we adopt the assumed situation. In the next section, we therefore point out the importance of the following two effects in the discussion of the observed time variation of the line flux. If the fluorescent lines are emitted from such a large region, then the observed time variation should be smeared with the light-crossing time of the region, which is roughly 100 s for the size of 3×10^{12} cm. On the other hand, we should take into account an apparent flux modulation of the fluorescent lines by an effect of the finite light speed, as described in the next section.

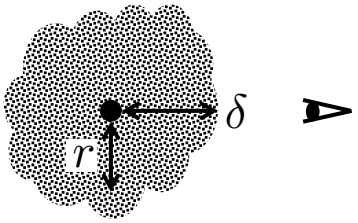

Figure 6.2: A schematic picture of the assumed situation of homogenously distributed matter.

6.2.2 Finite Light Speed Effect

We are now considering the fluorescent lines from matter that is exposed to X-rays from a X-ray pulsar, of which the emission profile is not spherically symmetric. Therefore, the fluorescent region, which is illuminated by X-rays from the X-ray pulsar, changes according to the rotation of the NS. As a consequence, the fluorescent region appears to show an apparent movement to the observer. The apparent movement affects the observed flux per unit time of the fluorescent lines, since the speed of light is finite, even if the circumstellar matter around the neutron star is homogeneous and uniform, and the intensity of X-rays from the NS stays constant. If the fluorescent region is going away from an observer with a velocity of $v_{\rm los}$ along the line of sight, then the emitted photons at the fluorescent region in 1 s are observed in $(1 + v_{\rm los}/c)$ s by the observer. Therefore, the intensity of the fluorescent line observed in 1 s decreases with a factor of $(1+v_{\rm los}/c)^{-1}$. On the other hand, the intensity observed in 1 s increases by a factor of $(1 - v_{\rm los}/c)^{-1}$ at the moment when the emission region is approaching to the observer. This phenomenon is similar to Doppler boosting, but the wavelength of the fluorescent lines does not change because the gas in the fluorescent matter is not moving, but the region of the fluorescent is changing. We call this the finite light speed effect (Yoshida et al. 2017).

As mentioned in the previous section, the fluorescent region of the pulsars is thought to extend to greater than 10^{12} cm. In case of the pulse period with more than 100 s, which is comparable with that of the pulsar indicating the pulse phase modulation of emission line flux, the speed of the change of the fluorescent region is comparable to the speed of light. Therefore, a significant effect of this finite light speed effect can be expected.

6.2.2.1 Model Calculation and Results

We demonstrated the finite light speed effect using the Monte Carlo simulation. Figure 6.3 shows a schematic drawing of a configuration of the simulation. In the simulation, a NS is located at the center of spherically uniform and homogeneous matter. We assume that X-rays are emitted at magnetic poles and that the magnetic axis is assumed to be tilted with an angle of β from the rotational axis. The inclination angle of the rotational axis is denoted by an angle i between the rotation angle and the line of sight. The intensity of the photons from a magnetic pole is assumed to be proportional to $\cos\theta$, where θ is the angle of direction of each photon from the magnetic axis. Although the illuminated region is indicated by the conic geometry for simplicity, the X-rays from the pulsar are emitted with the above given intensity distribution from the pole in our calculation. Based on the optical depth of the absorbing circumstellar material, the X-ray photons will be absorbed with an exponential probability. Once the absorption occurs, a fluorescent photon is immediately emitted, which can be detected by the observer. We calculate the propagation time of the individual photons from the magnetic pole to the observer. By assuming a constant emission rate of the photons from the magnetic pole, we generate an expected light curve by enumerating the arrival time of the photons.

We calculated six cases of the radius of the circumstellar matter, $r = 1 \times 10^{11}$, 3×10^{11}, 1×10^{12}, 3×10^{12}, 1×10^{13}, and 3×10^{13} cm, with a spin period of $P_{\rm spin} = 150$ s (supposed

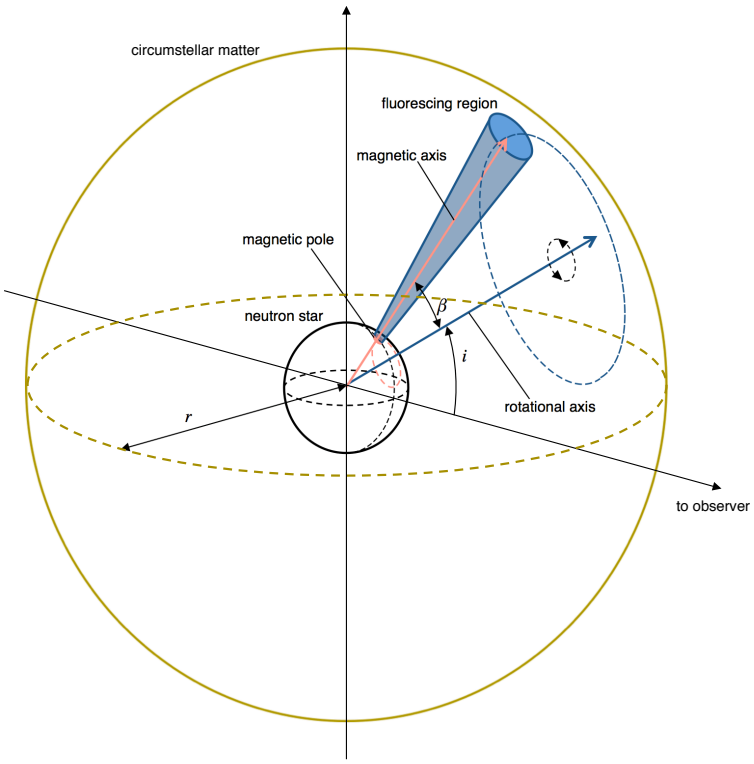

Figure 6.3: Geometry used in the Monte Carlo simulation. The NS is located at the center of the circumstellar matter with the radius of r, which is represented by the largest yellow circle. The blue and red arrows indicate the rotational axis and the magnetic axis, respectively. The blue cone, whose bottom is a magnetic pole, shows the fluorescing region at a certain phase. The red and blue circles with dashed lines indicate the trajectories of the magnetic pole and the magnetic axis, respectively. The size of the neutron star is enlarged to make it easier to see.

that of GX 1+4), $\beta = 45°$, and $i = 90°$. We folded the six generated light curves on the spin period by assuming the time origin to be a time when a direct photon from a magnetic pole was detected by the observer. The intensities of the folded light curves were normalized as the average flux to be unity and were plotted as a function of the spin phase in Figure 6.4. We can see the flux modulation by the finite light speed effect. The amplitude of the flux modulation becomes larger with the increasing radius of the circumstellar matter up to 1×10^{12} cm, while, in the cases of $r \geqslant 3 \times 10^{12}$ cm the amplitude gradually becomes smaller than that of 1×10^{12} cm, as the radius becomes larger. We can also see phase shifts as a change of the radius of the circumstellar matter, r, where a larger phase delay is seen in the larger radius.

In Figure 6.5, the modulation amplitude as a function of β is plotted for the six cases of the radius of the matter for $i = 90°$. We can recognize that the modulation amplitude becomes larger when increasing the angle of β from 0° to 90°. The dependence on the radius of matter is again found, as shown in Figure 6.4 (i.e., the amplitude is the largest at the radius of 1×10^{12} cm).

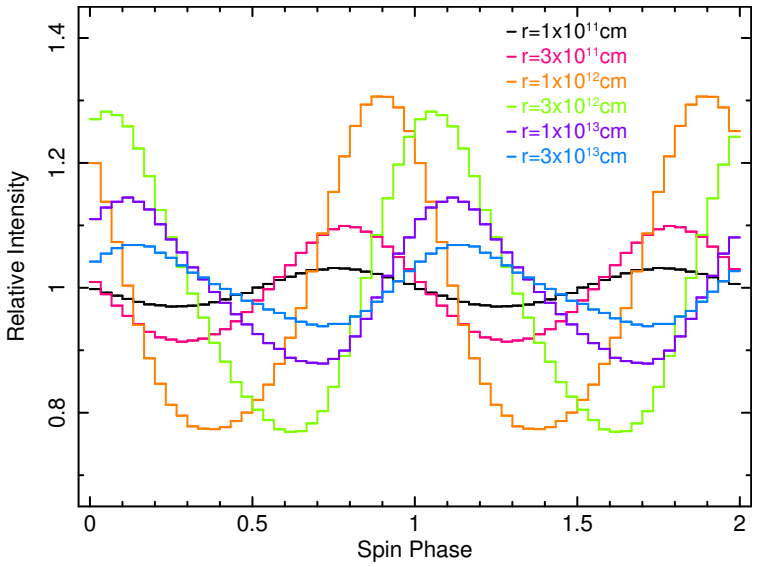

Figure 6.4: Examples of the simulated folded light curves of the fluorescent lines as a function of the spin phase of the NS. The light curves that were calculated by the Monte Carlo simulation were folded by the spin period of the NS by fixing the time origin (epoch) to be a time when a direct photon from the magnetic pole was detected by the observer. We assumed a common inclination angle of the rotation axis to be i=90° and angle between rotational axis and magnetic axis to be β=45°. Six different radii of the circumstellar matter were assumed, $r = 1 \times 10^{11}$, 3×10^{11}, 1×10^{12}, 3×10^{12}, 1×10^{13}, and 3×10^{13} cm, which are indicated by different colors. The obtained folded light curves were normalized by dividing by the average fluorescent flux.

If $i = 90°$, then the velocity of the apparent movement of the center of the fluorescent region along the line of sight, $v_{\rm los}$, is calculated as

$$v_{\rm los} \sim \frac{2\pi(r/2)\sin\beta\sin(2\pi\phi)}{P} \tag{6.4}$$

for an optically thin case, where $\phi(= 0.0\text{–}1.0)$ is the phase of the rotation of the fluorescent region from the origin defined as the direction of the observer. Therefore, $v_{\rm los}$ becomes large at a large β and at a large r, and hence the modulation amplitude of the line flux by the finite light speed effect becomes larger. The delay of the maximum phase is also understood by a long light travel time in a large size of the matter.

At a radius of 1×10^{13} cm, the light crossing time becomes ∼300 s, which is roughly two times larger than the supposed spin period. Therefore, the flux modulation by the finite light speed effect is smeared with the light crossing time. This smearing decreases the amplitude of the modulation. The competition between the finite light speed effect and the smearing effect determines the amplitude of the modulation and causes phase shifts and waveform-variations, as we can see in Figure 6.4.

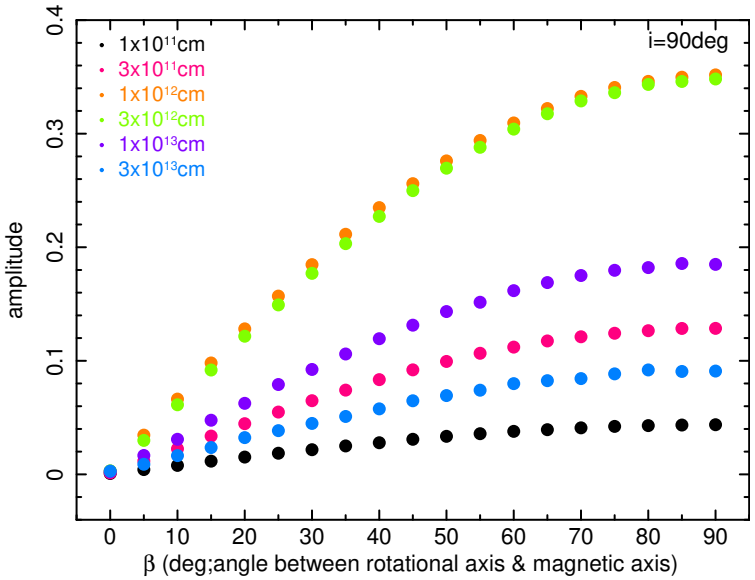

Figure 6.5: Relation between the amplitude of the flux modulation of the fluorescent lines and the angle of β, assuming the inclination angle of the rotation axis to be $i = 90°$. Six radii in Figure 6.4 were calculated. The radii of the circumstellar matter are indicated with different colors.

6.2.2.2 Application to GX 1+4

We used the simulation framework as described in the previous section to mimic the flux modulation of the fluorescent line observed in GX 1+4. Its iron K_α emission line shows the flux modulation according to the pulse period, with an amplitude of $7 \pm 1\%$, peaking at around 0.7–1.1 in the phase (see Figure 5.84).

We calculated the arrival time to the observer for each photon, considering six cases for a radius of the circumstellar matter, $r = 1 \times 10^{11}$, 3×10^{11}, 1×10^{12}, 3×10^{12}, 1×10^{13}, and 3×10^{13} cm, and the spin period, $P_{\rm spin} = 150$ s. The mean free path of the circumstellar matter was fixed at the optical depth of the neutral iron K-edge of 0.3, as derived in (Yoshida et al. 2017). The simulation was conducted for different angles of i and β in a range of 0° to 90° with a 5° step, respectively.

Figure 6.6 shows the calculated amplitude of the flux modulation of the fluorescent line on two-dimensional maps of the angles i and β for each radius. The calculated amplitude of the time variation for $r = 1 \times 10^{11}$ cm is less than 7% in any combination of the angles, while in cases of $r \geqslant 3 \times 10^{11}$ cm, a modulation amplitude of the 7% level can be seen in some combinations of i and β. The solid red lines indicate the position of the amplitude of 7%, and the dotted red lines indicate the acceptable region by the uncertainty (1%) of the observed amplitude, which were obtained from *Suzaku* observation.

The combination of the two angles, i and β, can also be restricted by an interpretation of the pulse profile. The pulse profile of GX 1+4 in lower energy range (up to 10 keV) has a prominent sharp dip, as shown in Figure 6.7(b). This sharp dip is interpreted as an obscuration or eclipse of X-ray emitting region at a vicinity of a neutron star surface by the

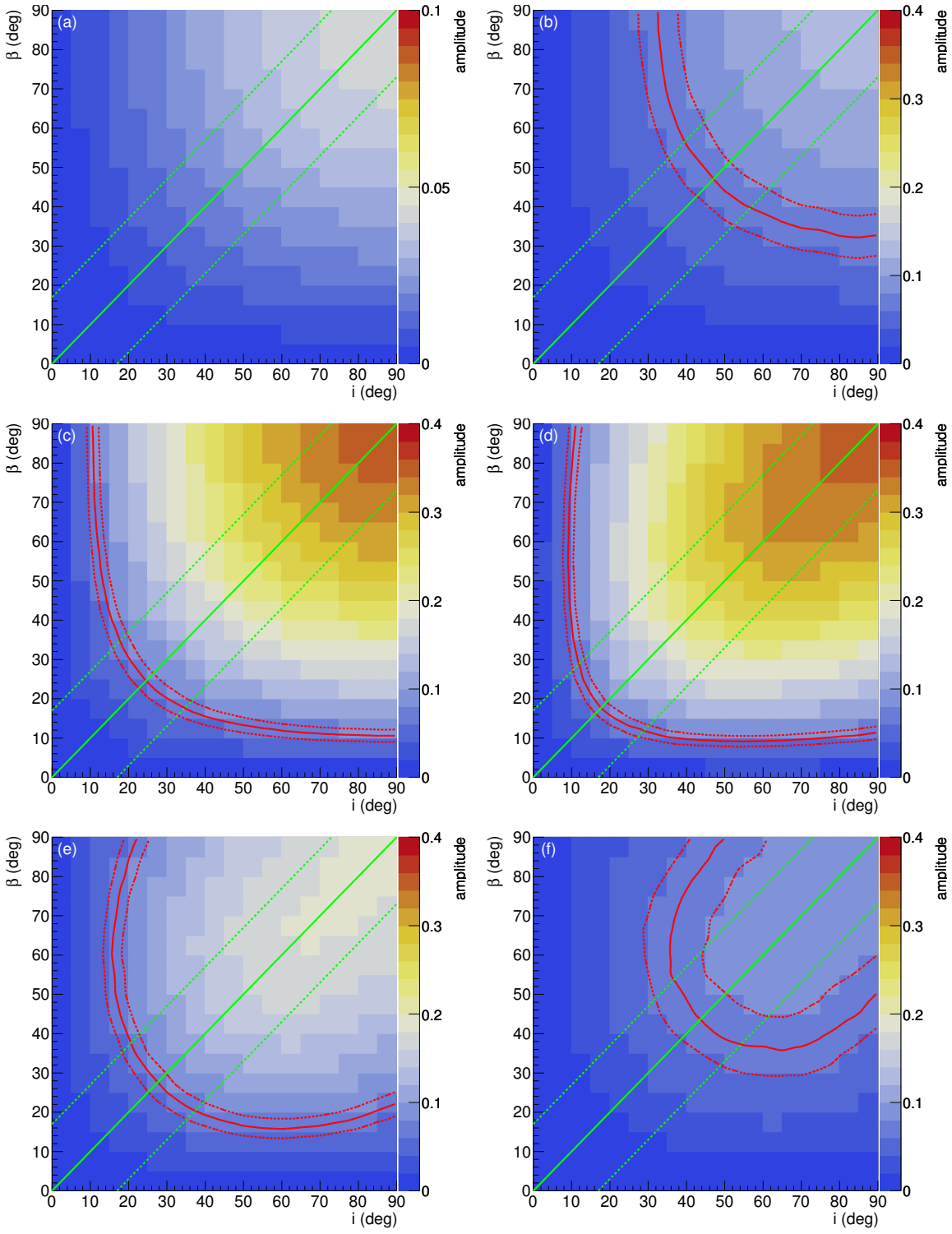

Figure 6.6: Distribution of calculated amplitude of the intensity modulation of the fluorescent line on a two-dimensional map of i and β. Six radii of the circumstellar matter are assumed; (a) $r = 1 \times 10^{11}$ cm, (b) $r = 3 \times 10^{11}$ cm, (c) $r = 1 \times 10^{12}$ cm, (d) $r = 3 \times 10^{12}$ cm, (e) $r = 1 \times 10^{13}$ cm, (f) $r = 3 \times 10^{13}$ cm. The solid red and the dotted red lines indicate the amplitude level of 7% and the acceptable regions derived by its errors, respectively. The solid green lines indicate the position of $i = \beta$. An acceptable range from the pulse profile ($i - 17^\circ \leqslant \beta \leqslant i + 17^\circ$) is indicated by dotted green lines.

accretion column to the magnetic poles of the pulsar (Galloway et al. 2000; 2001). Thus, the hot spot (i.e., magnetic pole) of the pulsar being at a base of the accretion column should face in the direction along the line of sight at least once a period. Therefore, i should be equal to β, with a certain acceptable range. We estimated an angle of accretion column viewed from a magnetic pole from the duration of the dip in the pulse profile. The dip was fitted by a Gaussian function and we got a width of the dip as 0.096 ± 0.005 (FWHM) in a unit of phase. This value is equivalent to $\theta_{\rm FWHM} = 35^\circ \pm 2^\circ$ in angle. We therefore estimated the acceptable range as $i - 17^\circ \leqslant \beta \leqslant i + 17^\circ$. In Figure 6.6, the solid green lines indicate $i = \beta$ and the dotted green lines indicate the acceptable range between i and β.

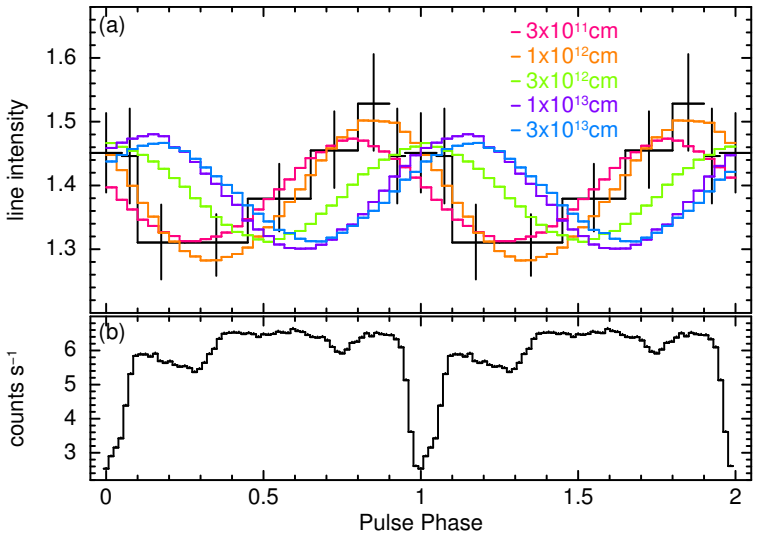

Figure 6.7: Flux modulation of the iron line and the pulse shape of GX 1+4, which is the same as shown in Figure 5.84. In panel (a), color lines show five samples of the simulated modulation curve. The angles i and β are tuned to have an amplitude of 7% and a dip condition of $i = \beta$. The assumed radii of circumstellar matter are indicated by different colors: red $r = 3 \times 10^{11}$ cm), orange ($r = 1 \times 10^{12}$ cm), green ($r = 3 \times 10^{12}$ cm), purple ($r = 1 \times 10^{13}$ cm), and blue ($r = 3 \times 10^{13}$ cm), respectively. The fluxes of the iron K_α line obtained from *Suzaku* observations are also plotted with black markers in the same panel. Panel (b) shows the epoch folded light curve in a energy range of 2–10 keV.

The finite light speed effect constrains the modulation phase of the fluorescent line with regard to the pulse shape of the continuum emission. In the case of GX 1+4, the sharp dip is considered to occur when a direct photon from a magnetic pole is detected by the observer. In Figure 6.7, the flux modulation of iron K_α emission line of GX 1+4 obtained from *Suzaku* and five typical calculated modulation samples, with an amplitude of approximately 7% and that satisfy $i = \beta$, are plotted as a function of the pulse phase. The simulated modulation curve with $r = 1 \times 10^{12}$ cm can reasonably reproduce the data modulation, but those with $r \geqslant 3 \times 10^{12}$ cm are mismatched with the data plots because of their inconsistent phase shifts. On the other hands, the modulation with an amplitude of 7% can not be reproduced with $r \leqslant 1 \times 10^{11}$ cm (see Figure 6.6).

In conclusion, even if the fluorescent matter is homogeneous and uniform, the observed flux modulation can be explained by the matter extending up to 10^{12} cm from the NS. This distance is much larger than the co-rotation radius and the Alfvén radius, even for the extraordinarily strong magnetic field of 10^{14} G.

Here, we discussed only one fluorescent region, though the emission from the NS arises from its two poles. Several previous works suggest the existence of an accretion disk in GX 1+4. Rea et al. (2005) discussed a reflection by a torus-like accretion disk. Galloway et al. (2001) interpreted the dip in the pulse profile as being due to the eclipse of the X-ray emitting region by the accretion curtain, which is formed by an accretion flow along with the magnetic field from the inner edge of the accretion disk, showing a schematic figure of accretion geometry. The size of the accretion disk is expected to be 10^{12} cm from its orbital period (Hinkle et al. 2006), and thus the fluorescent emission from the other side of the NS may be hidden by the accretion disk.

The finite light speed effect causes an flux modulation of the fluorescent lines with the rotation period of X-ray pulsars. This is due to the apparent movement of the fluorescent region, which is exposed to X-rays from the pulsar. The finite light speed effect thus can be expected to act across the X-ray pulsar source population. Therefore, for an interpretation of the flux modulation of the fluorescent lines from X-ray pulsars, this effect should be taken into account. This effect is efficient if the size of the fluorescent matter is comparable to the pulse period multiplied by the speed of light, or, in other words, the apparent movement speed of the fluorescent region is comparable to the speed of light. In the case of GX 1+4, the previously estimated fluorescent size (10^{12} cm) by Kotani et al. (1999), if true, matches to the above condition and a relatively strong effect can be expected. Actually, the flux modulation of GX 1+4 was detected and may be explained by this finite light speed effect. In the modulation of the iron line flux of GX 1+4, the maximum of the line flux does not coincide with either the minimum or maximum of the continuum emission over pulse phases. As these characteristics are similar to those seen in GX 301-2, and the line flux modulation amplitude of GX 301-2 is not large ($<10\%$), there might be suitable solution for the line flux modulations of GX 301-2 by this finite light speed effect. However, the finite light speed effect is just one possible solution for the line flux modulation.

6.3 Possible Origins of Modulating Absorption Edge Depth

It is generally difficult to determine an emission source or an emission region of the emission lines, while we can possibly restrict the region being responsible for the absorption edge to a place between the X-ray source and an observer. Thus, if the origin of the edge is clarified, the matter distributed around the NS can be restricted more assertively than by and independently with the information provided by the emission lines.

We detected significant variations of the depth of iron K-edge with spin period of NS in *Suzaku* observation of OAO 1657-415, GX 301-2, Vela X-1, and GX 1+4. The maximum depth of the iron edge occurs at the most diminished phase in broad energy range (0.5–20 keV), such as the dip for all of four sources. In 4U 1538-522, the depth of iron K-edge behaves similarly, although its statistical significance is not enough. The maximum and minimum values of the optical depth, τ, at the edge energy, are summarized in Table 6.1. Using these values, hydrogen column density $N_{\rm H} = \frac{\tau}{Z_{\rm Fe}\sigma_{\rm Fe}}$ are derived and given in Table 6.1. The estimated X-ray luminosities are also listed in the same table. The values listed in Table 6.1 are obtained from the data during whole observation for GX 301-2, Vela X-1, and GX 1+4, while those of OAO 1657-415 are derived from the data in the selected bright period. With the values summarized in Table 6.1, we restrict the structure and location of the plasma. In following, we call the two phases, at which the observed iron K-edge exhibits the maximum and minimum values of the depth, the deepest and the shallowest edge phase.

Table 6.1: Estimated column density of absorbing matter and X-ray luminosities.

Source	τ[a]		$N_{\rm H}$[b] (10^{23} cm^{-2})		$L_{\rm X}$ (10^{36} ergs s^{-1})
	...				
	min	max	min	max	
GX 301-2	0.65 ± 0.02	0.76 ± 0.03	6.4 ± 0.2	7.5 ± 0.3	8.5
Vela X-1	0.11 ± 0.02	0.20 ± 0.02	1.1 ± 0.2	2.0 ± 0.2	3.1
GX 1+4	0.35 ± 0.03	0.51 ± 0.05	3.4 ± 0.3	5.0 ± 0.5	8.9
OAO 1657-415 [c]	0.57 ± 0.05	0.75 ± 0.09	5.6 ± 0.5	7.4 ± 0.9	21

Notes.
[a] The depth of iron K-edge.
[b] The equivalent hydrogen column density calculated from the depth of iron K-edge and photoelectric absorption cross section of iron (Henke et al. 1993) assuming iron abundance relative to the hydrogen of 2.69×10^{-5} (Wilms et al. 2000).
[c] The values obtained from the data in the selected high intensity period (§ 5.3).

As described in § 6.2.1, the iron emission lines are considered to be fluorescent and originated from neutral atoms or lowly ionized ions. The edge energies indicated a consistent ionization degree with neutral or lowly ionized iron. We thus assume that the same matter is responsible for the absorption and the fluorescent line emission, which is illuminated by X-rays from the pulsars. Then, from the ratios of the absorption edge energy to the emission line energy derived from the *Suzaku* observations, the ionization state of iron in the matter was determined to $\rm Fe_{II-III}$ for all of GX 301-2, Vela X-1, GX 1+4, and OAO 1657-415,

which indicate the variations of iron K-edge depth with the pulse phase. The estimated ionization state of iron corresponds to a value of the ionization parameter ξ of less than 22.4 ($\log \xi < 1.35$) in the case of optically thick plasma (Kallman & McCray 1982; their model 4). As mentioned in § 2.2.4, the ionization parameter ξ characterizes the ionization state of the X-ray illuminated gas. Here, the gas, which is responsible for the absorption edge, is defined as the physical condition characterized by the ionization parameter ξ. In the following discussion, we therefore require the ionization parameter of the absorbing matter so as to satisfy the observed ionization state.

In order to interpret the modulation of the absorption edge depth with the pulse phase, we examine the following three interpretations; (1) X-ray flux modulations are a synthesis of two spectral components with different modulation pattern and with different depth of the absorption edge, (2) variations in the physical states of the absorption matter, such as ionization state, and/or density, according to the spin phase, or (3) the geometric changing, thus move of the emission region or the absorbing matter according to the pulse phase. In the following subsections, we discuss the details of these possibilities.

6.3.1 Two Spectral Components Influenced by Different Degree Absorption

If the X-ray spectrum consists of two components, which are influenced by different amount of absorption, and the synthesis fraction of these components changes, iron absorption K-edge depth varies apparently. That is to say, the observed spectra are composed by strongly absorbed and weakly absorbed components, and the pulse phase modulation of the depth of the edge are observed according to the competition between their fluxes. As a simple case, we assume that the amount of the absorption affecting the weakly absorbed component is $N_{\rm H} \lesssim 10^{22}$ cm^{-2}, where the iron K-edge can hardly be detected by our observation. We also assume the flux of one of the two components modulates according to the pulse phase, and the flux modulation of the other is negligibly small. If the flux of the strongly absorbed component changes, the depth is observed with the maximum value at the phase when the continuum flux becomes high. This is not the case of the observed result, in which the observed iron K-edge exhibits the maximum value of the depth, when the continuum flux dims in all of the four sources. Therefore, the flux of the weakly absorbed component varies more than the strongly absorbed one, in order to explain the observed result.

In order to investigate the flux variation of the weakly absorbed component with the pulse phase, we calculated spectral ratios, e.g., dividing the phase-resolved spectra by the phase-averaged spectrum. The resultant spectral ratios are given in Figure 6.8.

From the spectral ratio, we found that spectral shapes of GX 301-2 and Vela X-1 drastically change with spin phase of the pulsar. For GX 301-2, the spectral ratio of interval 6, which is the deepest edge phase, is almost flat up to 30 keV and dims across the broadband. The brightening in the range of 2–30 keV can be seen in the spectral ratio of interval 4, which is the shallowest edge phase, although there is a small change of the slope in the spectral ratio. From the spectral ratios of interval 4 and 6, there is no big changing of the spectral shape between the two intervals. Therefore, it is not plausible to be considered that the flux of a specified spectral component varies with pulse phase, and its variation causes the modulating depth of the iron K-edge. However, the cutoff in lower energy shows different trends between the spectral ratios of interval 4 and 6. It indicates that there are differences in amount of photoelectric absorption with pulse phase. Although the flux enhancement up to 10 keV in the spectral ration of interval 5 and that between 5 keV and 30 keV in the spectral ratio of interval 1 can be seen, these are unlikely to relate to the variation of the depth of the edge.

For Vela X-1, between the spectral ratio of interval 1 and 4, which are the deepest and the shallowest edge phase, respectively, apparent distinction of the spectral shape cannot be seen up to 20 keV. Therefore, any changing in the ratio between the fluxes of the possible two components is not plausible. However, there may be a component peaking around 15 keV, which is predominant in the spectral ratio of interval 3. If this component truly presents, the contribution of this component at interval 3 is likely to be different from that at interval 4. The depths of the edge in these intervals, however are shallow and their differences are small between interval 3 and 4. Therefore, the varying of the component peaking around 15 keV is unlikely to be the origin of the pulse phase modulation of the absorption edge depth.

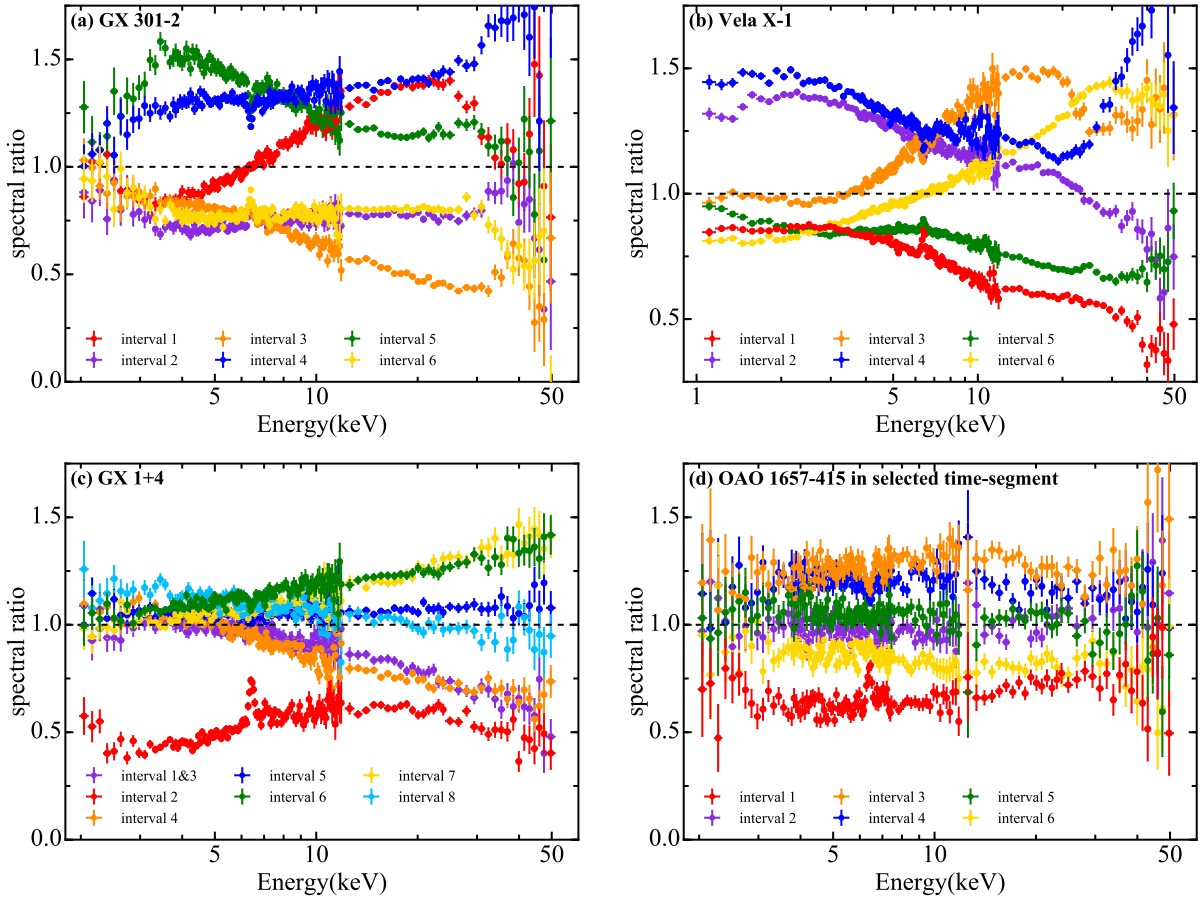

Figure 6.8: Phase-resolved spectral ratios to phase-averaged spectrum of GX 301-2 (a), Vela X-1 (b), GX 1+4 (c), and OAO 1657-415 (d). In case of GX 301-2, Vela X-1, and GX 1+4, the spectral ratios are calculated with the spectra obtained during whole observation, while the spectral ratios of OAO 1657-415 were calculated with dividing the phase-resolved spectra by the phase-averaged spectrum, which were derived in the selected time segment. Different colors of symbols in panel (a) to (d) correspond to the colors indicated in Figure 5.74, 5.75, 5.76 and 5.91, respectively. Dashed horizontal lines indicate a ratio equal to 1.

In spectral ratio of GX 1+4, the modulations below 7 keV was found to be small for all the phase-resolved spectra except interval 2, which is the deepest edge phase. The spectral ratio for the interval 2 did not show a simple absorption feature but implied the absence of a spectral component that mainly contributes in the energy range below 10 keV. In the whole spectral range from 2 keV to 50 keV, all the spectral ratio of OAO 1657-415 show fractional changing of spectral slope. Specifically, a slight spectral hardening is shown in the spectral ratio of interval 1 when the depth of the edge peaks, and the continuum flux dims. This is similar tendency to the case of GX 1+4. For these two sources, if the components contributing below 10 keV in the spectrum are observed at the phase except the dim phase, the increasing of the depth of iron K-edge at the dim phase can be interpreted as being attributed to the decreasing of this component. In other words, the component contributing below 10 keV in the spectrum would be the weakly absorbed component with a shallow absorption edge.

The sharp dip in the pulse profile of GX 1+4 is interpreted as being due to the eclipse of the X-ray emitting region by the accretion column of the pulsar (Dotani et al. 1989; Galloway et al. 2000), and the X-ray emitting region is thought to be the NS surface heated by the accretion matter. According to this interpretation, the X-ray from the vicinity of heated NS surface should be the weakly absorbed component and the X-ray from an emitting region away from the NS surface should be the strongly absorbed component. Therefore, the X-ray from the vicinity of heated NS surface must selectively avoid the absorption by the matter producing the edge.

Alternatively, if the X-ray coming from the region away from the NS surface is a reflection component, which intrinsically exhibits a distinct edge feature, the above stated condition is realized. If the reflection component plays the role as the strongly absorbed component, the flux variation of the component contributing below 10 keV as seen in the spectral ratio of GX 1+4 may be able to be responsible for the variation of the edge depth.

In order to examine the influence of the reflection component for the depth of the edge in the total spectrum, we simulated faked spectra using `reflect` in XSPEC (Magdziarz & Zdziarski 1995), in which the incident X-rays are reflected by neutral material. A model spectrum is calculated as the sum of the direct and the reflected component of a separately given incident spectrum. The shape of the incident spectrum is assumed to be composed of a blackbody and an exponential cutoff power-law. Their parameters, the temperature of blackbody, the photon index and the folding energy of the exponential cutoff power-law, and unabsorbed photon flux in range of 0.5–12.0 keV, were fixed to 1.8 keV, 0.46, 22 keV, and 1.33×10^{-1} photons s^{-1} cm^{-2}, respectively, which are derived from the phase-averaged fitting of GX 1+4 obtained by the *Suzaku* observation. The shape of the direct spectrum is also assumed to same as the incident spectrum, but its unabsorbed photon flux in range of 0.5–12.0 keV, $F_{\rm direct}$, is fixed to 1.38×10^{-1} photons s^{-1} cm^{-2}, which is derived from the fitting of the phase-resolved spectrum of GX 1+4 at interval 6 when the iron K-edge depth indicated the minimum value. Apart from these, the direct X-ray spectrum is affected by the influence of `edge` component at 7.1 keV with the depth of 0.35, which is the value at interval 6. The cosine of inclination angle in the `reflect` model is fixed to 0.95, at which the contribution of the reflection component to the edge feature depth in the total spectrum is the most effective. The simulation was conducted for different flux of the reflection component in a

range of $F_{\rm reflect} = 1.3 \times 10^{-4}$–$1.3 \times 10^{-2}$ photons s^{-1} cm^{-2} and an example of the simulated spectrum is given in Figure 6.9. Then we fitted these simulated spectra in the restricted energy range of 5–8 keV by a power-law multiplied by the `edge` component. Figure 6.10 shows resultant depths of the edge feature τ as function of $F_{\rm reflect}$. We found the τ remain at value of 0.35 up to $F_{\rm reflect} = 1.95 \times 10^{-3}$ photons s^{-1} cm^{-2}, and increases monotonically above this value. If the $F_{\rm reflect}$ is below this value,the reflection component is therefore not significantly responsible for the edge feature depth in the total spectrum.

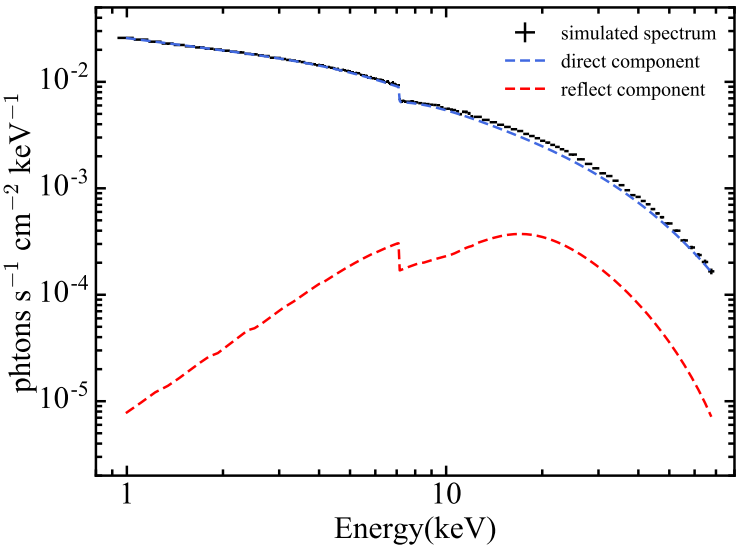

Figure 6.9: Example of the simulated spectra using the `reflect` model. The direct and reflect components are shown in blue and red dashed lines, respectively. The total spectrum (sum of the direct and the reflect components) is also plotted with black markers.

In order to fake the spectrum of interval 2, we simulated another spectrum with $F_{\rm reflect} = 1.95 \times 10^{-3}$ photons s^{-1} cm^{-2} and $F_{\rm direct} = 6.75 \times 10^{-2}$ photons s^{-1} cm^{-2}, which obtained by phase-resolved fitting of interval 2. The other parameters were fixed at the values used above simulation. Then this simulated spectrum in the restricted energy range of 5–8 keV is fitted by a power-law multiplied by the `edge` component. As a result, the depth of the edge was determined to be 0.37, which does not achieve the maximum edge depth of 0.51 ± 0.05 obtained from the phase-resolved fitting of interval 2. The simulated spectra and the best-fit model are shown in Figure 6.11 as well as the expected spectral model with the edge depth of 0.51 with red line. The difference between the simulated spectrum supposed interval 2 and the expected spectral model is obvious. Note that, if the reflection component sufficiently contributes the total spectrum in interval 2, influence by the Compton hump, which is a specific feature of the reflection seen around 20 keV in Figure 6.9, is expected to be caused in the spectral ratio of interval 2. However, the hump feature, in fact, does not appear in the spectral ratio of interval 2. Therefore, the X-ray reflection is unlikely to contribute the modulation of the absorption edge depth with pulse phase.

Consequently, it is not plausible that the modulation of the absorption depth is originated in the variation in the synthesis fraction of the two spectral components influenced by

different amount of absorption.

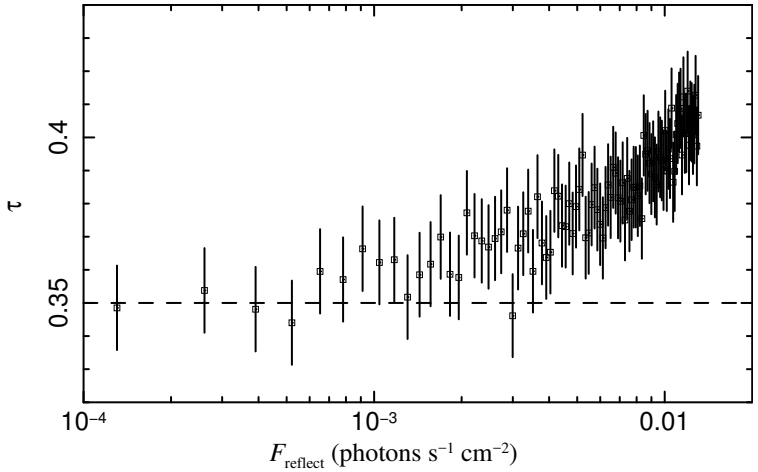

Figure 6.10: Resultant edge depths as a function of the photon flux of the reflect component, obtained from the fitting of the simulated spectra. Horizontal dashed line indicates the depth of the `edge` component given in the simulation.

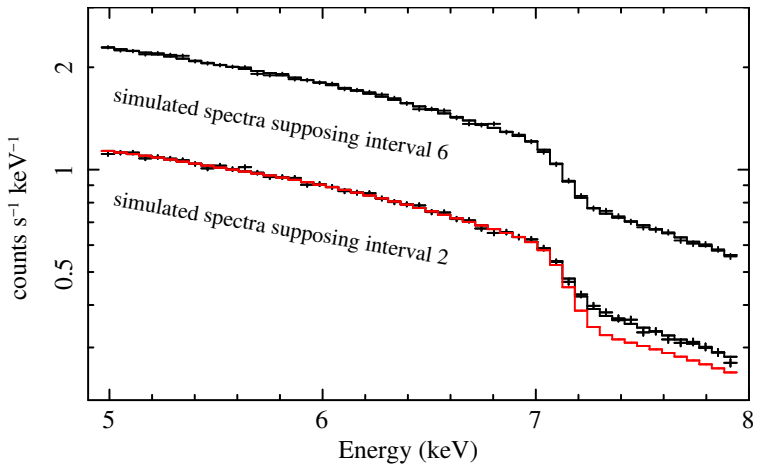

Figure 6.11: The simulated spectra supposed the observed spectra of interval 2 and 6 with best-fit model. The expected spectral model with $\tau = 0.51$ is also plotted with red line.

6.3.2 Physical State Variation of Absorption Matter

In this section, focused on physical state variation, in particular ionization state and pressure of the gas, we examine the modulation of the absorption depth with the pulse phase. Since X-rays from the pulsar is not isotropic, when the observed X-ray flux of the pulsar is intense, the matter located between the observer and the X-ray source is strongly irradiated by the X-rays. The irradiated matter hence is likely to occur changing of its ionization state. This means that the variation in the absorption edge depth may result from the change of number of iron ions being in certain ionization state, which are responsible for the absorption edge in interest. Here we investigate the time-scales of state variation of gas and examine the possibility of the variation of the absorption edge depth across the pulse phase with taking particular notice of ionization state and gas pressure.

If we assume that the matter irradiated by the X-ray source is optically thin, then the photoionization timescale is given by

$$t_{\rm ion} = \left[\int_{E_{\rm edge}}^{\infty} J(E) \sigma_{\rm Fe}(E) dE \right]^{-1} \tag{6.5}$$

where $J(E)$ is a mean intensity of ionizing radiation (in number of photons per unit time, unit area, and unit energy). Using the best-fit spectral model obtained from the phase-averaged fitting, the photoionization timescale $t_{\rm ion}$ of matter, which is located r away from the X-ray source i.e. NS, is plotted as a function of r for the four sources (GX 301-2, Vela X-1, GX 1+4 and OAO 1657-415) with colored lines in panel (a) of Figure 6.12.

Using radiative recombination rate coefficient $\alpha_{\rm r}(T)$ (in volume per unit time), we have for a recombination timescale:

$$t_{\rm rec} = \frac{1}{\alpha_{\rm r}(T) n_{\rm e}}, \tag{6.6}$$

where $n_{\rm e}$ is a number density of electron. From our estimated ionization parameter $\xi < 22.4$ for the optically thick case (Kallman & McCray 1982; their model 4), the gas temperature must be $\log(T(K)) = 4.0$–4.5 so as to X-ray heating balances the radiative cooling. At this commonly encountered gas temperature, the recombination rate coefficient of an iron atom is $\alpha_{\rm r} = 2.30 \times 10^{-12}$ cm^3 s^{-1} ($T = 10^4$ K; Nahar et al. 1997). Using the ξ parameter and the X-ray luminosity, the electron density $n_{\rm e}$ is given by $n_{\rm e} = \frac{L_{\rm x}}{\xi r^2}$, as a function of r. Given the electron number density as above with $\xi = 22.4$ and the gas temperature of $T = 10^4$ K, the recombination timescale is plotted against the radius from the X-ray source r for cases of GX 301-2, Vela X-1, GX 1+4 and OAO 1657-415 with colored lines in panel (b) of Figure 6.12.

The time scale of the spin period of the four pulsars (10–10^3 s) is also indicated with gray shaded regions in both panels of (a) and (b) of Figure 6.12. From these results, the time scale of ionization is shorter than the spin period at $r < 10^{12}$ cm. The time scale of recombination is also shorter than the spin period at $r < 10^{12}$ cm, and at this radius the number density of the electron is $n_{\rm e} > 10^{10}$ cm^{-3}. In such a region, the gas in the line of sight is ionized effectively, as observed X-ray flux from the pulsar increases, while the gas in the line of sight recombines along with decreasing of the observed X-ray flux. This effect can lead a modulation of ionization state of iron with pulse period.

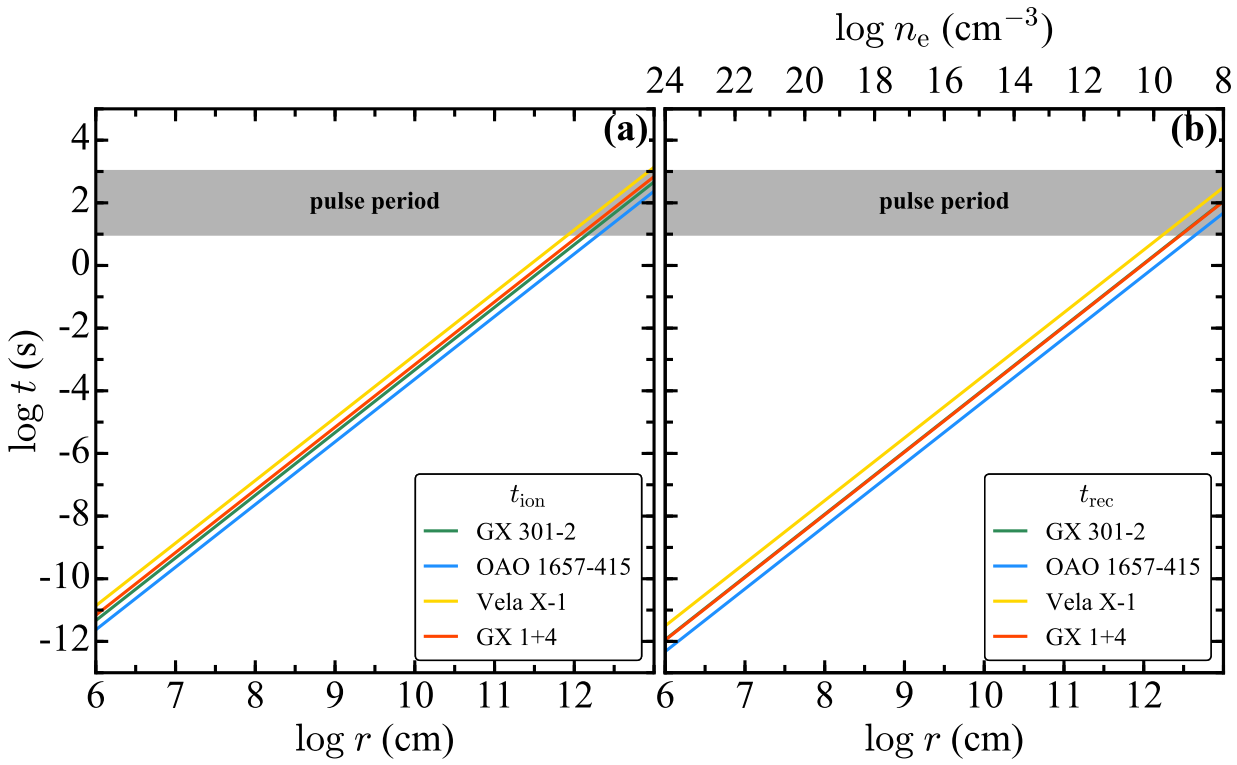

Figure 6.12: The time scales of the ionization (a) and the recombination (b) for each source calculated from Equation 6.5 and 6.6, respectively. The horizontal axis on upper of the panel (b) indicates the electron density given as $n_e = \frac{L_X}{\xi r^2}$ with $L_X = 10^{37}$ ergs s^{-1} and $\xi = 22.4$.

We also make a condition for a variation of the density of the gas. The change of the pressure of the gas propagates with the speed of sound c_s given as

$$c_s^2 = \frac{dP}{d\rho}, \tag{6.7}$$

where P and ρ are pressure and density of the gas, respectively. Assuming the ideal gas generally, the pressure P is written by

$$P = nkT \sim \frac{\rho}{m} kT, \tag{6.8}$$

where m is a mass of the particle in the gas. Then, the speed of sound is given as

$$c_s^2 = \frac{dP}{d\rho} \sim \frac{kT}{m}. \tag{6.9}$$

Therefore, the time scale of the changing in the density is written as,

$$t_\rho \sim \frac{\delta}{c_s} = \delta \sqrt{\frac{m}{kT}}, \tag{6.10}$$

where δ is a size of gas. Typical value of the sound speed is $c_{\rm s} = 9 \times 10^5$ cm s^{-1} if the gas consists mainly of hydrogen and the temperature is at the estimated value of $10^{4.0}$ K. The changing of the particle density would be caused by the ionization with the enhancement of X-ray irradiation or the recombination with the decreasing of X-ray irradiation. If the changing in the density eventually occurs due to the ionization or the recombination, it can be possible explanation for the variation of absorption edge depth.

If the above time scales are shorter than the spin period, the corresponding mechanisms may be able to become an origin of the modulation of the absorption edge depth. Thus the conditions are given as follows:

(a) $t_{\rm ion} < P_{\rm spin} \Leftrightarrow r < 10^{12}$ cm

(b) $t_{\rm rec} > P_{\rm spin} \Leftrightarrow n > 4.5 \times 10^{35} \cdot r^{-2}$ cm^{-3}, $r < 10^{12}$ cm

(c) $t_{\rho} < P_{\rm spin} \Leftrightarrow \delta < 9 \times 10^6$ cm

Note that given $N_{\rm H} \sim n\delta$ the requirement (c) is rewritten as $n > 6 \times 10^{16}$ cm^{-3} with $N_{\rm H} = 5 \times 10^{23}$ cm^{-2} obtained from the observation (see Table 6.1). If the variation in intensity of X-ray irradiation to the matter is attributed to changing of the ionization state of the matter, the requirement (a) and (b) are necessary and sufficient conditions for the matter in the gas. The relation between above three conditions is shown in Figure 6.13.

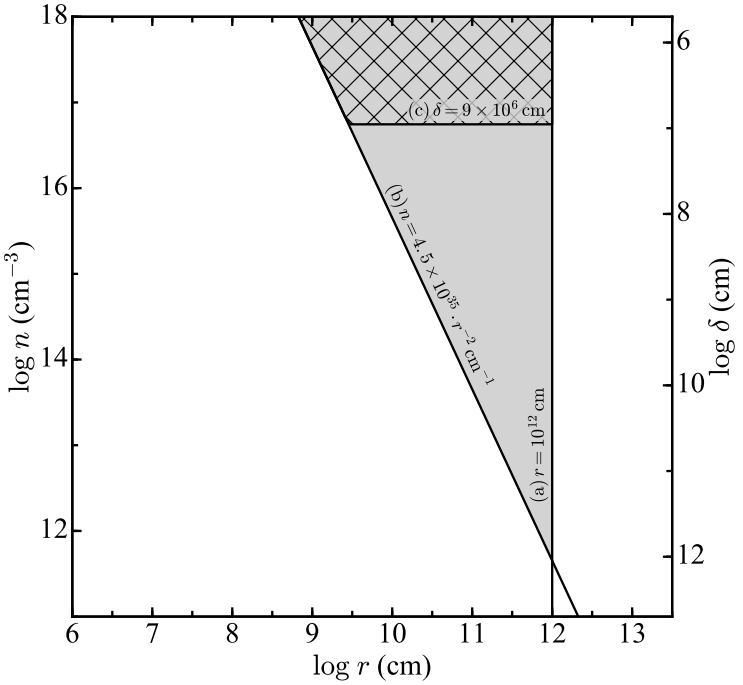

Figure 6.13: Particle density plotted as function of the distance from the NS. Black lines with texts are constraints on the parameters of the absorption matter corresponding to the requirement (a) to (c), and the gray colored region is allowed. The vertical axis on the right of panel indicate the expected thickness of absorption matter along the line of sight.

Figure 6.13 shows the allowed region for the requirements (a), and (b) with gray color. Implementing the requirement (c) simultaneously, the allowed region is reduced to the upper side within the region indicated with a reticular pattern. Using the hydrogen column density of $N_{\rm H} = 5 \times 10^{23}$ cm^{-2}, the geometric thickness of the absorption matter along the line of sight, δ, is calculated and indicated by the vertical axis on the right of the panel of Figure 6.13 with correspondent particle density. If we assume $r \sim \delta$, the distance from the NS is restricted to $r > 1 \times 10^{12}$ cm which is estimated with the ionization state. However, this condition does not match the requirement (a) and $r \sim \delta$ therefore must be denied. From these results, if the absorbing gas is located within the acceptable region shown in Figure 6.13 with the specified geometric thickness according to the densities, the changing of the state of gas along the line of sight can be a possible origin of the modulation of iron K-edge depth with pulse phase from the perspective of the time scales.

On the other hands, the enhancement of illuminating X-ray intensity to the gas makes the ionization state of the gas be higher, and resulted energy of the absorption edge should become high (see Figure 2.5). However, the fact, that the energies of edge being high in association with increasing continuum flux, was not observed with *Suzaku*. The ratio of iron K-edge energy to that of iron K$_\alpha$ line did not change significantly throughout the pulse phase, for GX 301-2, Vela X-1 (Figure 5.82 and 5.83). Furthermore, the energy ratios of GX 1+4 and OAO 1657-415 become large at phase when the continuous flux becomes minimum and the depth of iron K-edge indicates the maximum (Figure 5.84 and 5.91). These results are opposite tendency against the prediction from the above effect. From these observation results, the physical state variation of absorption matter in the line of sight is therefore not a plausible explanation for the pulse phase modulation of the absorption edge depth.

6.3.3 Geometric Variation of Absorption Matter

The changing in the amount of the matter along the line of sight by moving according to the NS spin of the emission region, or the absorbing gas itself, can be one of the possible explanation for the modulation of absorption edge depth with the pulse phase. Considering the case that the moving according to the NS spin phase of the emission region is responsible for the modulation of absorption edge depth, the absorbing matter should exist on the line of sight to the emission region. The emission region is thought to exist around the magnetic poles of the NS and its size is considered to less than the NS radius, namely 10^6 cm. The absorbing matter containing roughly neutral irons can not be expected to exist inside of the Alfvén surface, whose radius is more than 10^8 cm. By considering this geometry, even if the position of the emission region changes, a change of the absorption column density can not be expected, as long as the absorbing matter does not change.

Alternatively, if the absorption matter co-rotates with NS spin, variation of the edge depth with pulse phase can occur. The co-rotation with the NS spin implies that the absorbing matter should be confined by the magnetic field and hence it should be located at the Alfvén radius $r_{\rm A}$, or on its inside as shown in Figure 6.14. The outer of accretion disk and the wind from the companion star cannot be a cause of the pulse phase modulation of the depth of edge, because these locations can not have a variation with the spin period.

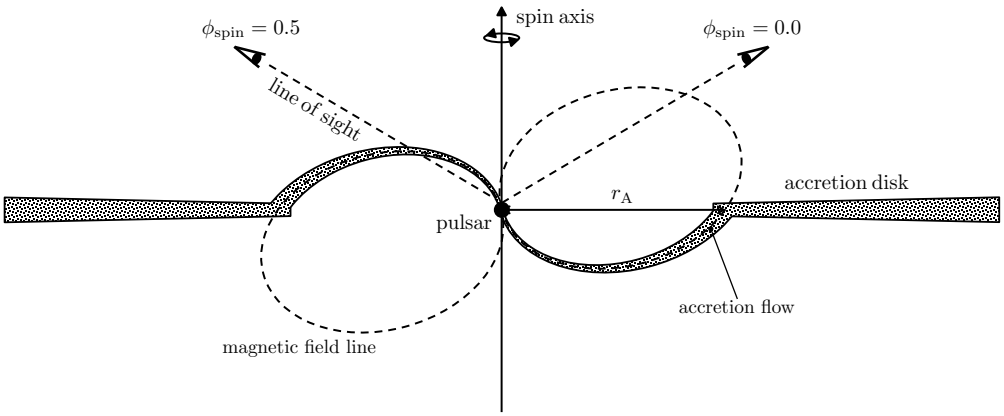

Figure 6.14: A schematic picture of the assumed situation of the absorbing matter co-rotating with the NS spin.

Substituting $R_* = 10$ km and $M_* = 1.4 M_\odot$ for the NS radius and mass, respectively, and the estimated X-ray luminosity $L_{\rm X}$ for each source in Equation 2.16, Alfvén radii for each source are calculated and are summarized in Table 6.2, where the magnetic field strengths at the NS surface of GX 301-2 and Vela X-1 are assumed to be $B_{\rm surf} = 3.0 \times 10^{12}$ G and $B_{\rm surf} = 2.2 \times 10^{12}$ G, which were derived from the CRSF in their *Suzaku* X-ray spectra (Suchy et al. 2012; Doroshenko et al. 2011), respectively. However, we tentatively assume the magnetic field strengths at the NS surface of OAO 1657-415 and GX 1+4 to be $B_{\rm surf} = 10^{13}$ G, since any CRSF have not been reported in their spectra (Barnstedt et al. 2008; Yoshida et al. 2017).

Since the absorbing matter being responsible for the absorption edge should be located

Table 6.2: Estimated magnetic field strengths and Alfvén radii.

Source	$B_{\rm surf}$ (G)	$r_{\rm A}$ (cm)
GX 301-2	3.0×10^{12}	5.7×10^{8}
Vela X-1	2.2×10^{12}	8.1×10^{8}
GX 1+4	1.0×10^{13}	1.4×10^{9}
OAO 1657-415	1.0×10^{13}	1.1×10^{9}

within the Alfvén radius, the requirement (d) $r \leqslant r_{\rm A} = 5 \times 10^8$–$10^9$ cm is given. Accordingly, the estimated size of the gas of $r > 10^{12}$ cm, based on the assumption that the size of gas and the distance from the X-ray source are similar ($r \sim \delta$), violates the condition, $r < r_{\rm A}$. Therefore, we have to remove the assumption ($r \sim \delta$). In any cases, the observed ionization state of iron ($\rm Fe_{II–III}$) gives the constraint of $\xi = \frac{L_{\rm X}}{nr^2} < 22.4$. The absorbing matter therefore should satisfy the requirement (e) $nr^2 > 4.5 \times 10^{35}$ cm^{-1} by assuming $L_{\rm X} = 10^{37}$ ergs s^{-1}, which is the same one to (b) mentioned in section § 6.3.2. The acceptable region of the requirement (d) and (e) are shown on r-n plane, in Figure 6.15. The region filled with yellow is for the magnetic field strength at the NS surface of $B_{\rm surf} = 10^{12}$ G, whereas the combined yellow-colored and blue-colored region is accepted in the case of $B_{\rm surf} = 10^{13}$ G. With the observed amount of change in the hydrogen column density of $\Delta N_{\rm H} = 10^{23}$ cm^{-2}, the geometric thickness of the absorption matter along the line of sight, δ, can be calculated for a given particle density and is indicated by the vertical axis on the right of the panel of Figure 6.15.

If we consider that the absorbing matter is the accreting matter along magnetic field lines, we have a relation among the mass accretion rate, $\dot{M}$, and r, $n(r)$, falling velocity, $v(r)$. Then, we have

$$\begin{aligned} \dot{M} &= \mu_{\rm gas} m_{\rm p} n(r) s(r) v(r) \\ &= \sqrt{2GM_*} r^{-1/2} \mu_{\rm gas} m_{\rm p} n(r) s(r) \end{aligned} \tag{6.11}$$

where $s(r)$ is a cross sectional area of the accretion flow, and $\mu_{\rm gas}$ is the gas mass per hydrogen atom, which is 1.3 for cosmic chemical abundances (Cox 2000). We assumed the velocity falling onto the NS, $v(r)$, to be the free fall velocity given by Equation 2.1. By assuming that all the kinetic energy liberated is converted to the radiation energy at the NS surface, namely $L_{\rm X} = GM_*\dot{M}/R_*$, the density in the accretion flow can be given by

$$n(r) = 1.3 \times 10^{27} \times r^{1/2} s(r)^{-1} \times \left(\frac{L_{\rm X}}{10^{37}\ {\rm ergs\ s^{-1}}}\right) \left(\frac{R_*}{10^6\ {\rm cm}}\right) \left(\frac{M_*}{1.4 M_\odot}\right)^{-3/2} {\rm cm^{-3}}. \tag{6.12}$$

The cross sectional area of the accretion flow is written by

$$s(r) = d(r) w(r), \tag{6.13}$$

where $w(r)$ and $d(r)$ are width and thickness of the accretion flow, respectively, and is assumed to be proportional to r^{γ}. If the width is given as $w(r) = \zeta r$, where ζ is an azimuthal angle of the accretion flow assumed to be independent on the radius, the thickness can be written as $d(r) = d_{\rm A}\,(r/r_{\rm A})^{\gamma-1}$, where $d_{\rm A}$ is the thickness at $r_{\rm A}$, and we obtain

$$s(r) = \zeta d_{\rm A} \left(\frac{r}{r_{\rm A}}\right)^{\gamma} \tag{6.14}$$

The azimuthal angle of the accretion flow can be estimated from the pulse phase duration at the deepest edge phase, and $\zeta = 0.3\pi$ is yielded (see Figure 5.82, 5.83, 5.84, and 5.91). Simply considering a conic geometry for the accretion flow, the index of γ is 2. According to Ghosh & Lamb (1979), the cross sectional area of the accretion flow $s(r)$ can be assumed to be proportional to r^3. Substituting Equation 6.14 into Equation 6.12 with $\gamma = 2$ and 3, we calculate the density in the accretion flow. Using values of $L_{\rm X} = 10^{37}$ ergs s^{-1}, $B_{\rm surf} = 10^{12}$ G, and $\zeta = 0.3\pi$, the calculated density in the accretion flow are plotted with dotted lines ($\gamma = 2$) and dashed lines ($\gamma = 3$) in Figure 6.15 for some cases of typical thickness of the accretion flow at the Alfvén radius, $d_{\rm A}$=10^4 cm, 10^5 cm, and 10^6 cm. As shown in Figure 6.15, in either case of $\gamma = 2$ and $\gamma = 3$, the accreting matter around the Alfvén radius satisfies the acceptable region mandated by the requirement (d) and (e), if it has the thickness of $d_{\rm A} = 10^4$ cm.

Consequently, if the absorption matter is at the Alfvén radius for $B_{\rm surf} = 10^{12}$ G ($r_{\rm A} = 3 \times 10^8$ cm) and has a particles density $n = 10^{19}$ cm^{-3}, the absorption matter consists of almost neutral atoms and forms a structure whose the geometric thickness along the line of sight is $\sim 10^4$ cm, which is roughly consistent with the estimated value from the accretion flow model stated above. Given these situations, variation of the amount of the absorption in line of sight due to the matter co-rotating with the NS spin can be a plausible explanation being responsible for the pulse phase modulation of the iron absorption edge depth.

So far, it has been pointed out by some authors, that the Alfvén shell is a possible site of the absorption matter with low ionization irons. Inoue (1985) estimated that Alfvén shell can be as dense as $n = 10^{19}$ cm^{-3} and $N_{\rm H} = 10^{23}$ cm^{-2} whose radius is 10^8–10^9 cm. This means that even with strong X-ray radiation of the order of $L_{\rm X} = 10^{37}$ ergs s^{-1}, the ionization parameter ξ will be 1–10^2 and the Alfvén shell can stay at such a low ionization state. Ichimaru (1978) calculates the thickness of the shell at the Alfvén radius to 10^4 cm from the length of the plasma penetration into the Alfvén shell (see equation 20 and 23 in Ichimaru 1978). This value is also consistent with our estimated values.

It is reported in this work that the depth of the iron K-edge is observed to increase at the dimming interval such as the dip. As stated on several occasions, the dip in the pulse profile is interpreted as being due to the eclipse of the X-ray emitting region by the accretion column of the pulsar at least for GX 1+4 (Galloway et al. 2000; 2001). Galloway et al. (2001) shows that the absorption column density, derived from the low energy cutoff, increased at the dip. This is good agreement with the results described here. The increasing in amount of absorption can be interpreted to be attributed to crossing the line of sight of the accretion column or curtain (Miller 1996). Then, assuming the magnetic field of the NS is purely dipolar and the magnetic and rotation axes of the NS are not aligned, only a fraction of field lines will intercept the disk at angles favorable for accretion, which carry matter to

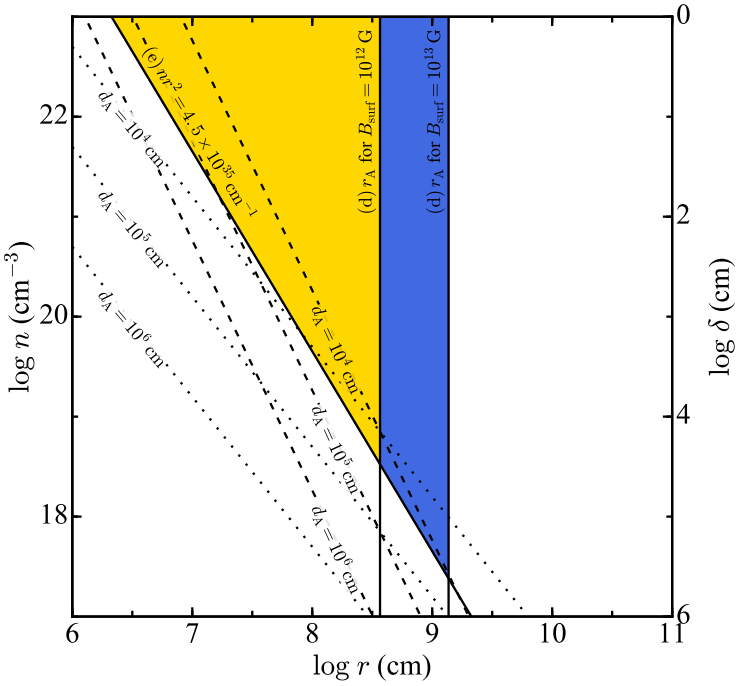

Figure 6.15: Particle density plotted as function of the distance from the NS. Black lines with texts are constraints on the parameters of the absorption matter corresponding to requirement (d) and (e), and the region filled with yellow is allowed for the magnetic field strength at the NS surface of $B_{\rm surf} = 10^{12}$ G, while the combined yellow-colored and blue-colored region is accepted in the case of $B_{\rm surf} = 10^{13}$ G. The vertical axis on the right of panel indicate the expected thickness of absorption matter along the line of sight. The estimated densities given as Equation 6.12 are indicated by dashed and dotted lines. See text for details.

the NS surface, and the footprint of the flow-bearing field lines will form an arc on the NS surface facing the magnetic pole (Basko & Sunyaev 1976). And the accretion matter formed a sheet will extend upward from this footprint. This sheet is the accretion curtain. In our used geometry with Equation 6.14, the thickness of the gas flow is sufficiently smaller than the width of the gas flow, if the thickness is the estimated value of 10^4 cm at the Alfvén radius. Therefore, for the configuration of the accretion flow, the geometry flattened toward the equator such as accretion curtain (Miller 1996; Galloway et al. 2001; latter shows the schematic figure of accretion geometry) may be plausible rather than a whole cone one.

As above stated, the fluorescent emission line and absorption edge of iron are considered to be originated from same matter. If the iron emission lines comes from the accreting matter along the magnetic field lines around Alfvén radius, the Doppler broadening of the iron line is expected with suitable amount depending on Kepler velocity at the radius. With the Alfvén radii listed in Table 6.2, the expected Kepler velocities $v_{\rm K}$are several thousands km s^{-1}. Defined $\beta_{\rm K} = v_{\rm K}/c$, the Doppler shift is expressed as $\Delta\epsilon = \epsilon_{\rm o}\beta_{\rm K}/(1-\beta_{\rm K})$, where $\epsilon_{\rm o}$ is a central energy of the emission line, and the energy shift by these velocities is thus 80–120 eV.

If the emission lines uniformly come from the accreting matter along the magnetic field lines around Alfvén radius, the line width is expected to be 50–70 eV in standard deviation. XIS does not have sufficiently energy resolution to detect this line broadening. The *Suzaku* XIS data did not show in fact the energy modulations of the iron K_α line (< 10 eV) in GX 301-2, Vela X-1, GX 1+4 and OAO 1657-415. If pulsar has the dipole magnetic field, accretion flow forms two accretion curtains. The accretion matter flowing along the curtains should have a high radial velocity, although this radial velocity does not always have to align to the line of sight. This may result an intrinsically broadened width of emission line produced by the curtains and the pulse phase modulation of the center energy of the line would be smeared. The energy modulation or the broadening line is able to be unraveled by the observation with both of sufficient photon statistics and much higher sensitivity for narrow emission lines.

6.4 Distribution of Iron Surrounding X-ray Pulsar

In § 6.2 and 6.3, the distance and the density of the responsible site of the lines and absorption edge of the iron are estimated. In this section, we discuss unified interpretation for the geometry and distribution of circumstellar matter around the X-ray pulsar.

6.4.1 Unified Picture

Our phase-resolved spectroscopy reveals that the iron absorption K-edge depth varies according to the pulse phase of the pulsar. The observed iron K-edge depth modulation with pulse phase can be explained by the absorption by the accreting matter along the magnetic field lines within the Alfvén radius, which is co-rotating with the NS. That is to say, shallowing the depth of iron absorption K-edge can be interpreted as a fact that the accreting matter moves out of our line of sight. However, we should note the fact that even at the phase when the depth of iron K-edge shallows, large amount of the absorption, corresponding to $N_{\rm H} = 10^{23}$ cm^{-2}, was observed (see Table 6.1). We cannot say whether this large amount of the absorption is caused by the accreting matter within the Alfvén radius, or rather the circumstellar matter located at outer of Alfvén radius.

Several authors discuss the reprocessing site that contributes to the 6.4 keV iron fluorescence line emission. In the case of Vela X-1, the presence of a line emission site within 5×10^{11} cm from the NS is proposed as an explanation for a dropping of the iron line flux with a factor of 20 during the eclipse observed by *Ginga* (Ohashi et al. 1984). Endo et al. (2000) found the broadening iron K_α line from the *ASCA* observation of GX 301-2, and that this broadening is in a range of one third to half of that expected from the free fall velocity at the Alfvén radius. They concluded that the iron lines originate within 10 $r_{\rm A}$ ($\sim 10^{10}$ cm) of the NS, i.e., inside of the accretion radius ($\sim 10^{11}$ cm). For OAO 1657-415, Audley et al. (2006) estimated the size of the emission region for the neutral iron line is within 5.7×10^{11} cm from the NS, utilizing the time interval of line intensity decaying during the eclipse observed by *ASCA*. The matter located in the region, between the Alfvén radius and the accretion radius, should be responsible for not only the fluorescent but also the photoelectric absorption.

For the four sources Vela X-1, GX 301-2, GX 1+4, and OAO 1657-415, which exhibit the pulse phase modulations of the iron K-edge depth, the relation between the absorption column density and the EW are follows; the EWs of iron line and photoelectric absorption column densities of GX 301-2, GX 1+4, and OAO 1657-415 are all large values ($EW > 100$ eV and $N_{\rm H} > 10^{23}$ cm^{-2}), while Vela X-1 exhibits the EW of 80 eV even at the absorption column density of $N_{\rm H} = 10^{22}$ cm^{-2}. The positive correlations between the iron emission line EW and absorption column density of GX 301-2 and GX 1+4 are consistent with the expected results from isotropic distribution of absorbing matter around the pulsar (Makino et al. 1985; Endo et al. 2000; Fürst et al. 2011b; Kotani et al. 1999). Our present results obtained from *Suzaku* observation of GX 301-2 and GX 1+4 are in agreement with the relations. Since both of absorption column and EW of OAO 1657-415 are large, OAO 1657-415 may be in the similar condition to those of GX 301-2 and GX 1+4. As above statements, there should be certain amount of the absorption matter between the Alfvén radius and the accretion radius. In this

region, the matter is not affected by the magnetic field of the pulsar, and may contribute the observed large amount of the absorption depth at the phase when the depth of iron K-edge shallows. If the matter located in this region surrounds the pulsar almost completely, the positive correlation between the column density and the EW in GX 301-2, GX 1+4, and OAO 1657-415 can be explained.

In the case of Vela X-1, although the positive correlation between absorption column and EW in range of $N_{\rm H} > 2 \times 10^{23}$ cm^{-2} was reported by Inoue (1985) and Nagase et al. (1986), the relation shows the deviation from the linear correlation at a small absorption column density with $N_{\rm H} < 2 \times 10^{23}$ cm^{-2}, where the EW is as large as 80 eV for any value of $N_{\rm H}$ ranging from 1×10^{22} cm^{-2} to 2×10^{23} cm^{-2} (see Figure 5 in Inoue 1985). This result implies that a thick matter with $N_{\rm H} > 10^{23}$ cm^{-2} must be present out of line of sight. The result of Vela X-1 obtained from *Suzaku* observation is consistent with these reports. In addition, we found that the iron absorption K-edge is clearly seen in the spectrum of Vela X-1, in spite of no indication of significant low-energy absorption corresponding to $N_{\rm H} = 10^{23}$ cm^{-2}. This is interpreted as that an emitting region, which emits mainly X-rays with < 7 keV, exists in the system, which is not influenced by the absorbing matter along the line of sight. In other words, this result indicates that the whole X-ray source in the system is not completely shrouded by the absorbing matter. Therefore, for Vela X-1, the matter, within the Alfvén radius as well as between the Alfvén radius and the accretion radius shrouds the X-ray emission from the NS incompletely.

6.4.2 Accreting Matter within Alfvén radius

In § 6.4.1, we argue that the absorbing matter is distributed in two regions separated by the Alfvén radius, and the matter within the Alfvén radius has the asymmetric structure. This section presents a discussion focusing on the accreting matter along the magnetic field lines within the Alfvén radius, which is responsible for the photoelectric absorption along the line of sight at the deepest edge phase.

In § 5.2 and 5.3, assuming that there is no variety in the ionization state of the absorption matter along the line of sight, we determine that of iron from the energies of the iron K_α emission line and iron absorption K-edge. However, it can be plausible that the ionization states of the absorbing matter in two regions separated by the Alfvén radius need not be of the same to each other. In other words, the matter originating the changing in the amount of the absorption along the line of sight and otherwise should be treated separately in the analysis. Therefore, considering the absorption by the matter within and beyond the Alfvén radius separately, we conduct an additional spectral analysis.

We fitted the phase-resolved spectra of GX 301-2, Vela X-1, GX 1+4, and OAO 1657-415 of the deepest edge phase, restricting the energy range to 5.8–7.8 keV as similar in § 5.2.3. For the spectral fitting in the restricted energy range, the model consisting of `powerlaw` × $\texttt{edge}_1$ × $\texttt{edge}_2$ + `gaussians` in XSPEC expression is applied to express the absorption by the iron in the two regions. In this model, $\texttt{edge}_1$ and $\texttt{edge}_2$ are assumed to represent the absorption edge by the matter beyond and within the Alfvén radius, respectively. The ratio of the energy of the iron K_β line to that of the iron K_α line was fixed to 1.103, which is for the neutral case (Yamaguchi et al. 2014), in the fitting. The center energy of nickel K_α line was also fixed to the value which was derived from the phase-resolved fitting of the the deepest edge phase. The energy and the depth of $\texttt{edge}_1$ component were fixed to the values obtained from the phase-resolved spectral fitting of the shallowest edge phase. The energy of $\texttt{edge}_2$ component was scanned changing the ratio to the fixed edge energy from 1.00 to 1.03 with a step of 0.001, while the depth of $\texttt{edge}_2$ component was allowed to be free. The resultant χ^2 values as a function of the energy of $\texttt{edge}_2$ are plotted in panel (a) of Figure 6.16–6.19. In the same panels, horizontal dashed and vertical dotted lines indicate the 90% confidence level and the expected energies of iron K-edge for several cases of ionization state expressed by accompanied notes. The values of the energy of $\texttt{edge}_2$ are constrained to 7.15 keV $< E <$ 7.31 keV, $E <$ 7.22 keV, 7.24 keV $< E <$ 7.40 keV, and 7.26 keV $< E <$ 7.45 keV, which correspond to the ionization states of iron of $\mathrm{Fe}_{\mathrm{II–VI}}$, $\mathrm{Fe}_{\mathrm{II–IV}}$, $\mathrm{Fe}_{\mathrm{III–VII}}$, and $\mathrm{Fe}_{\mathrm{III–VIII}}$, for GX 301-2, Vela X-1, GX 1+4, and OAO 1657-415, respectively. These determined ionization states of iron are equal to or higher than those obtained from the phase-resolved fitting with single absorption edge component (see § 6.3). And more specifically, the accreting matter along the magnetic field line has higher ionization state than that of the matter existing beyond the Alfvén radius, both of which are responsible for the absorption along the line of sight. Panel (b) of the same figures shows the sum of depths of two edge components as a function of the energy of $\texttt{edge}_2$. If the energy of $\texttt{edge}_2$ component is in acceptable range, these values are consistent within their errors with the maximum depths derived from the phase-resolved fitting with single absorption edge component, which are indicated by horizontal dashed lines in the same panels.

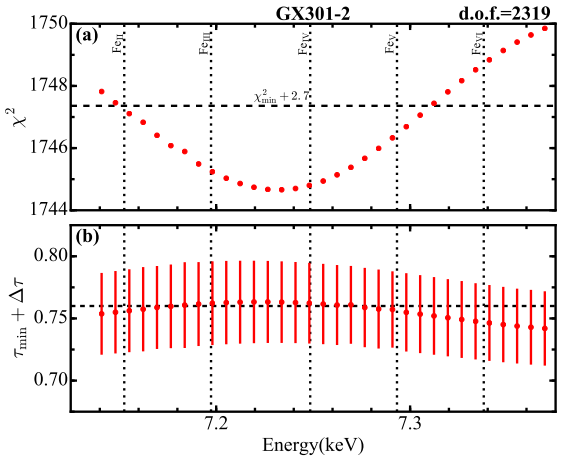

Figure 6.16: (a) Resultant χ^2 values as a function of energy of the iron K-edge ($\texttt{edge}_2$), obtained from the fitting with two absorption edge components with the number of degrees of freedom being 2319 for GX 301-2. The horizontal dashed lines represents the 90% confidence level. The expected energies of iron K-edge for some cases of ionization state are indicated by vertical dotted lines. (b) The sum of depths of the two absorption edge components. The horizontal dashed lines indicates the maximum depth across the pulse phase, which is obtained from the phase-resolved fitting with the single absorption edge component.

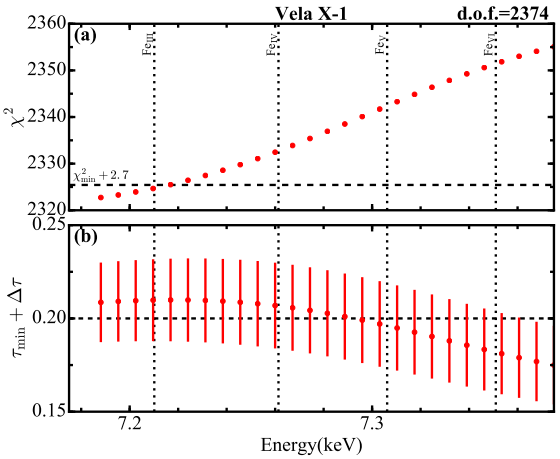

Figure 6.17: The same as Figure 6.16, but results for Vela X-1 with the number of degrees of freedom being 2374.

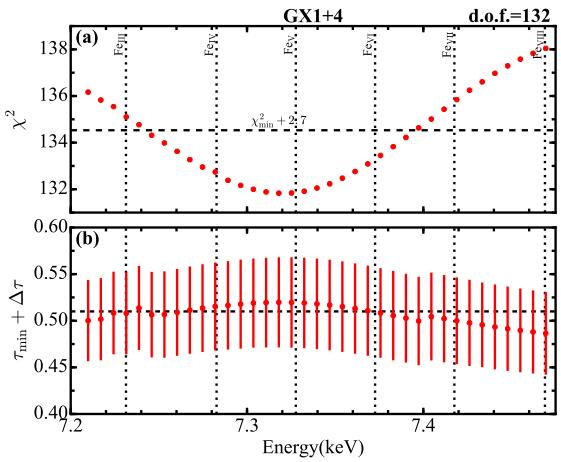

Figure 6.18: The same as Figure 6.16, but results for GX 1+4 with the number of degrees of freedom being 132.

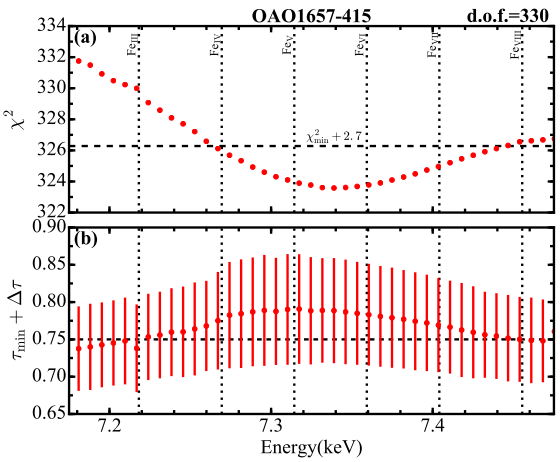

Figure 6.19: The same as Figure 6.16, but results for OAO 1657-415 with the number of degrees of freedom being 330.

Now, we can estimate the physical properties, the density and the distance, of the absorbing matter existing within the Alfvén radius with the ionization state obtained from above additional analysis. The determined ionization state of iron ($< \mathrm{Fe}_{\mathrm{VIII}}$, which is the highest ionization state in all of four sources) corresponds to a value of the ionization parameter ξ of less than 44.7 ($\log \xi < 1.65$) in the case of optically thick plasma (Kallman & McCray 1982; their model 4). Therefore the absorbing matter existing within the Alfvén radius should satisfy the requirement $nr^2 > 2.2 \times 10^{35}$ cm^{-1} by assuming $L_{\mathrm{X}} = 10^{37}$ ergs s^{-1}, so as to satisfy the observed ionization state. With this required condition, the acceptable region on r-n plane shown in Figure 6.15 is modified as shown in Figure 6.20. As a result, the restriction on both of the number density of the matter, n, and the distance between the matter and NS, r becomes laxer, because that on the ionization parameter ξ becomes laxer.

Consequently, if accreting matter along the magnetic field lines at the Alfvén radius is responsible for the absorption along the line of sight with a particles density of $n = 10^{18.5}$ cm^{-3}, and in which iron atoms are ionization state of $< \mathrm{Fe}_{\mathrm{VIII}}$, it forms a structure whose the geometric thickness along the line of sight is $\sim 10^{4.5}$ cm, which is three times larger than the estimated value from the accretion flow model stated in § 6.3.3.

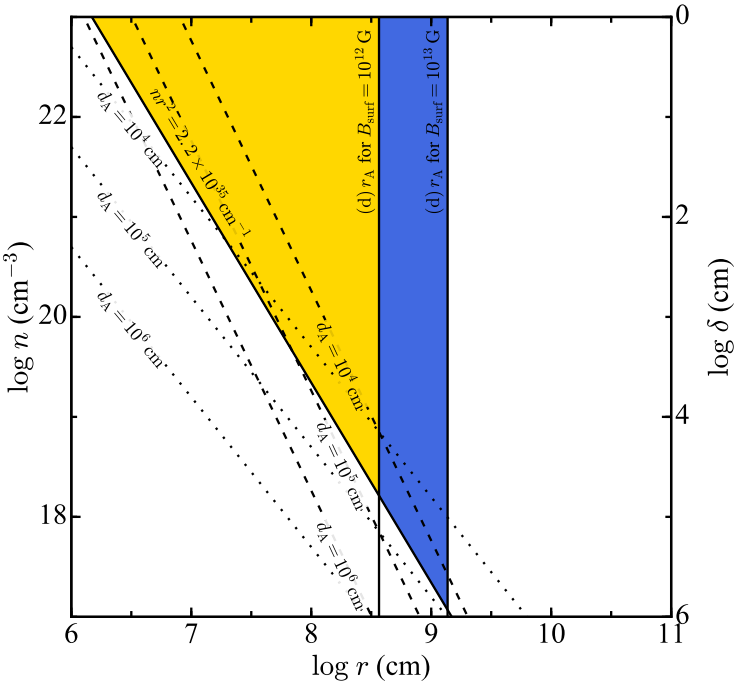

Figure 6.20: The same as Figure 6.15, but the requirement of the ionization state is given as $nr^2 > 2.2 \times 10^{35}$ cm^{-1}. See text for details.

The asymmetric reprocessing region, such as the accretion flow along the magnetic field lines within the Alfvén radius, may produce the pulsations in the fluorescent iron line observed with *Suzaku*, although the finite light speed effect is proposed the origin of the fluorescence line flux modulation with pulse phase and demonstrated in § 6.2.2. When the matter is trapped in the magnetosphere of the NS, its relative orientation to the X-ray beam does not

change with the rotation of the NS. If the iron line photons are isotropically emitted from such trapped matter, the pulse modulation of the line flux cannot be observed. However, when the thickness of the $N_{\rm H} > 5 \times 10^{23}$ cm^{-2}, which corresponds to the estimated value from the iron K-edge depth, the fluorescence iron line photons are not emitted with the same intensity in all direction, in other words, the reprocessing site emits fluorescence iron line photons anisotropically. Then, we can see the modulation of the fluorescence iron line flux with the rotation of the NS.

However, the accretion flow is just one of the possibility for the origin attributing to the pulse phase modulation of the line flux. The accretion wake is proposed as an iron fluorescence emission site with asymmetric structure, which surrounds the NS incompletely, by Choi et al. (1996) and Watanabe et al. (2006). Choi et al. (1996) reports Vela X-1 indicated the pulse phase modulation of iron line flux during the dip interval in the *Ginga* observation, which are interpreted that the accretion wake along the line of sight originates the iron fluorescent emission, while data obtained out of the dip in the observation indicated no significant modulation. Watanabe et al. (2006) suggests that the extra EW of the iron emission line of Vela X-1 at its orbital phase of 0.5, which can not be explained by the stellar wind alone, but can be attributed to the accretion wake. The emission line originated from the accretion wake therefore can be depended on the orbital phase. On the other hands, the modulation due to the asymmetric structure of the accretion flow should not change with the orbital phase. Therefore, the observation of the spin phase modulation at the various orbital phases would help to distinguish them. In addition to this, the observation of the spin phase modulation of center energy of line or line broadening must be helpful to determine the emission site of the iron line.

Moreover, when the modulation of the absorption edge depth with pulse phase originated in asymmetric structure of the accreting matter co-rotating with the pulsar spin is occurred, a variation of the ionization state of the matter along the line of sight is observed at the same time. Therefore the energy modulation of the absorption edge with pulse phase can be observed, if one observes with higher energy resolution.

Chapter 7

Conclusion

We performed a study of the APXPs focusing on the emission line and the absorption edge of iron, and investigated the properties of the matter surrounding the pulsar and related its strong magnetic field.

The detailed phase-averaged and phase-resolved spectroscopies of the X-ray pulsars were carried out by using the *Suzaku* observation. As results, iron K_α emission lines were observed at almost 6.40 keV from the all sources in our samples. We confirmed that these iron emission lines are produced through the fluorescent reprocessing of the X-rays from the X-ray pulsar by a low-ionized matter surrounding it. Clear modulations of the flux of the iron K_α emission line according to spin phase of the pulsar were detected from 4U 1907+097, 4U 1538-522, GX 301-2, and GX 1+4. We point out the apparent flux modulation of emission lines with rotation period of NS, due to the finite speed of light (we call this effect the "finite light speed effect"), if the mechanism of emission line is a kind of reprocessing, such as the fluorescence by X-ray irradiation from X-ray pulsars. We apply this effect to the observed spin modulation of the iron line flux of GX 1+4, and derive a possible emission site of the iron fluorescent.

We first discovered the significant modulations of the iron K-edge depth with pulse spin period of the NS from GX 301-2, Vela X-1, GX 1+4, and OAO 1657-415. And the same was seen for 4U 1538-522 with poorly statistical significance. The revealed changes of the iron K-edge depth with pulse phase can be explained by an interpretation that the accreting matter captured by the magnetic field lines of the pulsar, which co-rotates with the NS spin, is responsible for the absorption edge. From the observational results of the emission line and absorption edge of iron, we also speculate that iron surrounding X-ray pulsar distributes in the two region divided by the Alfvén radius, where the iron is in different physical conditions of ionization state and geometry. In particular, we propose that a structure of the accretion flow within the Alfvén radius is a flat form such as accretion curtain, and then we suggest that the asymmetry structure of the accreting matter within the Alfvén radius is another possible origin to be responsible for the line flux modulation with the pulse phase.

Bibliography

Anderson, S. F., Wachter, S., Margon, B., et al. 1994, ApJ, 436, 319

Asami, F., Enoto, T., Iwakiri, W., et al. 2014, PASJ, 66, 44

Ash, T. D. C., Reynolds, A. P., Roche, P., et al. 1999, MNRAS, 307, 357

Audley, M. D., Nagase, F., Mitsuda, K., Angelini, L., & Kelley, R. L. 2006, MNRAS, 367, 1147

Bai, T. 1980, ApJ, 239, 328

Barnard, J. J., & Arons, J. 1981, in BAAS, Vol. 13, Bulletin of the American Astronomical Society, 851

Barnstedt, J., Staubert, R., Santangelo, A., et al. 2008, A&A, 486, 293

Barthelmy, S. D., Barbier, L. M., Cummings, J. R., et al. 2005, Space Sci. Rev., 120, 143

Basko, M. M. 1978, ApJ, 223, 268

—. 1980, A&A, 87, 330

Basko, M. M., & Sunyaev, R. A. 1976, MNRAS, 175, 395

Becker, P. A., & Wolff, M. T. 2005a, ApJL, 621, L45

—. 2005b, ApJ, 630, 465

—. 2007, ApJ, 654, 435

Bellm, E. C., Fürst, F., Pottschmidt, K., et al. 2014, ApJ, 792, 108

Bildsten, L., Chakrabarty, D., Chiu, J., et al. 1997, ApJS, 113, 367

Blay, P., Negueruela, I., Reig, P., et al. 2006, A&A, 446, 1095

Blondin, J. M., Kallman, T. R., Fryxell, B. A., & Taam, R. E. 1990, ApJ, 356, 591

Blum, S., & Kraus, U. 2000, ApJ, 529, 968

Bodaghee, A., Rahoui, F., Tomsick, J. A., & Rodriguez, J. 2012, ApJ, 751, 113

Bodaghee, A., Walter, R., Zurita Heras, J. A., et al. 2006, A&A, 447, 1027

Bodaghee, A., Courvoisier, T. J.-L., Rodriguez, J., et al. 2007, A&A, 467, 585

Boerner, G., Hayakawa, S., Nagase, F., & Anzer, U. 1987, A&A, 182, 63

Boldt, E., & Leiter, D. 1987, ApJL, 322, L1

Bondi, H., & Hoyle, F. 1944, MNRAS, 104, 273

Bonnet-Bidaud, J. M., & Mouchet, M. 1998, A&A, 332, L9

Brainerd, J. J., & Meszaros, P. 1991, ApJ, 369, 179

Burderi, L., Di Salvo, T., Riggio, A., et al. 2010, A&A, 515, A44

Caballero, I., Pottschmidt, K., Marcu, D. M., et al. 2013, ApJL, 764, L23

Camero-Arranz, A., Pottschmidt, K., Finger, M. H., et al. 2012, A&A, 546, A40

Camero Arranz, A., Wilson, C. A., Finger, M. H., & Reglero, V. 2007, A&A, 473, 551

Chakrabarty, D. 1998, ApJ, 492, 342

Chakrabarty, D., & Roche, P. 1997, ApJ, 489, 254

Chakrabarty, D., Grunsfeld, J. M., Prince, T. A., et al. 1993, ApJL, 403, L33

Choi, C. S., Dotani, T., Day, C. S. R., & Nagase, F. 1996, ApJ, 471, 447

Choi, C. S., Nagase, F., Makino, F., et al. 1994, ApJ, 437, 449

Clark, G. W. 2000, ApJL, 542, L131

Clark, G. W., Woo, J. W., Nagase, F., Makishima, K., & Sakao, T. 1990, ApJ, 353, 274

Coburn, W., Heindl, W. A., Rothschild, R. E., et al. 2002, ApJ, 580, 394

Coe, M. J., Payne, B. J., Longmore, A., & Hanson, C. G. 1988, MNRAS, 232, 865

Coe, M. J., Roche, P., Everall, C., et al. 1994, MNRAS, 270, L57

Coe, M. J., Bird, A. J., Hill, A. B., et al. 2007, MNRAS, 378, 1427

Corbet, R. H. D. 1984, A&A, 141, 91

—. 1986, MNRAS, 220, 1047

Corbet, R. H. D., Markwardt, C. B., & Tueller, J. 2007, ApJ, 655, 458

Corbet, R. H. D., & Mukai, K. 2002, ApJ, 577, 923

Corbet, R. H. D., Sokoloski, J. L., Mukai, K., Markwardt, C. B., & Tueller, J. 2008, ApJ, 675, 1424

Cox, A. N., ed. 2000, Allen's astrophysical quantities (AIP Press, Springer)

Cox, N. L. J., Kaper, L., & Mokiem, M. R. 2005, A&A, 436, 661

dal Fiume, D., Orlandini, M., Cusumano, G., et al. 1998, A&A, 329, L41

Davidson, K., & Ostriker, J. P. 1973, ApJ, 179, 585

Day, C. S. R., Nagase, F., Asai, K., & Takeshima, T. 1993, ApJ, 408, 656

Doroshenko, V., Santangelo, A., & Suleimanov, V. 2011, A&A, 529, A52

Dotani, T., Kii, T., Nagase, F., et al. 1989, PASJ, 41, 427

Ebisawa, K., Day, C. S. R., Kallman, T. R., et al. 1996, PASJ, 48, 425

Eggleton, P. P. 1983, ApJ, 268, 368

Elsner, R. F., & Lamb, F. K. 1977, ApJ, 215, 897

Endo, T., Ishida, M., Masai, K., et al. 2002, ApJ, 574, 879

Endo, T., Nagase, F., & Mihara, T. 2000, PASJ, 52, 223

Enoto, T., Makishima, K., Terada, Y., et al. 2008, PASJ, 60, S57

Enoto, T., Sasano, M., Yamada, S., et al. 2014, ApJ, 786, 127

Farinelli, R., Ceccobello, C., Romano, P., & Titarchuk, L. 2012, A&A, 538, A67

Farinelli, R., Ferrigno, C., Bozzo, E., & Becker, P. A. 2016, A&A, 591, A29

Ferrigno, C., Becker, P. A., Segreto, A., Mineo, T., & Santangelo, A. 2009, A&A, 498, 825

Ferrigno, C., Farinelli, R., Bozzo, E., et al. 2013, A&A, 553, A103

Finger, M. H., Ikhsanov, N. R., Wilson-Hodge, C. A., & Patel, S. K. 2010, ApJ, 709, 1249

Finger, M. H., Koh, D. T., Nelson, R. W., et al. 1996a, Nature, 381, 291

Finger, M. H., Wilson, R. B., & Harmon, B. A. 1996b, ApJ, 459, 288

Frank, J., King, A., & Raine, D. J. 2002, Accretion Power in Astrophysics: Third Edition (Cambridge University Press), 398

Fukazawa, Y., Mizuno, T., Watanabe, S., et al. 2009, PASJ, 61, S17

Fürst, F., Kreykenbohm, I., Suchy, S., et al. 2011a, A&A, 525, A73

Fürst, F., Pottschmidt, K., Kreykenbohm, I., et al. 2012, A&A, 547, A2

Fürst, F., Suchy, S., Kreykenbohm, I., et al. 2011b, A&A, 535, A9

Fürst, F., Pottschmidt, K., Wilms, J., et al. 2014, ApJ, 780, 133

Galloway, D. K., Giles, A. B., Greenhill, J. G., & Storey, M. C. 2000, MNRAS, 311, 755

Galloway, D. K., Giles, A. B., Wu, K., & Greenhill, J. G. 2001, MNRAS, 325, 419

Ghosh, P., & Lamb, F. K. 1979, ApJ, 232, 259

Giacconi, R., Gursky, H., Kellogg, E., Schreier, E., & Tananbaum, H. 1971, ApJL, 167, L67

Giacconi, R., Gursky, H., Paolini, F. R., & Rossi, B. B. 1962, Physical Review Letters, 9, 439

Gruber, D. E., & Rothschild, R. E. 1984, ApJ, 283, 546

Grundstrom, E. D., Blair, J. L., Gies, D. R., et al. 2007, ApJ, 656, 431

Hatchett, S., & Weaver, R. 1977, ApJ, 215, 285

Hemphill, P. B., Rothschild, R. E., Markowitz, A., et al. 2014, ApJ, 792, 14

Hemphill, P. B., Rothschild, R. E., Fürst, F., et al. 2016, MNRAS, 458, 2745

Henke, B. L., Gullikson, E. M., & Davis, J. C. 1993, Atomic Data and Nuclear Data Tables, 54, 181

Hickox, R. C., Narayan, R., & Kallman, T. R. 2004, ApJ, 614, 881

Hinkle, K. H., Fekel, F. C., Joyce, R. R., et al. 2006, ApJ, 641, 479

Hung, L.-W., Hickox, R. C., Boroson, B. S., & Vrtilek, S. D. 2010, ApJ, 720, 1202

Ichimaru, S. 1978, ApJ, 224, 198

Illarionov, A. F., & Sunyaev, R. A. 1975, A&A, 39, 185

in 't Zand, J. J. M., Baykal, A., & Strohmayer, T. E. 1998, ApJ, 496, 386

Inoue, H. 1985, Space Sci. Rev., 40, 317

Ishisaki, Y., Maeda, Y., Fujimoto, R., et al. 2007, PASJ, 59, 113

Ives, J. C., Sanford, P. W., & Bell Burnell, S. J. 1975, Nature, 254, 578

Iwakiri, W. B., Terada, Y., Mihara, T., et al. 2012, ApJ, 751, 35

Jaisawal, G. K., & Naik, S. 2014, Bulletin of the Astronomical Society of India, 42, 147

—. 2015, MNRAS, 453, L21

Jaisawal, G. K., Naik, S., & Chenevez, J. 2018, MNRAS, 474, 4432

Jaisawal, G. K., Naik, S., & Epili, P. 2016, MNRAS, 457, 2749

Jaisawal, G. K., Naik, S., & Paul, B. 2013, ApJ, 779, 54

Janot-Pacheco, E., Ilovaisky, S. A., & Chevalier, C. 1981, A&A, 99, 274

Jenke, P. A., Finger, M. H., Wilson-Hodge, C. A., & Camero-Arranz, A. 2012, ApJ, 759, 124

Jones, C. A., Chetin, T., & Liller, W. 1974, ApJL, 190, L1

Kaaret, P., Cusumano, G., & Sacco, B. 2000, ApJL, 542, L41

Kaaret, P., Piraino, S., Halpern, J., & Eracleous, M. 1999, ApJ, 523, 197

Kaastra, J. S., & Mewe, R. 1993, A&AS, 97, 443

Kallman, T. R., & McCray, R. 1982, ApJS, 50, 263

Kaper, L., Lamers, H. J. G. L. M., Ruymaekers, E., van den Heuvel, E. P. J., & Zuiderwijk, E. J. 1995, A&A, 300, 446

Kaper, L., van der Meer, A., & Najarro, F. 2006, A&A, 457, 595

Kelley, R. L., Mitsuda, K., Allen, C. A., et al. 2007, PASJ, 59, 77

Klein, R. I., Arons, J., Jernigan, G., & Hsu, J. J.-L. 1996, ApJL, 457, L85

Klochkov, D. 2007, PhD thesis, Institut für Astronomie und Astrophysik, Universität Tübingen

Koh, D. T., Bildsten, L., Chakrabarty, D., et al. 1997, ApJ, 479, 933

Kohmura, T., Kitamoto, S., & Torii, K. 2001, ApJ, 562, 943

Kokubun, M., Makishima, K., Takahashi, T., et al. 2007, PASJ, 59, 53

Kotani, T., Dotani, T., Nagase, F., et al. 1999, ApJ, 510, 369

Koyama, K. 1985, in Galactic and Extra-Galactic Compact X-ray Sources, ed. Y. Tabaka & W. H. G. Lewin, 153

Koyama, K., Tsunemi, H., Dotani, T., et al. 2007, PASJ, 59, 23

Kreykenbohm, I., Wilms, J., Coburn, W., et al. 2004, A&A, 427, 975

Kreykenbohm, I., Wilms, J., Kretschmar, P., et al. 2008, A&A, 492, 511

Krimm, H. A., Holland, S. T., Corbet, R. H. D., et al. 2013, ApJS, 209, 14

Kühnel, M., Müller, S., Kreykenbohm, I., et al. 2013, A&A, 555, A95

Lamb, F. K., Pethick, C. J., & Pines, D. 1973, ApJ, 184, 271

Lang, F. L., Levine, A. M., Bautz, M., et al. 1981, ApJL, 246, L21

Langer, S. H., & Rappaport, S. 1982, ApJ, 257, 733

Leahy, D. A. 1987, A&A, 180, 275

Leahy, D. A., & Matsuoka, M. 1990, ApJ, 355, 627

Leahy, D. A., Matsuoka, M., Kawai, N., & Makino, F. 1989, MNRAS, 237, 269

Lei, Y.-J., Chen, W., Qu, J.-L., et al. 2009, ApJ, 707, 1016

Levine, A., Ma, C. P., McClintock, J., et al. 1988, ApJ, 327, 732

Levine, A. M., Bradt, H., Cui, W., et al. 1996, ApJL, 469, L33

Levine, A. M., Rappaport, S., Remillard, R., & Savcheva, A. 2004, ApJ, 617, 1284

Levine, A. M., Rappaport, S. A., & Zojcheski, G. 2000, ApJ, 541, 194

Liu, Q. Z., van Paradijs, J., & van den Heuvel, E. P. J. 2006, A&A, 455, 1165

—. 2007, A&A, 469, 807

Longair, M. S. 2011, High Energy Astrophysics (Cambridge University Press)

Magdziarz, P., & Zdziarski, A. A. 1995, MNRAS, 273, 837

Maitra, C., & Paul, B. 2013a, ApJ, 771, 96

—. 2013b, ApJ, 763, 79

Maitra, C., Paul, B., & Naik, S. 2012, MNRAS, 420, 2307

Makino, F., Leahy, D. A., & Kawai, N. 1985, Space Sci. Rev., 40, 421

Makishima, K. 1986, in Lecture Notes in Physics, Berlin Springer Verlag, Vol. 266, The Physics of Accretion onto Compact Objects, ed. K. O. Mason, M. G. Watson, & N. E. White, 249

Makishima, K., Koyama, K., Hayakawa, S., & Nagase, F. 1987, ApJ, 314, 619

Makishima, K., Mihara, T., Nagase, F., & Tanaka, Y. 1999, ApJ, 525, 978

Makishima, K., Ohashi, T., Sakao, T., et al. 1988, Nature, 333, 746

Makishima, K., Ohashi, T., Kawai, N., et al. 1990, PASJ, 42, 295

Manchester, R. N. 1995, Journal of Astrophysics and Astronomy, 16, 233

Masetti, N., Dal Fiume, D., Amati, L., et al. 2004, A&A, 423, 311

Masetti, N., Orlandini, M., Palazzi, E., Amati, L., & Frontera, F. 2006, A&A, 453, 295

Mason, A. B., Clark, J. S., Norton, A. J., Negueruela, I., & Roche, P. 2009, A&A, 505, 281

Mason, K. O., & Cordova, F. A. 1982, ApJ, 262, 253

Mason, K. O., Murdin, P. G., Parkes, G. E., & Visvanathan, N. 1978, MNRAS, 184, 45P

Matsumoto, H., Nakajima, H., Yamaguchi, H., et al. 2006, in Proc. SPIE, Vol. 6266, Society of Photo-Optical Instrumentation Engineers (SPIE) Conference Series, 626641

McCray, R. A., Shull, J. M., Boynton, P. E., et al. 1982, ApJ, 262, 301

Meszaros, P., & Nagel, W. 1985a, ApJ, 298, 147

—. 1985b, ApJ, 299, 138

Mihara, T. 1995, PhD thesis, , Dept. of Physics, Univ. of Tokyo (M95), (1995)

Mihara, T., Nakajima, M., Sugizaki, M., et al. 2011, PASJ, 63, S623

Miller, G. S. 1996, ApJL, 468, L29

Mitsuda, K., Bautz, M., Inoue, H., et al. 2007, PASJ, 59, 1

Morel, T., & Grosdidier, Y. 2005, MNRAS, 356, 665

Morgan, W. W., Code, A. D., & Whitford, A. E. 1955, ApJS, 2, 41

Mori, H., Iizuka, R., Shibata, R., et al. 2005, PASJ, 57, 245

Motch, C., & Janot-Pacheco, E. 1987, A&A, 182, L55

Mukherjee, U., & Paul, B. 2004, A&A, 427, 567

Mukherjee, U., Raichur, H., Paul, B., Naik, S., & Bhatt, N. 2006, Journal of Astrophysics and Astronomy, 27, 411

Nagase, F. 1989, PASJ, 41, 1

Nagase, F., Hayakawa, S., Sato, N., Masai, K., & Inoue, H. 1986, PASJ, 38, 547

Nagel, W. 1981a, ApJ, 251, 288

—. 1981b, ApJ, 251, 278

Nahar, S. N., Bautista, M. A., & Pradhan, A. K. 1997, ApJ, 479, 497

Naik, S., & Jaisawal, G. K. 2015, Research in Astronomy and Astrophysics, 15, 537

Naik, S., Maitra, C., Jaisawal, G. K., & Paul, B. 2013, ApJ, 764, 158

Naik, S., & Paul, B. 2003, A&A, 401, 265

Naik, S., Paul, B., & Ali, Z. 2011a, ApJ, 737, 79

Naik, S., Paul, B., & Callanan, P. J. 2005, ApJ, 618, 866

Naik, S., Paul, B., Kachhara, C., & Vadawale, S. V. 2011b, MNRAS, 413, 241

Naik, S., Dotani, T., Terada, Y., et al. 2008, ApJ, 672, 516

Nakajima, H., Yamaguchi, H., Matsumoto, H., et al. 2008, PASJ, 60, S1

Negueruela, I., Reig, P., Coe, M. J., & Fabregat, J. 1998, A&A, 336, 251

Nelson, R. W., Salpeter, E. E., & Wasserman, I. 1993, ApJ, 418, 874

Nespoli, E., Fabregat, J., & Mennickent, R. E. 2010, A&A, 516, A94

Odaka, H., Khangulyan, D., Tanaka, Y. T., et al. 2013, ApJ, 767, 70

—. 2014, ApJ, 780, 38

Ohashi, T., Inoue, H., Koyama, K., et al. 1984, PASJ, 36, 699

Okazaki, A. T., & Negueruela, I. 2001, A&A, 377, 161

Ozawa, M., Uchiyama, H., Matsumoto, H., et al. 2009, PASJ, 61, S1

Parkes, G. E., Murdin, P. G., & Mason, K. O. 1978, MNRAS, 184, 73P

—. 1980, MNRAS, 190, 537

Paul, B., Dewangan, G. C., Sako, M., et al. 2002, in 8th Asian-Pacific Regional Meeting, Volume II, ed. S. Ikeuchi, J. Hearnshaw, & T. Hanawa, 355–356

Pradhan, P., Maitra, C., Paul, B., Islam, N., & Paul, B. C. 2014, MNRAS, 442, 2691

Pradhan, P., Paul, B., Paul, B. C., Bozzo, E., & Belloni, T. M. 2015, MNRAS, 454, 4467

Pravdo, S. H., Becker, R. H., Boldt, E. A., et al. 1977, ApJL, 215, L61

Pringle, J. E., & Rees, M. J. 1972, A&A, 21, 1

Raichur, H., & Paul, B. 2010, MNRAS, 401, 1532

Rea, N., Stella, L., Israel, G. L., et al. 2005, MNRAS, 364, 1229

Reig, P. 2011, Ap&SS, 332, 1

Reig, P., Chakrabarty, D., Coe, M. J., et al. 1996, A&A, 311, 879

Reig, P., & Coe, M. J. 1999, MNRAS, 302, 700

Reig, P., Słowikowska, A., Zezas, A., & Blay, P. 2010, MNRAS, 401, 55

Reig, P., Torrejón, J. M., Negueruela, I., et al. 2009, A&A, 494, 1073

Reynolds, A. P., Bell, S. A., & Hilditch, R. W. 1992, MNRAS, 256, 631

Reynolds, A. P., Quaintrell, H., Still, M. D., et al. 1997, MNRAS, 288, 43

Riquelme, M. S., Torrejón, J. M., & Negueruela, I. 2012, A&A, 539, A114

Rivers, E., Markowitz, A., Pottschmidt, K., et al. 2010, ApJ, 709, 179

Sadakane, K., Hirata, R., Jugaku, J., et al. 1985, ApJ, 288, 284

Sako, M., Kahn, S. M., Paerels, F., et al. 2002, in High Resolution X-ray Spectroscopy with XMM-Newton and Chandra, ed. G. Branduardi-Raymont

Sasano, M., Makishima, K., Sakurai, S., Zhang, Z., & Enoto, T. 2014, PASJ, 66, 35

Schönherr, G., Wilms, J., Kretschmar, P., et al. 2007, A&A, 472, 353

Serlemitsos, P. J., Soong, Y., Chan, K.-W., et al. 2007, PASJ, 59, 9

Staubert, R., Klochkov, D., & Wilms, J. 2009, A&A, 500, 883

Staubert, R., Klochkov, D., Wilms, J., et al. 2014, A&A, 572, A119

Staubert, R., Pottschmidt, K., Doroshenko, V., et al. 2011, A&A, 527, A7

Steele, I. A., Negueruela, I., Coe, M. J., & Roche, P. 1998, MNRAS, 297, L5

Suchy, S., Fürst, F., Pottschmidt, K., et al. 2012, ApJ, 745, 124

Suchy, S., Pottschmidt, K., Rothschild, R. E., et al. 2011, ApJ, 733, 15

Sugizaki, M., Yamamoto, T., Mihara, T., Nakajima, M., & Makishima, K. 2015, PASJ, 67, 73

Sugizaki, M., Mihara, T., Serino, M., et al. 2011, PASJ, 63, S635

Takahashi, T., Abe, K., Endo, M., et al. 2007, PASJ, 59, 35

Tanaka, Y. 1986, in Lecture Notes in Physics, Berlin Springer Verlag, Vol. 255, IAU Colloq. 89: Radiation Hydrodynamics in Stars and Compact Objects, ed. D. Mihalas & K.-H. A. Winkler, 198

Tarter, C. B., Tucker, W. H., & Salpeter, E. E. 1969, ApJ, 156, 943

Tawa, N., Hayashida, K., Nagai, M., et al. 2008, PASJ, 60, S11

Terada, Y., Mihara, T., Nakajima, M., et al. 2006, ApJL, 648, L139

Terada, Y., Enoto, T., Miyawaki, R., et al. 2008, PASJ, 60, S25

Thompson, T. W. J., & Rothschild, R. E. 2009, ApJ, 691, 1744

Thompson, T. W. J., Tomsick, J. A., Rothschild, R. E., in't Zand, J. J. M., & Walter, R. 2006, ApJ, 649, 373

Titarchuk, L. 1994, ApJ, 434, 570

Todoroki, S., Kitamoto, S., Yoshida, Y., & Murakami, H. 2012, PASJ, 64, 101

Uchiyama, H., Ozawa, M., Matsumoto, H., et al. 2009, PASJ, 61, S9

van der Meer, A., Kaper, L., van Kerkwijk, M. H., Heemskerk, M. H. M., & van den Heuvel, E. P. J. 2007, A&A, 473, 523

Vasco, D., Staubert, R., Klochkov, D., et al. 2013, A&A, 550, A111

Verner, D. A., Ferland, G. J., Korista, K. T., & Yakovlev, D. G. 1996, ApJ, 465, 487

Vrtilek, S. D., Raymond, J. C., Boroson, B., & McCray, R. 2005, ApJ, 626, 307

Warner, B., Peters, W. L., Hubbard, W. B., & Nather, R. E. 1972, MNRAS, 159, 321

Watanabe, S., Sako, M., Ishida, M., et al. 2006, ApJ, 651, 421

Waters, L. B. F. M., & van Kerkwijk, M. H. 1989, A&A, 223, 196

West, B. F., Wolfram, K. D., & Becker, P. A. 2017a, ApJ, 835, 129

—. 2017b, ApJ, 835, 130

White, N. E., Mason, K. O., Huckle, H. E., Charles, P. A., & Sanford, P. W. 1976, ApJL, 209, L119

White, N. E., & Pravdo, S. H. 1979, ApJL, 233, L121

White, N. E., Swank, J. H., & Holt, S. S. 1983, ApJ, 270, 711

Wilms, J., Allen, A., & McCray, R. 2000, ApJ, 542, 914

Wilson, C. A., Finger, M. H., & Camero-Arranz, A. 2008, ApJ, 678, 1263

Wilson, C. A., Finger, M. H., Coe, M. J., Laycock, S., & Fabregat, J. 2002, ApJ, 570, 287

Wojdowski, P., Clark, G. W., Levine, A. M., Woo, J. W., & Zhang, S. N. 1998, ApJ, 502, 253

Wojdowski, P. S., Liedahl, D. A., Sako, M., Kahn, S. M., & Paerels, F. 2003, ApJ, 582, 959

Yahel, R. Z. 1980, ApJ, 236, 911

Yamada, S., Makishima, K., Nakazawa, K., et al. 2011, PASJ, 63, S645

Yamada, S., Uchiyama, H., Dotani, T., et al. 2012, PASJ, 64, 53

Yamaguchi, H., Eriksen, K. A., Badenes, C., et al. 2014, ApJ, 780, 136

Yamamoto, T., Mihara, T., Sugizaki, M., et al. 2014, PASJ, 66, 59

Yamamoto, T., Sugizaki, M., Mihara, T., et al. 2011, PASJ, 63, S751

Yoshida, Y., Kitamoto, S., & Hoshino, A. 2017, ApJ, 849, 116

Yoshida, Y., Kitamoto, S., Suzuki, H., et al. 2017, ApJ, 838, 30

Zane, S., Ramsay, G., Jimenez-Garate, M. A., Willem den Herder, J., & Hailey, C. J. 2004, MNRAS, 350, 506